Three-Dimensional Imaging of Ionospheric Irregularities at Midlatitudes Using Global Navigation Satellite System

Weizheng Fu

Department of Communications and Computer Engineering
Graduate School of Informatics
Kyoto University

This dissertation is submitted for the degree of
Doctor of Philosophy

January 2023

Acknowledgements

With the completion of this thesis, my graduate study is coming to an end. It is my wish to extend my sincere gratitude and high appreciation to my supervisors, Prof. Mamoru Yamamoto and Assoc. Prof. Tatsuhiro Yokoyama of Research Institute for Sustainable Humanosphere (RISH), Kyoto University. Their consistent guidance and tireless assistance during my Ph.D study enabled me to finish my research and helped me become an independent researcher.

I would also like to express my great appreciation to Dr. Nicholas Ssessanga for his guidance towards the success of this study. Without his help, my research would not have progressed so smoothly.

Appreciation also goes to Prof. Hiroyuki Hashiguchi and Assoc. Prof. Koji Nishimura who provided valuable suggestions and comments on my research. Thanks to the laboratory secretary Ms. Sachiko Shikata for her hospitality, logistical, technical and work support during my study. Thanks to my friends, Yuan Wang, Erlu Chuai, Peng Liu, Lehui Wei, and Zezhong Li. I will never forget the time in Kyoto.

Thanks to Prof. Guanyi Ma at National Astronomical Observatories, Chinese Academy of Sciences (NAOC) who assisted me in many ways to finish up this thesis.

Special thanks go to Japan Science and Technology Agency (JST) for my Ph.D degree scholarship.

Last but not least, I gratefully acknowledge the support from my parents and girl friend Xunyue for their dedication. It was their unconditional love that gave me strength to complete my long career as a student.

Abstract

The Earth's ionosphere is a partially ionized gas (plasma) that envelops the Earth from approximately 60 to 1000 km in altitude, exhibiting a dynamic dispersive nature in space and time. Characterizing and understanding the ionospheric irregularities is of paramount importance because of their impact on the propagation of trans-ionospheric radio waves used in applications such as satellite navigation and radio astronomy research.

The nighttime mid-latitude ionosphere is frequently perturbed with two main classes of irregularities: medium-scale traveling ionospheric disturbances (MSTIDs) in the F region and sporadic E (Es) in the E region. Earlier observations and theoretical analysis on such ionospheric irregularities support the postulation of coupled E and F regions and coupled conjugate hemispheres. The research of this thesis attempts at asserting this notion and elucidating the causes and effects of the coupled ionosphere while using Global Navigation Satellite System (GNSS) total electron content (TEC) measurements. For the last three decades, the cost-effective use of GNSS has expanded our ability to monitor ionospheric dynamics in great detail and near-real time. However, the study of the coupled ionosphere using GNSS-TEC remains challenging due to the mixture of E- and F-region perturbations under the commonly used single-thin-shell approximation. A coherent two-dimensional (2-D) and three-dimensional (3-D) picture of the dynamics from both E and F regions is essential in interpreting the physical underpinning.

In response to this problem, a double-thin-shell model has been developed to parameterize the integrated 3-D density perturbations, wherein the mid-latitude nighttime plasma instabilities are assumed to be concentrated at E and F layers. By using the double-thin-shell approach, four days with events of nighttime MSTIDs were used to investigate the E-F coupling over Japan and interhemispheric coupling over Japan and Australia (geomagnetic conjugate regions). For the first time, the morphology and dynamics of the ionosphere perturbations in both E and F regions can be obtained simultaneously with ground-based GNSS TEC. In the local E and F regions, reconstruction results support the E-F coupling theory: the coexisting E- and F-region irregularities are interconnected by magnetic field lines, sharing similar alignments, propagation directions and phase velocities. In the hemisphere-coupled ionospheres, reconstruction results provide the evidence that F-region geomagnetic conju-

gate irregularities in both hemispheres are mainly driven by the Es layers in the summer hemisphere. The Es layer in the summer hemisphere subsequently triggers local E-F coupling and interhemispheric coupling. Additionally, supplemented with multi-source data from ionosondes, ICON (neutral wind), COSMIC (electron density) and Swarm (magnetic field), observation results suggest that in the winter hemisphere, Es layers show dissipation during the interhemispheric coupling process; thermospheric winds and non-equipotential magnetic field lines are presumed candidates for the interhemispheric asymmetry in MSTIDs amplitudes and growth rates.

Although the double-thin-shell model has proved to be effective for analyzing the E-F coupling process, the missing height dimension in these 2-D analyses may pose limitations on the information that we can infer. Therefore, a continuous and broad 3-D distribution of ionospheric electron densities (IEDs) during the E-F coupling is required. In the 3-D tomography for ionospheric irregularities, the reconstruction of Es layer is difficult due to its thin thickness and the representation errors in tomography. To overcome these problems, a novel 3-D computerized ionospheric tomography (CIT) technique has been developed to reconstruct the daytime sporadic E by using the dense GNSS-TEC measurements over Japan. The vertical solutions in the E region were constrained by using the time-dependent empirical orthogonal functions (EOFs) from a Chapman model function tuned to manually scaled ionosonde observations. A similar method was then applied to the simultaneous 3-D reconstruction of E- and F-region irregularity structures during the E-F coupling. For the first time, the altitude-time variation of the irregularities in both E and F regions can be tracked by CIT with ground-based GNSS-TEC. During the E-F coupling process, a small rise in the Es layers was observed, and the height of F2 peak layer varies in the $\sim$5–50 km range, which is anti-correlated with the F-region perturbations. These 3-D reconstruction results further suggest that the electrodynamic forces dominate the morphology and dynamics of Es and MSTIDs during the nighttime coupling process.

Table of contents

List of figures

List of tables

Abbreviations

AGW	**Atmospheric Gravity Wave**
CIT	**Computerized Ionospheric Tomography**
DOY	**Day of Year**
EIA	**Equatorial Ionization Anomaly**
Es	**Sporadic E**
FAI	**Field Aligned Irregularities**
GEONET	**GNSS Earth Observation Network**
GNSS	**Global Navigation Satellite System**
GPS	**Global Positioning System**
IED	**Ionospheric Electron Density**
IGRF	**International Geomagnetic Reference Field**
IPP	**Ionosphere Pierce Point**
ISR	**Incoherent Scatter Radar**
IRI	**International Reference Ionosphere**
JST	**Japan Standard Time**
LEO	**Low Earth Orbit**
LOS	**Line of Sight**
MEF	**Midlatitude Electric Field Fluctuation**
MMF	**Midlatitude Magnetic Field Fluctuation**
MSTID	**Medium-scale Traveling Ionospheric Disturbance**
MUR	**Middle and Upper Atmosphere Radar**
RTI	**Range-Time-Intensity**
SNR	**Signal-to-Noise Ratio**
STEC	**Slant Total Electron Content**
SVD	**Singular Value Decomposition**
TEC	**Total Electron Content**
TECP	**TEC Perturbation**
VTEC	**Vertical Total Electron Content**

Chapter 1

Introduction

The Earth, in altitudes of about 60 to 1000 km, is engulfed by a dispersive chaotic dynamic quasi-neutral plasma (ionosphere) stratified in layers/regions labeled D (below 90 km), E (90–150 km) and F (150–500 km). At mid- and low-latitudes, two primary ionospheric irregularities are frequently observed: sporadic E (Es) in the ionospheric E region and medium-scale traveling ionospheric disturbances (MSTIDs) in the F region. Both of these irregularities exhibit an occurrence highly correlated with intense trans-ionospheric signal scintillations, which may lead to the information loss and phase slips due to lock-off of satellite signals. The drastic increase and ubiquitous day-to-day dependence of complex inter-connected technological networks on precise space-borne communications or trans-ionospheric signals have elevated the demand to understand and characterize such ionospheric irregularities.

Sporadic E (Es) are thin layers of metallic ion plasma occasionally appearing at altitudes of $\sim$100 km in the ionospheric E region (e.g., Whitehead, 1989). MSTIDs are wave-like plasma density perturbations in the F region with horizontal wavelengths of a few hundred kilometers, phase velocities of $\sim$100 m/s, and periods between 15 to 60 min (Hunsucker, 1982). One of the intriguing aspects of nighttime mid-latitude Es and MSTIDs is the shared northwest-southeast (NW-SE) (northeast-southwest; NE-SW) aligned frontal structures propagating towards the equator-westward direction in the Northern (Southern) Hemisphere. Electrodynamic mechanisms, that is, the Es-layer instability in the E region and the Perkins instability in the F region, are suggested as the probable mechanisms behind these irregularities with directional preference (e.g., Tsunoda and Cosgrove, 2001). However, recent simulation works have found that the growth rates of typical MSTIDs cannot be satisfied by a standalone Perkins instability and inferred a coupled effect involving the Es-layer instability coupled to the Perkins instability (Cosgrove and Tsunoda, 2004; Tsunoda, 2006; Yokoyama et al., 2008). Figure 1.1 shows a schematic diagram of the spatial

relationship between Es and MSTIDs in the Northern Hemisphere during the E-F coupling process. Geomagnetic field lines (**B**) connect the irregularities in two regions, which share a similar wavefront, a common propagation direction, and phase velocity. In fact, the E-F coupling process is more intricate. Studies have found that MSTIDs are simultaneously observed in geomagnetic conjugate regions of different hemispheres with matching crests and troughs (Otsuka et al., 2004). In this interhemispheric coupling process, the polarization electric fields generated by E- and F-region irregularities can be mapped to the opposite hemisphere along the geomagnetic field lines, thus generating the geomagnetic conjugate MSTIDs in different hemispheres, as shown in Figure 1.2.

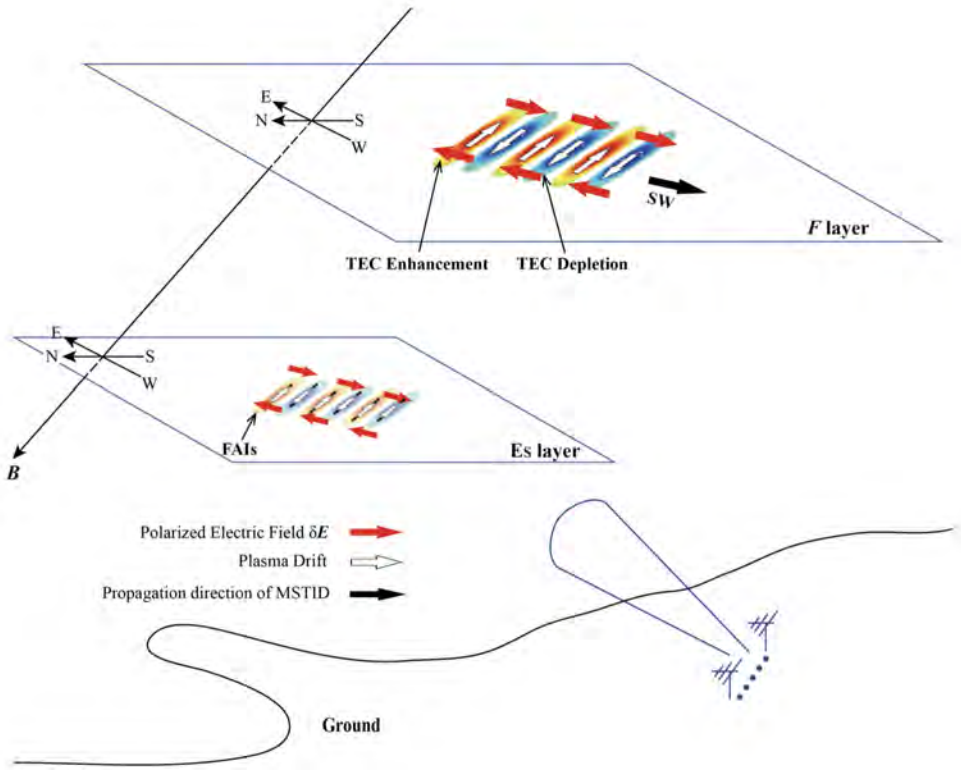

Fig. 1.1 Sketch of the spatial relationship between nighttime Es and MSTIDs in the Northern Hemisphere during the E-F coupling. Adapted from Liu et al. (2019).

In the recent years, the ionospheric local E-F and interhemispheric coupling processes have been analyzed by numerical simulations (Cosgrove, 2007; Cosgrove and Tsunoda, 2004; Tsunoda and Cosgrove, 2001; Yokoyama, 2014; Yokoyama et al., 2009) and joint observational experiments (Hysell et al., 2018; Liu et al., 2019, 2020; Narayanan et al., 2018; Otsuka et al., 2007; Saito et al., 2007; Xie et al., 2020). There is a belief that the generation and development of MSTIDs and conjugate MSTIDs could be related to many factors, such as Es layers, thermospheric winds, and electric/magnetic fields. However, due to the lack of

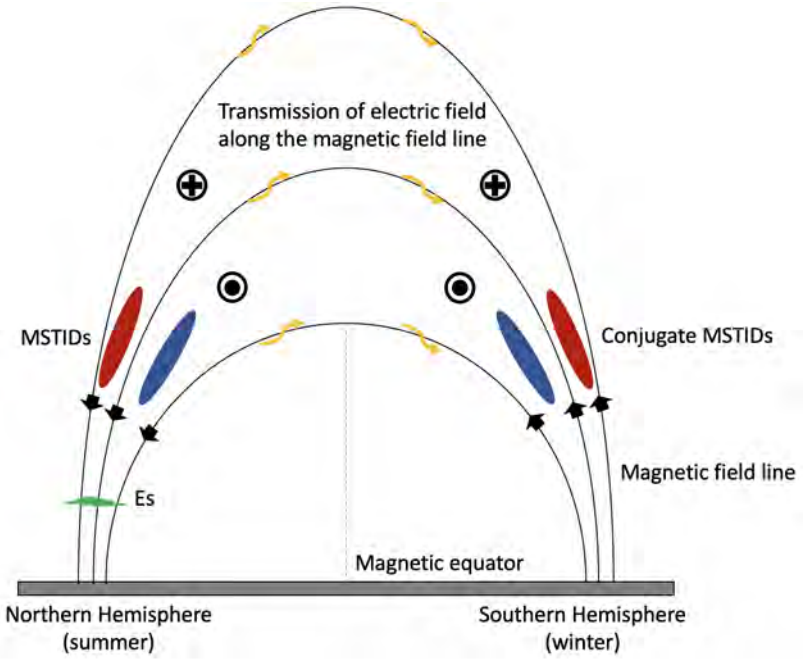

Fig. 1.2 Schematic diagram of the interhemispheric coupling process.

a broad simultaneous observation of ionospheric E and F regions in both hemispheres, the causes and effects of E-F and interhemispheric coupling are not yet fully understood.

For the last three decades, the cost-effective use of Global Navigation Satellite System (GNSS) has expanded our ability to monitor ionospheric dynamics in great detail and near-real time. Total electron content (TEC) is a vital parameter in the study of ionospheric dynamics, which refers to the integration of electron density along the signal propagation path and can be effectively measured by the dual-frequency GNSS receivers. Densely distributed regional and global GNSS receivers have offered a window to probe the structure and analyze the evolution of ionospheric dynamics in detail. However, such two-dimensional (2-D) information has both E- and F-region irregularities intermingle. In addition, most studies have focused only on the simplistic 2-D ionospheric structures, especially in the F region where electron density concentration dominates in the ionosphere. To determine the causes and effects of the coupled ionosphere, information from both the ionospheric E and F regions are important .

The purpose of this thesis is to provide a comprehensive analysis of the irregularity evolution and the key factors that cause and control the local E-F and interhemispheric coupling. Research focuses on the ionosphere over Japan where different types of ionospheric observations are prevalent. Data over Australian continent, the geomagnetic conjugate region of Japan, are also used to analyze the coupling process between different hemispheres. TEC

measurements from regional dense GNSS receiver network are used to reconstruct the 2-D and three-dimensional (3-D) structures of both Es and MSTIDs with high spatiotemporal resolution and high precision. Additionally, data from multiple instruments such as ionosondes, radars, and space-based observations, are also incorporated into the analysis to provide information on the plasma density structuring, thermospheric wind, and electric/magnetic field variations, which can help interpret the MSTID generation and development mechanisms in the E-F coupling and interhemispheric coupling process. This research is expected to contribute to and/or connect to wide different fields, such as ground-based augmentation system (GBAS) in GNSS application, as well as improved skills in predicting and mitigating ionospheric signal scintillation, especially over Japan.

This thesis is divided into six chapters. Chapter 2 provides the background theory pertaining to the Earth's ionosphere, discusses various techniques used to measure ionospheric parameters, and describes more in-depth review of mid-latitude Es and MSTIDs. A novel method of double-thin-shell model for 2-D reconstruction of E-F coupling over Japan is presented and discussed in Chapter 3. In Chapter 4, several cases of nighttime MSTIDs are analyzed to study the E-F and interhemispheric coupling processes in Japanese and Australian longitudinal sector by using GNSS observations as well as multi-source data. In addition to these 2-D reconstructions and analyses, chapter 5 discusses the 3-D tomography for ionospheric irregularities,including daytime Es and nighttime E-F coupling. Chapter 6 gives final summary and conclusions.

Chapter 2

Background Theory

2.1 The Ionosphere

The Earth's atmosphere surrounds the Earth and is the basis for all life on Earth. The atmosphere is mainly composed of nitrogen, oxygen and argon. Additionally, some trace gases are present, such as methane, carbon dioxide, ozone, and several noble gases, as well as water vapor in varying amounts. The typical atmospheric composition above 100 km is shown in Figure 2.1.

This thesis focuses on the Earth's ionosphere, an important part of the atmosphere that extends from $\sim$60 to 1000 km above the sea level. This region consists of ionized gas (plasma), which is produced by ionization process due to radiation from extreme ultraviolet (EUV) and high-energy X-rays; at the same time, from a macroscopic point of view, the created plasma is of charge neutrality and remains in dynamic equilibrium through the recombination process. Although the plasma content is significantly less than that of neutral gases, these charged particles profoundly influence the ionospheric properties. Characterizing the ionosphere is therefore important due to its spatial and temporal dynamic dispersive nature, which influences the propagation of trans-ionospheric radio waves utilized in applications such as satellite navigation, surveillance communication, and radio astronomical studies.

2.1.1 Ionization and Recombination Processes

The energy for producing ion-electron pair (ionization) mainly comes from the solar EUV radiation (for the day-side Earth) and X-rays (for the night-side Earth) (Kelley, 2009; Nishimura et al., 2021). Usually, the ionization process in the ionosphere is described by the following equations

$$A + h\nu \rightarrow A^{+} + e^{-} \tag{2.1a}$$

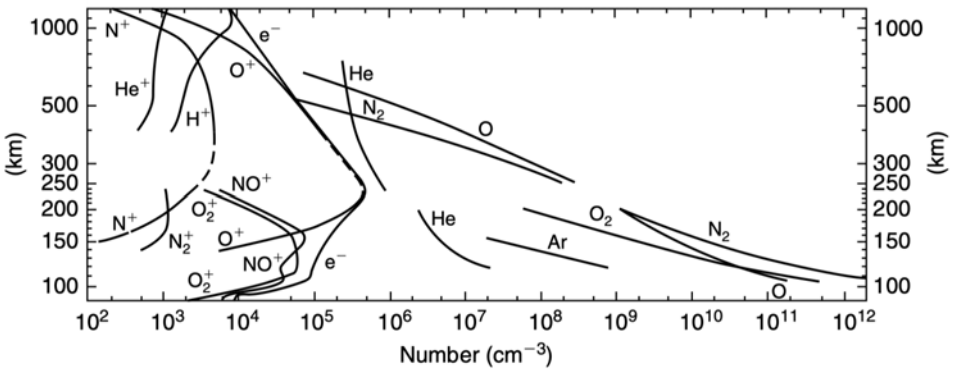

Fig. 2.1 Typical daytime atmospheric composition based on some experimental data. Adapted from Kelley (2009).

$$AB + hv \rightarrow AB^{+} + e^{-} \tag{2.1b}$$

where A and AB are the neutral atoms and molecules, A^{+} and AB^{+} denote the ions generated from ionization process, hv represents the energy from incident photon, and e^{-} is the free electron.

Recombination process is defined as the combination of an ion and an electron to form a neutral molecule or atom, the efficiency of which depends mainly on the mean free path. Therefore, recombination is more pronounced at lower altitudes of the ionosphere where neutral particle density is larger. The recombination (ionospheric loss process) usually have two different types, as manifested in Equation (2.2). The slow and fast recombination are radiation and dissociation processes, respectively (Ratcliffe et al., 1972):

$$A^{+} + e^{-} \rightarrow A + hv(\text{slow}) \tag{2.2a}$$

$$AB^{+} + e^{-} \rightarrow A + B(\text{fast}) \tag{2.2b}$$

The factor that limits the peak plasma density is the recombination rate, which in turn depends heavily on the type of ion present in the plasma and its corresponding interaction with the neutral gas (Kelley, 2009). Throughout the recombination process, the ionosphere maintains its state of dynamic equilibrium. The variation of electron density can be explained by the combination of photochemical equilibrium and advection. The ion continuity equation can be expressed as (Rishbeth and Garriott, 1969)

$$\frac{\partial n_i}{\partial t} = (P_i - L_i) - \bigtriangledown \cdot n_i \mathbf{v_i} \tag{2.3}$$

where n_i represents ion density, P_i and L_i are the rates of production and loss, $\bigtriangledown \cdot n\mathbf{v}$ indicates the ion transport and diffusion, which is strongly associated with magnetic field.

2.1.2 Composition of the Ionosphere

The Earth's atmosphere is vertically stratified and can be classified by a representative temperature profile, as shown in Figure 2.2. Troposphere is located at an altitude of ∼10–15 km, and is the lowest region in the atmosphere. Due to adiabatic cooling, the temperature continues to decrease with increasing altitude. In the stratosphere, the temperature increases due to the presence of ozone (∼10–50 km). The ozone molecules absorb the UV radiation from the Sun and subsequently release thermal radiation. In the mesosphere (∼50–85 km), the minimum temperature is associated with the absence of ozone and effective heat transfer. At ∼85–600 km altitudes, the absorption of solar radiation leads to the rapidly increased temperature in the thermosphere.

In the atmosphere, particles at altitudes >60 km are weakly ionized. Therefore, this region is usually referred to as the ionosphere. The Earth's ionosphere in some sense forms the interface between the atmosphere and space (Kelley, 2009). The distribution of ions and electrons is not uniform due to the absorption of solar radiation of different wavelengths at different altitudes. The combination of ionization, recombination, and exponential increase in neutral atmospheric density with decreasing altitude provides a simple explanation for the vertical profile of the ionosphere, as shown in the rightmost subplot of Figure 2.2. From this subfigure, the ionosphere consists of the whole thermosphere, part of the mesosphere and the exosphere (above 600 km; not shown in this plot), and can be divided into different layers according to the plasma density, i.e., D (about 60–90 km), E (about 90–150 km), and F regions (about 150–500 km). The main characteristics of ionospheric D, E, and F layers are shortly summarized in Table 2.1.

Table 2.1 Main characteristics of different ionospheric layers

Layer	D	E	F
Altitude range	60–90 km	90–150 km	150–500 km
Prevalent ions	H_3O^+, NO_3^-	O_2^+, NO^+	O^+
Typical electron density (daytime)	$\sim 10^8$–10^{11} m^{-3}	$\sim 10^{11}$ m^{-3}	$\sim 10^{12}$ m^{-3}
Typical electron density (nighttime)	–	$\sim 10^{10}$–10^{11} m^{-3}	$\sim 10^{11}$–10^{12} m^{-3}

The ionospheric F region is the main contributor to the trans-ionospheric signal scintillation due to its variability and high electron concentration ($\sim 10^{11}$–10^{12} m^{-3}). During the

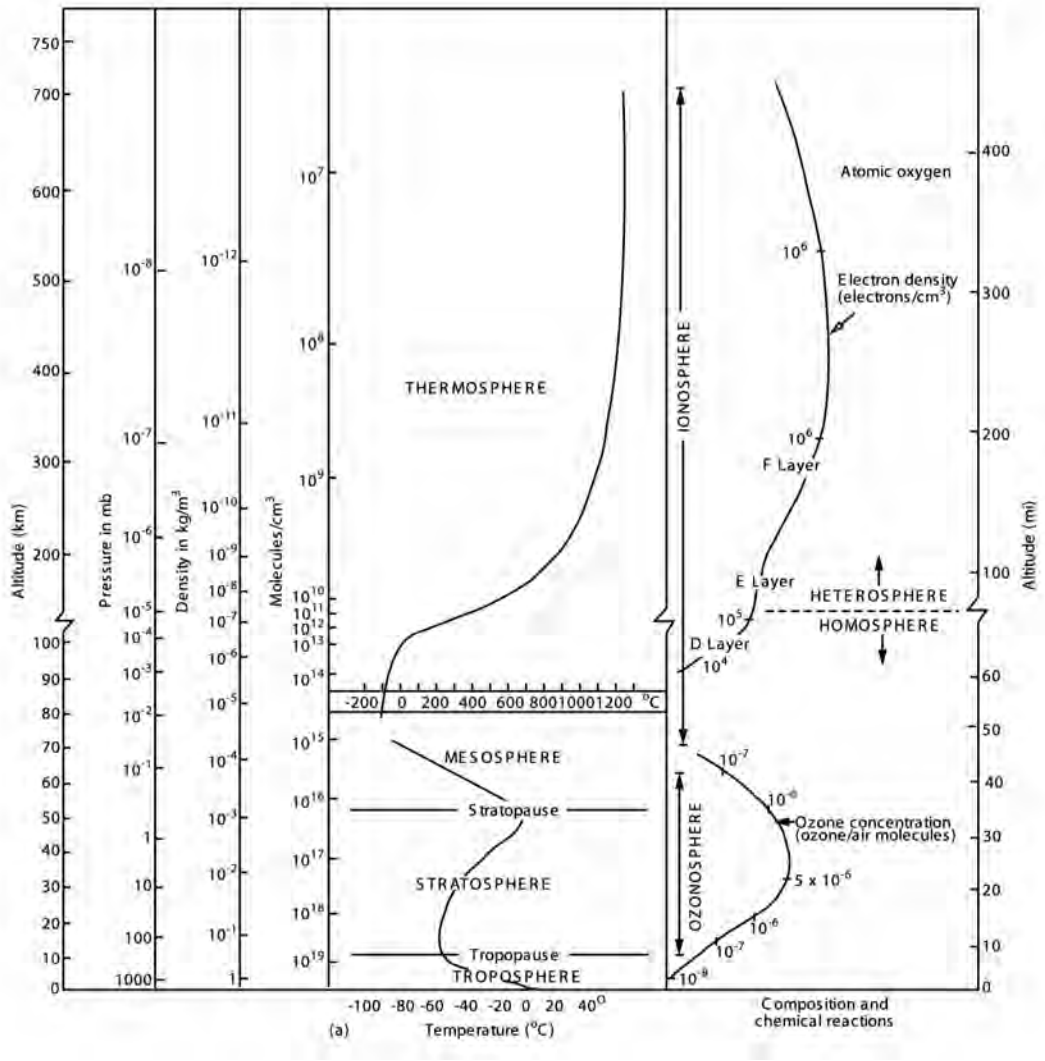

Fig. 2.2 Typical profiles of the Earth's atmosphere. Adapted from Rocken et al. (1997).

daytime, the F layer is splitted into F1 and F2 layers. The F2 layer is at altitudes from ∼200 km up to the height of plasma density peak, where the plasma density is larger compared to the F1 layer at lower altitudes. The F2 layer arises due to a decrease in the degree of ionization and recombination during the day. At night, electron densities at F1 layer decay significantly.

The electron concentration in the ionospheric E region ($\sim 10^{10}$–10^{11} m^{-3}) is lower than that in the F region. At altitudes around 100 km, clouds of enhanced electron density are occasionally generated and can also lead to ionospheric irregularities and cause trans-ionospheric signal scintillations.

The D region has the least amount of ionization ($\sim 10^8$–10^{11} m^{-3}). In this region, the recombination rates are extremely high due to the relatively high density of neutral particles, which leads to the disappearance of D region at night.

2.1.3 Variation Characteristics of the Ionosphere

The ionosphere is controlled by basic ionospheric physics, mainly photochemical equilibrium (at lower altitudes) and plasma transport (at higher altitudes) (Qian et al., 2008). Photochemical process is the basic mechanism of the ionosphere, which mainly affect the production and disappearance of charged particles. Transport mechanism refers to a series of thermodynamic (e.g., radiation absorption and heat exchange in the thermosphere and ionosphere), kinetic (mainly including a series of fluctuations and circulation in the thermosphere), and electrodynamic (the movement of charged particles in the electromagnetic field and possible contact or collision with neutral molecules) processes that allow the transport of charged particles from one location to another. The complicated characteristics exhibited by the ionosphere in space and time are mainly caused by these mechanisms, which vary with time, geographic location (latitude, longitude), solar activity, magnetospheric and bottom atmospheric activity (McNamara, 1991).

The ionization in the ionosphere is mainly caused by the Sun. Due to the more intense solar radiation in equatorial region, the electron density is significantly higher at low latitudes, leading to a more pronounced latitudinal variation. The Earth revolves on its own axis, which leads to the diurnal variations of ionosphere. The ionospheric plasma density shows an increase after sunrise and reaches a maximum in the afternoon. The variation of electron density does not exhibit a strong solar zenith angle dependence (approximately 0° at noon and 90° at sunrise and sunset), because the F2 layer where electron density concentration dominates in the ionosphere is mainly influenced by plasma transport mechanisms. During the night, the ionospheric electron density decreases again. The decrease in electron density in F2 layer and lower regions (F1, E, and D regions) are associated with the recombination process and photochemistry, respectively. The Earth revolves around the Sun, which causes the variation of the position of sunlight incident on the Earth and triggers the seasonal variations of the ionosphere. The ionospheric electron density shows higher values in the hemispheric summer due to the higher ionization levels. The maximum time scale of ionospheric variation corresponds to the solar activity cycle, which is about 11 years. Different solar activities result in different ionization of the ionosphere, thus causing different ionospheric electron densities.

In addition to the regular variations, the ionosphere study is complicated and difficult to summarize and predict due to the irregular variations caused by sudden changes in solar

radiation and high-energy cosmic rays, neutral atmospheric fluctuations and geomagnetic disturbances. For example, solar flare with sudden enhanced solar radiation may trigger ionospheric storms, producing strong density enhancement or depletion in the ionosphere. In addition, traveling ionospheric disturbances (TIDs) are wave–like plasma density in the ionosphere. Most of them are caused by atmospheric gravity waves (AGWs), produced by ion-neutral molecular collisions (Hines, 1960). However, the generation mechanism of the nighttime mid-latitude MSTIDs (classified by wavelengths) is mainly associated with electrodynamic forces, which is the focus of this thesis.

2.2 Ionospheric Sounding Techniques

The discovery of the ionosphere came from the observation of radio waves. In the early 20th century, by using the ionosphere, Marconi transmitted the first radio signals over the Atlantic Ocean. In 1902, Heaviside and Lodge attributed this phenomenon to the reflection of radio waves on free electrons. The existence of the ionosphere was not confirmed until 1924 when Appleton conducted radio wave experiments. Since then ionospheric physics as a discipline has emerged and developed with the aim of understanding the origin of the ionized upper atmosphere and its effect on radio wave propagation. The ionospheric study is important for human society because the ionosphere can exert great impacts on the radio wave propagation. On the one hand, industries such as radio and television stations, use the ionosphere for long-distance or even global radio broadcasts. On the other hand, ionospheric irregularities can strongly interfere with radio signals, which greatly reduces the reliability of applications that use trans-ionospheric signals. In such cases, corrections must be made to these applications.

From another point of view, it is these different ionospheric measurement techniques (radio wave observations) that allow us to better understand how the ionosphere varies in time and space. Generally, the ionospheric sounding methods can be divided into two main types: in situ and remote sensing techniques. An example of the former is sounding rockets, which can be used for detecting the composition of the ionosphere at lower altitudes (e.g., Gylvan Meira Jr, 1971). In fact, to meet the needs of long-time and large-scale ionospheric observation, most of the current data sets rely on the latter, i.e., remote sensing techniques. In the following, the basic principles of several frequently used remote sensing techniques for ionospheric sounding will be shortly introduced, including ionosondes, incoherent scatter radars, GPS, and radio occultation.

2.2.1 Ionosonde

The ionosonde can yield vertical profiles of ionospheric electron density up to, but not exceeding, the height of the highest concentration of charged particles. Currently, ionosondes are one of the most accurate tools for measuring ionospheric parameters.

The ionosonde modulates time-varying pulses with a frequency band of ∼0.1–30 MHz, transmits signals vertically to the zenith and receives reflected echoes at the same location (Rodger and Jarvis, 2000). In the ionosphere, radio waves are reflected when the critical frequency of radio waves (f_c) is equal to the plasma frequency (f_p), at which point the refractive index n equals zero (signals with frequencies above f_c will penetrate the ionosphere without reflection). From the law of refraction, f_c can be expressed as

$$f_c = \frac{1}{2\pi}\sqrt{\frac{e^2 N_e}{m_e \varepsilon_0}} \tag{2.4}$$

where e is elementary charge, N_e is electron density, m_e is electron mass, and ε_0 is the permittivity of free space.

After measuring the time delay (τ) of signal propagation for each single frequency, the relationship between the virtual height ($h' = \frac{1}{2}c\tau$, c is the speed of light) of the ionosphere and the corresponding signal frequency can be obtained (i.e., vertical ionogram), which allows us to derive the ionospheric electron density profile. The reason we call h' virtual height is that according to the Snell's law, radio waves do not propagate as fast in a charged medium as they do in a vacuum. That is to say, h' is not true and is generally larger than the real height of reflection point. More details on the ionosonde derivation process for electron density profiles can be found at Huang and Reinisch (1996). To solve the problem that ionosonde cannot provide information above the height of F-region electron density peak, ionosondes payloads were also deployed on the satellite, e.g., Alouette and ISIS satellites (Barrington and Hartz, 1968; Bilitza et al., 2004).

2.2.2 Incoherent Scatter Radar

The proposed system theory of incoherent scatter radar (ISR) can be traced back to about 70 years ago (Gordon, 1958). Since then, ISR has become a powerful instrument for measuring ionospheric plasma bulk properties in terms of electron density, electron/ion temperature, and ion drift velocity, which has greatly contributed to the analysis and study of the ionosphere.

Unlike ionosonde, based on the scattering of radio waves on free electrons, ISR can detect information at all altitudes of the Earth's ionosphere and provide height profiles of ionospheric parameters as a function of time. ISR operates in the frequency of about 40–1300

MHz, which is much higher than the plasma frequency in the ionosphere (Beynon and Williams, 1978). The pulsed signals emitted by this radar can penetrate the ionosphere, with a small portion of the incident electromagnetic waves being scattered by ionospheric electrons due to the Thomson Scatter effect and then received by ISR. More details of the ISR measurements can be found at, e.g., Woodman and Hagfors (1969), Schunk and Nagy (1978), and Rodrigues (2008).

In the early days, to increase the signal-to-noise ratio (SNR), ISRs were designed with high-powered pulsed signal transmitters and mechanically rotating large-aperture antennas, which brought about the defects of bulky and complex systems; nowadays, to solve these problems, phased-array radars are being developed vigorously. In some cases, ISRs can be equipped with steerable antennas or multiple antenna baselines and can provide two- or three-dimensional information about the ionosphere.

2.2.3 GPS

Total electron content (TEC) is an important parameter in the study of ionosphere, which represents the integrated value of electron density along the line of sight (LOS) from a transmitter to a receiver (1 TEC unit (TECU)=10^{16} el/m^2). The ionosphere, as a dispersive medium, affects the propagation of radio waves (causing group delay and phase advance), which is proportional to the frequency and ionospheric electron density (Ma et al., 2014). To this effect, the cost-effectiveness and rapid development of the GNSS infrastructure, particularly receivers, has effectively broadened the spatial and temporal scales over which ionosphere dynamics are probed. Currently, ground-based GNSS receivers with a considerable number are distributed around the world. Among the GNSSs, the most well-known is the Global Positioning System (GPS), developed and established by the United States. Nowadays, other countries have also developed their own positioning systems, e.g., Global Orbiting Navigation Satellite System (GLONASS) by Russia, Galileo by European Union, and BeiDou by China. Although many receivers started tracking multiple GNSS satellite constellations, this research mainly focuses on the GPS.

The architecture of the GPS system is divided into three main sections: the Space Segment, the Control Segment, and the User Segment, which corresponds to GPS satellite constellation, stations that monitors the status of the control satellite and decides to send commands and uplink signals, and user GPS receivers, respectively. The GPS satellite orbital altitude is approximately 20,200 km and the constellation consists of six orbital planes with an orbital inclination of 55° and an angle of 60° between adjacent orbits. This design makes the GPS space segment require a minimum of 24 satellites to ensure that at least four satellites are visible simultaneously from any location on the ground (except for the Antarctic

and Arctic regions), thus allowing the receiver to resolve location information. To keep the system working in the event of a satellite failure and to enhance its performance, GPS is now operating as a 32-satellite system with significantly enhanced global coverage. The following describes the principle of ionospheric TEC measurement using ground-based GPS observations.

TEC acquisition using dual-frequency observations

In the ionosphere, the refractive index is related with the density of free electrons (N_e) and the frequency of the radio wave (f). In 1932, Appleton studied the theory of the influence of the upper atmosphere on electromagnetic waves and summarized the formula for the refractive index in the ionosphere, called the Appleton-Hartree Equation (Appleton, 1932):

$$n^2 = 1 - \frac{X}{1 - jZ - \frac{Y^2 \sin^2\theta}{2(1-X-jZ)} \pm \left[\frac{Y^4 \cos^4\theta}{4(1-X-jZ)^2} + Y^2 \cos^2\theta\right]^{1/2}} \tag{2.5}$$

In this equation,

$$X = N_e e^2 / \varepsilon_0 m \omega^2 = f_p^2 / f^2 \tag{2.6a}$$

$$Y = eB/m\omega = f_h/f \tag{2.6b}$$

$$Z = f_v/f \tag{2.6c}$$

where n is the complex refractive index, f_p is the plasma frequency, f_h is the electron cyclotron frequency, f_v is the electron-neutral collision frequency, ω is the angular frequency of traveling wave, B is the magnitude of the geomagnetic field, θ is the angle between the propagation vector of the incident wave and the direction of the geomagnetic field.

For electromagnetic waves at high frequency (HF) band or higher (e.g., GPS signals), the phase refractive index (n_p) in the ionosphere can be simplified from Equation (2.5) as

$$n_p = 1 - \frac{e^2 N_e}{8\pi^2 \varepsilon_0 m_e f^2} \tag{2.7}$$

The group refractive index (n_g) is related to the phase refractive index (n_p) by the following relationship:

$$n_g = n_p + f\frac{dn_p}{df} \tag{2.8}$$

Thus, from Equations (2.7) and (2.8), the group refractive index (n_g) is given by

$$n_g = 1 + \frac{e^2 N_e}{8\pi^2 \varepsilon_0 m_e f^2} \tag{2.9}$$

After denoting $b = \frac{e^2}{8\pi^2\varepsilon_0 m_e}$, the phase advance ($\Delta t_p$) and the group delay ($\Delta t_g$) caused by the ionosphere to the radio wave can be calculated from

$$\Delta t_p = \int_l \frac{1}{c}(n_p - 1)dl = -\frac{b}{cf^2}\int_l N_e dl = -\frac{b}{cf^2}\text{TEC} \tag{2.10}$$

$$\Delta t_g = \int_l \frac{1}{c}(n_g - 1)dl = \frac{b}{cf^2}\int_l N_e dl = \frac{b}{cf^2}\text{TEC} \tag{2.11}$$

where $\text{TEC} = \int_l N_e dl$ is the integral of the electron density in the propagation path and is generally denoted as VTEC (vertical TEC) when its ray path is perpendicular to the ground plane, and as STEC (slant TEC) otherwise.

The GPS satellites broadcast information on two L-band carrier signals (currently L1 and/or L2 with an additional L5 available in the near future). With a dual-frequency receiver, two observables for the receiver-satellite range measurements at each operating band, i.e., the pseudorange (P_i) and the carrier phase (L_i) observations, can be generated as

$$P_i = \rho + c(\delta_t - \delta_s) - I_i + T + \varepsilon \tag{2.12}$$

$$\frac{c}{f_i}L_i = \rho + c(\delta_t - \delta_s) + I_i + T + \frac{c}{f_i}N_i + \frac{c}{f_i}w + \varepsilon' \tag{2.13}$$

where i is 1 or 2 corresponding to f_1 (1.57542 GHz) or f_2 (1.2276 GHz) frequency, ρ is the actual distance between receiver and satellite, δ_t and δ_s are the errors from receiver clock and satellite clock, respectively, I_i is the ionospheric correction corresponding to f_i, T is the tropospheric delay, N_i is the integer ambiguity of L_i, w is the wind-up term, and ε and ε' are the other errors and the noises in the observations (Lu et al., 2021b).

From Equations (2.8)–(2.13), the TEC from a satellite to a receiver can be obtained from the difference between pseudorange measurements,

$$\text{TEC}_g = \frac{(f_1 f_2)^2}{b(f_1^2 - f_2^2)}(P_2 - P_1) \tag{2.14}$$

and the difference between carrier phase measurements,

$$\text{TEC}_p = \frac{(f_1 f_2)^2}{b(f_1^2 - f_2^2)}\left(\frac{cL_1}{f_1} - \frac{cL_2}{f_2} + \frac{cN_1}{f_1} - \frac{cN_1}{f_1}\right) \tag{2.15}$$

In principle, TEC_g and TEC_p should be equal to each other. However, due to the 2π ambiguity in the phase measurements, TEC_p from the differential phase is a relative value but with a higher precision; the TEC_g extracted from pseudoranges contains larger observation noise (Ma et al., 2014). In order to obtain the STEC with a high precision, a differential

phase-dependent baseline (B_{rs}) is introduced by fitting TEC_p to TEC_g (Mannucci et al., 1998)

$$B_{rs} = \frac{\sum_{i=1}^{M}(\mathrm{TEC}_{gi} - \mathrm{TEC}_{pi})\sin^2\alpha_i}{\sum_{i=1}^{M}\sin^2\alpha_i} \tag{2.16}$$

where M is the number of measurements without a cycle slip, α_i is the elevation angle from the receiver to the satellite. In this process, the unknown integer ambiguities in TEC_{pi} are abandoned. In Equation (2.16), $\sin^2\alpha_i$ is a weighting factor to increase the reliability caused by multi-path effects in pseudorange measurements at low elevation angles. After smoothing, the STEC with high precision can be obtained:

$$\mathrm{TEC} = \mathrm{TEC}_p + B_{rs} \tag{2.17}$$

Figure 2.3 shows an example of STEC obtained from phase measurements (left), pseudoranges measurements (middle), and pseudorange-leveled carrier phases results (right). Therefore, it is clear that the STEC obtained from pseudorange-leveled carrier phases is free of ambiguities and has lower noise and multi-path effects than that from the phases and pseudoranges.

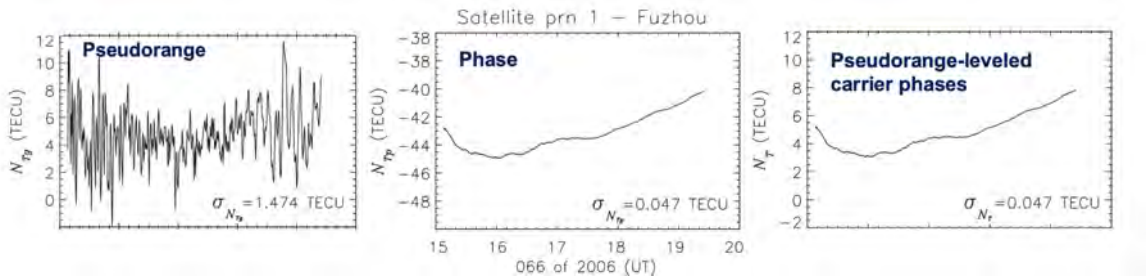

Fig. 2.3 STEC obtained from phase measurements (left), pseudoranges measurements (middle), and the leveled method (right). Adapted from Ma et al. (2014).

With this method, in the obtained TEC, effects on phase and pseudorange common to both frequencies (e.g., clock offsets, tropospheric delay) are removed, but frequency-related effects are still present (e.g., multi-path and the differential instrumental biases) (Ma et al., 2014). In addition, TEC measurements with satellite elevation angles (α) smaller than 35° usually need to be excluded to suppress the multipath effect. This setting was also adopted in this research.

Single-thin-shell model

In the ionospheric study, for simplicity and uniformity of calculation, a single-thin-shell model assumption is usually used to convert STEC to VTEC. This model assumes an

infinitesimally thin layer at a constant height (h_s) represents the whole 3-D ionosphere. The geometric relationship is shown in Figure 2.4, wherein R represent receiver. Compared with other models, the single-thin-shell model has a simple structure and can effectively model the ionosphere in most cases.

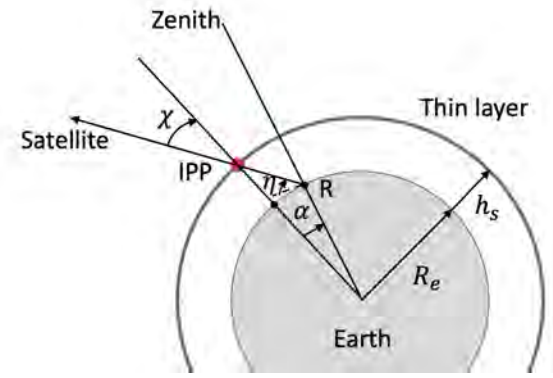

Fig. 2.4 The geometric relationship in single-thin-shell model.

In the single-thin-shell model, the ionospheric height (h_s) is generally set to the height of the electron density peak (usually at 300–450 km) in order to keep the total amount of electrons approximately equal above and below the single-layer height (Sardon et al., 1994); the total electron content along the ray path from the receiver to the satellite is assumed to be concentrated at the intersection of the ray path with the single layer, i.e., the IPP (ionospheric pierce point; the red dot in Figure 2.4). The zenith angle on the line between IPP and the satellite can be calculated as

$$\chi = \arcsin\left(\frac{R_e \cos\eta}{R_e + h}\right) \tag{2.18}$$

where R_e is the mean Earth radius, η is the elevation from the receiver to the satellite. Therefore, the absolute VTEC at IPP can be obtained as

$$\mathrm{VTEC} = (\mathrm{sTEC} - b_r - b_s) \cdot \cos\chi \tag{2.19}$$

where sTEC is the observed STEC, b_r and b_s are the instrumental biases from receiver and satellite, respectively.

Usually, the instrumental biases are solved by a grid method to determine the absolute TEC. The grid method divides the entire 2-D ionosphere into a number of grids and assuming that the VTEC at a particular time is considered to be identical at any point within one grid block. Generally, the instrumental biases (b_r and b_s) are assumed to remain stable within one day (Ma and Maruyama, 2003). For each epoch, with many receivers and satellites, an

overdetermined matrix can be constructed as

$$\begin{bmatrix} \cdots & \cdots & \cdots & \cdots \\ 0 & \sec\chi_{(j-1)k} & 1 & 1 \\ \cdots & \cdots & \cdots & \cdots \\ 0 & \sec\chi_{jk} & 1 & 1 \\ \cdots & \cdots & \cdots & \cdots \\ 0 & \sec\chi_{j(k+1)} & 1 & 1 \\ \cdots & \cdots & \cdots & \cdots \end{bmatrix} \begin{bmatrix} \cdots \\ \mathrm{VTEC}_i \\ \cdots \\ b_{sj} \\ \cdots \\ b_{rk} \\ \cdots \end{bmatrix} = \begin{bmatrix} \cdots \\ \mathrm{sTEC}_{(j-1)k} \\ \cdots \\ \mathrm{sTEC}_{jk} \\ \cdots \\ \mathrm{sTEC}_{j(k+1)} \\ \cdots \end{bmatrix} \tag{2.20}$$

where i, j, and k represent the serial number for grid, satellite, and receiver, respectively. We can use mathematical methods, such as least squares, to fit and obtain optimal solutions to a overdetermined matrix consisting of many observations over an epoch. In addition to the grid method, many other methods can also be used for determining the absolute TEC, such as Kalman filtering approach (Sardon et al., 1994), neural network parameter estimation method (Ma et al., 2005), 2-D polynomial fitting model (Lanyi and Roth, 1988), and spherical harmonic function (Schaer et al., 1996).

2.2.4 Radio Occultation

The principle of radio occultation was first announced by Pannekoek in 1904. In the 1960s, JPL (Jet Propulsion Laboratory) refined the concept and proposed the use of occultation for atmospheric sounding (Fishbach, 1965; Fjeldbo and Eshleman, 1968). After the development of GPS in the late 1980s, the navigation signals were used for occultation to detect the Earth's atmosphere. The GPS/MET experiment in 1995 verified the feasibility of radio occultation method for the atmospheric detection (Hajj and Romans, 1998).

Radio occultation observation uses a constellation of Low Earth Orbit (LEO) satellites to receive the dual-frequency signals from GNSS satellites. Because of the lower orbit, LEO satellites have a larger orbital speed than GNSS satellites. During the revolution, the fast-moving LEO satellites track the ascent or descent of the GNSS satellite behind the Earth's limb. Therefore, radio occultation can obtain information of the atmosphere from the trans-atmospheric radio signals. The main occultation system currently in use is COSMIC (Constellation Observing System for Meteorology, Ionosphere, and Climate), which was successfully launched on April 14, 2006 by the United States in cooperation with Taiwan. Six satellites in COSMIC-2 mission are operational after June 25, 2019, providing uniform global data coverage with several thousand electron density profiles daily, especially near the equatorial region (Cherniak et al., 2021). The scheme of COSMIC radio occulation remote

sensing is shown in Figure 2.5, wherein G_1 is the occulted navigational satellite, G_2 is the reference satellite, L is the LEO satellite receiver, $G_n \cdots G_{n+2}$ are satellites for measuring the orbital parameters of low orbital satellites, and A is the ground-based station for receiving radio occultation observation and data analysis (Liou, 2010).

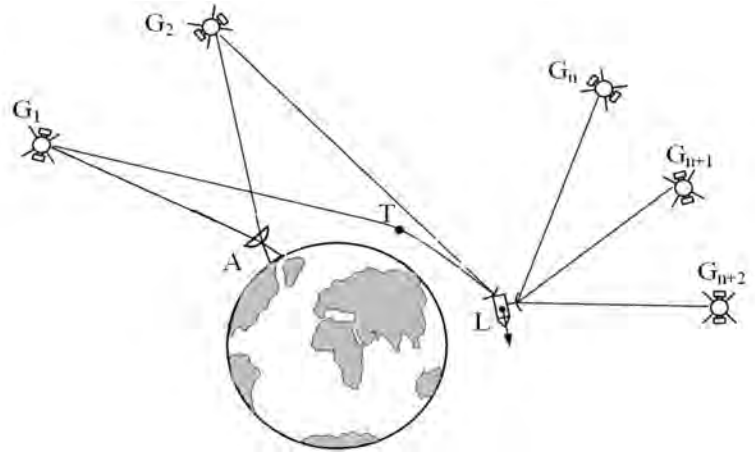

Fig. 2.5 Scheme of COSMIC radio occulation remote sensing. Adapted from Liou (2010).

The duration of one occultation event for atmospheric detection is about 5 minutes. Generally, for ionospheric observation by using ocultation, the sampling rate is 1 Hz (vertical resolution of ∼2 km) from the LEO altitude to around 50–60 km. In radio occultation, the satellite-receiver ray path is not a straight line due to the ionospheric refractive index. However, the bending angles of the GPS carriers (f_1 and f_2) when crossing the ionosphere are quite small and can be ignored (the vertical altitude distances affected by the bending angle are on the order of several kilometers) (Schreiner et al., 1999). Therefore, the atmospheric parameters, such as ionospheric electron density, atmospheric temperature and humidity, can be derived after using the Abel integral transform (Arras, 2010). The details of occultation data retrieval can be found at Liou (2010) and Schreiner et al. (1999). One of the advantages of occultation measurements is that they are not limited by geography and can be distributed to various locations around the globe for space-based observations of the ionosphere. However, because of its fast movement, radio occultation is not able to record the ionospheric parameters in a significantly small area and over a continuous period of time.

2.3 Overview of Es

Sporadic E (Es) refer to thin layers (0.6–2 km) of metallic ion plasma at the lower ionospheric E region (∼95–120 km) (Houminer et al., 1997; Whitehead, 1989; Wu et al., 2005). In this region, collisions with neutral particles significantly affect the motion of ions, so that ions

moves with wind and electrons remain magnetized (Haldoupis, 2012). After the invention of ionospheric sounding techniques, sporadic E layers have been studied intensively over many years, by using ionosondes (Whitehead, 1972, 1989), radars (Miller and Smith, 1975), rockets (Yamamoto et al., 1998), GNSS (Maeda and Heki, 2014), and radio occultation (Arras and Wickert, 2018). In the Northern Hemisphere, a typical horizontal wavelength of $\sim$100 km is observed for the frontal structure of mid-latitude Es, propagating northward in the morning, southward in the afternoon, and southwestward in the evening with speeds of 30–100 m/s (Maeda and Heki, 2015; Sinno et al., 1964). Sporadic E can last from a few minutes to several hours, causing scintillations on radio waves due to their strong vertical electron density gradient, which is proportional to the radio frequency.

Currently, the "wind shear" theory is widely accepted for explaining the Es generation mechanism (e.g., Axford, 1963; Whitehead, 1961), in which vertical shears in horizontal neutral wind can cause long-lived metal ions to move in the vertical direction and converge into thin and dense plasma layers, under the combined action of ion-neutral collisional coupling and geomagnetic Lorentzian forcing (Haldoupis et al., 2006). By using a high-resolution Ca^+ lidar, Ejiri et al. (2019b) have observed the occurrence of Kelvin–Helmholtz instabilities (producing turbulence coupled to the plasma) in the neutral atmosphere whose density changed temporarily or spatially. In this region, it is reasonable to assume the presence of slowly recombining metal ions, since the major components in this altitude range (NO^+ and O_2^+ ions) can affect the generation efficiency of large density enhancements. Metal ions, such as Fe^+, Na^+, Mg^+, and Ca^+, mainly come from the evaporation of small micrometeorites that cross the Earth's orbit (Kopp, 1997). These metal ions can last for several days and are transported by atmospheric dynamics, accompanied by electrons moving along the magnetic field lines to maintain charge neutrality (Plane, 2003).

The ion momentum equation can be used for describing the Es formation. Usually, the simplified form ignores the pressure gradient forces at the E-region height and the electric field forces at middle and low latitudes (Chimonas and Axford, 1968). Then the ion momentum equation in steady state is simplified to include only ion-neutral collisions and geomagnetic forces (Haldoupis, 2011)

$$m_i \upsilon_i (\mathbf{v}_i - \mathbf{U}_n) - e\mathbf{v}_i \times \mathbf{B} = 0 \tag{2.21}$$

where m_i and υ_i are the ion mass and ion-neutral collision frequency, $\mathbf{v}_i$ and $\mathbf{U}_n$ are the ion drift and neutral wind velocity vectors, respectively, e is the electronic charge, and $\mathbf{B}$ is the geomagnetic field. In the Northern Hemisphere, after setting a Cartesian (x, y, z) coordinate system of geomagnetic south, geomagnetic east and vertically up ($\mathbf{v}_i(u, v, w)$, $\mathbf{U}_n(U, V, W)$, $\mathbf{B}(-B\cos I, 0, -B\sin I)$; I represents the magnetic dip angle), the vertical ion drift velocity

(w) at steady state (vertical wind component $W \approx 0$) can be obtained from Equation (2.21) as

$$w = f_z V + f_m U \tag{2.22}$$

Here the dimensionless parameters f_z and f_m are the zonal and merdional "ion drift factors":

$$f_z = \frac{(\upsilon_i/\omega_i)\cos I}{1+(\upsilon_i/\omega_i)^2} \tag{2.23a}$$

$$f_m = \frac{\cos I \sin I}{1+(\upsilon_i/\omega_i)^2} \tag{2.23b}$$

where υ_i/ω_i is the ratio of ion-neutral collision frequency to ion gyrofrequency. With the motion of electrons and ions, Es may form where the absolute value of gradient of ion drift velocity $\left(\frac{dV}{dz}\right)$ is large and w is close to zero.

As shown in Figure 2.6, the vertical shears in the zonal and meridional winds correspond to the two different processes of vertical ion convergence (f_z and f_m) in Equation (2.23). In Figure 2.6(a), the zonal shear mechanism $\left(\frac{dV}{dz}\right)$ is characterized by a westward wind above and an eastward wind below, where the horizontal component of the magnetic field is $B_H = B\cos I$. Because the ions drift with winds (west above and east below), they are Lorentz-forced ($eV_{\text{west}}B_H$ and $eV_{\text{east}}B_H$) to move downwards and upwards, and gradually form a thin layer at $V = 0$ of the wind shear null. Figure 2.6(b) shows the meridional wind shear $\left(\frac{dV}{dz}\right)$ mechanism (a northward wind above and a southward wind below), in which the ions drift with wind in the horizontal direction while being constrained by the Lorentz force to gyrate perpendicularly to the inclined magnetic field lines (Haldoupis, 2012). Little different with the case in the zonal wind shear mechanism, ions are forced to move along the magnetic field lines with the meridional wind ($U_{\text{north}}\cos I$ and $U_{\text{south}}\cos I$), and converge towards the wind shear null ($U = 0$) and form a thin layer.

The altitude dependence of layer-forming efficiency of the zonal and meridional wind shear mechanisms is caused by different ion drift factor dependence on $r = \upsilon_i/\omega_i$. At altitudes of $\sim$ 125 km, $r \approx 1$; at lower (upper) altitudes the zonal (meridional) wind shear mechanism becomes dominant. At altitudes >120 km, the ions are more magnetized due to the reduced ion-neutral collision frequency, and the ability of a zonal wind to move them across the magnetic field is weakened; at altitudes <120 km, the less magnetized ions reduce the action of the Lorentz force, and allow the vertical shears in the zonal wind dominant in the Es formation (Haldoupis, 2012). As observed by ionosondes, most Es are situated below about 120 km where vertical plasma drift becomes collision-dominated (Haldoupis et al., 2006). That is to say, most of the Es layers are controlled by vertical zonal wind shear, i.e.,

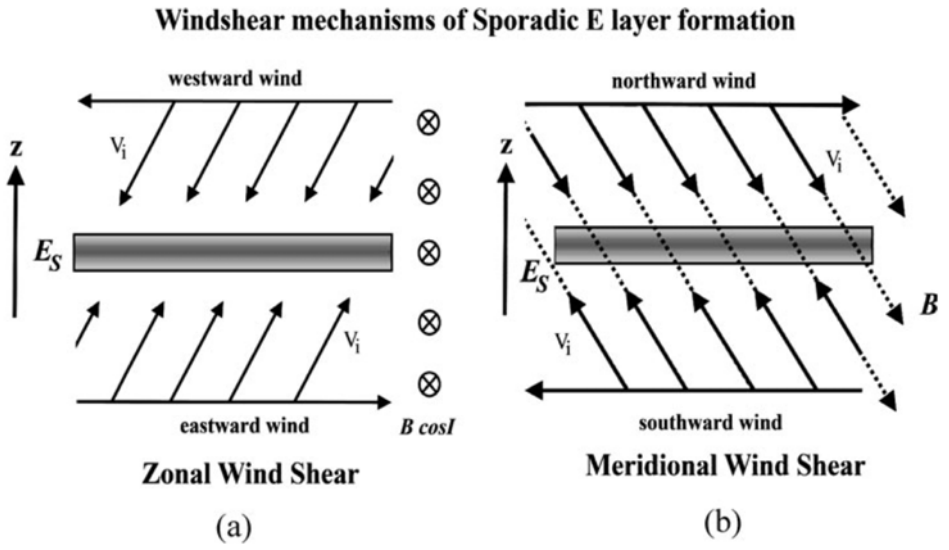

Fig. 2.6 Zonal (left) and meridional (right) wind shear theoretical mechanisms of sporadic E layer formation in the Northern Hemisphere. Adapted from Haldoupis (2012).

in the Northern Hemisphere, with westward winds above and eastward, or smaller, westward winds below.

As shown by the Es distribution map observed by COSMIC occultation in Figure 2.7, it is worth noting that stronger and more frequent Es layers occur in the midlatitude ionosphere, which is associated with the inclination of the Earth's magnetic field (Luo et al., 2021). In the equatorial and polar regions, the magnetic field lines are nearly horizontal and have large magnetic dip angles, which makes ions difficult to converge vertically to form a thin layer. In addition, electric fields in these two areas are strong and cannot be neglected. In the polar region, particle precipitation is the main reason for Es formation (Nygren et al., 1984). Further, it can also be inferred from the Figure 2.7 that the Es occurrence and intensity show an obvious annual cycle with maximum values in the summer hemisphere (Arras and Wickert, 2018). This pronounced seasonal dependence of Es layers cannot be simply satisfied by the wind shear theory alone. Haldoupis et al. (2007) indicate that this could be associated with the annual variation of sporadic meteor deposition in the upper atmosphere, since the Es occurrence and intensity depends directly on the content of metal ions determined by meteorite deposition.

In addition to the Es annual variation, at an altitude of about 100 km in the midlatitudes, Pancheva et al. (2003) found a connection between tidal winds and Es altitude variations. As shown in Figure 2.8, Es layers show semi-diurnal/diurnal periodicity. This phenomenon is associated with the atmospheric tides, which are the main source of the vertical shears

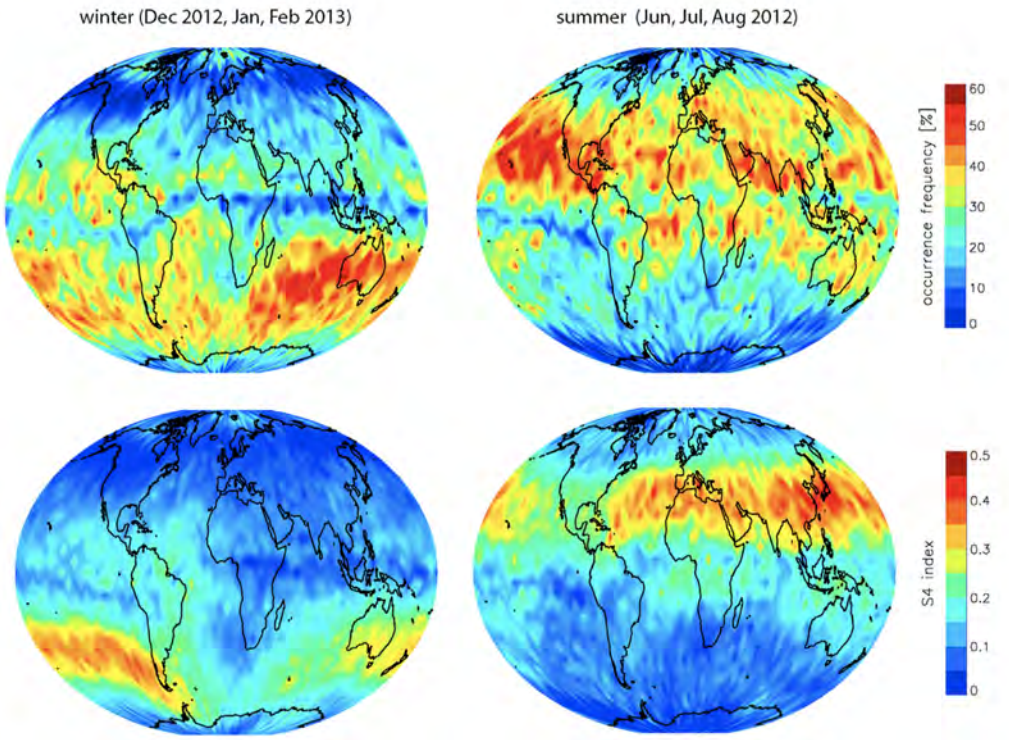

Fig. 2.7 Global distribution maps of Es occurrence (upper row) and intensity (lower row) in different seasons. Adapted from Arras and Wickert (2018).

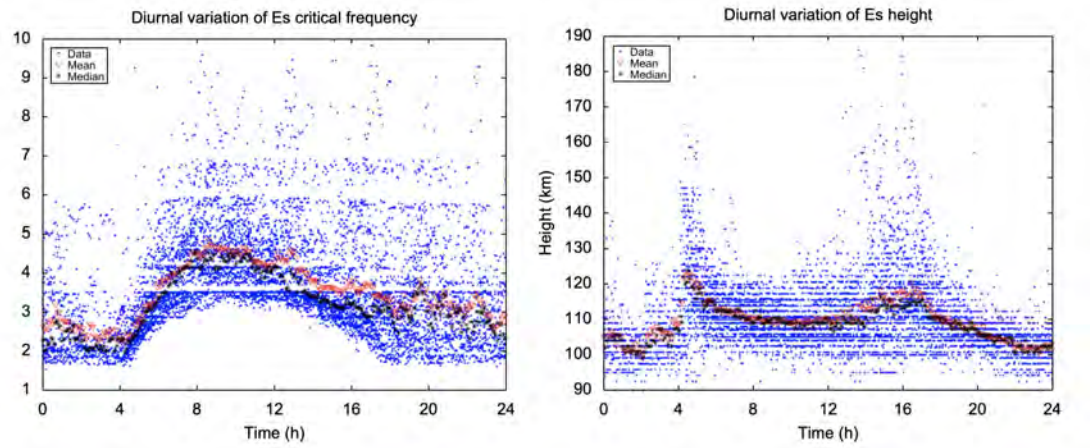

Fig. 2.8 Diurnal variations critical frequency foEs (left) and corresponding height hmEs (right). Adapted from Šauli and Bourdillon (2008).

of horizontal winds and affect the vertical motion of Es layers (Mathews, 1998). After the formation, the Es layers usually descend with tidal phases and eventually disappear due to the gradually increased metallic ion recombination rates. Through simulation, Andoh et al. (2021, 2022) have successfully proven that the day-to-day variations of Es is related with tidal effects, and verified that sporadic E is not "sporadic" as the name implies, but is an ionospheric phenomenon that occurs periodically. The 22-26 h variation period observed by ionosonde further suggests that planetary waves may also be influencing Es development (Šauli and Bourdillon, 2008). However, the correlation between Es appearance or strength with solar activity is not obvious, according to the long-term Es observations (Maksyutin et al., 2001).

2.4 Overview of Nighttime MSTIDs

Traveling ionospheric disturbances (TIDs) are the wavelike disturbances manifested as electron density irregularity or TEC variations in the ionospheric F region. According to their scale sizes, TIDs can be divided into small-scale TIDs (SSTIDs), medium-scale TIDs (MSTIDs) and large-scale TIDs (LSTIDs) (Rieger and Leitinger, 2002). The classification and characteristics of TIDs are shown in Table 2.2. Generally, the generation of LSTIDs and MSTIDs are considered to be related with AGWs (atmospheric gravity waves); the generation of relatively smaller scales of MSTIDs or SSTID are thought to be related with AWs (acoustic waves), which propagate isotropically outward (Huang et al., 2019).

Table 2.2 Classification and characteristics of TIDs

Classification	Period	Horizontal wavelengths	Velocity
LSTIDs	30 min to 3 hr	>1000 km	400–1000 m/s
MSTIDs	15 min to 1 hr	100–1000 km	100–300 m/s
SSTIDs	a few minutes	10–100 km	<200 m/s

Since last century, MSTIDs have been observed and studied by different ionospheric sounding techniques (e.g., Berkner and Wells, 1934; Bowman, 1990). Recent MSTID observations by using GNSS-TEC and all-sky airglow images have found that the daytime and nighttime MSTIDs show different characteristics. Especially, the generation of nighttime MSTIDs cannot be simply explained by AGWs, due to their NW-SE (NE-SW) alignment and southwestward (northwestward) propagation direction in the Northern (Southern) Hemisphere (Kelley and Miller, 1997). Such midlatitude nighttime MSTIDs are thought to be caused by electrodynamics (Tsunoda and Cosgrove, 2001) and therefore have been named as electrified MSTIDs (EMSTIDs) (Narayanan et al., 2018), which are the main focus of this thesis.

2.4.1 Formation

In 1990s, the 2-D structure of nighttime MSTIDs was first captured by 630-nm airglow imagers and GNSS-TEC (Mendillo et al., 1997; Saito et al., 1998a). Statistical analysis have found that in the Northern Hemisphere, the nighttime MSITDs show a NW-SE alignment and have a southwestward propagation direction, with wavelengths of 100–500 km, periods of 0.5–1.5 hour, and phase velocities of ∼100 m/s (Kotake et al., 2007; Shiokawa et al., 2003a). In addition, observations have found that the nighttime mid-latitude MSTIDs occur simultaneously in different hemispheres and have mirrored structures symmetrical along the magnetic equator (Martinis et al., 2019; Otsuka et al., 2004). By using multiple instruments, the nighttime MSTID occurrence has been observed to reach a maximum in the summer and a secondary peak in the winter, especially over the East Asian sector (∼100°E–180°E) (e.g., Kil and Paxton, 2017; Shiokawa et al., 2003a), as shown in Figure 2.9. In order to explain the above characteristics of MSTIDs, it is necessary to understand their generation mechanisms.

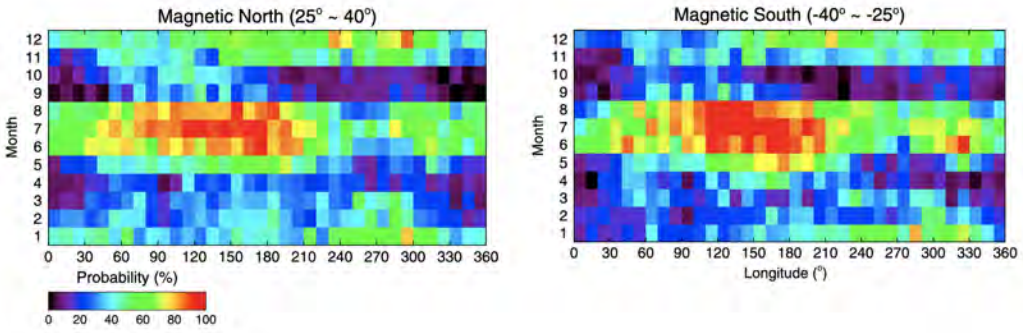

Fig. 2.9 Occurrence possibility of nighttime midlatitude MSTIDs at midlatitudes of different hemispheres. Adapted from Kil and Paxton (2017).

Mid-latitude electric field fluctuations (MEFs) caused by nighttime mid-latitude MSTIDs have been detected by space-based observations (e.g., Saito et al., 1998b, 1995). Combining the airglow images and DMSP satellites, the observation results show that the perturbed electric fields toward southwest (northeast) where the intensity of airglow observation results increases (decreases) (Shiokawa et al., 2003b) . Since the 630.0 nm airglow intensity is associated with the field-line integrated Pedersen conductivity (Σ_P) (Otsuka et al., 2002), the generation of polarization electric field can be elucidated by Figure 2.10. For example, in the Northern Hemisphere, it is assumed that under the perturbation condition, Σ_P perturbations exhibit a NW-SE alignment; if the ionospheric current traverses the perturbation band, a polarized electric field ($\mathbf{E}_1$) will be generated to maintain the current continuity (Otsuka et al.,

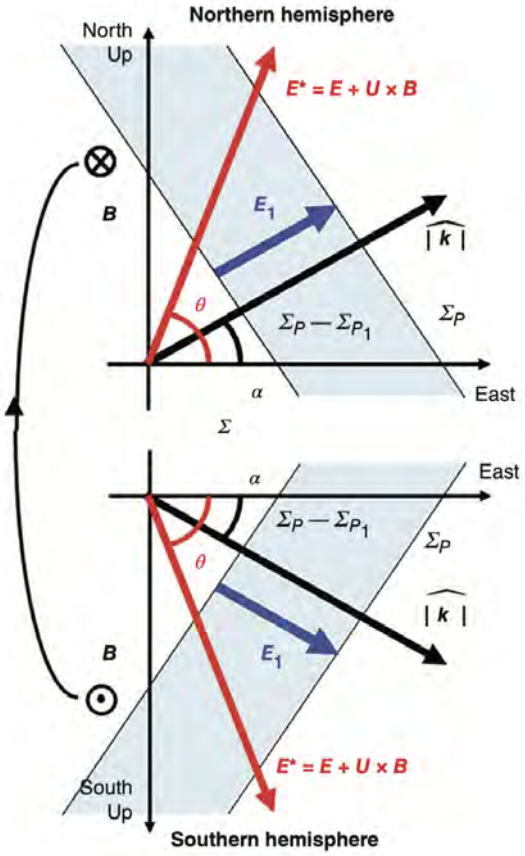

Fig. 2.10 Schematics of the generation of polarization electric field under the perturbation conditions. Adapted from Otsuka (2021).

2007). The field line–integrated electric current in the F region can be expressed as

$$\mathbf{J} = \Sigma_P(\mathbf{E} + \mathbf{U} \times \mathbf{B}) = \Sigma_P \mathbf{E}^* \tag{2.24}$$

where $\mathbf{E}$ is the background electric field, $\mathbf{U}$ is the thermospheric neutral wind, $\mathbf{E}^*$ is the effective electric field. In the ionosphere, the background electric field ($\mathbf{E}$), whose generation is related with the F-region dynamo process, is much smaller than and anti-parallel to $\mathbf{U} \times \mathbf{B}$ (Heelis, 2004). That is, $\mathbf{E}^*$ and $\mathbf{U} \times \mathbf{B}$ as well as $\mathbf{J}$ share same directions. Generally, thermospheric winds are not significantly affected by the ionosphere and its irregularities, because the time constant of the ion drag affecting the neutral wind is usually larger than the period of irregularities (Narayanan et al., 2018). At nighttime, according to the empirical model (Horizontal Wind Model (HWM); Drob et al. (2015)), the thermospheric winds are usually equatorward and eastward, which makes $\mathbf{J}$ direct pole-eastward.

Under such conditions, the polarization electric fields ($\mathbf{E}_1$) should be generated to maintain the current continuity ($\mathbf{J} = \Sigma_P \mathbf{E}^*$=const):

$$\Sigma_P \mathbf{E}^* \cdot \hat{\mathbf{k}} = (\Sigma_P - \Sigma_{P1})\{\mathbf{E}^* + \mathbf{E}_1\} \cdot \hat{\mathbf{k}} \tag{2.25}$$

where $\hat{\mathbf{k}}$ is a unit wave vector of the frontal structure, $\mathbf{E}_1$ points northeastward (southwestward) in the regions of low (high) intensity (Shiokawa et al., 2003b). In such cases, $\mathbf{E}_1$ moves the plasma up and down through the $\mathbf{E}_1 \times \mathbf{B}$ drift, thus causing the plasma perturbations in the MSTID structures and the nearly sinusoidal variations of the F peak height. This physical process can be explained by the Perkins instability, which will be presented later in detail. In this process, Σ_P and $\mathbf{E}_1$ will grow with time if the Perkins instability condition is satisfied.

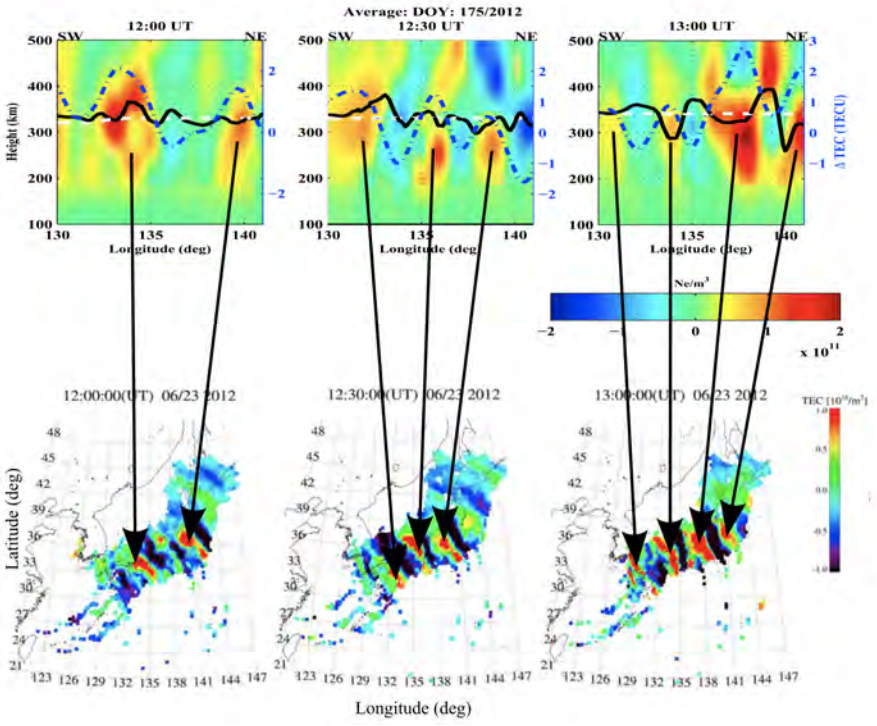

Fig. 2.11 Vertical structure of MSTIDs reconstructed by GNSS-TEC and tomography. Adapted from Ssessanga et al. (2015).

Ssessanga et al. (2015) have successfully reconstructed the vertical structure of MSTIDs by using GNSS-TEC and a tomography technique, and the results are shown in Figure 2.11. The sinusoidal oscillation of plasma density (n_{e1}) of the MSTID structure can be satisfied by (Shiokawa et al., 2003b)

$$n_{e1} = \frac{-i}{\omega} v_1 \frac{\partial n_e}{\partial z} \cos I \cos \phi \tag{2.26}$$

where v_1 is perturbation plasma velocity, ω is angular frequency of MSTIDs, ϕ is azimuth of the MSTID propagation direction clockwise from the magnetic north. In fact, Shiokawa et al. (2003b) have performed a simulation, and results suggest that the polarization electric fields also show sinusoidal oscillation within the MSTID structures; an electric field perturbation with an amplitude of 1.2 mV/m can result in a 50-km variation of F2 peak height, wherein the plasma drift with a vertical velocity of ∼25 m/s.

2.4.2 Perkins Instability

As mentioned previously, the Perkins instability can well explain the directional preference of the MSTID frontal structures (Perkins, 1973). During nighttime, the ionization and recombination in the ionosphere are reduced due to the absence of solar radiation. In such a case, at midlatitudes, the F-layer altitude is in dynamic equilibrium: the vertical upward plasma drift caused by the eastward electric fields (**E**) and/or the thermospheric winds towards the equator is almost equals to the downward plasma drift caused by the gravity-induced ion diffusion (g/υ). Thus, an equation that uses the effective electric field to describe this equilibrium can be expressed as

$$\frac{\mathbf{E}^* \cos\theta}{B} \cos I = \frac{g}{\langle \upsilon \rangle} \sin^2 I \tag{2.27}$$

where θ is the angle between $\mathbf{E}^*$ and geomagnetic east, I is the dip angle of the magnetic field, $\langle \upsilon \rangle$ is plasma density-weighted, field-line integrated collision frequency ($\langle \upsilon \rangle = \frac{\int n_e \upsilon dz}{\int n_e dz}$; dz represents an integral over the distance along the magnetic field line), which is proportional to Σ_P. Since the neutral atmospheric density exponentially increases with decreasing altitude, $\langle \upsilon \rangle$ decreases (increases) as the F layer rises (falls). In Equation (2.27), for example, even if $\mathbf{E}^*$ strengthens and causes an increase in upward plasma velocity, $\langle \upsilon \rangle$ on the right side will decrease, leaving the left and right sides in equilibrium.

However, the generation of polarization electric fields disrupts this balance. Under the situation in Figure 2.10, wavelike perturbation in Σ_P is aligned from NW to SE in the Northern Hemisphere; an increasing (decreasing) polarization electric field in the Σ_P decreasing (increasing) region are generated to maintain current continuity. In the wave vector ($\hat{\mathbf{k}}$) direction, the current continuity equation can be expressed as

$$\langle \upsilon \rangle E^* \cos(\theta - \alpha) = (\langle \upsilon \rangle - \langle \upsilon \rangle_1)\{E^* \cos(\theta - \alpha) + E_1\} \tag{2.28}$$

where α is the angle between the geomagnetic east and $\hat{\mathbf{k}}$, $\langle \upsilon \rangle_1$ is the decrease in collision frequency, and E_1 is the associated increase in the electric field. Within the region of low

Pedersen conductivity, the enhanced eastward component of E_1 can raise the F-layer altitude. Therefore, from Equation (2.28), the net upward drift velocity of the F-region plasma can be expressed as

$$\begin{aligned} V_u &= \frac{\mathbf{E}^* \cos\theta + \mathbf{E}_1 \cos\alpha}{B} \cos I - \frac{g}{\langle \upsilon \rangle - \langle \upsilon \rangle_1} \sin^2 I \\ &= \frac{\langle \upsilon \rangle_1}{\langle \upsilon \rangle - \langle \upsilon \rangle_1} \frac{\mathbf{E}^* \cos I}{B} \sin(\theta - \alpha) \sin\alpha \end{aligned} \tag{2.29}$$

From 2.10, V_u is positive when $\hat{\mathbf{k}}$ (or $-\hat{\mathbf{k}}$) lies between $\mathbf{E}^*$ and east, that is $\theta > \alpha > 0$. In such a case, the balance between the gravitational force and background electric field force is disrupted, because the upward drift cannot be compensated by the downward diffusion. From Perkins (1973), the linear growth rate of the Perkins instability can be written as

$$\gamma_P = \frac{E_0^* \cos I}{BH} \sin(\theta - \alpha) \sin\alpha = \frac{g \sin^2 I}{\langle \upsilon \rangle H} \frac{\sin(\theta - \alpha) \sin\alpha}{\cos\theta} \tag{2.30}$$

where H is the atmospheric scale height. The growth rate reaches the maximum when $\alpha = \theta/2$.

2.4.3 E-F Coupling

Although the Perkins instability can well explain the directional preference of the nighttime mid-latitude MSTIDs, there are still some research gaps that need to be filled: the equator-westward propagation direction (theoretically, the MSTIDs should move with the background plasma); the linear growth rate calculated from Equation (2.30) is too small to satisfy the MSTID growth rate derived from real observation (Kelley and Makela, 2001). The simulation in Yokoyama et al. (2008) has further validated these conclusions. In addition, theoretical analysis inferred a coupled effect from polarized Es structures (Es-layer instability) coupled to the Perkins instability, which is important to explain the nighttime MSTID creation (Tsunoda and Cosgrove, 2001).

According to the Es-layer instability, the polarization electric fields within Es are generated by the wind-shear theory (mainly in zonal direction) through the Hall polarization process, and the vertical Pedersen drift acts to enhance the initial perturbation (Cosgrove and Tsunoda, 2002). Similar to the Perkins instability, the azimuth of the wavefront in the plasma density perturbation has a significant effect on the growth rate of the Es layer instability (Yokoyama et al., 2004). The linear growth rate of the Es-layer instability can be written as

(Tsunoda, 2006)

$$\gamma_E = \frac{U_E \cos I}{H_U \rho_i} \left(\frac{\sum_H^{Es}}{\sum_P^{Es} + \sum_P^E + \sum_P^F} \sin\alpha \cos\alpha - 1 \right) \tag{2.31}$$

where U_E is the E-region zonal wind velocity, $H_U \equiv (1/U^E \partial U^E/\partial z)^{-1}$ is the scale length of the vertical shear of U_E, $\rho_i = \upsilon_{in}/\omega_i$, where υ_{in} and ω_i are the ion-neutral collision frequency and ion angular gyrofrequency, respectively, $\sum_H$ and $\sum_P$ are the field-line integrated Hall and Pedersen conductivities in the designated region, respectively. Variations in Hall (Pedersen) conductivity are sensitive to the height modulation of the Es (F) layer and are essentially equivalent to density perturbations (Yokoyama and Hysell, 2010).

From Equations (2.30) and (2.31), in the coupled ionospheric E and F region, the growth rate of the coupled instability can be expressed as (Tsunoda, 2006)

$$\gamma_P^c = \gamma_P + \frac{\sum_H^{Es}}{\sum_P^{Es} + \sum_P^E + \sum_P^F} \frac{U_E \cos I}{H_U} \cos^2\alpha \tag{2.32a}$$

$$\gamma_E^c = \gamma_E + \frac{E_0^* \cos I}{\rho_i B H} \sin(\theta - \alpha) \sin\alpha \tag{2.32b}$$

Since $H \gg H_U$, the second term in Equation (2.32a) comes from the Hall drift in the F region produced by the E-region polarization electric field, and is much larger than γ_P; the second term in Equation (2.32b) comes from the Pedersen drift in the E region produced by the F-region polarization electric field, and is much smaller than γ_E. That is to say, the Es layers are important for the MSTIDs development, but not vice versa.

According to the observation results in Saito et al. (2007) and Ejiri et al. (2019a), field aligned irregularities (FAIs) in E and F regions share similar characteristics, indicating that the perturbed electric field is transmitted along the magnetic field lines (**B**) between the E and F regions. In fact, neutral wind and polarization electric field in the E region drive strong currents in the Es layer. Most of the current is confined within the Es layer, while only a small fraction of the current (20 nAm^{-2}) flows out of the Es layer and couples into field-aligned currents with the F region (Yokoyama and Stolle, 2017). Yokoyama et al. (2009) and Yokoyama and Hysell (2010) have performed 3-D simulations of MSTID generation through E-F coupling (Perkins instability in the F region and Es-layer instability in the E region). Their simulation results in Figure 2.12 verified that the Es layers, especially the polarization electric fields in the E region, play a major role in seeding and amplifying the perturbations in the F region. When the effective electric field (northeastward) satisfies the condition that allows for the Perkins instability to occur, the wavelengths of the E- and F-region perturbations are similar at the beginning, indicating the polarized electric field

generated in the E region is transmitted along magnetic field lines **B** to the F region and modulates the plasma density in the F region (Yokoyama et al., 2009). In such a case, based on the rough estimation of the mapping factor ($\sqrt{\sigma_0/\sigma_p}$; σ_0 and σ_p are the parallel and Pedersen conductivities, respectively), a 10 km-scale perpendicular electric field in the E (F) region can map for 1000 km (10000 km) along a geomagnetic field line **B** (Yokoyama, 2014). That is, for a small-scale polarization electric field in the same hemisphere, the mapping efficiency is large enough to cause no or very little attenuation.

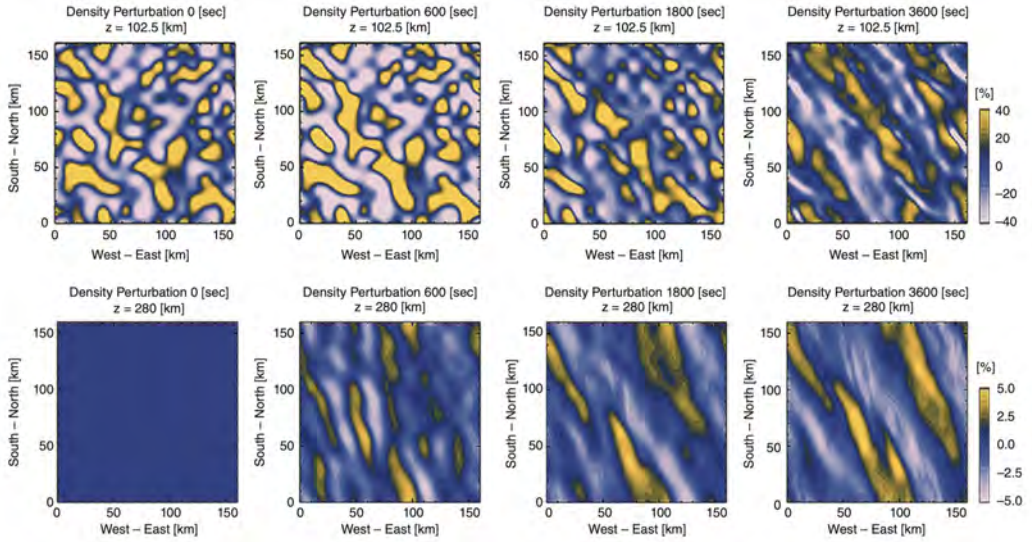

Fig. 2.12 The 3-D simulation results of the E-F coupling. Top (bottom) panel shows the plasma density perturbation at 102.5 (280) km altitudes. Adapted from Yokoyama et al. (2009).

As MSTIDs develop, large-scale perturbations have greatly enhanced. Similar situation occurs at E region. This could be related with the wavelength dependence of Perkins instability and Es-layer instability: the Es layer with very long wavelength has a small growth rate and does not play a pivotal role in seeding the F-region Perkins instability; structures with shorter perturbations tending to saturate at low amplitudes (Yokoyama, 2013; Yokoyama et al., 2008). In addition, one important thing that needs to be noted is that within the Es layer, the E-region neutral winds toward the equator can be affected by the tidal winds, such that the E-region neutral winds rotate clockwise (anticlockwise) in the Northern (Southern) Hemisphere. The E-region rotational wind shear could be responsible for the equator-westward propagation of MSTIDs in the F region, which has been validated by simulations in Yokoyama et al. (2009, 2008): the NW–SE structures in the F region are stationary if the E-region meridional wind is absent; the E-region rotational wind shear produces southwestward phase propagation in both E and F regions even though there is

no background electric field. Particularly, the observed phase velocities of MSTIDs are comparable to the E-region neutral wind velocities (Larsen, 2002).

2.4.4 Interhemispheric Coupling

As analyzed above, the nighttime mid-latitude MSTIDs are electrified. The polarization electric fields can be mapped to the opposite hemisphere (with comparable scale size) along the magnetic field line (**B**), although certain attenuation may need to be considered (Yokoyama, 2014). By using airglow images, Narayanan et al. (2018) simultaneously observed the geomagnetic conjugate MSTIDs, as shown in Figure 2.13. MEFs caused by these MSTID structures are observed in geomagnetic conjugate regions, which indicates that and the coupling process in local E and F regions and/or in different hemispheres is accompanied by field-aligned currents. This field-aligned current can produce a magnetic field change perpendicular to the direction of the main magnetic field, which we call it as midl-atitude magnetic field fluctuations (MMFs). Figure 2.14 shows the global distribution of occurrence rates of MMFs in different seasons for 2002–2003 by using CHAMP spaceborne measurements. Results show that the nighttime MSTIDs mainly occur at 15°–40° magnetic latitude. Consistent with earlier regional statistic results (Shiokawa et al., 2003a), these MSTIDs show maximum occurrence in summer, followed by winter. In addition, the longitudinal variation can also be observed: larger MMF occurrence rates appear over the East Asia/Oceania and Europe/Northern Atlantic Ocean during summer, while over the American continents during winter.

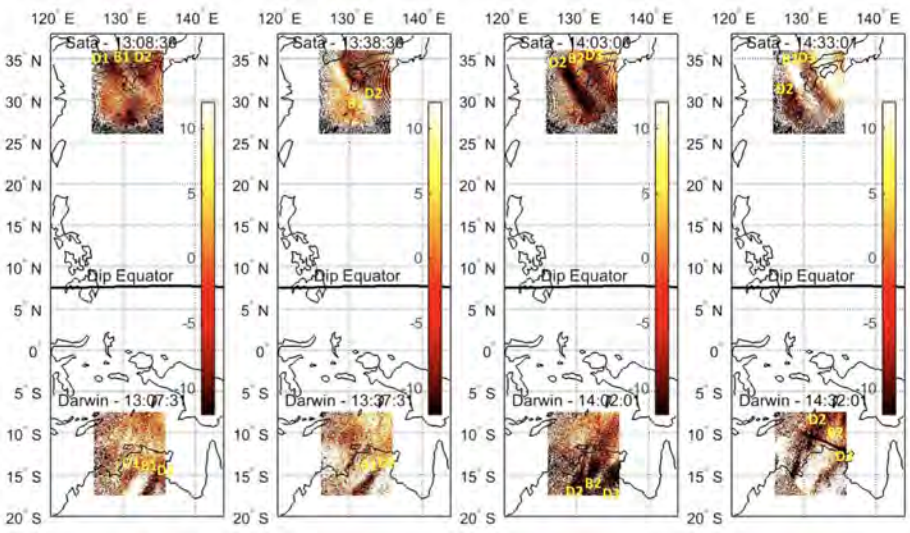

Fig. 2.13 Simultaneous observations of conjugate MSTIDs over Japan and Australia using airglow images. Adapted from Narayanan et al. (2018).

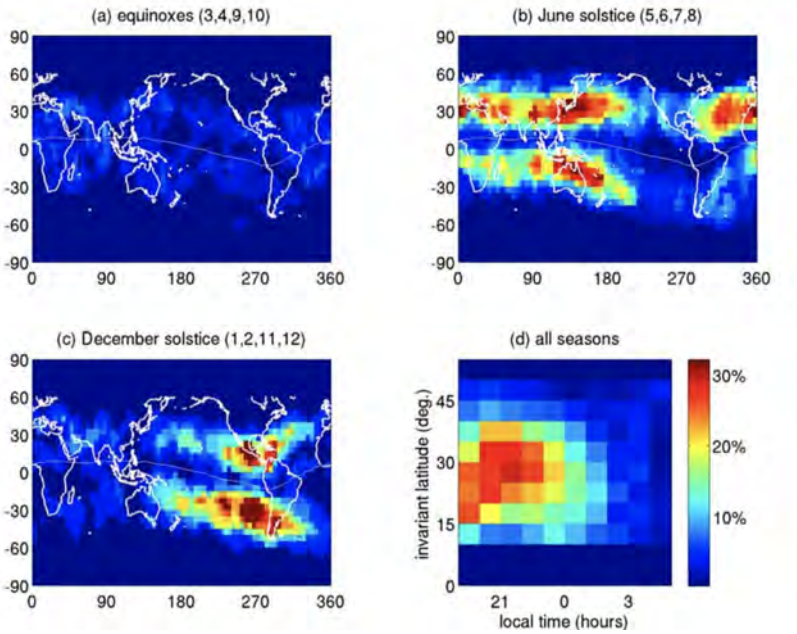

Fig. 2.14 (a–c) Global distribution of occurrence rates of MMFs different seasons for 2002–2003. (d) Occurrence distribution as a function of invariant latitude versus local time. Adapted from Park et al. (2009b).

The ionospheric coupling process between E and F regions can explain this phenomenon. That is, the occurrence of Es layer may cause the longitudinal variation of nighttime mid-latitude MSTIDs (Otsuka et al., 2008): from Figure 2.7 and 2.14, it can be seen that the regions of occurrence of Es with certain intensity (indicated by S4 index) and MSTIDs are basically coincident. In addition, the seasonal variation of MSTIDs (the maximum and secondary occurrence peak of MSTIDs in summer and winter; shown in Figure 2.9) could be associated with the interhemispheric coupling. By using the long-term radio occultation observations, Liu et al. (2020) inferred that the MSTIDs are closely related to the effect of E-F coupling and interhemispheric coupling; Lee et al. (2021) found that the MSTID generation is also affected by some factors other than Es, e.g., the growth rate of the Perkins instability, AGWs, and the F-region conductance. Park et al. (2016) have also verified that the polarization electric fields related with Es and MSTIDs in the summer hemisphere play an important role in the formation of conjugate MSTIDs in different hemispheres. Especially, the Es in the summer hemisphere could be the main factor that affects and controls the formation and development of MSTIDs in both hemispheres, since the Poynting flux is directed from the summer to winter hemisphere, and Es layers show high occurrence rates in summer.

Chapter 3

A Double-thin-shell Approach in the Study of E-F Coupling

The GNSS system provides an efficient and high-precision means for ionospheric research. Currently, the regional to global densely distributed ground-based GNSS receiver networks have greatly contributed to the detection and analysis of ionospheric irregularities of different scales, e.g., daytime sporadic E (Maeda and Heki, 2014, 2015), MSTIDs (Otsuka, 2021; Otsuka et al., 2008), and LSTIDs induced by magnetic storms (Borries et al., 2009). However, during the E-F coupling process, Es and MSTIDs of different altitudes usually have simultaneous occurrence. In such a condition, the exploitation of single-thin-shell model (previously described in Section 2.2.3) in the E-F coupling process is difficult because of the impossibility of observing irregularities in both E and F regions simultaneously. Additionally, the utilization of single-thin-shell approach may "shadow" the Es layer due to its low amplitude (usually below 1–2 TECU). In some cases where the main plasma density fluctuations or enhancements are located far below or above the F2 peak (e.g., daytime Es), the error in assuming a single shell at F-region altitudes could be disastrous to industry and applications that depend on trans-ionospheric signals. Therefore, a new method of simultaneously imaging the ionospheric E- and F-region perturbations needs to be developed.

3.1 Data

GEONET (GNSS Earth Observation Network), a nationwide dense GNSS array in Japan consisting of more than 1,200 receivers, can provide GNSS-TEC measurements with high spatial and temporal resolution due to its high density ($\sim$25 km) and sampling rate (30 s). At a data rate of 30 s, every recording is more than 5000 satellite–receiver paths (Saito et al.,

1998a). The distribution of GEONET stations (black dots) is plotted in Figure 3.1, and the NE-SW red dashed line from (33.5°N, 134°E) to (37.5°N, 141°E) indicates the region with the most data points.

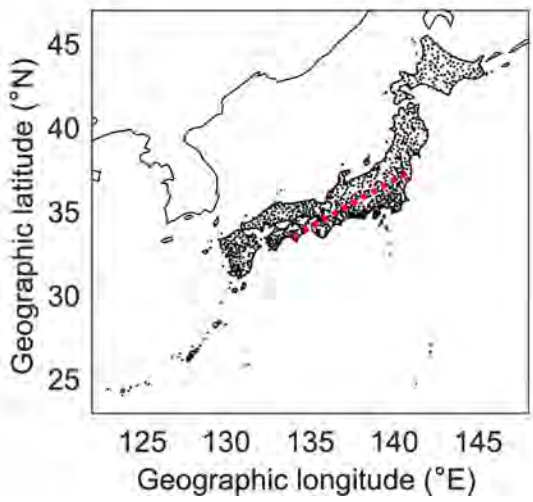

Fig. 3.1 Distribution of GEONET stations (black dots) over Japan. The red dashed line from (33.5°N, 134°E) to (37.5°N, 141°E) indicates the region with most data points.

Following the TEC derivation methods in Section 2.2.3, the STEC here were derived from pseudo-range and phase measurements, and the unknown ambiguities in the phase measurements were corrected by the corresponding pseudorange measurements (Ma et al., 2014). In addition, the instrumental biases inherent in satellites and receivers were assumed to remain stable within one UT (universal time) day (Ma and Maruyama, 2003). STEC with elevation angles smaller than 35° were negated to mitigate the multi-path effects and reduce the errors in the placement of ionospheric piercing points which are sizable at low elevation angles. Considering the accuracy of absolute TEC estimation is about a few TECU, hence making a resolve of low amplitude Es densities uncertain, TEC perturbation (TECP) component rather than the absolute TEC is obtained after deducting a 30-min data running average (centered on the epoch of the LOS) from each STEC:

$$\mathrm{TECP} = \mathrm{STEC} - <\mathrm{STEC}>_{30\mathrm{min}} \tag{3.1}$$

Data corresponding to arc segments less than 30 min are excluded to avoid spurious perturbations. Theoretically, the TECP precision level improves to within 0.01–0.02 TECU, which corresponds to 1% of the wavelength of GPS signals L1 (19 cm) and L2 (24 cm). An example of TECP and STEC comparison is shown in the Figure 3.2, wherein the yellow lines represent TECP, gray lines are the results of 30-min running average, and black lines

are the derived STEC. The top and bottom subfigures are chosen from the events of daytime Es and nighttime MSTIDs, respectively. From Figure 3.2, it is clear that the obtained TECP can effectively describe the perturbations within the STEC series, so that the amplitudes and positions of the Es and MSTIDs can be filtered and tracked.

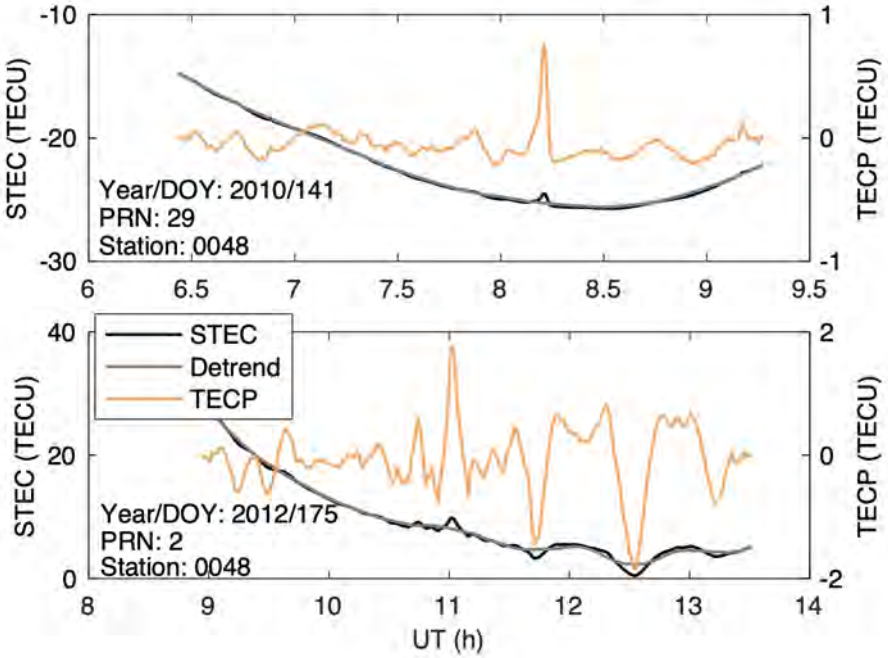

Fig. 3.2 An example of the time series of STEC and TECP on 21 May 2010 (DOY 141) and 23 June 2012 (DOY 175). Yellow lines represent TECP, gray lines are the 30-min running average, and black lines are the derived STEC.

3.2 Double-thin-shell Model

In order to analyze the E-F coupling, the simultaneous reconstruction of E- and F-region plasma density is important. Heuristically, a double-thin-shell approach upgraded from the single-thin-shell model was developed. In fact, the double-thin-shell model has been used to better estimating the ionospheric absolute TEC, e.g., Hernández-Pajares et al. (1999) obtained a global ionospheric map based on a two-layer model to reduce the errors inherent to the one-layer model, and Shukla et al. (2009) designed a two-shell model, at altitudes of 500 km and 300 km, to resolve the Equatorial Ionization Anomaly (EIA) density gradients over the Indian region. Maruyama et al. (2021) also parameterized a regional ionosphere that partially encapsulates EIA, with two shells located at high and low altitudes learned from a training data set. In their results, TEC precision was better than in a single-thin-shell

approximation, and the EIA was captured adequately. The following are the settings in this research different from the previous studies:

1. The shell altitudes are fixed pre-analysis.
2. Rather than absolute TEC values, the TECP components are ingested.
3. Analysis is over the Japanese archipelago, where the dense GNSS receiver network GEOENT is ideal in analyzing small density perturbations.

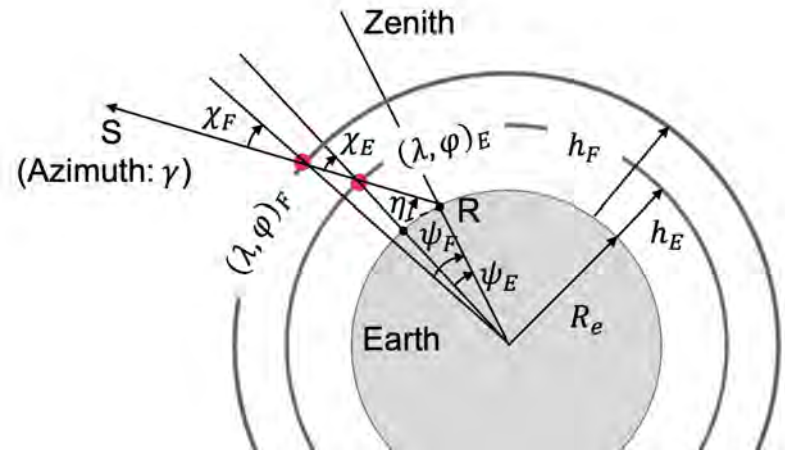

Fig. 3.3 Typical geometric relation of a GNSS satellite (S) and a receiver (R) in double-thin-shell approximation.

A typical geometric relation of a GNSS satellite (S) and a receiver (R) in the double-thin-shell approximation is shown in Figure 3.3. The slant TECP is assumed to be the summation of the contributions in two thin-shell layers located at two constant heights (E shell and F shell):

$$\mathrm{TECP}^S = \mathrm{STEC}_E^S + \mathrm{STEC}_F^S \tag{3.2}$$

Although TECP is relatively small, STEC_E^S and STEC_F^S can have large positive and negative values. Even so, the reconstruction of STEC_E^S and STEC_F^S becomes possible if there are a sufficient number of ray paths that cross the reconstruction region at E and F shells. The latitude (λ_i) and longitude (φ_i) of ionosphere pierce point (IPP, shown as red points in Figure 3.3), and the local satellite zenith angle (χ_i) in each shell (i = E, F for different shell heights) can be calculated as

$$\lambda_i = \arcsin(\sin\lambda_R \cos\psi_i + \cos\lambda_R \sin\psi_i \sin\gamma) \tag{3.3a}$$

$$\varphi_i = \varphi_R + \arcsin\left(\frac{\sin\psi_i \sin\gamma}{\cos\lambda_i}\right) \tag{3.3b}$$

$$\chi_i = \arcsin\left(\frac{R_e}{R_e + h_i}\cos\eta\right) \tag{3.3c}$$

$$\psi_i = \frac{\pi}{2} - \eta - \chi_i \tag{3.3d}$$

where λ_R and φ_R are the latitude and longitude of the receiver (R), γ and η are the azimuth and elevation angle of the satellite (S), R_e is the mean radius of the Earth, ψ_i is the geocentric angle, and h_i is the shell height. Based on the earlier studies on E- and F-region irregularities (Maeda and Heki, 2015; Saito et al., 1998b) that utilized ground-based GNSS-TEC and a single-thin-shell approach, h_i is set to 100 km and 300 km for the E and F shells, respectively.

Considering the ionospheric irregularities usually occur at altitudes ∼95–125 km (∼250–350 km) in E (F) region (Haldoupis et al., 2006; Yang et al., 2015), the maximum uncertainty of the phase front structures manifested in the projections on the ground is about 20 km (45 km), under the double-thin-shell approximation with two constant heights. At a given shell (i = E, F), the relationship between vertical TECP (TECP_i^V) and slant TECP is

$$\mathrm{TECP}_i^S = \mathrm{TECP}_i^V / \cos\chi_i \tag{3.4}$$

Here the ionosphere in the double-thin-shell approximation is assumed to be divided into different cells, and the vertical TECPs within a cell in each shell were assumed to be uniform. To make the statistical quantity meaningful, the minimum IPP number inside a cell was set to 3. With all the slant TECPs from GNSS observations, a mixed determined system of the linear equations can be constructed based on Equations (3.2) and (3.4):

$$\begin{bmatrix} \cdots & \cdots & \cdots & \cdots & \cdots \\ 0 & \sec\chi_{E_{(j-1)k}} & 0 & \sec\chi_{F_{(j-1)k}} & 0 \\ \cdots & \cdots & \cdots & \cdots & \cdots \\ 0 & \sec\chi_{E_{jk}} & 0 & \sec\chi_{F_{jk}} & 0 \\ \cdots & \cdots & \cdots & \cdots & \cdots \\ 0 & \sec\chi_{E_{j(k+1)}} & 0 & \sec\chi_{F_{j(k+1)}} & 0 \\ \cdots & \cdots & \cdots & \cdots & \cdots \end{bmatrix}_{M\times N} \begin{bmatrix} x_1 \\ \cdots \\ x_n \\ \cdots \\ x_N \end{bmatrix}_{N\times 1} = \begin{bmatrix} \cdots \\ \mathrm{TECP}^{S_{(j-1)k}} \\ \cdots \\ \mathrm{TECP}^{S_{jk}} \\ \cdots \\ \mathrm{TECP}^{S_{j(k+1)}} \\ \cdots \end{bmatrix}_{M\times 1} \tag{3.5}$$

j and k represent the satellite and receiver number, x_n is the unknown vertical TEC perturbation in the nth grid (the E- and F-region unknown densities are compressed into a column vector of N cells) and M is the total number of observations. For convenience, I simplify

Equation (3.5) to

$$\vec{Y} = \mathbf{A}\vec{X} + \vec{E} \tag{3.6}$$

$\vec{Y}$ and $\vec{E}$ represent observations and errors, respectively, and coefficient matrix $\mathbf{A}$ is generally a sparse with columns assumed to be linearly independent. To adequately solve Equation (3.6), I used the singular value decomposition (SVD), which has numerically stable properties and can avoid unrealistic solutions (Ma et al., 2014). If the matrix $\mathbf{A}$ is of dimension M×N, then through SVD we can obtain

$$\mathbf{A} = \mathbf{U}\mathbf{D}\mathbf{V}^T \tag{3.7}$$

$\mathbf{U} \in \mathbb{R}^{M\times M}$ ($\mathbf{V} \in \mathbb{R}^{N\times N}$) is an orthonormal matrix composed of left (right) singular vectors of $\mathbf{A}$, associated with singular values or weights contained in a rectangular diagonal matrix $\mathbf{D} \in \mathbb{R}^{M\times N}$; T represents matrix transpose. An r-dimensional sub-space of singular vectors is used to represent $A \approx \mathbf{U}_r\mathbf{D}_r\mathbf{V}_r^T$ with a representation of 95% of the total variance, thus the final solution of $\vec{X}$ can be calculated as

$$\vec{X} \approx \mathbf{V}_r\mathbf{D}_r^{-1}\mathbf{U}_r^T\vec{Y} \tag{3.8}$$

where $\mathbf{U}\mathbf{U}^T = \mathbf{I}$ and $\mathbf{V}\mathbf{V}^T = \mathbf{I}$ are used. A more detailed description of SVD and its application to inverse problems can be found in Golub and Van Loan (2013).

3.3 Validation

In this research, the analyzed region covers 30°N–42°N, 130°E–140°E for the E shell and 28°N–45°N, 128°E–145°E for the F shell. Due to the different scale sizes of E- and F-region irregularities, the resolution in E and F shells was set to 0.15° and 0.5°, respectively, for the adequate realization of the instabilities. The temporal resolution was set to 2.5 minutes. That is, in each epoch, the electron density perturbations were assumed stationary, such that in Equation (3.5) $N = 8676$ and $M > 10000$.

Another notable thing is that GPS satellites orbit the Earth at a great speed (orbit at altitudes of ∼20200 km at speeds of ∼3.8 km/s). Considering the elevation and azimuth angles, the IPP velocities at both E and F shells may sometimes approximate the actual instability phase velocities. In such cases, results are difficult to discern, because the spatial and temporal changes are highly mixed. Fortunately, during the nighttime events analyzed in this thesis, the IPP drifts were predominant Northward. An example of the IPP drift velocities in the NE-SW direction (parallel to the propagation direction of MSTIDs) on 21 May 2010 is shown in Figure 3.4. From the results, with a minimum satellite elevation angle of 35° and

a structure at F shell elongated NW–SE and propagating southwestward at ∼100 m/s, the average estimated error to bear in our analysis was ∼20% of the actual velocity.

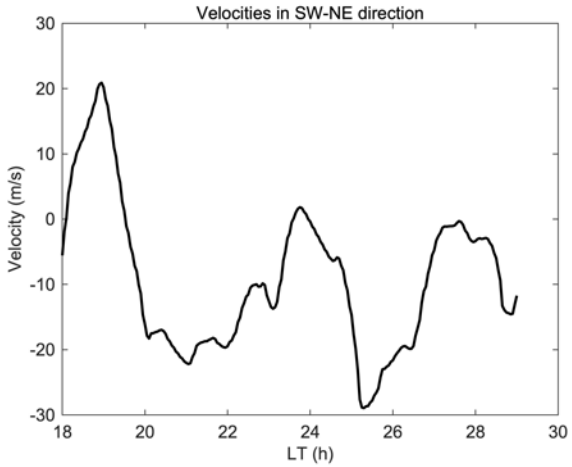

Fig. 3.4 IPP drift velocities in the NE-SW direction on 21 May 2010 (DOY 141).

This validation part mainly addresses two questions to raise confidence in the proposed double-thin-shell model technique: (1) Is the technique able to reconstruct or place the perturbations at the appropriate shell? With disregard to the difference in night and day ionosphere density concentrations, here, as a test case, I analyzed a carefully selected daytime Es event on 21 May 2010 (DOY 141), previously analyzed by Maeda and Heki (2014) when the F-region was deemed quiet. The reasoning was that at daytime a well-developed and highly conducting E region limits polarization electric fields that could facilitate the E–F coupling (Kelley, 2009). Therefore, the signal should be from the E shell, and the F-shell noise dominated. (2) What is the noise threshold below which structures in E and F shells are distinguishable? Because nighttime F-shell structures are known to be dominant in amplitude and scale when compared to E-region structures, here, structures were simulated in both E and F regions, and then synthetic STEC were used to analyze the algorithm fidelity when the F-region structure amplitudes and noise level were varied.

3.3.1 An Event of Daytime Sporadic E

The comparison of reconstruction results from single- and double-thin-shell approaches is shown in Figure 3.5. The leftmost column is the TECP maps under the single-thin-shell approximation adapted in Maeda and Heki (2014). The right two columns are the horizontal TECP distribution at E (a–c) and F-shell heights (d–f) of the daytime Es event during 17:00–17:30 JST (Japan Standard Time), on 21 May 2010 (DOY 141). From Figure 3.5, in

both single- and double-thin-shell models, the east–west (E–W) aligned frontal structure of Es at 35°N–36°N has been observed. In addition, consistent with the observation results in Maeda and Heki (2014), the migration of this frontal structure is southwestward, with a mean speed of ∼80 m/s; the maximum horizontal scale of this Es structure can reach ∼350 km in E-W, ∼30 km in north–south (N–W). To our confidence, the F shell (F region), is noise dominated. Thus, the algorithm can adequately reconstruct the irregularities to the correct shell.

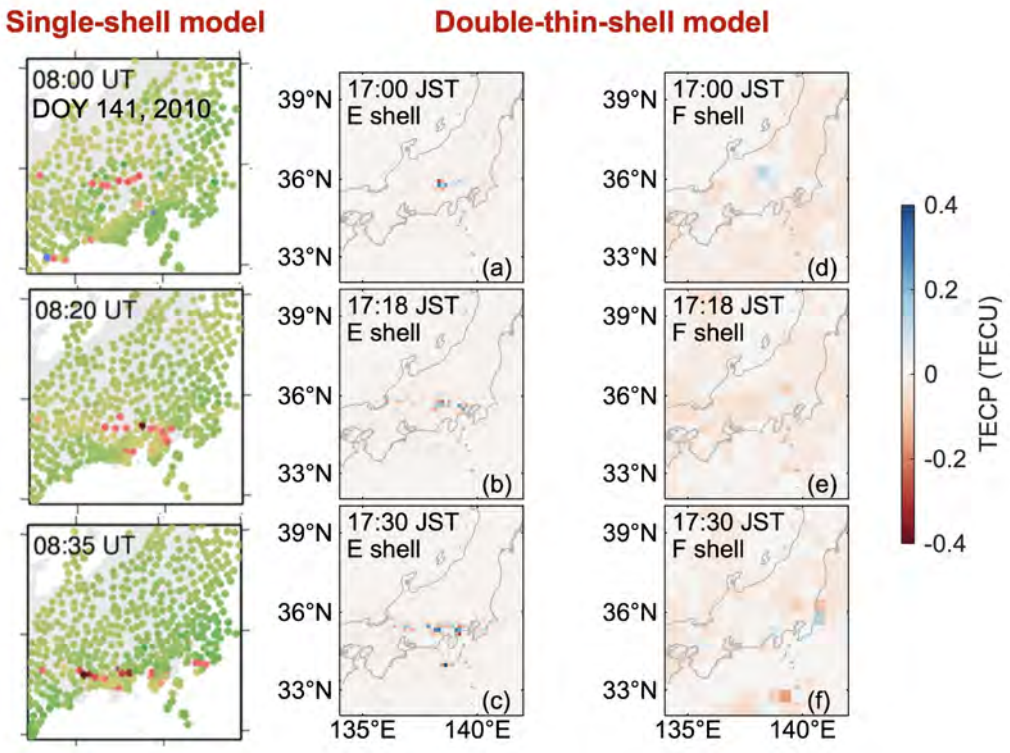

Fig. 3.5 Snapshots of TECP maps under single-thin-shell approximation (leftmost column; adapted from Maeda and Heki (2014)) and at E- (a–c) and F-shell (d–f) heights, at various time epochs from 17:00 to 17:30 JST (Japan Standard Time) on 21 May 2010 (DOY 141)

3.3.2 Simulation

For further validation, a 2-D simulation using the real geometry of GNSS satellites and receivers was performed.

As shown in Figure 3.6(a–b), irregularities are input in different shell heights to simulate Es and MSTIDs. Considering the IPP distribution as shown in subplots (c–d), the focus is on the region with dense data points that exhibits high fidelity (bounded with yellow dashed lines

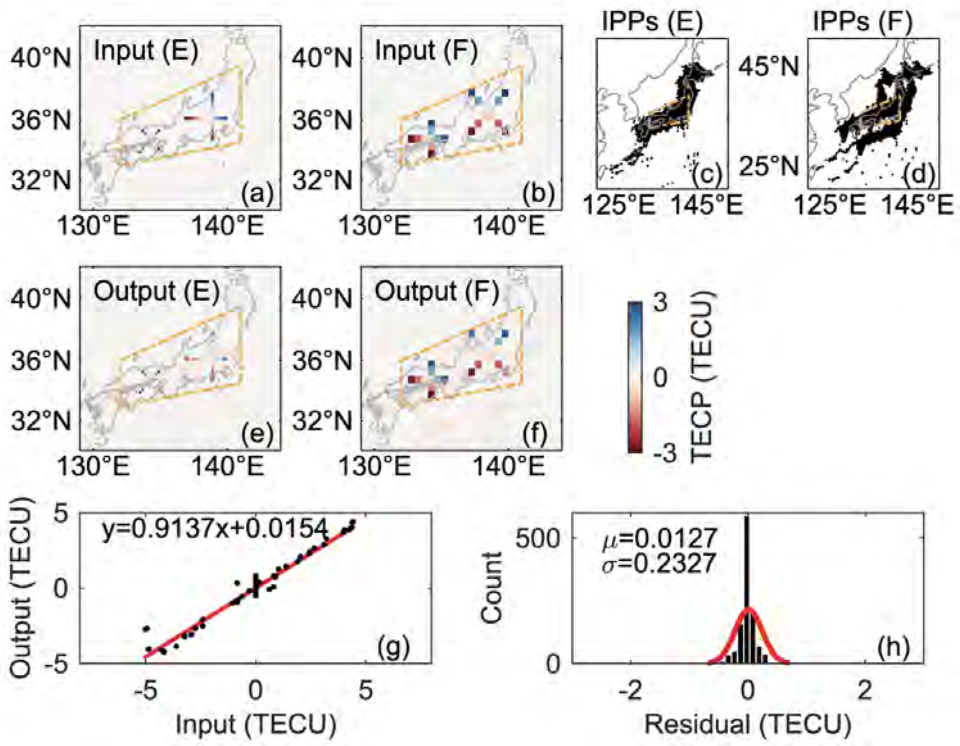

Fig. 3.6 2-D maps of input (a, b), IPP distribution (c, d), output (e, f) irregularities at E- and F-shell heights, a scatter of input and output TECP values (g) and a distribution of residuals (h) using GNSS signal rays at 17:30 JST, on 21 May 2010 (DOY 141). The yellow dashed line indicates a region, where reconstruction is of highest confidence level.

in Figure 3.6). In this simulation, noise has not been considered. The two simulated cross irregular structures with amplitudes varying within -3–3 TECU (range of most TECPs during MSTID events) were set up in E and F regions. To clearly present the results, the horizontal scales (range of MSTID wavelengths) of input "+" ("x") irregularities were about 250 km (180 km) and 280 km (310 km) in E- and F-shell heights, respectively. About 16000 real signal rays from GNSS observations at 17:30 JST, on 21 May 2010 (DOY 141) were used. The simulated slant TECPs were then generated as an integral of density perturbations along the ray paths determined from the observation geometry of GNSS satellites and more than 1200 receiver stations from the GEONET. Subplots (e, f) of Figure 3.6 show the reconstructed structures: in the area with densely distributed IPPs, the reconstructions at the different shell heights are clearly distinguishable and consistent with the input irregularities in both position and amplitude. In addition, a control data set from 88 GEONET receivers is used to specify the precision. A scatter of input and output TECP values, and a distribution of residuals are plotted in the subplots (g, h). The results suggest a high correlation between input and output values: the gradient to least square fit (red solid line) is 0.91 in subplot (g); the mean (μ) of

residuals is 0.01, and the standard deviation (σ) is 0.23 TECU; about 50% of the residuals lie within the first bin (the width of each bin is about 0.1 TECU), and 89% of the data lie within $\mu \pm \sigma$.

Similarly, simulations of two other cases were also analyzed: input irregular structures either in E- or F-shell height, and the results are shown in Figure 3.7. As inferred from the results, the reconstruction still agrees with the input irregularities; the mean (μ) and standard deviation (σ) of residuals are small, although the errors are slightly larger when only the E-region irregularities present. From all the results above, the double-thin-shell approach can successfully reconstruct the E- and F-region irregularities simultaneously under the condition of no noise.

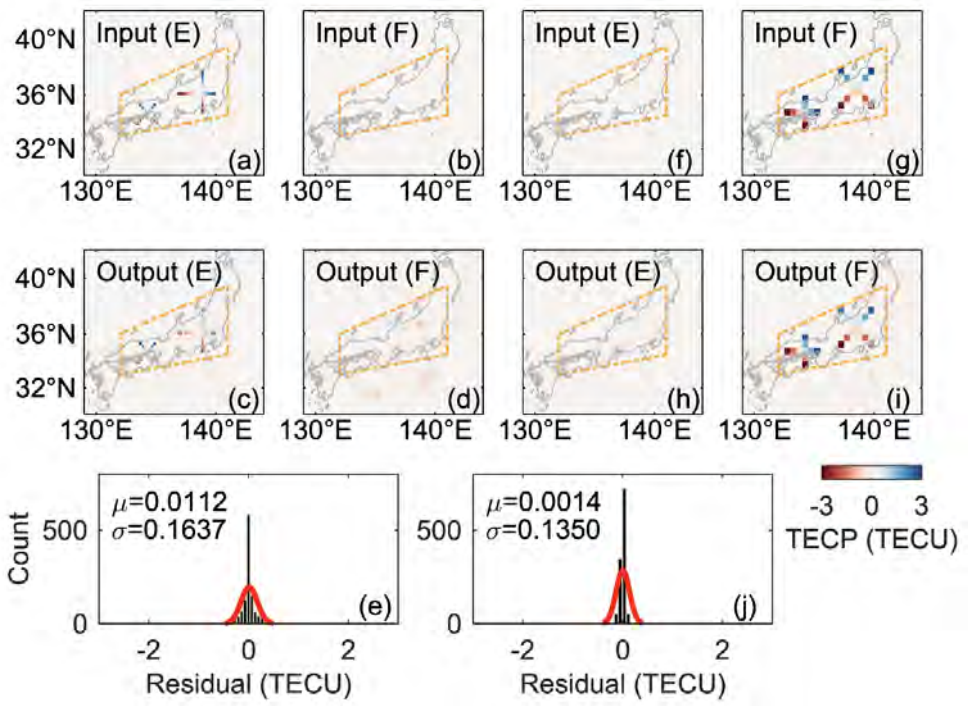

Fig. 3.7 2-D maps of input irregularities only in E shell (a–b), output irregularities (c–d), and corresponding residual distribution (e). 2-D maps of input irregularities only in F shell (f–g), output irregularities (h–i), and corresponding residual distribution (j).

To specifically evaluate the algorithm performance in the E region, reconstructions were analyzed under different ratios of E to F region input structure amplitudes (IE/IF). In addition, as stated earlier, the ratios of the standard deviation of noise to F-region input amplitude (N/IF) were also varied. The input irregularities were in the same position as in Figure 3.7(a–b), and the constant input amplitude in the F region was set to 2 TECU (most possible amplitude of TECP in MSTID events). In Figure 3.8, subplots (a–c) show the

reconstructed results in E region with IE/IF=0.1, 0.2, and 0.3, under the condition of N/IF=0. In subplots (d–i), IE/IF=0.5 and N/IF altered. Based on the reconstructed results, even if strong irregularities exist in the F region, E-region irregular structures are well reconstructed when IE/IF$\geq$0.3 and the amplitude of noise not exceeding the amplitude of the E-region irregularities.

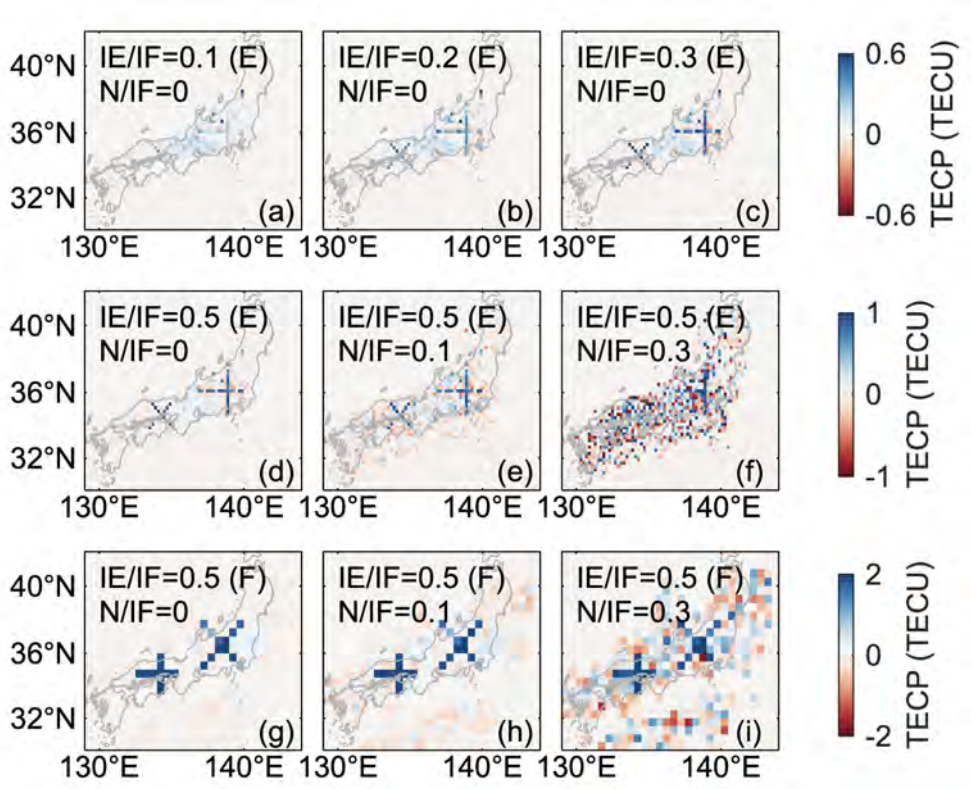

Fig. 3.8 2-D maps of output irregularities at different ratios of input amplitude in E and F regions (IE/IF) (a–c), and different ratios of noise standard deviation to input amplitude in F region (N/IF) (d–i).

Chapter 4

Case Studies of E-F and Interhemispheric Coupling

During the summer, the nighttime mid-latitude MSTIDs show higher occurrence possibility in the Japan-Australia sector (∼100°E–180°E) than other regions, as shown in Figure 2.9. Consistent with the E-F coupling theory, the occurrence of Es with a relative intensity is equally high in these regions, as shown in the bottom row of Figure 2.7. In addition, the E-F coupling process is more intricate, to the extent that MSTIDs are simultaneously observed in the geomagnetic conjugate regions (different hemispheres) with matching crests and troughs as shown in Figure 2.13 and 2.14. However, due to the limited observation area, resolution, and methods, comparing the temporal relationship between the occurrence of Es and MSTIDs is difficult, and thus the causes and effects in the E-F and interhemispheric coupling are not yet fully understood. Therefore, a comprehensive analysis of the local E-F and interhemispheric coupling is required to deepen our understanding of the generation and development mechanisms of nighttime electrified MSTIDs.

4.1 E-F Coupling

In this section, the local E-F coupling process over Japan were mainly analyzed using the dense-distributed ground-based GNSS-TEC and a double-thin-shell approach. The distribution of receiver network (GEONET) is shown in Figure 3.1. The setup of the double-thin-shell model and TECP is the same as in Chapter 3: two shell heights were set to 100 km and 300 km for the E and F shells, respectively; TECP were obtained after deducting a 30-min data running average from each STEC; the analyzed region overs 30°N–42°N, 130°E–140°E for the E shell and 28°N–45°N, 128°E–145°E for the F shell; in the analyzed

region, the resolution was set to 0.15° in E shell and 0.5° in F shell, and 2.5 minutes in time. Since nighttime MSTID occurrence over Japan maximizes around the June solstice (Shiokawa et al., 2003b), two nighttime events were selected for analysis into this period: June 23, 2012 (DOY 175) and June 11, 2007 (DOY 162). Both days are manifested with MSTIDs, but the amplitudes are different. To mitigate ionospheric disturbances due to other factors such as geomagnetic storms, the ionospheric conditions on the selected events were K<4 and |Dst|<30 (Ma et al., 2014). The K index is from data provided by Kakioka magnetic observatory at (36.2°N, 140.2°E).

Based on the simulation results in Section 3.3.2, to reduce the ambiguity of the structures in E shell, reconstructions with IE/IF<0.3 were excluded. The region with most data points, bounded by yellow dashed lines in Figure 3.6, is the focus. As validation, reconstructions in this region are compared to observations from Kokubunji ionosonde and the middle and upper atmosphere radar (MUR).

4.1.1 Event on 23 June 2012

The event on 23 June 2012 (DOY 175) is a typical example of nighttime MSTIDs shown in Ssessanga et al. (2017). According to the 2-D TECP maps provided by NICT (National Institute of Information and Communications Technology, in Japan; data accessible at https://aer-nc-web.nict.go.jp/GPS/DRAWING-TEC/), for this event, the MSTIDs form at ∼11:00 UT (UT = JST-9) and end at ∼20:00 UT, and show maximum intensity at ∼13:00 UT. Subplots (a–h) in Figure 4.1 show the 2-D horizontal TECP distribution maps at E- (a–d) and F-shell (e–h) heights under the double-thin-shell approximation, during 19:30–22:00 JST. Bottom subplots (i–l) are the 2-D TECP maps using the same parameters (height: 300 km; grid resolution: 0.15°) as Tsugawa et al. (2018) under the single-thin-shell approximation. Black dashed lines indicate the alignment azimuth of the apparent frontal structures. Gray arrows represent the drift direction (read by eye according to the reconstructed results in a time series). Black dots in subplots b, c, f, and g denote arbitrarily chosen points along the wavefront in the E region (100 km) and the corresponding points in the F region (300 km) following geomagnetic equal potential lines estimated from the International Geomagnetic Reference Field (IGRF) model (Alken et al., 2021). As predicted in the electrodynamic theory of mid-latitude nighttime E–F coupling, E and F layer density enhancements/depletions are observed to be connected with geomagnetic equal potential lines.

Before 19:30 JST, the E- and F-region irregularities develop but with a small amplitude; probably the early stages of the coupling process. Of course, in this analysis, I cannot pinpoint exactly when instabilities commence, because at the early stages of development, the amplitudes are primarily below the GNSS noise level. After 19:30 JST, the intensity and

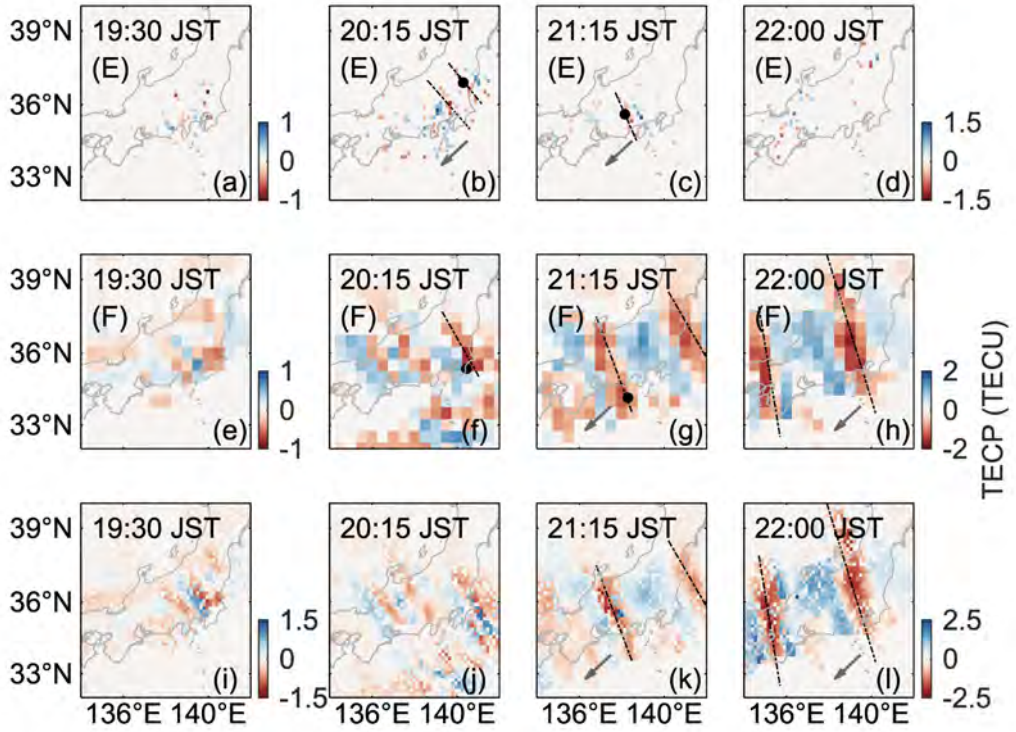

Fig. 4.1 Snapshots of TECP maps at E- (a–d) and F-shell heights (e–h), at various time epochs from 19:30 to 22:00 JST on 23 June 2012 (DOY 175). The subplots in the bottom (i–l) show the 2-D TECP maps obtained by the single-thin-shell approach. Black dashed lines indicate the alignment azimuth of the apparent frontal structures, gray arrows indicate the drift direction, black dots indicate the locations at E and F shells connected by the geomagnetic field line.

horizontal scale of E- and F-region irregularities both appear enhanced. Particularly at 20:15 and 21:15 JST, the E- and F-region irregularities migrate southwestward and have preferred NW–SE alignment.

In the top two rows, the average horizontal scales of the E- and F-region irregular structures are about 150 km and 500 km in length and about 30 km and 120 km in width. From the works of Farley Jr (1959), such scale sizes are sufficient for polarization electric fields to map efficiently along magnetic field lines, with coupled E–F regions as a subsequent. A look at both shells, the structures in E and F regions show maximum intensity at around 20:15 and 22:00 JST, respectively, and the F-region structures are well defined than those in the E region: this might be the consequences of the thin layer of Es and the coupling dynamics, wherein the Es layer is easily saturated, and the F-region instability is greatly enhanced in the coupling process, and thus a stronger structuring at the F region. I estimated the center drift phase velocity of the front structures, and the mean migration was about 100

m/s, with a maximum value exceeding 120 m/s. Faster velocities appeared with the rapid development of E-region irregularities. The E- and F-region irregularities connected by the same geomagnetic field lines had similar propagation parameters. Because these velocities are comparable to observed E-region neutral wind velocities (U_E) (Larsen, 2002), I further emphasize the suggestion that the phase velocity of the NW–SE structure in E and F regions is U_E controlled. The theoretical and simulation works of Tsunoda (2006) and Yokoyama et al. (2009) have also underscored the role played by U_E: the E-region rotational wind shear produces southwest phase propagation of the NW–SE structure in both E and F regions even though there is no background electric field, and the NW–SE structures are stationary if the E-region meridional wind is absent. In addition, due to the significant spatiotemporal variation of the E-region neutral wind, the F-region gravity waves may also be a potentially important factor in the propagation of NW–SE structures over a large area in the form of traveling ionospheric disturbances (Yokoyama et al., 2009).

At 22:00 JST, the Es structures were damped out, while the MSTIDs intensified, with two frontal structures exhibiting a spatial wavelength separation of $\sim$200 km. Compared to 20:15 JST, the structures at 22:00 JST are more clockwise, but with the orientation angle more acute at the south most frontal structure. The 3-D E–F coupling simulations by Yokoyama et al. (2009) also insinuated that orientation angle decreases as the magnetic dip angle decreases southward. Indeed, the azimuth and scale of the structures from the double-thin-shell model (subplots g–h) are consistent with the orthodox single shell results (subplots k–l). However, on further analysis, a phase difference (less than 50 km) between structures in subplots g–h and subplots k–l was observed: possibly a consequence of utilizing different grid resolutions and the IPP drift error in the two-shell model. Nonetheless, this discrepancy is not large to affect our analysis of the physical underpinnings.

Ionosondes are among the accurate tools for probing the ionospheric plasma density. Here, I consider Kokubunji ionosonde station (located within the region of most GNSS data points in Japan, shown as black triangle in Figure 4.2(c, d); Ssessanga et al. (2017)) observations for validation purposes. Figure 4.2(a–d) shows the reconstructed 2-D TECP maps at E-shell height and the Kokubunji ionograms, at 20:15 and 22:15 JST when E- and F-region irregularities reach the maximum intensity. Subplot (e) shows the variation of the foEs (the critical frequency of Es) obtained from ionosonde observations and reconstructed TECPs (a 2-km thickness is assumed (Maeda and Heki, 2014)) at Kokubunji area (a 0.3° grid), from 20:00 to 22:30 JST. During 20:00–22:30 JST, the foEs observed by Kokubunji ionosonde reached the maximum amplitude ($\sim$15 MHz) at around 20:15 JST. The foEs decreased and remained at a relatively low level ($\sim$6 MHz) after 21:00 JST, but had a transient enhancement ($\sim$10 MHz) at 22:15 JST. The reconstructed results agree with the

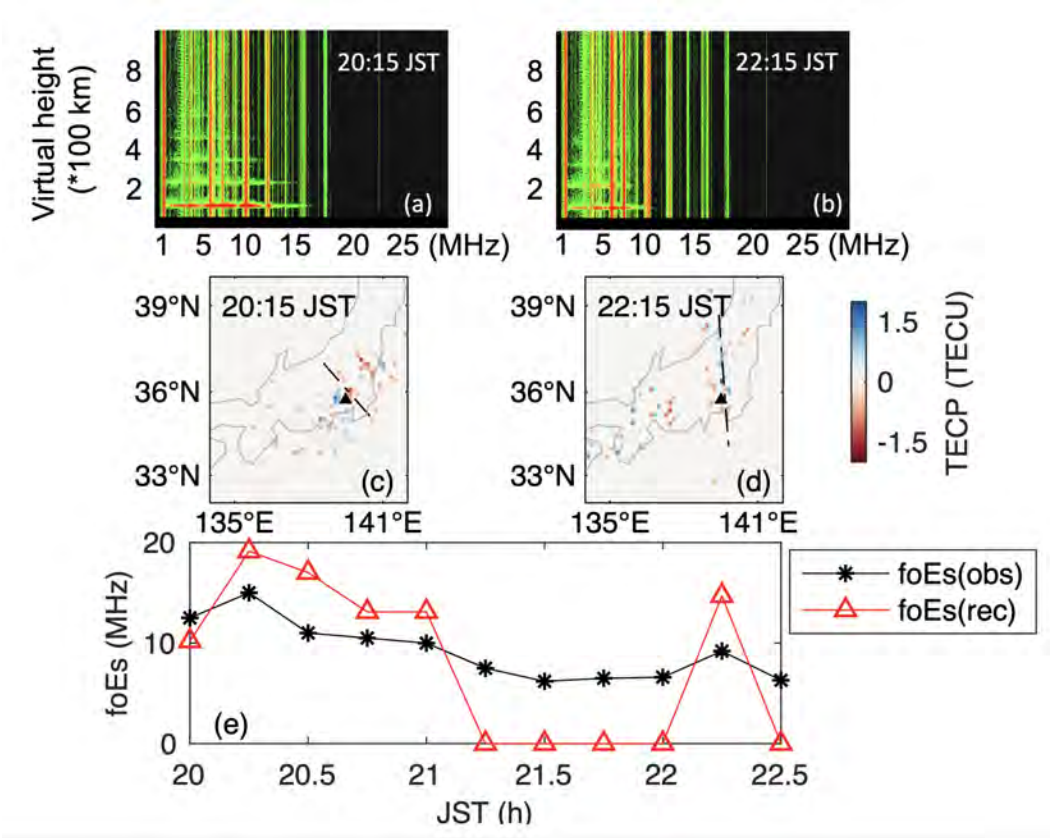

Fig. 4.2 Ionogram observed by Kokubunji ionosonde (a, b), and snapshots of TECP maps at E shell height (c, d) at 20:15 and 22:15 JST on 23 June 2012 (DOY 175). Black triangle represents the location of Kokubunji ionosonde. (e) The variation of the foEs obtained from ionosonde observations (foEs(obs)) and reconstructed TECPs (foEs(rec); a 2 km thickness is assumed) at Kokubunji area during 20:00–22:30 JST.

ionosonde observations: the E-region frontal structure with a high intensity is approaching the Kokubunji area at 20:15 and 22:15 JST; the foEs variations obtained by ionosonde observations (foEs(obs)) and reconstructions (foEs(rec)) are consistent within 5 MHz. Since reconstructions with IE/IF<0.3 are excluded and foEs are low, the reconstructed TECPs with small amplitude at 21:15–22:00 JST are about zero at Kokubunji area. In addition, the maximum perturbation components of E-region TEC at Kokubunji area are 0.91 TECU (19.16 MHz) and 0.53 TECU (14.62 MHz) at 20:15 and 22:15 JST, respectively, with larger amplitudes but consistent proportions with those of foEs assuming a thickness of 2 km. Furthermore, except at 21:15, 21:30 and 22:30 JST when foEs is low, the ionograms clearly reveal the presence of blanketing Es from 19:30 to 24:00 JST as in Figure 4.2(a–b). That is to say, the radio waves at least up to foF2 cannot penetrate the Es layer, which indicates that the structuring in the Es layer is insignificant (Maruyama et al., 2006).

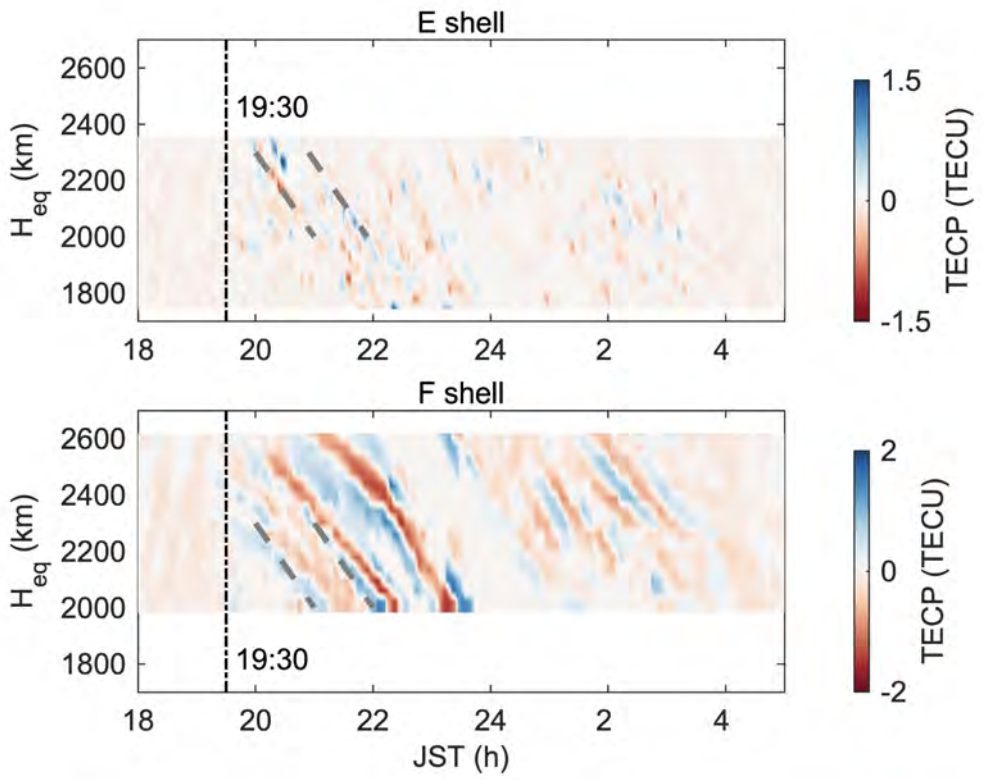

Fig. 4.3 Time variation of TECPs on 23 June 2012 (DOY 175) along the northeast–southwest red dashed in Figure 3.1. H_{eq} is the equatorial crossing height of the magnetic field line piercing each shell. The top and bottom panels represent E- and F-shells, respectively. The black and gray dashed lines represent the occurrence time of perturbations and the alignment of evident downward-sloping stripes, respectively. Evident, particularly between 20:00–23:59 JST, is the southwestward propagating wavefronts in both E- and F-region.

Figure 4.3 shows the time variation of E- and F-region TECPs at nighttime on 23 June 2012 (DOY 175), with a time resolution of 2.5 min along the line from northeast to southwest indicated as the red dashed line in Figure 3.1. Here I introduced a parameter called H_{eq}. As shown in Figure 4.4, red points (A and B) are ionospheric regions connected by a same magnetic field line, and H_{eq} represents the equatorial crossing height of the magnetic field line piercing each shell. The irregularities of different shells at the same H_{eq} are considered to be related to each other through a magnetic field line. The grid resolution in Figure 4.3 was about $0.3^\circ \times 0.5^\circ$ in E- and F-shell heights. The black and gray dashed lines represent the occurrence time of perturbations and the alignment of evident downward-sloping stripes, respectively. For the strong post-sunset MSTID event in Figure 4.3, the evident downward-sloping stripes at the same H_{eq} indicate irregularities in E and F regions are connected by a magnetic field line and share a similar wavefront with an NW–SE alignment and a

southwestward propagation. The occurrence time of the perturbations in E and F regions is almost similar, at ∼19:30 JST. The maximum amplitude in the E region occurs earlier (∼20:15 JST) than that in the F region (∼22:00 JST), but the F-region irregularities show higher intensity. In the later hours of the night, the F-region structures exist in the latitudes and durations when E-region structures are not seen or weak. For the post-midnight MSTID event on 23 June 2012 (DOY 175), the E- and F-region perturbations develop after ∼0:00 JST and last until ∼4:00 JST. The Es layer and MSTIDs share a similar amplitude and duration of structure formation but show smaller intensity than the pre-midnight event.

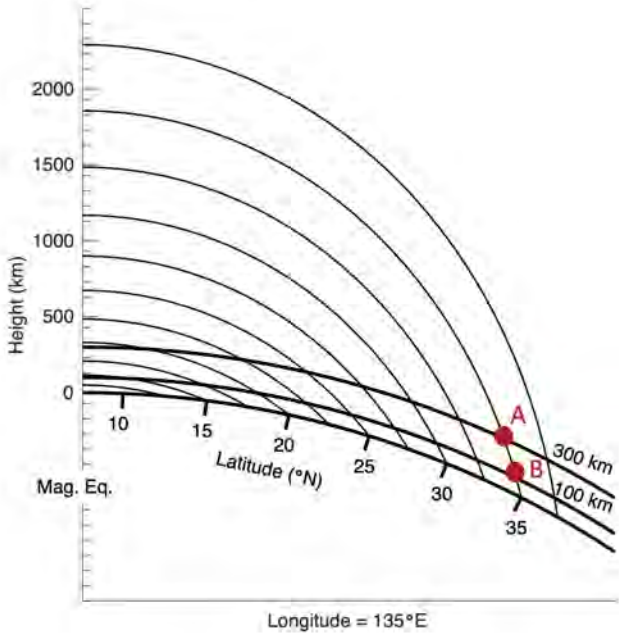

Fig. 4.4 A sketch of magnetic lines from the magnetic equator to low and mid latitudes. Red points (A and B) are ionospheric regions connected by a same magnetic field line, and H_{eq} represents the equatorial crossing height of the magnetic field line piercing each shell.

4.1.2 Event on 11 June 2007

Since the mid-latitude FAI in E region is considered associated with the horizontal inhomogeneity of an Es layer (Maruyama et al., 2006), the structured coherent backscatter radar echoes, so-called quasi-periodic (QP) echoes, are associated with Es layers and usually used to indicate the Es dynamics and morphology (Maruyama et al., 2000; Saito et al., 2007; Xie et al., 2020). MUR, located at 34.9°N, 136.1°E, Shigaraki, Japan, has been used for detecting backscatter echoes from plasma irregularities in both E region (Yamamoto et al., 1994) and F region (Saito et al., 2002). For this event, I used the observations from MUR to

further validate our results. Three transmission beams pointing nearly to the geographic north (azimuth angle: -13.92°–17.67° about the geography north, zenith angle: 51.09°–59.01°) are selected.

The horizontal TECP distribution maps at E- and F-shell heights during 19:00–23:00 JST, on 11 June 2007 (DOY 162), are shown in Figure 4.5. Black dashed and gray arrows and black dots represent the same as in Figure 4.1. Black stars denote the location of MUR, and the black crosses indicate an example of a regions, where the radar beam intersects the ionosphere at 100 km (E shell) and 300 km (F shell). The transmission beam was pointed to the geographic north (azimuth: 0°, zenith: 52.07° and 57.84° in E and F regions, respectively).

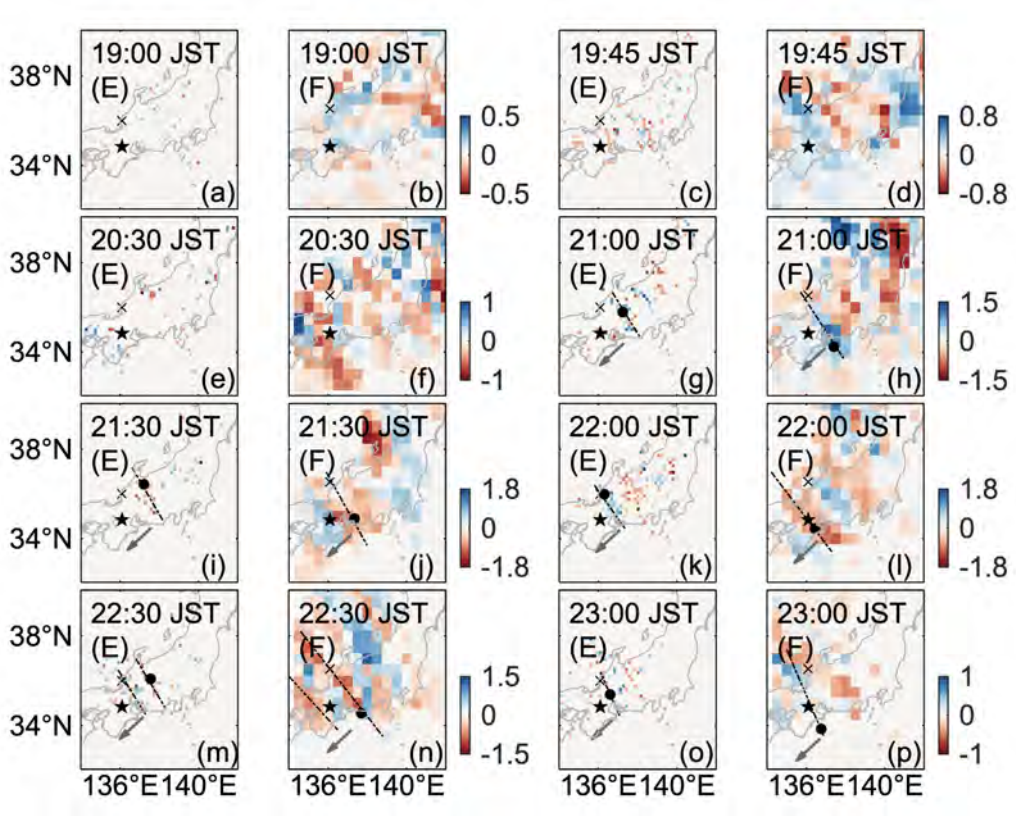

Fig. 4.5 Same as Figure 4.1 but for 11 June 2007 (DOY 162). Black stars are the location of MUR, black crosses represent the observation regions with an altitude of 100 km (E region) and 300 km (F region), where the transmission beam was pointed to the north (azimuth: 0°, zenith: 52.07° and 57.84° in E and F regions, respectively), black dots indicate denote the locations at E (100 km) and F shells (300 km) connected by a geomagnetic field line.

Compared to the results in Figure 4.1, E-region irregularities in Figure 4.5 (before 22:00 JST) are similar in size, but E- and F-region maximum amplitudes (in areas with dense data points) are less by approximately 20%. In Figure 4.5, the duration of structure formation

in E and F regions are similar: the E- and F-region irregularities both appear enhanced at ∼19:00 JST, and reach the maximum amplitude at around 21:30–22:00 JST. The irregular structures in E and F regions share a common southwestward migration and a similar NW–SE wavefront. The irregularities in E and F regions, which share similar propagation parameters, are considered connected by a same geomagnetic field line, as shown by the frontal structures in the subplots during 21:00–23:00 JST.

Worth noting is that the F-region structures in Figure 4.1 depict a longer wavelength and larger amplitude and are well defined than structures in Figure 4.5. This result supports 3-D simulations of F-region Perkins instability in Yokoyama et al. (2008): structures showed a wavelength dependence with shorter perturbations tending to saturate at low amplitudes. I also presume that the density perturbations in Figure 4.5 dominate at altitudes lower than 300 km. Consequently, the reconstructions are poor due to the increased error in IPP spatial distribution. A strengthened mid-latitude Northern Hemisphere poleward wind could have forced the plasma downwards such that the instability structuring and amplitudes are limited. That is to say, from the theory of a coupled E–F region (Tsunoda, 2006), the duration of structure formation and structuring of the instabilities depend on the ratio of field-line-integrated Hall conductivity to Pedersen conductivity (which is proportional to ion-neutral collision frequency, υ_{in}). However, at lower altitudes, υ_{in} is expected to increase and background plasma densities to decrease exponentially due to enhanced recombination rates. Besides, υ_{in} is inversely proportional to the F instability polarization electric fields. This has been shown to be the case observationally in Narayanan et al. (2014).

Since the size of the irregularities measured by the radar backscatter may be several meters, while that detected by the GNSS–TEC measurements is on an order of ten to hundred kilometers, strong backscatter signals and km-scale density enhancement/depletion to a certain extent may not depict an exact direct relationship. Still, from the general relative change in density, and an assumption that meter-scale structures populate a wider spatial area than the radar field of view, I can obtain several important physical underpinnings based on these results and validate the algorithm to a certain extent. Figure 4.6 shows the range-time-intensity (RTI) maps of echo power observed by MUR on the night of 11 June 2007 (DOY 162), where AZ and ZE represent the azimuth and zenith angles of the transmission beams, respectively. Negative (positive) azimuth corresponds to west (East). In each subplot, the region in observation (E or F) is indicated in parentheses. Gray solid lines in middle panels are the mean variation of TECPs within a $0.6^\circ \times 0.15^\circ$ ($2^\circ \times 0.5^\circ$) grid covering the radar observation regions at E (F) shell height. According to the E-region RTI subplots, the eastern most beam (AZ=17.2°) detected the echoes first (∼20:00 JST) and then followed by other beams. Therefore, movement must have been westward. The inclined striation pattern

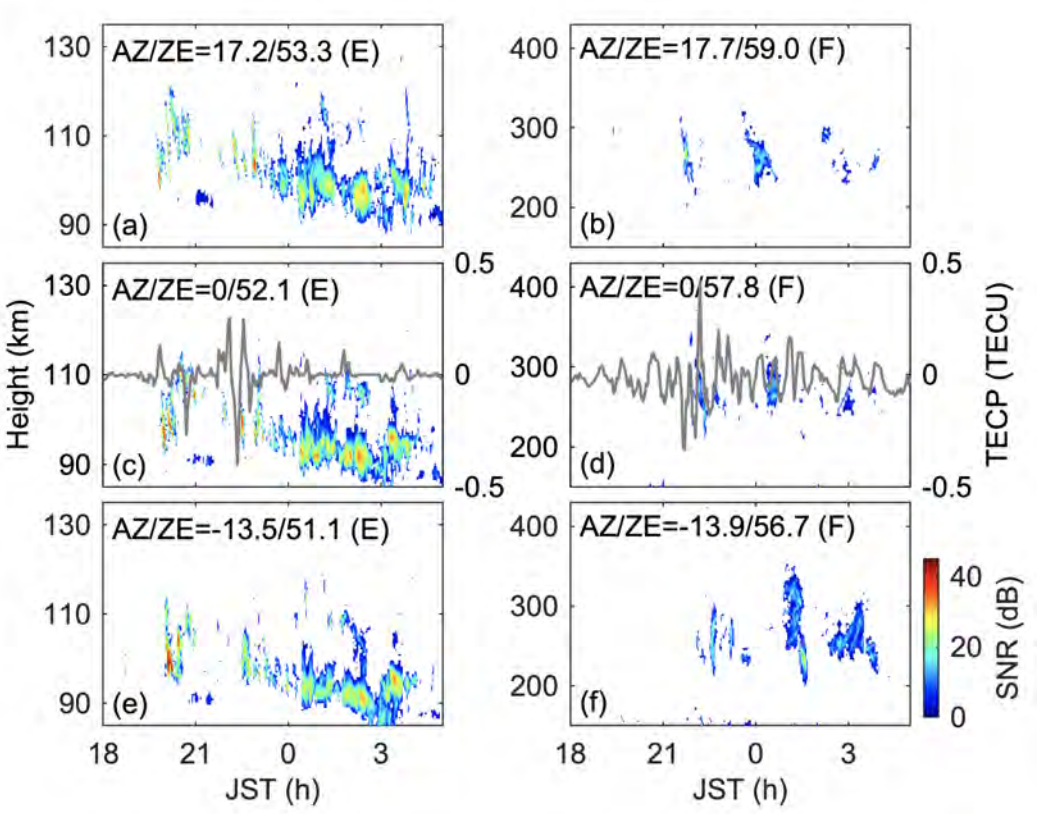

Fig. 4.6 Range-time-intensity plots of echo power observed with the MUR on 11 June 2007 (DOY 162). AZ and ZE represent azimuth and zenith of the transmission beams, respectively, the gray solid lines represent the mean variation of TECPs in the radar observation regions.

indicates the occurrence of well-defined QP echoes during ∼19:30–24:00 JST, with a period of about 10 min. Besides, continuous echoes associated with lower altitudes are observed after ∼24:00 JST. In the F region, the weak echoes are received from ∼21:00 to ∼4:00 JST, and evident irregularities are observed at around 22:00, 1:00, and 3:00 JST with a reduced amplitude. According to the observations of Doppler velocity, the antennas facing further northeast can receive the intense echoes faster, and the Doppler velocity observed by MUR is negative when the first QP echoes were received (∼20:00 JST), which indicate that the E-region irregularities in the echoing region are moving southwestward. The echo strength: particularly observations by radar beam (AZ/ZE=-13.5°/51.1°), between ∼18:00 and 24:00 JST, the echo is “short-live” but with a stronger SNR (signal-to-noise ratio). On the other hand, between ∼00:00 and 06:00 JST, echoes are frequent but with a slight reduction in SNR and a descent in altitude. During the later period, the TEC component shows a quasi-quiet variation; we think, due to plasma density reduction following the altitude descent, the integrated density variations are below the TEC noise level.

Saito et al. (2007) has identified that the horizontal scale of QP echoes is about a few tens of kilometers and is much smaller than those in the F-region MSTIDs. In Figure 4.6 subplot (c), the occurrence time of E-region irregularities observed by GNSS-TEC (∼20:00, 22:00, and 23:30 JST) is consistent with that of QP echoes observed by MUR, and the fluctuation of TECPs becomes small after 24:00 JST when continuous echoes were observed by MUR. The continuous echoes are less dynamic than the QP echoes, indicating a development of weak spatial structuring in electron density within an Es layer (Maruyama et al., 2006). The average of absolute E-shell TECPs peak amplitude, where the QP echoes are intense (e.g., ∼20:00, 22:00, and 23:30 JST), is ∼0.3 TECU, which translates to ∼11 MHz if a 2 km thickness is assumed; this frequency is above a foEs threshold above which QP echoes are generally detected in ionosonde observations over Japan (Mungufeni et al., 2021). Despite the consistency, a slight time delay is noticeable in the expected alignment of TECP depletions (negative) and QP echoes: this might be due to the errors in IPP spatial distribution. In addition, "x" is the point, where the beam intersects the 100 km layer, but not the actual echo points, where magnetic fields are perpendicular to the MUR beam.

In the subplot (d), the F-region FAIs are plotted together with F-shell perturbations from the point indicated by "x" in Figure 4.5, where the radar beam is projected to pierce the F shell at 300 km. Evidently, at around 22:00 JST, the largest undulations in GNSS–TEC coincide with intense echo stratifications in the MUR observations. However, not all undulations are accompanied by FAIs, probably due to low amplitudes or out of view of the radar beam. Saito et al. (2002, 2008) and Otsuka et al. (2008) and references therein have also shown a summer nighttime common occurrence of MSTIDs and FAIs over Japan, and the occurrence of FAIs is related to the intensity of MSTIDs.

Same as Figure 4.3 but for 11 June 2007 (DOY 162), Figure 4.7 shows the time variation of E- and F-region TECPs in H_{eq} at nighttime, along the line from northeast to southwest indicated as the red dashed line in Figure 3.1. The black and gray dashed lines represent the occurrence time of perturbations and the alignment of evident downward-sloping stripes, respectively. For this event, the E- and F-region irregularities are of similar duration of structure formation and intensity, but the occurrence time of the downward-sloping stripes is about 10 min earlier in the E region than in the F region. During ∼19:30–23:00 JST when QP echoes were obvious in the MUR observation, the evident downward-sloping stripes indicate the E- and F-region irregularities share a similar wavefront with an NW–SE alignment and a southwestward propagation with a phase velocity of 80–150 m/s. The clear inclined striations at ∼21:00–22:00 JST at the same H_{eq} indicate the E- and F-region irregularities are related to each other through a magnetic field line. During ∼24:00–4:00 JST when radar continuous echoes (a lower height and weaker power in the echoing region (Maruyama et al., 2006))

were observed, the E- and F-region irregularities show a reduced amplitude and remain at a lower level (∼0.5 TECU). Similar to the results in Figure 4.3, the duration of large-intensity downward-sloping stripes (∼1 TECU) is longer in the F region (from ∼21:00 to 2:00 JST) than in the E region (from ∼21:00 to 24:00 JST). This indicates that once formed the F-region structures can sustain longer, which corroborates the observations made by Narayanan et al. (2018).

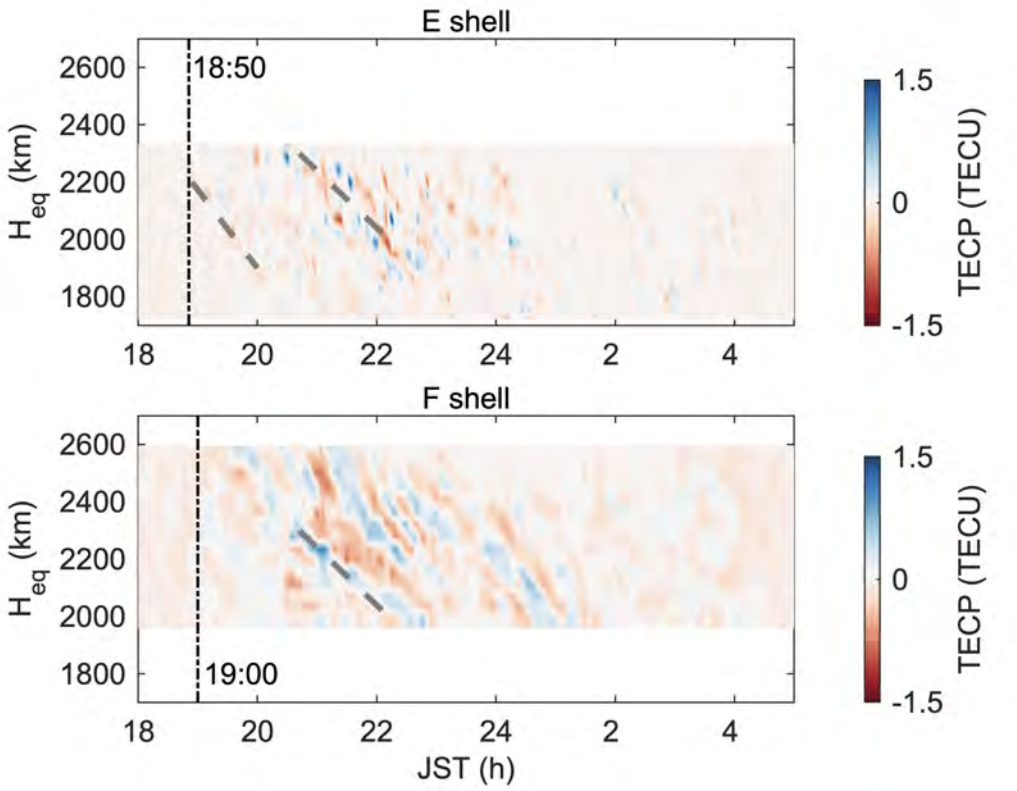

Fig. 4.7 Time variation of TECPs at E- (top) and F-shell heights (bottom) on 11 June 2007 (DOY 162), along the line from northeast to southwest indicated as the red dashed line in Figure 3.1. The black and gray dashed lines represent the occurrence time of perturbations and the alignment of evident downward-sloping stripes, respectively.

4.2 Interhemispheric Coupling

The observations (Narayanan et al., 2018; Otsuka et al., 2004; Valladares and Sheehan, 2016) and simulations (Yokoyama, 2014) of nighttime MSTIDs in the geomagnetic conjugate regions (different hemispheres) have verified the existence of interhemispheric coupling. However, until now, there are no direct observations to determine the causes and effects

of the coupling between different hemispheres. A complete understanding of the upper atmosphere electrodynamics is still a far-fetched idea that requires probing from different instrumentation on a larger spatial scale. The double-thin-shell approach has attempted to partially fill this void by providing a broad horizontal scale and a high-resolution sneak view into the mid-latitude ionosphere E- and F-region during night irregularities; more important is that the deductions from the reconstructions have proved complementary to other types of observations. In this section, observations from multiple instruments in both E and F regions are required to increase the horizontal scale and temporal resolution, and provide different ionospheric information; conjugate regions in Japan and Australia are the focus since both Es and MSTIDs have been frequently observed in the East Asian sector (Kil and Paxton, 2017). Two nighttime MSTID events of similar amplitudes in July (summer in the Northern Hemisphere) and December (summer in the Southern Hemisphere), 2019, were selected for analysis. To mitigate anomalies due to external forcings such as geomagnetic storms, the selected events are from quiet days with $K<4$ and $|Dst|<30$.

4.2.1 Data

In this research, GNSS-TEC measurements are still the primary tool for probing the ionosphere; TECP, obtained after deducting a 30-min data running average, were also used rather than absolute TEC. Figure 4.8(a) shows the distribution of ground-based GNSS receivers and ionosondes in these areas. Gray dashed lines represent the magnetic dip (0°, $\pm20^\circ$, $\pm50^\circ$) calculated from International Geomagnetic Reference Field (IGRF) model. Compared to the dense GEONET over Japan with more than 1000 receivers, the network over Australia consists of approximately 450 sparsely distributed stations with a bias toward the southeast. For a 30-s data cadence, more than 5000 (1800) ray paths are recorded over Japan (Australia) with a cut-off elevation angle of 35°. Figure 4.8(b–c) shows an example of IPPs from GNSS rays. The epoch is arbitrarily selected, and the altitude is 300 km. The disparity in the distribution of the IPP points follows that of the two networks. Because the Japanese archipelago is narrow and vividly stretches northeast to southwest, the red dashed line in Figure 4.8(b) indicates the region with the most data points where reconstructions are of better accuracy.

Yellow squares in Figure 4.8(a) show the distribution of ionosondes used in this study, located at Wakkanai (45.16°N, 141.75°E geographic; 59.89°magnetic dip, calculated from IGRF model), Kokubunji (35.71°N, 139.49°E geographic; 49.67°magnetic dip), Yamagawa (31.20°N, 130.62°E geographic; 45.38°magnetic dip), Canberra (35.32°S, 149.00°E geographic; -65.96°magnetic dip), Townsville (19.63°S, 146.85°E geographic; -48.87° magnetic dip), and Darwin (12.45°S, 130.95°E geographic; -39.48° magnetic dip). I adapted ionogram

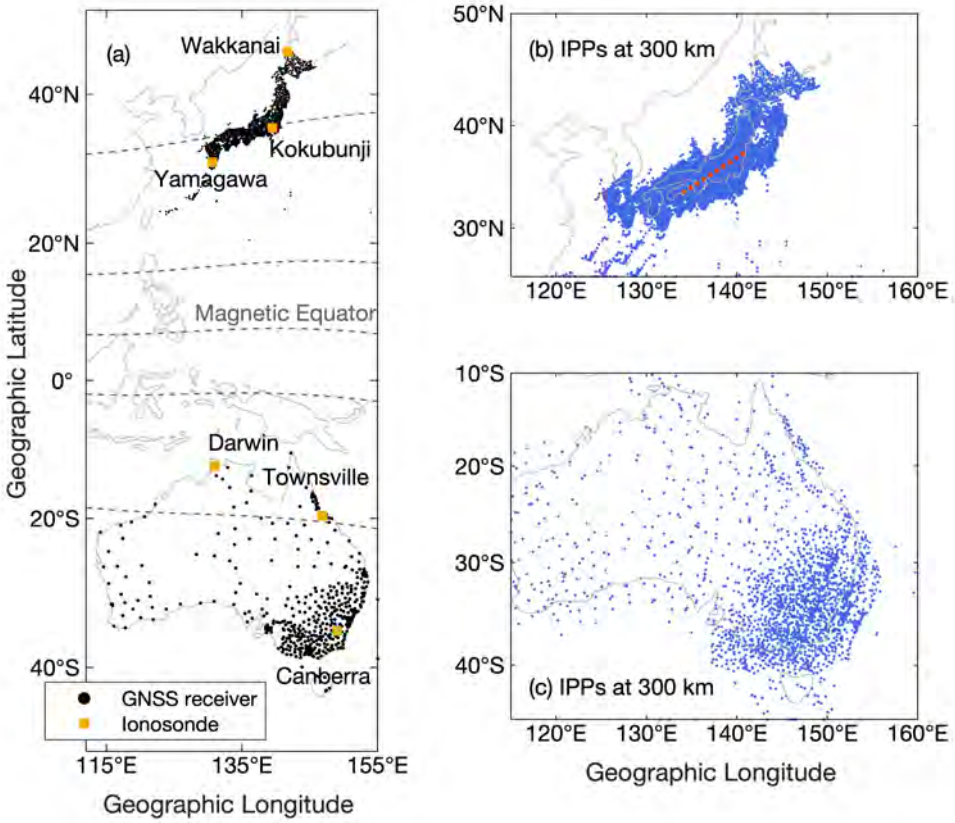

Fig. 4.8 (a) Distribution of GNSS stations (black dots) and ionosondes (yellow squares). Gray dashed lines represent the magnetic dip (0°, ±20°, ±50°). (b–c) Blue dots represent the distribution of IPP at 10:00 UT on 29 July 2019, at 300 km altitude. Red dashed line indicates the region with most data points over Japan.

observations to indicate the variation of Es-layer intensity at those ionosonde locations. In this section, the Es parameters (critical (foEs) and blanketing (fbEs) frequencies) in Japan and Australia are provided by the manual-scaled (at 1-hour interval) and auto-scaled (at 5-min interval) ionogram parameters, respectively, since the ionogram automatic processing algorithm in Japan cannot detect small fbEs values. On an ionogram, foEs indicates the maximum frequency of the Es echo trace, while fbEs denotes the minimum frequency of the F-layer trace (Narayanan et al., 2018). foEs and fbEs determine the frequency bands in which radio waves can be partially reflected or pass through the Es layer (Maruyama et al., 2006), where fbEs is the peak density of the quasi-uniform layer (i.e., signals lower than this frequency cannot pass through this layer), and foEs is the peak density of clumps within this layer. Thus, the difference between foEs and fbEs (foEs-fbEs) is often used to represent the degree of density structuring in the Es layer (Otsuka et al., 2008).

In addition to the ground-based observations, spaceborne measurement were also used in this research, e.g., electron density profiles provided by COSMIC radio occultation, magnetic field variations provided by Swarm satellites, and thermospheric winds provided by the Michelson Interferometer for Global High-resolution Thermospheric Imaging (MIGHTI) on the ICON spacecraft. The details of the COSMIC measurement principle were described in Section 2.2.4. The Swarm mission comprises a constellation of three satellites, in polar orbits at two different altitudes of $\geq$460 km for Alpha(A) and Charlie(C), and $\geq$530 km for Bravo(B). Each satellite has a Absolute Scalar Magnetometer (ASM) and a Vector Fluxgate Magnetometer (VFM) for measuring Earth's magnetic field at 1 Hz resolution, and a Langmuir Probe for measuring in-situ electron densities at a 2 Hz resolution (Olsen et al., 2015). In this section, I used the level-1b products of electron density and magnetic field from satellites A and C because they are at the same orbital altitude. The MIGHTI on the ICON spacecraft provides neutral wind data from 90 to 300 km altitude by using 557.7 nm (green channel) and 630.0 nm (red channel) airglow emission observations. More details on instruments and data validation can be found at Makela et al. (2021) and Harding et al. (2021). Following the work of Harding et al. (2022), above and below 180 km, I used the neutral wind data from red channel and green channel, respectively.

4.2.2 Event on 29 July 2019

Figure 4.9 shows the snapshots of TECP maps at various time epochs from 10:00 to 14:00 UT on 29 July 2019 (DOY 210), which are obtained by using the single-thin-shell approach at 300 km altitude, following the method in Tsugawa et al. (2018). Following the difference in the distribution of the ground GNSS receivers, the horizontal spatial resolution of the images in the Northern (Japan) and Southern (Australia) hemispheres is 0.15° and 0.5°, respectively. In each image, reconstructions are from perturbations collected over a 2-minute window: that is, the ionosphere is assumed stationary within this window. Gray dashed lines represent the magnetic dip at $\pm$50° obtained from IGRF model, orange and blue circles indicate the geomagnetic conjugate regions over Japan (summer) and Australia (winter), the black dashed lines drawn along the irregularities indicate the alignment azimuths of the apparent frontal structures, which are NW-SE (NE-SW) in the Northern (Southern) Hemisphere, gray arrows denote the southwestward (northwestward) drift direction in the Northern (Southern) Hemisphere.

In Figure 4.9(a), in the region circled by the orange line, irregular ionospheric density perturbations (maximum value: 0.34 TECU) are observed over the Japan Archipelago after sunset at 10:00 UT (19:00 JST) at higher latitudes (>43°N). Meanwhile (10:00 UT; 20:00 AEST (Australia Eastern Standard Time)), as shown in subplot (e), east-west (E-W) aligned

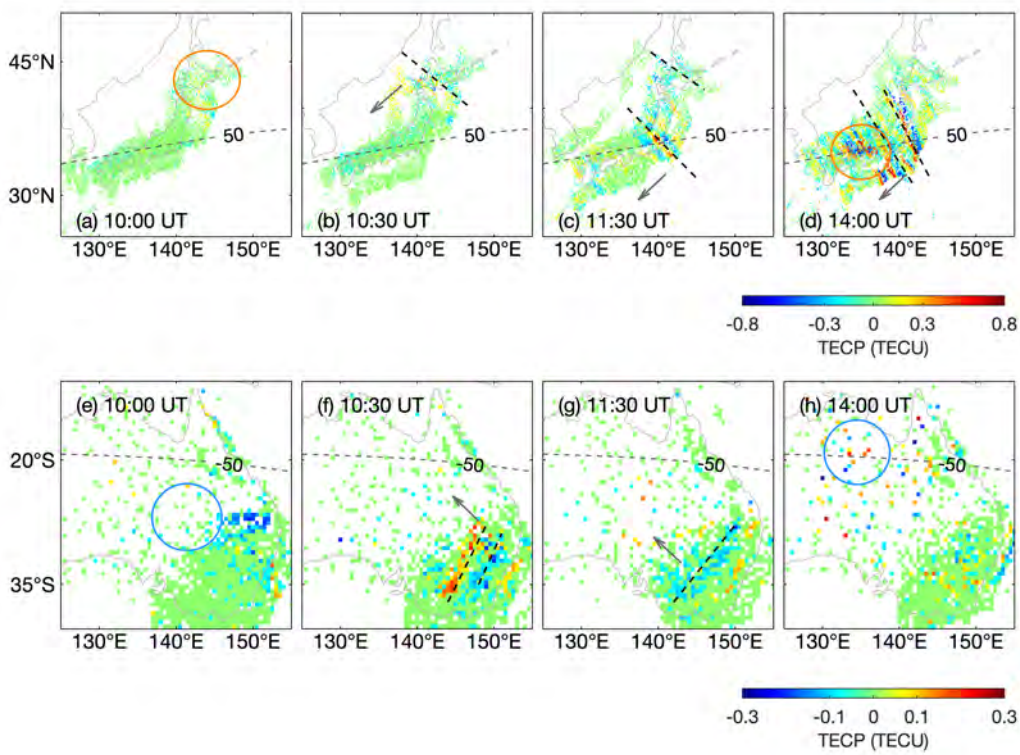

Fig. 4.9 Snapshots of TECP maps at various time epochs from 10:00 to 14:00 UT on 29 July 2019 (DOY 210), obtained by the single-thin-shell approach at 300 km altitude. Gray dashed lines represent the magnetic dip at $\pm 50^{\circ}$, orange and blue circles indicate the geomagnetic conjugate regions over Japan (summer) and Australia (winter), black dashed lines indicate the alignment azimuths of the apparent frontal structures, gray arrows denote the drift direction.

density depletions and irregular perturbations with small amplitudes (<0.17 TECU) are observed in the eastern part of the blue circle, about less than half of those in the summer hemisphere (Japan). Soon, these E-W aligned irregularities disappear and obvious NE-SW frontal structures form at higher latitudes in both hemispheres. This is eminent in the 10:30 UT images (b (Japan) and f (Australia)) with wavelike tilted irregularity structures. Still, the maximum amplitude of the frontal structure is significantly larger in the summer hemisphere (Japan; $\sim$0.47 TECU) than in the winter hemisphere (Australia; $\sim$0.22 TECU). Later, after around 11:30 UT, the wavebands over Japan propagate to lower latitudes ($\sim$35°N; 50° magnetic dip) and develop rapidly over this region. The conjugate MSTIDs at lower latitudes over Australia (-50° magnetic dip) are not very clear, due to the low-amplitude perturbations and the sparse GNSS data points. At 14:00 UT, significant conjugate MSTIDs are observed within the encircled regions . From 10:00 to 14:00 UT, MSTIDs in the summer hemisphere (Japan) develop and reach the maximum intensity of 0.80 TECU, while the

conjugate MSTIDs in the winter hemisphere (Australia) nearly maintain a constant amplitude (∼0.15-0.24 TECU). Ignoring the sparse distribution of GNSS data over the Australian region, the small amplitudes of TECPs suggest a weak development of MSTIDs in the winter hemisphere (geomagnetic conjugate region).

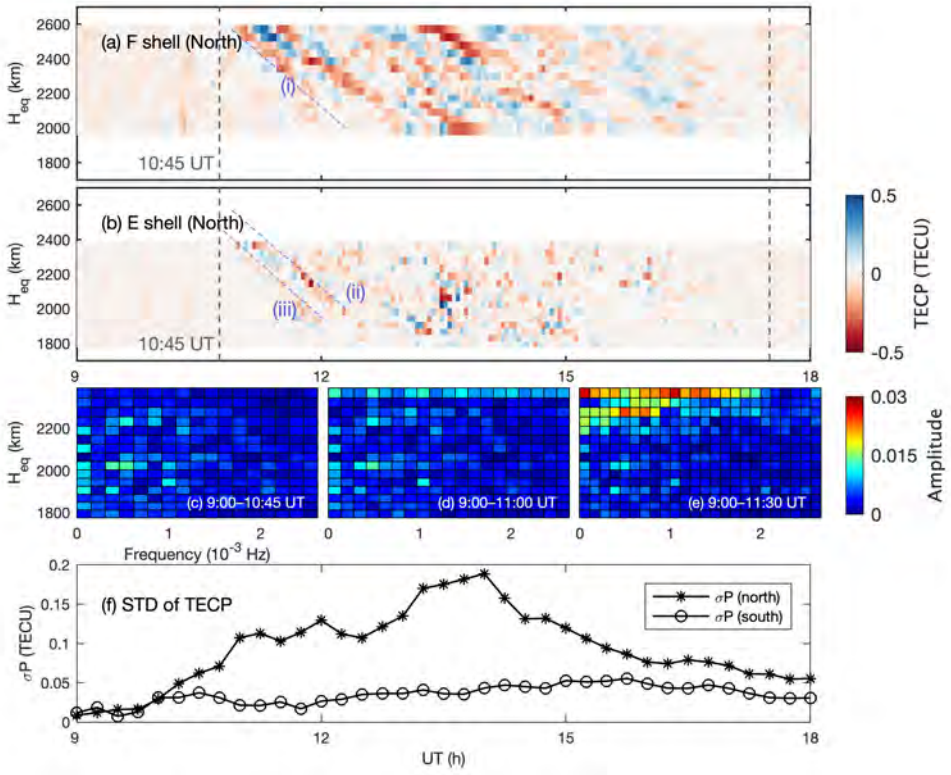

Fig. 4.10 (a–b) Time variation of TECPs in E and F shells in Japan on 29 July 2019 (DOY 210) along the northeast–southwest red dashed line in Figure 4.8(b). H_{eq} represents the equatorial crossing height of the magnetic field line piercing each shell. Blue dashed lines indicate the alignment of evident downward-sloping stripes, and gray dashed lines represent the duration of perturbations in the F region over the analyzed area. (c–e) E-region reconstruction results of fast Fourier transform (FFT) in different time periods. (f) Time variation of the standard deviation of TECPs (σP) in different hemispheres.

The parameters of the double-thin-layer model and the analyzed region are set as in the Chapter 3, except that the time resolution is increased to 2 minutes from 2.5. From the results in Figure 4.9(a–d), this analyzed region also coincides with the fast-growing region of the MSTID structures. Subplots (a–b) in Figure 4.10 show the time variation of TECPs on 29 July 2019 (DOY 210) during 9:00–18:00 UT (18:00–3:00 JST) along the NE-SW red dashed line in Figure 4.8(b). H_{eq} represents the equatorial crossing height of the magnetic field line piercing each shell, as shown in Figure 4.4. The irregularities of different shells at the same H_{eq} are considered to be connected by a same magnetic field line. Blue dashed lines are drawn

along the obvious irregularities and indicate the alignment of evident downward-sloping stripes, gray dashed lines represent the duration of F-region perturbations over this analyzed area. Obvious irregularities in both E and F regions occur over this area after ∼10:45 UT. We also performed a fast Fourier transform (FFT) analysis on the E-region reconstruction results of different time periods (from 9:00 UT to 10:45/11:00/11:30 UT) to further verify the existence of phase fronts in the E region. As shown in subplots (c–e), based on the FFT analysis, the E-region coherent sizable disturbances were detected at higher latitudes after ∼10:45 UT, which confirms the phase fronts within the E-shell keograms in subplot (b). In fact, the duration of strips (i) and (ii) in subplots (a–b) is the same; the disappearance of TECP at around 12:00 UT in strip (i) is due to satellite movement, such that the IPP points drift away from the red dashed line in Figure 4.8(b). Evident downward-sloping stripes (i) and (ii) in subplots (a–b) have similar H_{eq} and gradients, indicating the occurrence of E-F coupling: the irregularities in different regions are connected by a magnetic field line, and share a similar NW-SE wavefront propagating to the southwest with a phase velocity of ∼100 m/s. More importantly, the small-amplitude irregularities in the E region indicated by stripe (iii) are about 30 min earlier than stripe (i) in the F region and stripe (ii) in the E region. As inferred from Figure 4.9, MSTIDs in Japan (summer) propagate to lower latitudes (∼35°N), and then the amplitudes develop rapidly in this region after around 11:30 UT. The earlier occurrence of Es further supports the theory that Es layer plays a major role in amplifying the Perkins instability in the F region via electromagnetic coupling along the geomagnetic field lines (Cosgrove, 2013; Yokoyama et al., 2009).

To study the MSTID activity, Saito et al. (2001) used the standard deviations of TECP within one hour to represent amplitude of TEC perturbations caused by MSTIDs, and results show a good correlation between the standard deviation of TECP with horizontal structures of TEC perturbations on the 2-D maps. I follow the same to avoid occasional sizable errors in TECPs; for each epoch, over the whole region (either Japan or Australia), a standard deviation of TECPs (σP) is computed. Considering the propagation of MSTIDs and the less data points over Australia, this parameter can only represent the relative intensity variation over the region with most data points. In Figure 4.10(f), the σP in different hemispheres are plotted every 15 min to indicate the time variation of the irregularity intensity, wherein the σP over Japan and Australia are represented by asterisks mark and circle, respectively. From the results in Figure 4.9, the ionospheric irregularities over Japan (summer) develop at higher latitudes at about 10:00 UT and reach the maximum at around 14:00 UT; irregularities show weak development in Australia (winter) during the MSTID event. Consistent with these conclusions, in Figure 4.10(f), σP(north) (in Japan) start to increase after 10:00 UT and reach the maximum at around 14:00 UT; in Australia, the irregularity intensity (σP(south)) shows

a small increase in the initial phase (at ∼10:00 UT) with the development of MSTIDs in the summer hemisphere (Japan), but then the activity of conjugate MSTIDs remains constant throughout the MSTID event.

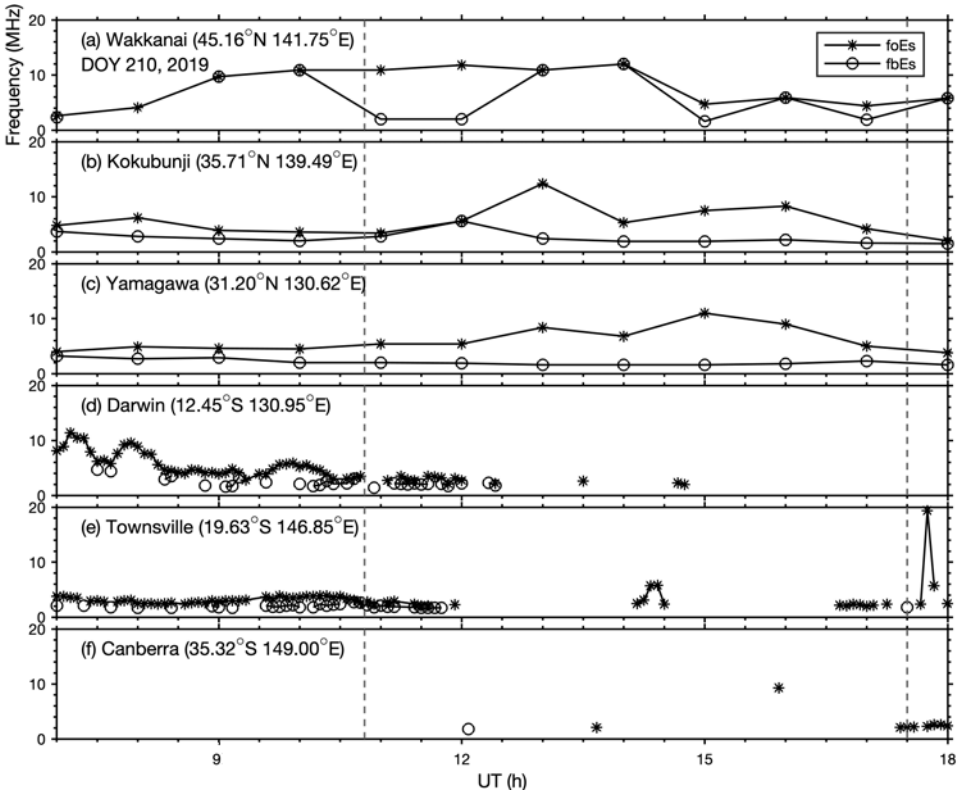

Fig. 4.11 The ionosonde measurements from Wakkanai, Kokubunji, Yamagawa, Canberra, Townsville, and Darwin, comprising of foEs (asterisks) and fbEs (circle) from 7:00 to 18:00 UT on 29 July 2019 (DOY 210). Gray dashed lines are the same as Figure 4.10, representing the duration of perturbations over the region with most data points in Japan (summer).

To further validate the GNSS-TEC observation results in Japan and to supplement information on the Es layer over Australia, the ionosphere parameters provided by six ionosondes from 7:00 to 18:00 UT at DOY 210, 2019, are plotted in Figure 4.11 to show the variation of Es-layer intensity in conjugate regions, wherein foEs is represented by asterisks mark, fbEs by circle. Gray dashed lines represent the same as in Figure 4.10. Generally, the absence of values for foEs or fbEs indicates the nonexistence of sporadic or blanketing E in the ionogram at that particular time. From Figure 4.11(a–c), in the summer hemisphere (Japan), consistent with GNSS-TEC results in Figures 4.9 and 4.10, the variations of large foEs values (>8 MHz) and foEs-fbEs (>5 MHz) suggest that the Es layers form earlier at higher latitudes (Wakkanai), and propagate to lower latitudes (Kokubunji and Yamagawa). During this process, foEs and foEs-fbEs amplitude decreases equator-ward, indicating a

gradual decrease in Es-layer activity. Similar cases can be found in Narayanan et al. (2018), where the E region structure becomes weak in the late hours of MSTID event, while the F region structure can sustain longer once formed. This is understandable because the growth time required for the MSTID formation is rather short in the E-F coupling process (Yokoyama et al., 2009). Observations at Kokubunji ionosonde, located within the region of most GNSS data points, show enhancement after 11:00 UT with maximum intensity at around 14:00 UT; this result is consistent with the E-region reconstruction results in Figure 4.10(b). After the onset (at $\sim$10:45 UT) of the coupling process in the summer hemisphere (Japan), in the winter hemisphere (Australia), at Townsville and Darwin, preexisting Es layers show a reduced intensity with foEs$<$3 MHz; foEs-fbEs$\approx$1 MHz; an indication of a less structured in the Es layer (Maruyama et al., 2006). Further, the Es layers over Townsville and Darwin show dissipation at around 12:00 UT and later exhibit an intermittent occurrence. As shown in Figure 4.9 and 4.10, at $\sim$12:00 UT, the rapid development of MSTIDs and Es layers with large foEs values over Japan (summer) suggest the occurrence of strong E-F coupling in the Northern (summer) Hemisphere; conjugate MSTIDs in the Southern (winter) Hemisphere also move over Townsville and Darwin from higher latitudes. I consider that the disruption of Es layers over Australia (winter) is most likely related to the electrodynamic factors in this particular period, since Es layer cannot easily be dissipated by simple diffusive motion once it is formed (Yokoyama et al., 2005). Additionally, after $\sim$17:30 UT over Townsville, the sporadic E layer reappears and shows enhancement in the late hour of the MSTID event, which may be due to the weakening of the controlling role from electrodynamic factors at this time.

We also supplement the ground-based observations with space-based observations from COSMIC occultation and Swarm satellites. Although the E-region information from COSMIC occultation have been used for statistical analysis of E-F coupling (Liu et al., 2020), here for case study, we only qualitatively analyze the E-region electron density due to the relatively low accuracy below 200 km. Same as Figure 4.9, the background in Figure 4.12 (a–b) is the TECP map obtained by using single-thin-shell approach at 10:45 UT, orange squares are the locations of ionosondes, and circles in different hemispheres indicate the geomagnetic conjugate regions. In Figure 4.12(b) (over the Austrian continent), the dark blue and gray solid lines are traces of COSMIC occultation tangent points; dark blue and gray represent points in ionosphere E- (below 150) and F-region (above 150 km) altitudes, respectively. Along each trace, gray dots show the location of the maximum electron density along the inverted density profile. The blue triangles indicate the location of the E-region peak electron densities: only included on traces when the density perturbation caused by Es is larger than the density at the E region top ($\sim$150 km). Purple lines represent the traces of

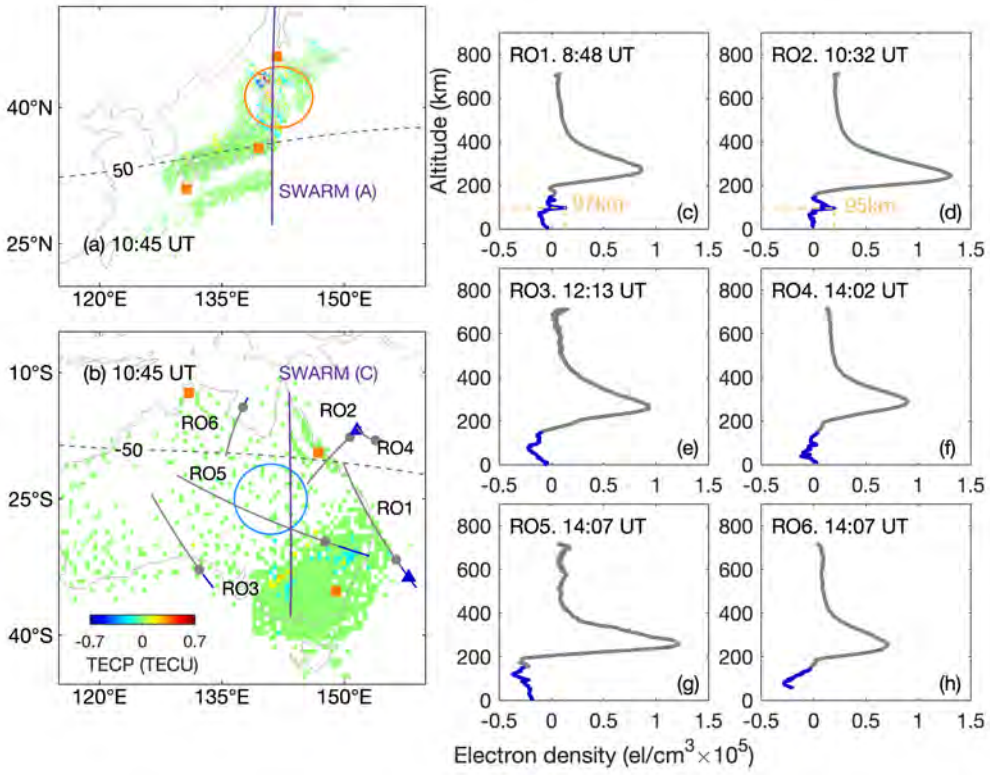

Fig. 4.12 (a–b) Gray (dark blue) solid are traces of COSMIC occultation tangent points at F (E) region altitude,gray dots (blue triangles) are locations of maximum electron density in the F (E) region along each trace. Purple solid lines represent the traces of Swarm satellites. Background is the ground-based GNSS-TECP map at 10:45 UT on 29 July 2019 (DOY 210), orange squares are the locations of ionosondes, circles in different hemispheres indicate the geomagnetic conjugate regions. (c–h) Results of COSMIC constellation vertical electron density profiles at different epochs.

Swarm satellites at around 10:45 UT, when they cross the conjugate region. Subplots (c–h) in Figure 4.12 show the results of COSMIC constellation vertical electron density profiles at different epochs. From the GNSS-TEC results, significant MSTIDs (maximum: 0.67 TECU) are observed at ∼50°–60° magnetic dip in the summer hemisphere (in the region circled by the orange line), while the conjugate MSTIDs are weak (maximum: 0.23 TECU) in the winter hemisphere. From occultation observations over Australia (winter), no particularly strong Es layer is observed; electron density perturbations at ∼100 km are relatively large in RO1 and RO2 profiles at around 8:50 and 10:30 UT; the observed Es-layer activity is low even within the conjugate MSTIDs (as inferred from RO6 trajectory and Figure 4.9(h)).

Figure 4.13(a–h) shows the observation results from Swarm satellites along the traces in Figure 4.12, at around 10:45 UT on 29 July 2019 (DOY 210). The two Swarm observations have a time difference of ∼15 min, but this is considered minimal and the observations are

analyzed as simultaneous. Following Yokoyama and Stolle (2017), magnetic field variations are obtained by subtracting CHAOS-7 model predictions for the core, lithosphere, and large-scale magnetospheric fields (Finlay et al., 2020). The first four rows in Figure 4.13 shows the in situ electron density, and radial (dB_L; positive outward), zonal (dB_ϕ; positive horizontal eastward), and parallel components ($dB_{||}$; along the mean magnetic field) of residual magnetic fields, respectively, plotted over magnetic dip. $dB_{||}$ arises from diamagnetic currents owing to plasma density gradients around and within the depletions, and the magnetic field variation perpendicular to the main field direction (dB_L and dB_ϕ) is related to the field-aligned currents (Lühr et al., 2003). The field-aligned sheet current density and diamagnetic current strength are not correlated (Park et al., 2009a). Since the coupled electrodynamics between the E and F regions and between different hemispheres are accompanied by significant field-aligned currents, mid-latitude electric field fluctuations (MEFs) or midlatitude magnetic field fluctuations (MMFs) are usually only observed in the perpendicular components with an amplitude of a few nT (Yokoyama and Stolle, 2017). Many research works have already verified the close relationship between MMEs/MMFs with Es and MSTIDs (Burke et al., 2016; Park et al., 2015, 2009b; Saito et al., 1998b; Wan et al., 2020).

In Figure 4.13, magnitudes of MMFs in the perpendicular components (dB_L and dB_ϕ) are comparable for different hemispheres (summer hemisphere values are slightly larger), but the electron density fluctuations are much larger in the summer hemisphere (Japan), as observed by GNSS-TEC in Figure 4.12(a). Subplots (i–j) show a scatter of perpendicular components (left) and electron density with parallel magnetic field variation (right) during the nighttime MSTID event on 29 July, 2019 (DOY210). The orange and blue dots correspond to the observations in summer (Japan) and winter (Australia) hemispheres, respectively. Similar to the example in Yokoyama and Stolle (2017), in subplots (c–f), perpendicular components (dB_L and dB_ϕ) depict a weak negative correlation (correlation coefficient; r=-0.35) in the summer hemisphere (Japan), and a near zero or no correlation (r=0.08) in the winter hemisphere (Australia). The poor correlation between the perpendicular components of magnetic field variations in Australia (winter) could be attributed to the complicated small-scale structures (Yokoyama et al., 2015; Yokoyama and Stolle, 2017). Since Swarm A and C orbit at an altitude of $\sim$450 km, which is above the average F2 peak density location, and MMFs and MSTIDs share similar climatology and morphology characteristics (Park et al., 2015, 2009b), then a simultaneous observation of perpendicular MMFs in conjugate regions indicates the detection of flowing inter-hemispheric field-aligned current associated with MSTIDs. As for the parallel components, the anti-correlation between density and $dB_{||}$ is more obvious in the summer hemisphere (Japan; r=-0.87) than in the winter hemisphere (Australia; r=0.61). This result further provides the evidence that more significant plasma

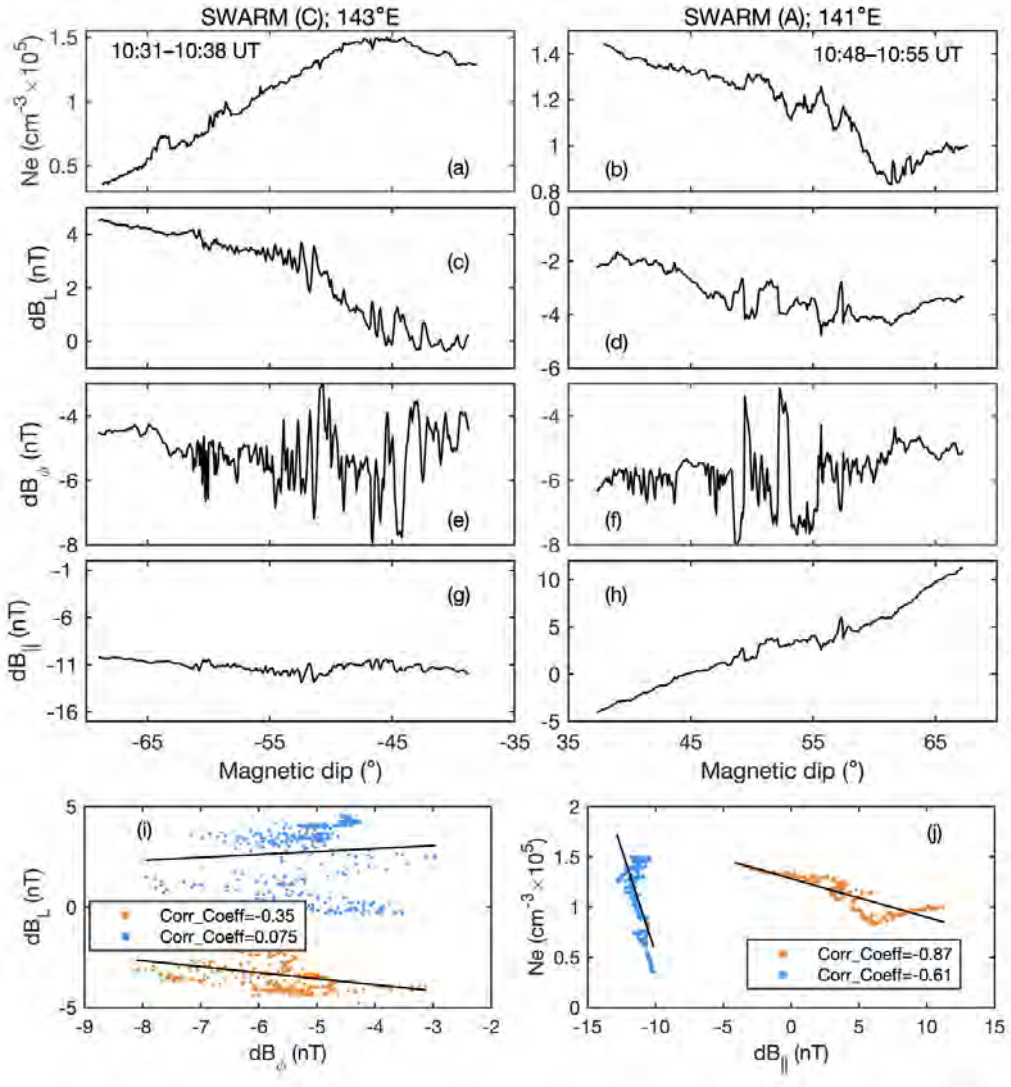

Fig. 4.13 (a–f) In situ electron density, and radial (dB_L), zonal (dB_ϕ), and parallel components ($dB_{||}$) of residual magnetic fields observed by the Swarm A and C satellites along the traces in Figure 4.12, on 29 July, 2019 (DOY 210). (i–j) A scatter of perpendicular components (left) and the electron density with parallel magnetic field variation (right) during this nighttime MSTID event. The orange and blue dots correspond to the observations in summer (Japan) and winter (Australia) hemispheres, respectively.

density variation occurs in the summer hemisphere. This disparity could be related to the growth rate of Perkins instability (γ_P). As previously described in Equation 2.30, γ_P is greatly affected by $\mathbf{U} \times \mathbf{B}$, since the F-region preexisting background electric field $\mathbf{E}$ due to dynamo process is much weaker compared to the $\mathbf{U} \times \mathbf{B}$ electric field component (Otsuka, 2021). Thus, under the above argument, we suggest that the poor correlations in the winter hemisphere (density and $dB_{||}$, dB_L and dB_ϕ), were a result of unfavorable ionospheric background conditions for MSTID growth leading to reduced amplitudes in that hemisphere.

4.2.3 Event on 26 December 2019

On December 26 2019 (DOY 360), conjugate MSTIDs in the winter hemisphere show greater intensity than the event on July 29 (DOY 210), 2019. Figure 4.14 shows the 2-D TECP maps for this day at various epochs from 7:00 to 14:00 UT, which are obtained by using the single-thin-shell approach at 300 km height. Orange and blue circles indicate the geomagnetic conjugate regions over Australia (summer) and Japan (winter), and black solid line represents the solar terminator. Before sunset (9:00 UT; 19:00 AEST), distinct ionospheric irregularities ($\sim$0.7 TECU) form in the region bounded by the gray solid lines over Australia (summer) at lower latitudes ($\sim$20°S); electron density depletions with small amplitudes ($\sim$0.2 TECU) are observed at higher latitudes ($\sim$35°S; circled by the orange line in subplot (f)). The irregularities during the day are most possibly seeded by AGWs, because the daytime E-region conductivity is much larger than that of the F region, thus causing larger currents to close mainly in the E region and limiting polarization electric fields that could facilitate the E-F coupling (Heelis et al., 2012; Kelley, 2009). Under such conditions, the propagation direction of this disturbance structure is most likely equatorward since equatorward propagating AGWs could cause a larger amplitude of TEC perturbations than AGWs propagating in other directions (Hooke, 1968). The density depletions at higher latitudes propagate roughly to the northwest, while the exact direction of the irregularity structure at lower latitudes is difficult to determine due to the sparse GNSS data points over this region.

At around 9:00 UT (19:00 AEST) near sunset, the AGW-seeded irregularities at lower latitudes show a drop in amplitudes and disappear (or propagate to the region beyond GNSS detection); F-region density enhancements/depletions form at higher latitudes ($\sim$35°S; bounded by orange circle in subplot (g)). Subsequently, at $\sim$10:00 UT (20 AEST) after sunset, significant NE-SW aligned MSTID structures (0.32 TECU) are observed at higher latitudes ($\sim$35°S) of Australia (summer), propagating northwestward. In the winter hemisphere (Japan), conjugate irregularities aligned in NW-SE caused by the interhemispheric coupling appear at higher latitudes ($\sim$45°N; circled by the blue line in subplot (i)) at around 11:15 UT

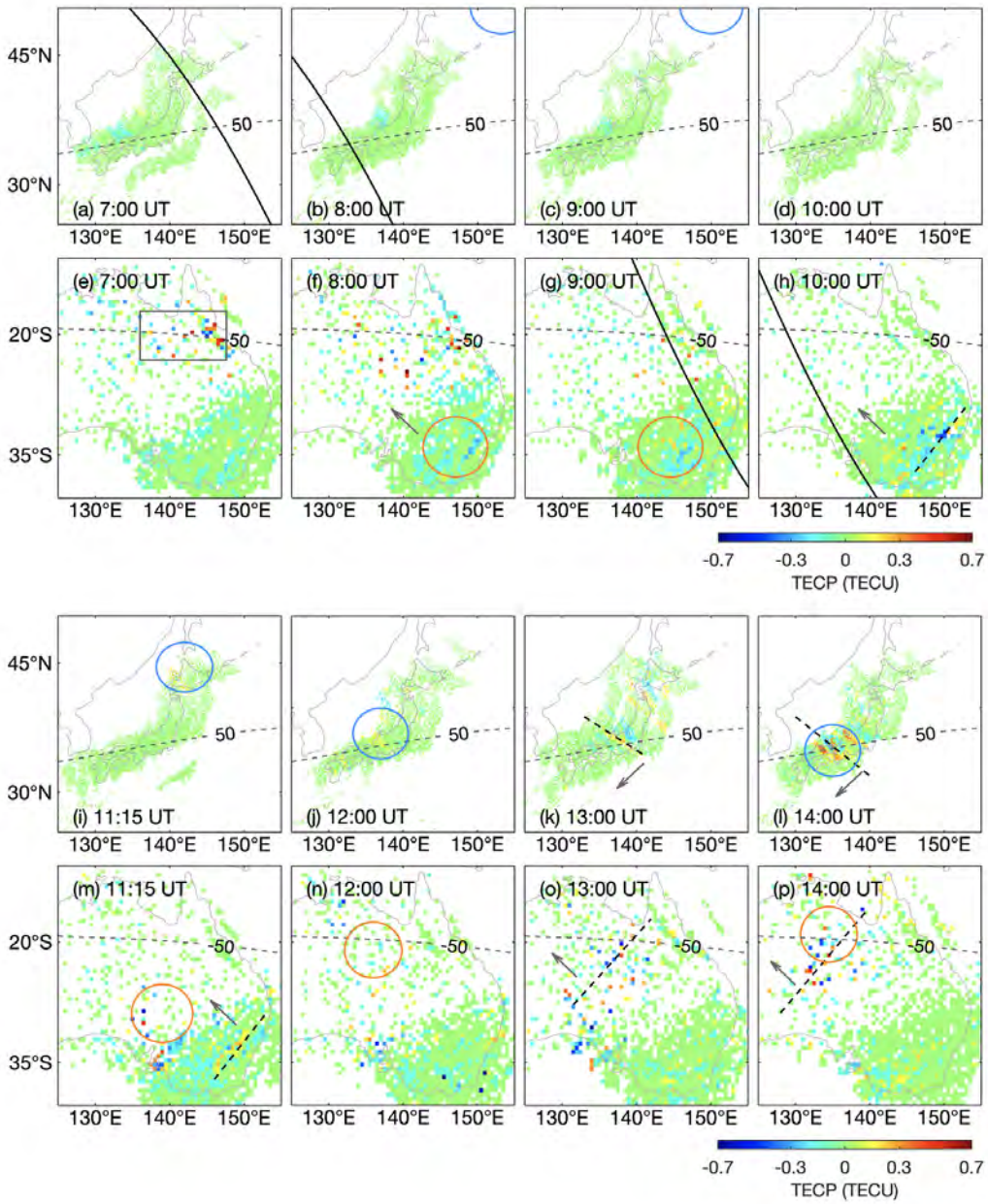

Fig. 4.14 Same as Figure 4.9 but for 26 December 2019 (DOY 360), snapshots of TECP maps at various time epochs from 6:00 to 14:00 UT. Gray dashed lines represent the magnetic dip at $\pm 50^{\circ}$, solid orange and blue circles indicate the geomagnetic conjugate regions over Australia (summer) and Japan (winter), black solid line represents the solar terminator, rectangle bounded by gray solid line indicates the region where irregularities occur before sunset, black dashed lines indicate the alignment azimuths of the apparent frontal structures, gray arrows denote the drift direction.

(20:15 JST), and then propagate to lower latitudes (∼35°N; circled by the blue line in subplot (j)) at around 12:00 UT (21:00 JST). The MSTIDs in different hemispheres are symmetric about the magnetic equator, sharing similar phase velocities of ∼100 m/s and propagating toward equator-westward direction. From 11:15–13:00 UT, the tilted irregularities over Japan (winter) develop to obvious wavelike structure. Still, the intensity of conjugate MSTIDs is larger in the summer hemisphere (0.42–0.60 TECU) than the winter hemisphere (0.15–0.34 TECU). At around 14:00 UT, the conjugate MSTIDs over Japan (winter) develop to the maximum intensity close to (but less than) that in Australia (summer).

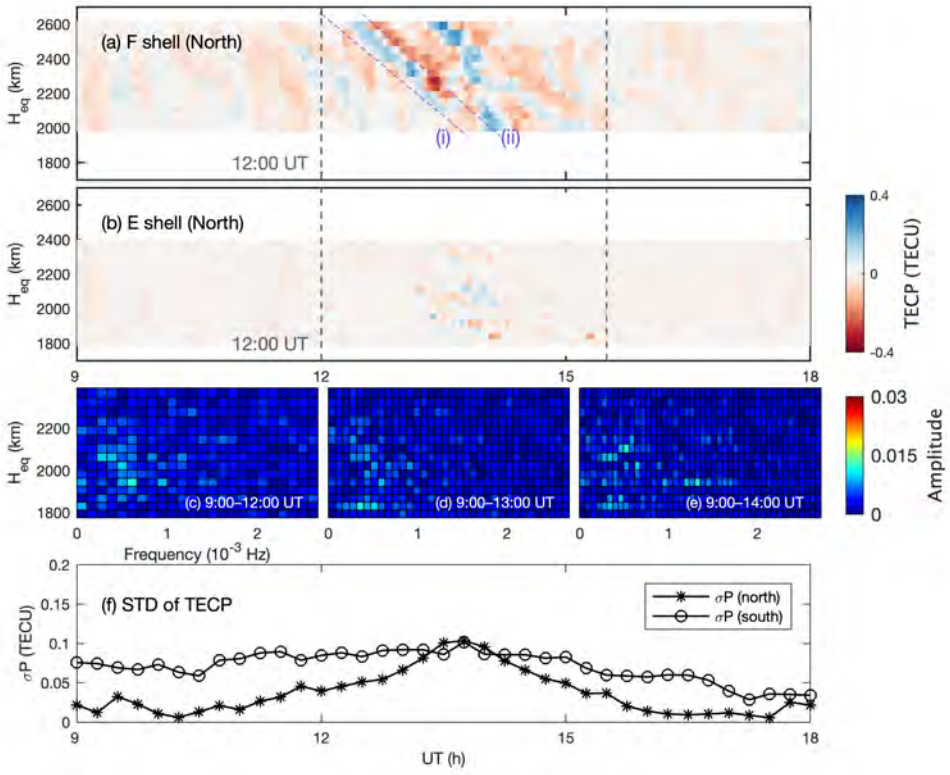

Fig. 4.15 Same as Figure 4.10 but for 26 December 2019 (DOY 360). (a–b) Time variation of TECPs in E and F shells along the northeast–southwest red dashed line over Japan in Figure 4.8(b). (c–e) E-region reconstruction results of FFT in different time periods. (f) Time variation of the standard deviation of TECPs (σP) in different hemispheres.

Same as Figure 4.10 but for 26 December 2019 (DOY 360), Figure 4.15 show the time variation of E- and F-region TECPs at E- and F-shell heights, the E-region reconstruction results of FFT, and the standard deviation of TECPs (σP) in different hemispheres. For this event, in the analyzed region with most data points over Japan (winter), evident downward-sloping stripes occur after ∼12:00 UT at the F-shell height, and reach the maximum intensity at around 14:00 UT. However, at the E-shell height, noise or the mixture of noise and low-

amplitude irregularities dominate, especially when the irregularity intensity is high in the F region. Similar cases were reported in the simulation section 3.3.2, where the E-region reconstruction performance deteriorates if strong irregularities exist in the F region and weak irregularities exist in the E region. The low development of E-region disturbances during this time period has also been verified by the FFT analysis on the E-region reconstruction in subplots (c–e), where no weak phase fronts are lurking within the noise. That is to say, in the winter hemisphere (Japan), the Es layer does not have a significant effect on the MSTIDs in the F region through local E-F coupling. This phenomenon coincides with the inference obtained from the hemisphere-coupled simulations in Yokoyama (2014); that MSTIDs in the winter hemisphere may be driven by the irregularities in the summer hemisphere through the hemisphere-coupled electrodynamics.

The standard deviations of TECPs (σP) in different hemispheres on 26 December 2019 (DOY 360) are plotted in subplot (f) to indicate the time variation of irregularity intensity. Results indicate that irregularities are continuously observed over Australia (summer) but with a reduction in amplitude after $\sim$14:00 UT; over Japan (winter), MSTID structures form after $\sim$11:15 UT, and develop to the maximum intensity at around 14:00 UT; the conjugate MSTIDs in the Japan (winter) decay more rapidly compared to MSTIDs in Australia (summer). It is important to note that at around 14:00 UT when σP reaches its maximum in both hemispheres, the MSTID intensity is still larger in Australia (summer) but the sparse data points limit the exact representation of the intensity. Compared to the variation of σP in Figure 4.10, the maximum amplitude of disturbance (σP) over Japan is reduced by half, while that over Australia region is doubled.

To obtain more information on E-region activity in both hemispheres, the ionosphere parameters foEs and fbEs were plotted in Figure 4.16 as in Figure 4.11, but for event 26 December 2019 (DOY 360). The time is from 5:00 to 18:00 UT. Gray dashed lines represent the duration of the perturbations over the region with most data points in Japan (winter), as in Figure 4.15. Similar to the Es-layer variation in the winter hemisphere discussed in the previous section, frequently observed Es layers with small amplitudes (foEs$<$5 MHz, foEs-fbEs$<$2.5 MHz) over Wakkanai, Kokubunji and Yamagawa show reduced foEs ($<$3 MHz) and foEs-fbEs ($<$1 MHz) values during the interhemispheric coupling process. The ionograms over Wakkanai, Kokubunji, and Yamagawa during 12:00–15:30 UT further validate the results obtained by using the double-thin-shell approach in Figure 4.15 (a–b), i.e., the Es layer has a very low development during the conjugate MSTIDs in the winter hemisphere (Japan). In the Southern Hemisphere (summer), as observed by the ground-based GNSS-TEC in Figure 4.14, ionospheric F-region irregularities occur over Australia before sunset. Before 9:00 UT (19:00 AEST), sporadic and blanketing E layers over Townsville and

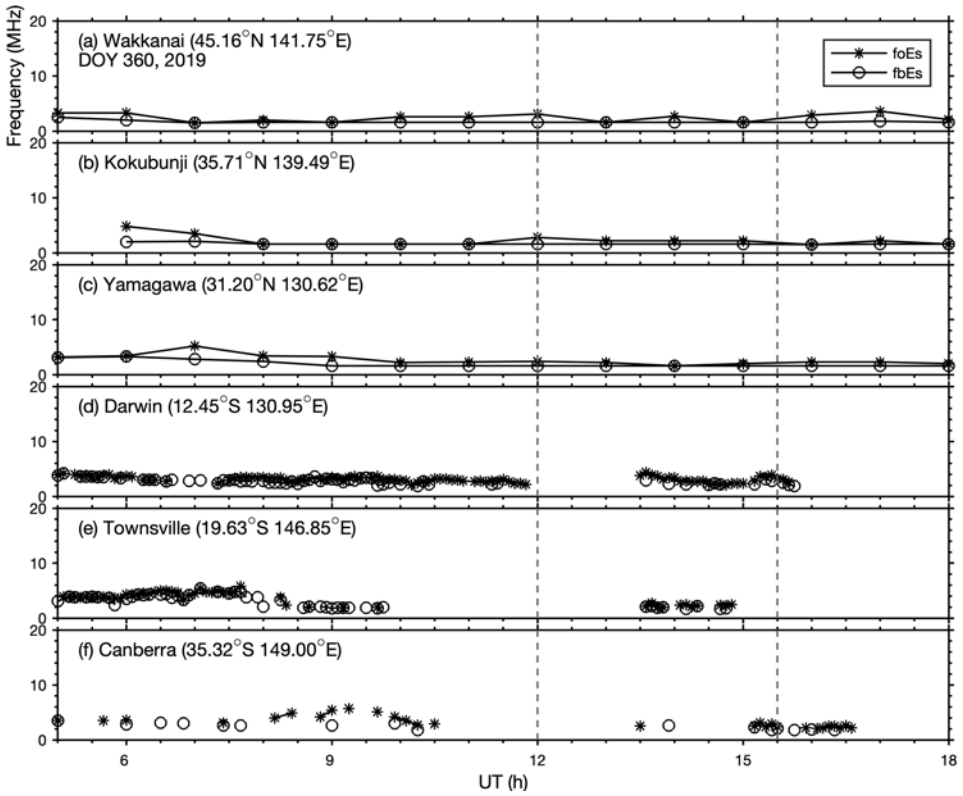

Fig. 4.16 The ionosonde measurements from Wakkanai, Kokubunji, Yamagawa, Canberra, Townsville, and Darwin, comprising of foEs and fbEs from 5:00 to 18:00 UT on 26 December 2019 (DOY 360). Gray dashed lines are the same as Figure 4.15, representing the duration of perturbations over the region with most data points in Japan.

Darwin at lower latitudes are frequently observed in the ionograms, which may be associated with the daytime sporadic E activity or the irregularities observed before sunset. At 9:00 UT, both foEs and the difference between foEs and fbEs show enhancement over the Canberra ionosonde, followed by the formation of distinct NE-SW aligned frontal structures in this region as shown in Figure 4.14(g–h), from which the occurrence of E-F coupling in the Southern Hemisphere can be inferred. Subsequently, in Figure 4.16(e–f), after the onset of local E-F coupling, the Es layers coupled with MSTIDs are observed at lower latitudes, at 13:30 UT, over Townsville and Darwin. It is worth noting that, at around 9:00 UT, the foEs ($<$6 MHz) and foEs-fbEs ($<$3 MHz) in the summer hemisphere (Australia) on DOY 360 in Figure 4.16 are significantly less than those on DOY 210 in Figure 4.11. One reasonable explanation is that the Es plasma density is higher in Japan (Northern Hemisphere) around the June solstice than in Australia (Southern Hemisphere) around the December solstice (Wu et al., 2005), and the E-region conductivity near the solar terminator is still large enough to short out the polarized electric field. Or, the presence of MSTIDs seeded by AGWs may have

generated favorable conditions to the development of the Perkins instability, e.g., enhanced background electric field (Yokoyama, 2014), which makes the effects of Es layer in the E-F coupling become less pronounced.

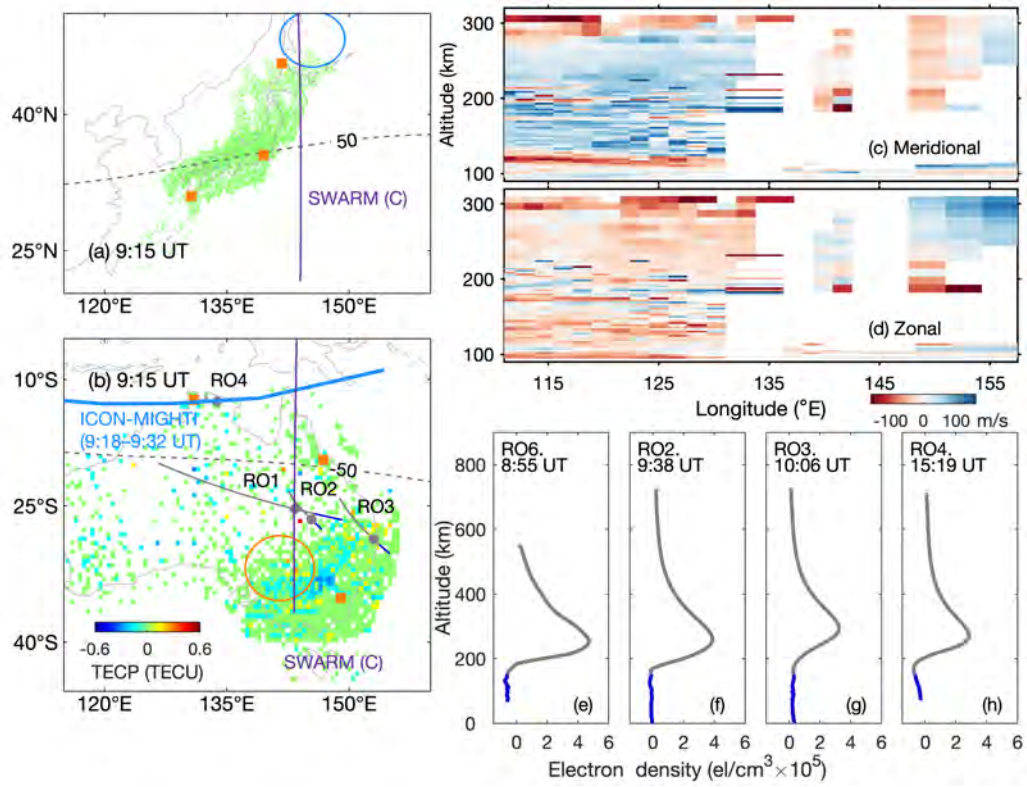

Fig. 4.17 (a–b) Gray (dark blue) solid lines are traces of COSMIC occultation tangent points in F (E) region, gray dots are locations of maximum electron density along each trace, orange and blue circles indicate the conjugate regions in the summer and winter hemispheres. Purple and blue solid lines represent the traces of Swarm satellites and ICON-MIGHTI neutral winds, respectively. Background is the ground-based GNSS-TECP map at 9:15 UT on 26 December 2019 (DOY 360). (c–d) Meridional and zonal wind profiles (positive northward and eastward) measured by ICON-MIGHTI at the same locations above. (e–h) Results of COSMIC constellation vertical electron density profiles at different epochs.

Same as Figure 4.12 but for 26 December 2019 (DOY 360), Figure 4.17 (a) shows the 2-D TECP map at 9:15 UT (19:15 AEST) and traces of space-based observations including Swarm (purple lines), COSMIC (gray and dark blue lines) and ICON-MIGHTI (blue line). At around 9:15 UT, the NE-SW aligned frontal structures start to form and develop at higher latitudes in the summer hemisphere (Australia; in the vicinity of the orange circle region), while no irregularities are observed by GNSS-TEC in the winter hemisphere (Japan). Subplots (c–d) show the meridional and zonal wind profiles (positive northward and eastward) measured by ICON-MIGHTI at the locations shown by the blue solid line in subplot (b).

As observed in Figure 4.14, at 9:15 UT the solar terminator is crossing Australia. Due to the high activity of AGWs in the solar terminator (Forbes et al., 2008), the ICON-MIGHTI data along this trajectory have many blanks: Otsuka (2021) briefly discusses that the vertical wavelength of AGWs is affected by the background neutral wind, with waves propagating against the background winds exhibiting longer intrinsic vertical wavelength and reaching higher altitudes. In due process, to conserve kinetic energy, the amplitude of the neutral wind oscillation increases (which in return affects the air-glow profiles). Therefore, we think, it is this rapid variation in the profiles that leads to increased error in the retrieved wind data, thus rendering the data unusable. The data continuity is good on the dusk side (110°E–135°E), and the results indicate that at ∼200-km altitude, the equatorward and westward neutral winds prevail over this area before sunset. On the night side (135°E–160°E), the thermospheric winds show great fluctuations. However, we found that on the night side, the neutral wind conditions in the E region can support the generation of the Es layer, since wind shear is observed in both meridional and zonal directions over this area (Haldoupis, 2012). In fact, this wind shear indeed amplified the Es layer: as shown in Figure 4.16, over Darwin in the vicinity of the observation area, (foEs-fbEs) show enhancement (from $<$1 to 1.7 MHz) at around 9:40 UT after sunset. In addition, no significant electron density perturbations caused by Es layer are observed by COSMIC occultation for this MSTID event. Since GNSS-TEC observations are sensitive only to ionospheric irregularities with high electron density (or large foEs) (Maeda and Heki, 2014), occultation events at ∼9:00–10:00 and 15:00 UT do not capture the weak Es layers (∼4 MHz) observed by Townsville and Darwin ionosondes, even in RO4 event close to Darwin.

Figure 4.18 (a–h) shows the observation results of in situ electron density, dB_L, dB_ϕ, and $dB_{||}$, from Swarm satellites along the traces in Figure 4.17 (a), at around 9:00 UT on 26 December 2019 (DOY 360). The derivation method of the residual magnetic field is the same as that used for Figure 4.13. At higher latitudes in the Northern Hemisphere (winter) beyond GNSS detection ($>$55° magnetic dip; within the blue circle region in Figure 4.17(a)), drops and perturbations in electron density are observed without accompanied MMFs. We think this structure may be the results of nighttime mid-latitude ionospheric trough, which is mainly driven by neutral winds (He et al., 2011). In the Southern Hemisphere (summer), relatively moderate electron density variations are detected at -40°– -30° magnetic dip, which could be the same disturbances seeded by AGWs before sunset as shown in Figure 4.14(e). The speculation of AGWs is supported by the thermospheric wind observations in Figure 4.17(c–d), wherein significant variations exist in the lower thermosphere (∼200 km in both meridional and zonal directions). Near this region, the AGWs would presumably be the strongest since AGWs propagating against the background winds can propagate vertically to

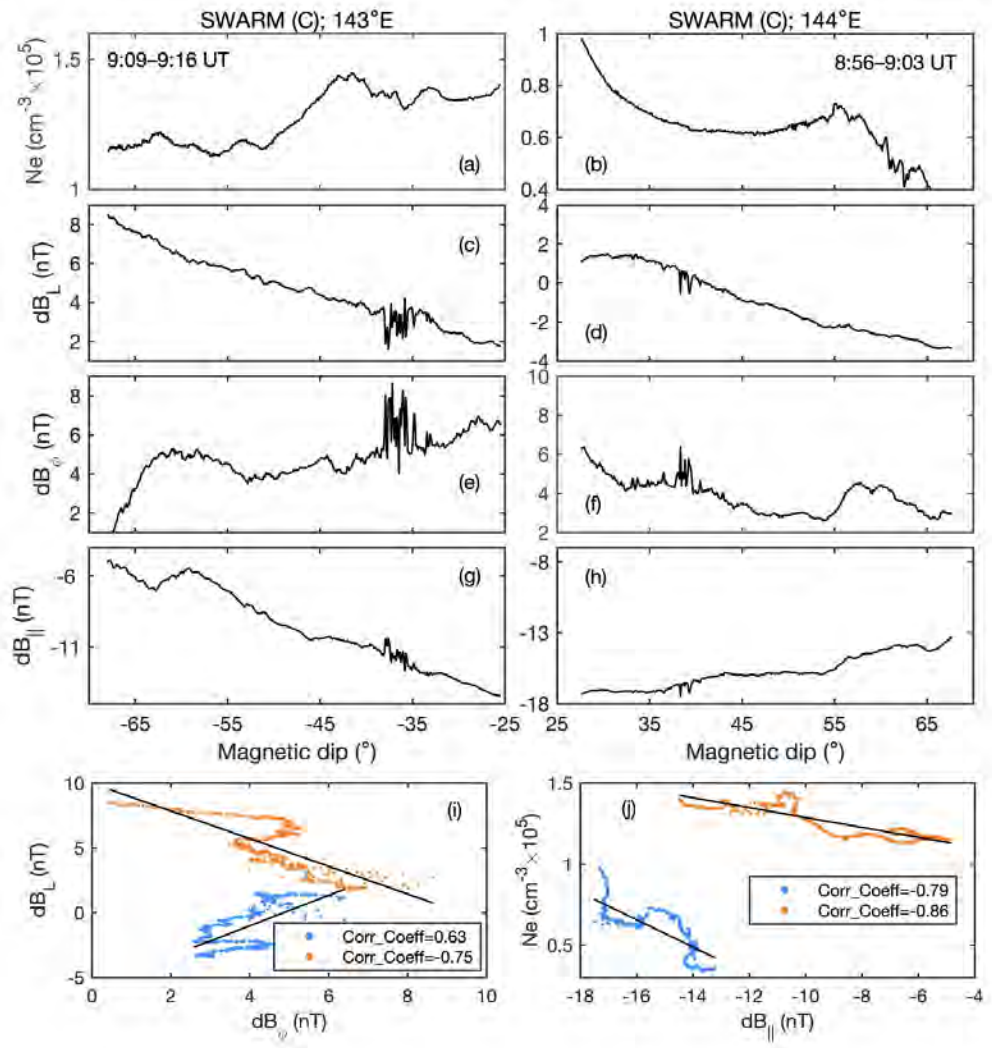

Fig. 4.18 (a–b) In situ electron density, and radial (dB_L), zonal (dB_ϕ), and parallel components ($dB_{||}$) of residual magnetic fields observed by the Swarm A and C satellites along the traces in Figure 4.17, on 26 December, 2019 (DOY 360). (i–j) A scatter of the variation in magnetic field perpendicular components (left), and electron density with parallel magnetic field variation (right) during this nighttime MSTID event. The orange and blue dots correspond to the observations in summer (Australia) and winter (Japan) hemispheres, respectively.

higher altitudes and then weaken due to viscosity and thermal conductance (Pitteway and Hines, 1963). Due to the limited distribution of GNSS distribution, this irregularity structure is not observed by GNSS-TEC in Figure 4.17(a). The fluctuations caused by this irregularity are observed in both perpendicular (dB_L, dB_ϕ) and parallel ($dB_{||}$) components of residual magnetic fields in the conjugate regions ($\sim\pm37^\circ$ magnetic dip) of both hemispheres, as shown in Figure 4.18 (c–h). However, different from the results in Figure 4.13, the intensity and magnitude of these magnetic field fluctuations in the summer hemisphere (Australia) are significantly greater, which could be caused by the differences in ionospheric conductivity and electric field between these two geomagnetic conjugate regions (Park et al., 2009b). That is, MMFs amplitudes are related to field-aligned currents which are dependent to effective electric field ($\mathbf{E}^* = \mathbf{E} + \mathbf{U} \times \mathbf{B}$) and ionospheric conductivity, that are larger in the summer hemisphere since the F-region conductance is proportional to the plasma density (Lee et al., 2021) and equatorward wind ($\mathbf{U}$) which is larger in the summer hemisphere (Tepley et al., 2011).

In the GNSS-TEC observations of Figure 4.17(b), at -65°– -60° magnetic dip (within the orange circle region) in the Southern Hemisphere (summer) before sunset, MSTIDs form with a small amplitude. In the subplot (a) of Figure 4.18 at around 9:15 UT, small-scale undulations of in situ electron density are also observed by Swarm A satellite in the corresponding region. However, compared to the developed MSTID structures at lower latitudes (-35° magnetic dip), fluctuations with large wavelengths but small intensities are observed only in dB_ϕ and $dB_{||}$ in geomagnetic conjugate regions. The fact that no corresponding perturbations in dB_L indicates that the field-aligned currents are small in the initial phase of MSTID development, and the perturbations in dB_ϕ could be related to the apparent zonal propagation of AGWs caused by solar terminator (Forbes et al., 2008; Miyoshi et al., 2009). Subplots (i–j) in Figure 4.18 show a scatter of the variation in magnetic field perpendicular components (left), and electron density with parallel magnetic field variation (right), during the nighttime MSTID event on 26 December, 2019 (DOY 360). The orange and blue dots correspond to the observations in summer (Australia) and winter (Japan) hemispheres, respectively. The orange and blue dots correspond to the observations in summer (Australia) and winter (Japan) hemispheres, respectively. From Figure 4.18, negative correlations between electron density and parallel magnetic field variation are observed in both hemispheres (r=-0.86 and -0.79 for the summer (Australia) and winter (Japan) hemispheres, respectively); dB_L and dB_ϕ show anti-correlation in the summer hemisphere (Australia; r=-0.75) and correlation in the winter hemisphere (Japan; r=0.63). Although the correlation/anti-correlation is still weaker in the winter hemisphere compared to the summer hemisphere, the performance is much improved compared to the results in Figure 4.13, especially in the perpendicular components (dB_L and

dB_ϕ). I suggest that such ionospheric background conditions (e.g., effective electric field) may favor the Perkins instability growth (as described in Equation 2.30) and persist for some time (until the maximum amplitude of MSTIDs at around 14:00 UT), which subsequently lead to the formation of geomagnetic conjugate MSTID structures in the winter hemisphere, with maximum amplitudes close to those in the summer hemisphere.

4.3 Discussion

Controlling role of Es in the summer hemisphere

This study has simultaneously analyzed the nighttime mid-latitude E- and F-region 2-D structuring and evolution when electrodynamic influenced irregularities (Es and MSTIDs) are present. According to the reconstructed results, geomagnetic conjugate MSTIDs aligned in NW-SE (NE-SW) were simultaneously observed in the Northern (Southern) Hemisphere; over Japan area, irregularities with similar NW-SE alignments and propagation parameters were also observed in both E and F region. As described in Section 2.4, the Es-layer instability and Perkins instability are two mechanisms that can explain the ionospheric irregularities with directional preference (Cosgrove and Tsunoda, 2004; Perkins, 1973); the Es layers play an important role in amplifying the Perkins instability, and the fastest growth of the coupled instability occurs when the unstable conditions on NW–SE perturbation are satisfied in both E and F regions (Yokoyama et al., 2009). Yokoyama (2014) suggested that MSTIDs observed in the winter hemisphere may be driven by the Es layer in the summer hemisphere. Narayanan et al. (2018) have found that the presence of Es layers in one hemisphere is sufficient enough to form conjugate MSTIDs. Lee et al. (2021) concluded that conjugate MSTIDs in the winter hemisphere are associated with MSTIDs in the summer hemisphere; the summer hemisphere MSTIDs are related with the occurrence of Es in the summer hemisphere. Corroborating the earlier analyses and expositions on the morphology and dynamics in the coupling process obtained through observation and simulation (Liu et al., 2019; Saito et al., 2007; Yokoyama et al., 2009), the reconstruction results by using GNSS-TEC and a double-thin-shell approach (Figure 4.3, 4.7, 4.10 and 4.15) indicate that during the nighttime MSTID event, Es layers were observed only in the summer hemisphere and appear $\sim$30 min earlier than the MSTIDs in the F region; in the summer hemisphere, the coupled E- and F-region irregularities share similar alignment, propagation direction, and phase velocity, and are related to each other through a magnetic field line; conjugate MSTIDs in the winter hemisphere appear later and disappear earlier than the MSTIDs in the summer hemisphere. These results further support the evidence that the F-region conjugate structures in both hemispheres are mainly driven by the Es layer in the summer hemisphere through local E-F coupling and interhemispheric

coupling. Furthermore, it might be also reasonable to assume that the phase velocity of geomagnetic conjugate structures are controlled by the E-region neutral wind velocities in the summer hemisphere due to the comparable velocities and the important role of E-region meridional wind in MSTID propagation (Larsen, 2002; Yokoyama et al., 2009). Earlier simulation works of Tsunoda (2006) and Yokoyama et al. (2009) emphasized the contribution of the neutral winds in the Es layer on the MSTID propagation: even without the background electric field, the rotational wind shear in the E region produces southwest phase propagation in both E and F regions for the NW-SE structures; however, these structures are stationary if the E-region meridional wind is absent.

Difference in MSTID structuring and development

In Figures 4.1 and 4.5, the Es structures on 23 June 2012 (DOY 175) (before 22:00 JST) and 11 June 2007 (DOY 162) have similar horizontal scales. However, the horizontal scale and intensity of MSTID structures in Figure 4.5 are smaller than those in Figure 4.1. This difference in MSTID structuring and development in the summer hemisphere ought to depend on several factors that include the F-region background condition, the Es-layer intensity, and the duration of Es layer formation.

For MSTID event on 23 June 2012 (DOY 175), preexisting turbulences that cannot be captured by GNSS-TEC have possibly perturbed the E (e.g., neutral wind shear) and F regions (e.g., gravity wave). In Figure 4.3, the E- and F-region irregularities detected by GNSS-TEC both develop after $\sim$19:30 JST. However, the irregular structures in E and F regions reach the maximum amplitude at around 20:15 JST ($\sim$1.5 TECU) and 22:00 JST ($\sim$2 TECU), respectively. The much shorter time scale of the well-developed Es may be due to the thinner Es layer, the larger growth rate of the Es-layer instability (Cosgrove and Tsunoda, 2004), and the weak polarization electric fields from the F region (Cosgrove, 2013). During 20:30–22:30 JST, the intensity of the Es layer reduced slightly, but the amplitude of F-region wave-like structures increase rapidly and reach the maximum. This fast development of irregularities in the F region could be attributed to the amplification of Perkins instability by large polarization electric fields via geomagnetic field lines, since the E-region irregularities determined by the double-thin-shell approach have a typical horizontal scale of $\sim$150 km, which is able to produce polarization electric fields on this scale at nighttime with more rapid onset of non-linearity (Cosgrove, 2013). At 22:15 JST, after the larger scale NW–SE structures are developed in the F region, the enhanced amplitude and elongated scale length of Es layer could result from the reinforced Es-layer courtesy of the polarization electric fields mapping from the F region (Yokoyama et al., 2009).

In a similar time period (∼19:00–24:00 JST) on 11 June 2007 (DOY 162), MSTID structures with smaller horizontal scale and intensity, and a similar duration of structure formation of Es and MSTIDs, were observed. In Figure 4.7, the evident downward-sloping stripes in the E region appear ∼10 min earlier, a time scale that agrees with the simulation results of the F-region response in the early stage of E–F coupling process (Cosgrove, 2007; Yokoyama et al., 2009). As discussed in Section 4.1.2, the lower heights (<300 km) of the F-region irregularities, which could be caused by the poleward (or weak equatorward) neutral wind, can limit the instability structuring and amplitudes (Narayanan et al., 2014). In addition, the weaker Es layer (∼20% maximum amplitude decrease compared with 23 June 2012 (DOY 175)) on 11 June 2007 (DOY 162) can cause lower growth rate of the variation of the integrated Pedersen conductivity in the F region, which delays the development of MSTID structures (Yokoyama et al., 2009). Using GNSS-TECPs with a double-thin-shell approach, the time scale of the full development of Es-layer structuring is about 160 min (from ∼18:50 to 21:30 JST), which is about 100 min larger than that on 23 June 2012 (DOY 175) (from ∼19:30 to 20:15 JST). Less sharp perturbation gradients in the E region on 11 June 2007 (DOY 162) produce smaller polarization electric fields associated with gradient drift instability (Cosgrove, 2013), which can lead to the perturbation related to the Perkins instability tending to saturate at a smaller amplitude. Even so, the Es-layer instability still amplified the Perkins instability on 11 June 2007 (DOY 162): the time scale for producing large modulations in the F region has been shortened to about 1.5 h (from ∼19:00 to 20:30 JST) from 2 to 3 h (without an Es layer) (Cosgrove, 2007). This mechanism could also be an explanation for the smaller intensity MSTIDs before sunrise on 23 June 2012 (DOY 175) in Figure 4.3, and after sunset on 29 July, 2019 in Figure 4.10.

Decrease in Es-layer intensity in the winter hemisphere

From ionosonde observations in Figure 4.11 and 4.16, continuous Es layers with small amplitudes (foEs<3 MHz) in the winter hemisphere show further intensity reduction and dissipation after the interhemispheric coupling. In fact, in earlier works, e.g., Narayanan et al. (2018), the amplitude reduction and dissipation of Es may have been observed. However, the limited observation area in comparison to the scale of MSTIDs limited their conclusions on the temporal relationship between the occurrence of Es and MSTIDs. Further investigations have shown that under quiet conditions, the vertical structure of electric field arising from sunset electrodynamic processes can result in the enhancements or disruption of Es layer (Abdu et al., 2014): at nighttime, when E region conductivity is significantly reduced, and the closure path for the wind-driven currents in the F region is limited, the ions drift with the neutral gas to reduce the collisional force. Thus, the distribution of winds and conductivity

will subsequently modify the distribution of ionization and thereby change the ionospheric conductivity and the ion drag on the neutral gas (Heelis et al., 2012). Then, in the E region, the polarization electric field will be larger in the zonal direction ($E_x^p \approx \frac{\sigma_H}{\sigma_P} E_y$; the Hall-to-Pedersen conductivity ratio $\left(\frac{\sigma_H}{\sigma_P}\right)$ is large in the E region (Haldoupis et al., 2003)), and its final value depends on the polarization field established in the meridional direction and the current-closure system coupled to the F region through the field-aligned currents (Haldoupis et al., 2003, 1996). Now, if the integrated Pedersen conductivity in the region above Es is comparable to that within the Es patch, the polarized electric field will be reduced accordingly (Haldoupis et al., 2003). In addition, the variation of the integrated Pedersen conductivity in the F region is large during the MSTID formation (Yokoyama et al., 2009). Therefore, the preexisting Es layer is easier to show intensity reduction or even dissipation in the winter hemisphere, with a reasonable inference that the polarization electric field within the small-amplitude Es layers (foEs$<$3 MHz, foEs-fbEs$<$1 MHz) is small, and the integrated Pedersen conductivity within Es is easily comparable to that above Es when interhemispheric coupling occurs.

For the MSTID event on 29 July 2019 (DOY 210), only small-amplitude conjugate structures formed in the F region. Es layers in the winter hemisphere (Australia) start to show intensity reduction and dissipation when conjugate MSTIDs move over the region. During this period, poleward meridional wind could be dominant in the Southern Hemisphere (winter), as it can push the plasma to lower altitudes where enhanced recombination occurs, thus reducing the amplitude of conjugate structures and enhancing the Pedersen conductance (Shiokawa et al., 2003b). For another event on 26 December 2019 (DOY 360), conjugate MSTIDs in Japan (winter) develop to a maximum amplitude close to that in Australia (summer). In such cases, equatorward thermospheric winds in both hemispheres can be inferred during the formation of conjugate MSTIDs, which favor the MSTID generation (Yokoyama, 2014). However, in the solstice period, meridional thermospheric winds at midlatitudes are not perfectly symmetric and often have a trans-equatorial component from summer to winter hemisphere (Tepley et al., 2011). Of course, the smaller equatorward wind in the winter hemisphere results in a larger Pedersen conductance in that hemisphere, but certainly not with the same effect as the poleward wind. For this event, Es layers in the winter hemisphere (Japan) start to decrease in amplitude ($\sim$12:00 UT) about 1 hour after the appearance of conjugate irregularities over Japan ($\sim$11:15 UT), i.e., when conjugate MSTIDs develop to a certain magnitude. Based on the above results, I suggest that the variation in integrated Pedersen conductivity leading to decrease in amplitude or even dissipation of the low-amplitude Es layer in the winter hemisphere is influenced by conjugate MSTIDs and thermospheric winds (in that hemisphere), but the former is more pivotal. Due to the nature

of our results and sensitivity of data used in analysis, we could not ascertain the impact of a dissipating weak Es-layer (in winter hemisphere) on the summer hemisphere dynamics. However, based on previous simulation results, e.g., Yokoyama (2014), this impact would be limited on the Es in the winter hemisphere.

Thermospheric wind

Thermospheric winds could play an important role in the MSTID generation and development, since the effective electric field ($\mathbf{U} \times \mathbf{B}$) dominants the linear growth rate of Perkins instability, as described in Equation 2.30. These winds are not significantly affected by the MSTID formation because the time constant of the ion drag affecting the neutral wind is usually larger than the period of MSTIDs (Narayanan et al., 2018). At night when the E region conductivity is small, the thermospheric wind dynamo fluctuations can produce polarization electric fields in the F region; partially shorted out by the conductivity in the local E region or conjugate hemisphere (Buonsanto and Foster, 1993; Chen et al., 2020). Usually this phenomenon is accompanied by equatorward meridional winds (Buonsanto et al., 1990): which has been validated by the thermospheric wind measurements made with the Fabry-Perot interferometer (FPI) (Narayanan et al., 2018). Yokoyama (2014) have found through simulations that NW-SE (NE-SW) oriented MSTIDs occur simultaneously in geomagnetic conjugate regions of the Northern (Southern) Hemisphere, if F-region neutral wind satisfies the unstable condition (equator-eastward) in both hemispheres and a sporadic-E layer is given only in the summer hemisphere.

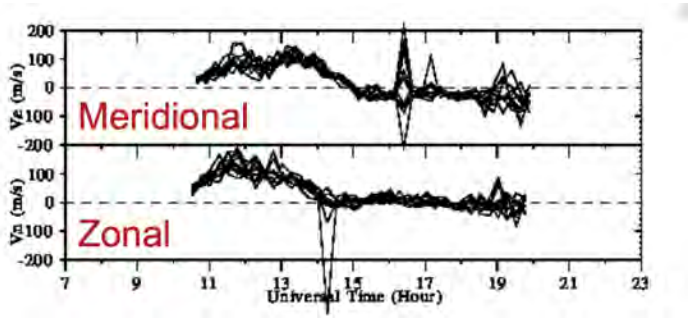

Fig. 4.19 Thermospheric wind measurements over Darwin on 26 December, 2019 (DOY 360).

From the subplot (f) in Figures 4.10 and 4.15, the similarity of σP variation curves and the difference in amplitude between July and December in Japan may imply that local thermospheric wind conditions play an important role in determining the level of MSTID activity. On 26 December 2019 (DOY 360), in Australia (summer), NE-SW

aligned MSTIDs form at around 9:00–10:00 UT. From FPI observations over Darwin (https://stdb2.isee.nagoya-u.ac.jp/omti/data/html/fp04/2019/FP042191226_wind.html), equator-eastward meridional winds were observed (maximum at ∼12:00 UT) and turned zero or weak poleward at about 14:00 UT, as shown in Figure 4.19. After the rapid reduction or redirection of meridional wind at 14:00 UT, MSTIDs in the summer hemisphere show a decrease in both amplitude and scale. In the Northern Hemisphere (winter), NW-SE aligned conjugate MSTIDs propagate to Japan at around 11:15 UT; after 2-3 hours of development, conjugate MSTIDs develop to an intensity close to that of the summer hemisphere; subsequently, the intensity of conjugate MSTIDs decreases rapidly. We infer that the thermospheric winds in the Northern Hemisphere (winter) are most likely equator-eastward during 11:15–14:00 UT; after 14:00 UT, the thermospheric winds in both hemispheres show a decrease in amplitude and a shift in direction; the intensity of conjugate MSTIDs in Japan (winter) decreases with a much larger rate than that in Australia (summer), which could be related to the decoupling of the winter hemisphere from the summer hemisphere. As for the other event on 29 July 2019 (DOY 210), as I previously inferred, poleward meridional winds prevail in the winter hemisphere , which is unfavorable for Perkins instability. Under such condition, only conjugate MSTIDs with a small amplitude were observed in the winter hemisphere. The generation of this conjugate structure could be associated with the effective $\mathbf{U} \times \mathbf{B}$ background electric field in the hemisphere coupled ionosphere (Narayanan et al., 2018). Moreover, from Figures 4.13 and 4.18, I can also infer that ionospheric background conditions in the winter hemisphere can in turn affect the field-aligned current sheets associated with NW-SE aligned MSTID structure in the summer hemisphere. The correlation coefficient for perpendicular components (dB_L and dB_ϕ) in the summer hemisphere is -0.35 on 29 July 2019 (DOY 210) when ionospheric background conditions in the winter hemisphere are not favorable for Perkins instability, but improved to -0.75 on 26 December 2019 (DOY 360) when ionospheric background conditions in the winter hemisphere satisfy the conditions for Perkins instability. Similar cases were also observed by simulation in Yokoyama (2014) that even if the instability conditions are satisfied in the summer hemisphere, unfavorable F-region thermospheric winds in the winter hemisphere will largely suppress the growth of MSTIDs in both hemispheres.

Amplitude asymmetry of conjugate MSTIDs

For both events, the MSTIDs were observed more intense in the summer hemisphere. Several factors could be associated with the amplitude asymmetry of conjugate MSTIDs in different hemispheres, e.g., thermospheric wind and non-equipotential magnetic field line. Narayanan et al. (2018) found that the amplitude of conjugate MSTIDs tend to differ in different

hemispheres particularly in the later hours after their formation. Our GNSS observations on 29 July 2019 (DOY 210) further validated this conclusion, because the conjugate MSTIDs in the winter hemisphere maintain a weak development, while the amplitude difference reaches its maximum when the MSTIDs in the summer hemisphere develop to the maximum intensity after a few hours. In addition, for the event on 26 December 2019 (DOY 360) when thermospheric winds satisfy the Perkins instability in both hemispheres, this amplitude difference is more pronounced in both early and late stages of MSTID development in the winter hemisphere, often greater than 50%.

As we inferred previously in the last section, in the winter hemisphere, the meridional components of thermospheric winds are poleward on 29 July 2019 (DOY 210) and weak equatorward (compared to the summer hemisphere) on 26 December 2019 (DOY 360), respectively. Compared to the condition in the summer hemisphere, the meridional winds in the winter hemisphere will push plasma to the lower altitudes where recombination enhances, thus reducing the ambient plasma densities and the amplitude of conjugate MSTIDs (in return increasing the Pedersen conductivity). Moreover, magnetic field lines are not perfectly equipotential after MSTID formation due to the current closure in the ionosphere through field-aligned current (Yokoyama, 2014). As we discussed earlier, the Es layer in the summer hemisphere drives the conjugate MSTIDs in both hemispheres. That is to say, the mapping efficiency of polarization electric field should be higher from E in the summer hemisphere to the F region in the summer hemisphere than to the F region in the winter hemisphere (Yokoyama, 2014). In such cases, the finite mapping efficiency of an electric field from the summer hemisphere to the winter hemisphere should be considered, which is positively related to the spatial scales of irregularities and negatively related to the integrated Pedersen conductivity (Farley Jr, 1959; Yokoyama et al., 2004). Therefore, the combination effect of mapping efficiency and thermospheric wind may reduce the polarization electric field in the winter hemisphere, leading to a weakening of the amplitude of conjugate MSTIDs in the winter Hemisphere.

Further, the slower growth rate of conjugate MSTIDs in the winter hemisphere may also be caused by the weaker polarization electric field mapping from the summer hemisphere. From Figure 4.14 and 4.16, E-F coupling process in Australia (summer) started at $\sim$9:00 UT and distinct NE-SW aligned structures were observed at $\sim$10:00 UT (0.32 TECU). In the opposite hemisphere, conjugate irregularities were first observed over Japan at $\sim$11:15 UT and formed wavelike structures over this area at $\sim$13:00 UT (0.30 TECU). That is, in the winter hemisphere, the smaller F-region conductivity and effective electric field $\mathbf{U} \times \mathbf{B}$ may lead to a smaller growth rate of the coupled instability (Es-layer instability coupled to Perkins instability; as shown in Equation 2.32a. Thus, the time required for the growth of Perkins

instability in the winter hemisphere through interhemispheric coupling is longer (about one hour) than that in the summer hemisphere that is amplified through local E-F coupling.

Chapter 5

3-D Tomography for Ionospheric Irregularities

In the previous section, the 2-D structures of Es and MSTIDs have been well studied by using the double-thin-shell model and GNSS-TEC measurements. Although such results are encouraging, the missing height dimension in these 2-D analyses may pose limitations on the information that we can infer. Therefore, a continuous and broad 3-D distribution of ionospheric electron densities (IEDs) is required. However, the fidelity of most tomography techniques is biased toward the reconstructions of F region, dominant in electron density concentration of the ionosphere, and with the utmost hindrance to trans-ionospheric radio waves; the thin thickness of Es and representation errors in tomography make the 3-D reconstruction of the coupled ionosphere a challenge. That is to say, the reconstruction of Es is pivotal for the tomography of the nighttime E-F coupling. In response to this, a novel 3-D tomography method should be developed. In this chapter, the 3-D structure of daytime sporadic E was first reconstructed, and similar methods were then applied to the tomography for nighttime E-F coupling.

5.1 Computerized Ionospheric Tomography

Computerized ionospheric tomography (CIT), first proposed by Austen et al. (1988), has been used for reconstructing IED distributions in a vertical plane from a large number of irregularly sampled GNSS-TEC measurements. Since GNSS signal intersects many altitudes of the ionosphere, a 3-D representation of its structure is enabled with CIT. Usually, CIT follows the voxel-based model, which divides the 3-D ionosphere into different voxels, as shown in Figure 5.1. Ill-posedness and ill-conditionedness are some of the major challenged

due to an irregular distribution of GNSS satellites and receivers within the region of interest: some voxels are not traversed by any satellite-receiver rays, and the discrete approximation to the integral leads to IED being very sensitive to errors contaminated in TEC data. The early development and improvement of different CIT methods were made to solving these thorny problems (e.g., Raymund et al., 1990; Saito et al., 2017; Ssessanga et al., 2015). Lu et al. (2021a) and references therein have conducted a comprehensive review on the CIT development and confirmed the effectiveness of CIT in the 3-D ionosphere reconstruction.

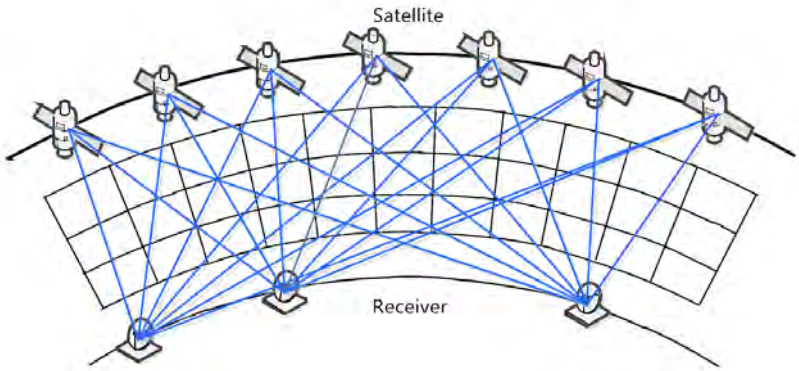

Fig. 5.1 Schematic diagram of the 3-D ionosphere under the voxel-based model.

In the voxel-based model, the 3-D regional volume to be imaged is divided into n voxels, and each voxel (j) is assumed to have an unknown uniform distribution of electron densities x_j. Then STEC (y_i) corresponding to the satellite-receiver ray signal path is represented as a finite sum over the voxels

$$y_i = \sum_{j=1}^{n} a_{ij} x_j + e_i \tag{5.1}$$

where a_{ij} is the length of the ray in intersected voxel (j), otherwise zero; e_i represents both instrumental and representative errors. For many STEC ($\vec{Y}$), Equation (5.1) is expressible in a compact matrix form as

$$\vec{Y} = \mathbf{A}\vec{X} + \vec{E} \tag{5.2}$$

Of course, the fact that $\vec{E}$ exists in Equation (5.2) and in practice due to satellite-ground receiver geometric constraints and restrictions on exposure time to avoid averaging dynamics, the number of measurements (m) is generally much less than the required number of unknowns (n). Therefore, solving Equation (5.2) necessitates a different approach than a direct matrix inversion. A rich literature exists on different methods that could be employed to obtain $\vec{X}$ that minimizes the error ($\vec{E}$). For example, the ill-conditionedness of CIT can be reduced by using algebraic method (e.g., iterative reconstruction (Austen et al., 1988), SVD (Hong et al., 2017)), statistical approach (e.g., Kalman Filtering (Scherliess et al., 2004),

Bayesian estimation (Norberg et al., 2015)) and artificial neural networks (Granat and Na, 2000) in equation solving or result estimation. Furthermore, some additional information from multiple instruments (e.g., Chartier et al., 2012; Rius et al., 1997; Ssessanga et al., 2021) and virtual data (e.g., Lu et al., 2021b; Yao et al., 2014) can also be assimilated to reduce the condition number thus mitigate the ill-posedness of CIT.

5.2 3-D Tomography for Daytime Sporadic E

Sporadic E (Es) are electron density inhomogeneities manifested in the ionospheric E region. At mid-latitude area, during the daytime, Es is suggested to occur due to reinforced metallic (of meteoric origin) ionization in altitude range ∼95–120 km (e.g., Whitehead, 1989). The details of Es were described in Section 2.3. As previously mentioned, the success of tomography for Es is crucial for the 3-D reconstruction of nighttime coupling process. In this section, a novel tomography has been developed to obtain the spatial-temporal (4-D) coverage of daytime Es to fully track the trajectory and distribution of plasma densities during the formation and occurrence of Es. The Es events during the daytime are chosen because E-region conductivity is generally high and short-circuits the polarized electric field that facilitate the E-F coupling (Kelley, 2009). In such a case,sporadic E layer in the E region is the object of most concern in the ionosphere.

5.2.1 Algorithm

There have been previous efforts to reconstruct the Es structure using GNSS. For example, Muafiry et al. (2018) used the detrended STEC and a CIT technique with continuity constraints to regularize the least-squares inverse problem and separately generated different block solutions of the 3-D structure of daytime Es over the Kanto and Kyushu Districts in Japan. In each block, the resolutions were 0.16° in the north-south direction, 0.20° in the east-west direction, and 30 km in the up-down direction. From the results, Muafiry et al. (2018) were able to deduce that Es patches lie at an altitude of ∼100 km, and the horizontal drifts corroborated earlier existing literature. Here, instead of applying ad-hoc constraints to local regional blocks, here a two-step method that adapts ionosonde and ground-based GNSS observations is used to reconstruct high-resolution 3-D maps of Es over the whole mid-latitude Japan area. First, I reconstruct a more accurate F region structure and then exploit the solution to estimate the 3-D Es structure.

Step 1: F region reconstruction

Here, to reconstruct the ionosphere, especially in the F region with a high fidelity, a multiplicative algebraic reconstruction technique (MART) from the row-action iterative scheme family is selected (Raymund et al., 1990). This is because MART is memory efficient and ensures positivity, which is mandatory for ionosphere electron densities $\vec{X}$. The high fidelity, particularly in reconstructing F region densities with MART, have already been demonstrated in Raymund et al. (1990) and Ssessanga et al. (2017). MART is implemented as

$$x_j^{k+1} = x_j^k \Big(\frac{y_i}{\langle \vec{a}_i, \vec{X}^k \rangle} \Big)^{\lambda_k a_{ij} / \|a_{ij}\|}, j = 1, 2, 3 \cdots, N \tag{5.3}$$

where $\vec{a}_i$ represents the ith row vector in matrix $\mathbf{A}$; x_j^k is the jth unknown at the kth iteration; $\langle \vec{a}_i, \vec{X}^k \rangle$ is the simulated TEC, an inner product of the ith row of $\mathbf{A}$ and a column of $\vec{X}$ values at the kth iteration; λ_k is the relaxation factor selected in range $0 < \lambda_k < 1$, set to 0.2 in this work based on Raymund et al. (1990) and Ssessanga et al. (2017).

The computational procedure in Equation (5.3) requires an initial guess ($\vec{X}_0$), which highly influences the fidelity and the rate of convergence (Das and Shukla, 2011). This is one of the weak points that MART suffers as a reconstruction algorithm. To improve fidelity, I estimate a smooth $\vec{x}_0$ from the observations (STEC), following the works of Raymund et al. (1990) and Ssessanga et al. (2017): the 3-D regional ionosphere is assumed to be spanned by a set of empirical orthogonal functions (EOFs) Φ. These are derived from an ensemble composed of the ionosphere at different epochs that are representative of the regional ionosphere under different conditions. The ensemble can be generated from an empirical model, here I used International Reference Ionosphere (IRI)-2016 model, the details of which can be found at Bilitza et al. (2017). To accurately represent F region peak densities, the International Union of Radio Science (URSI) foF2 model recommended for ocean areas, and the newly included improved hmF2 model (Satellite and Digisonde Model of the F2-Layer Height (SDMF2)) (Bilitza et al., 2017; Shubin, 2015; Shubin et al., 2013) were triggered in the IRI settings. For each epoch in one day that was analyzed, Φ was generated from an ensemble of dimension $n \times 49$, covering day time (06:00–18:00 JST), sampled at a 2-hour interval, and spanning 7 days centered on a required day. At most, Φ constituted three orthogonal functions that represented 98% of the ensemble power. From the above setting, the initial guess is represented as $\vec{X}_0 = \Phi \vec{b}$, where $\vec{b}$ is a set of coefficients to be determined. According to Equation (5.2), we can obtain

$$\vec{Y} = \mathbf{A}\Phi\vec{b} \tag{5.4}$$

and the solution to the initial guess obtained as $\vec{X}_0 = \Phi(\mathbf{A}\Phi)^{\dagger}\vec{Y}$, where $(\mathbf{A}\Phi)^{\dagger}$ denotes the pseudo inverse of $\mathbf{A}\Phi$.

Step 2: E region reconstruction

Signal rays from GNSS satellites to ground-based receivers pass through the ionospheric D, E, F regions and plasmasphere with significantly different contributions to daytime STEC. I assumed the electrons in the signal ray paths concentrate in altitude ranging from 80 to 1000 km, since the D region is generally populated with relatively weakly ionized plasma (Kelley, 2009), and the plasmasphere, particularly during the summer daytime in the northern hemisphere, varies mildly and contributes up to 10% to the ground GNSS vertical TEC in the mid-latitude area (Belehaki et al., 2004; Yizengaw et al., 2008). Therefore, the E region contribution can be deduced as $\mathrm{STEC_E} \approx \mathrm{STEC} - \mathrm{STEC_F}$. For each ray, at a specific epoch, $\mathrm{STEC_F}$ was estimated as an integral of densities along the line of sight through step-1 3-D reconstructed ionosphere covering altitudes 180–1000 km. The $\mathrm{STEC_E}$ residues are then utilized in the reconstruction of the E region structure covering 80–180 km in altitude.

Due to the relatively small thickness of the Es structure, a high vertical resolution is needed to resolve the density distribution. However, in ground-GNSS data CIT analysis, the accuracy in the vertical domain is low due to the lack of horizontal ray paths (Razin and Voosoghi, 2016). To vertically constrain the solution, I again employ EOFs, but following a different procedure from that discussed in step-1: different electron density ensembles ($Ens(t_{hr})$) were used to generate a family of subsets of EOFs(t_{hr}) assumed to span the E region 3-D space at intervals/windows (t_{hr}) of 1 hour, covering the period 06:00–18:00 JST. The $Ens(t_{hr})$ members were based on a Chapman model function (Chapman, 1931)

$$N_e = N_m * \exp\left(0.5 * \left(1 - \frac{h - h_m}{H} - \exp(-\frac{h - h_m}{H})\right)\right) \tag{5.5}$$

which I could adjust so that the Es layer mimics a thickness of $\sim$2 km as depicted in rocket (Whitehead, 1989) or GNSS radio occultation observations (Zeng and Sokolovskiy, 2010). h, H, N_m and h_m represent the height of any desired point along the profile, the scale height, Es intensity and its height location (hmEs), respectively. To compose each $Ens(t_{hr})$, N_m and h_m were assumed from Gaussian distributions with moments (mean and standard deviation) derived from manually scaled ionosonde Es observations (foEs and hmEs) covering 30 days. The threshold for Es occurrence was 5 MHz (Aarons and Whitney, 1968). Yellow triangles in Figure 5.2 show a network of four ionosondes considered in the analysis, i.e., stations at Kokubunji (35.71°N, 139.49°E), Yamagawa (31.20°N, 130.62°E), Wakkanai (45.16°N, 141.75°E), and Okinawa (26.68°N, 128.15°E). Based on the work of Ssessanga et al. (2017),

who utilized the same network of ionosondes and GNSS receivers, Kokubunji ionosonde was found to be located in the region most data points and best CIT reconstructions. Thus, because the aim is to additionally reconstruct a clear Es height variation, Kokubunji ionosonde data were used in determining the standard deviation (σ) of the h_m distributions as follows: The Es height within the interval, t_{hr}, was assumed to nearly remain stable from one day to the next (Šauli and Bourdillon, 2008). Then for each t_{hr} and ionosonde in the network, I computed a mean (μ_h) and standard deviation (σ_h), from which I derive the standard deviation of h_m Gaussian distribution for each ionosonde based on Kokubunji hmEs (h_m^{ko}) as

$$\sigma = \begin{cases} 0.5\sigma_h, & |h_m^{ko} - \mu_h| \leq 0.5\sigma_h \\ 2\sigma_h, & |h_m^{ko} - \mu_h| \geq 2\sigma_h \\ \sigma_h, & otherwise \end{cases} \tag{5.6}$$

To further emphasize the dominance of data from a region of most data points, in an $Ens(t_{hr})$ of 1000 members, the contribution from different ionosonde distributions was reduced with increasing distance away from the region of most data points: Kokubunji (40%), Yamagawa (30%), Okinawa (20%), and Wakkanai (10%). In addition, from the NICT ionosonde database, both automatic and manually scaled ionosphere parameters are accessible, but the latter with a lower time resolution (1 hour) and better accuracy. Because our study is on small-scale structures that demand a certain degree of preciseness, I selected manually scaled observations for analysis.

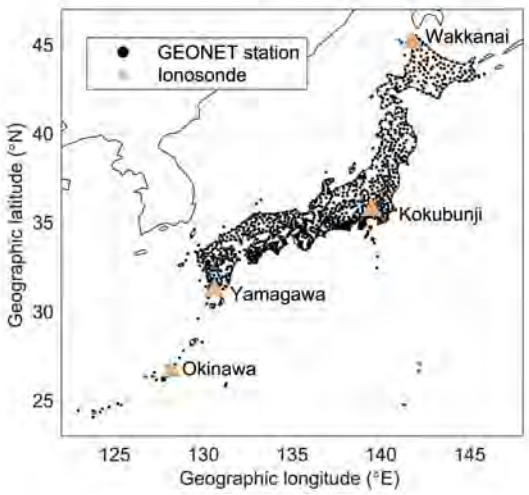

Fig. 5.2 Distributions of GEONET stations (black dots) and ionosondes (yellow triangles).

The challenge in using the Chapman function was an appropriate selection of the scale heights (H) that would reproduce the E region structure and the exact altitude of electron

density peak. Heuristically, better results were obtained when some vectors in a selected EOFs(t_{hr}) set were either emphasized or damped by a factor

$$P_i = e^{-EOF(t_{hr})_i/SF} \tag{5.7}$$

where P_i is the scale size of ith radial orthogonal basis vector in EOFs(t_{hr}) and SF is a learned scale factor. Note that I are not changing the direction of the basis vectors but rather the amplitude; this analysis is further discussed in the next section.

To reconstruct the 3-D E region structure ($\vec{X}_E^{t_e}$) at a particular epoch (t_e), I solved a system

$$\vec{Y}_E^{t_e} = \mathbf{A}_E^{t_e}\vec{X}_E^{t_e} + \vec{E}_E^{t_e} \tag{5.8a}$$

$$\vec{Y}_E^{t_e} = \mathbf{A}_E^{t_e}\mathbf{M}(t_{hr})\vec{b}_E^{t_e} + \vec{E}_E^{t_e}, \vec{X}_E^{t_e} = \mathbf{M}(t_{hr})\vec{b}_E^{t_e} \tag{5.8b}$$

$$\vec{Y}_E^{t_e} = \mathbf{C}_E^{t_e}\vec{b}_E^{t_e} + \vec{E}_E^{t_e}, \mathbf{C}_E^{t_e} = \mathbf{A}_E^{t_e}\mathbf{M}(t_{hr}) \tag{5.8c}$$

where all symbols mean the same as in step-1, with subscript E implying E region. $\mathbf{M}(t_{hr})$ is an orthogonal matrix formulated using a subset of $EOFs(t_{hr})$ representing 98% of the variation in $Ens(t_{hr})$, and t_{hr} is the time interval that includes t_e. $\vec{b}_E^{t_e}$ are coefficients to be determined that define different optimal combinations of radial EOFs at each horizontal grid point.

To adequately solve Equation (5.8), the SVD method was selected because of its numerically stable properties (Fan and Ma, 2014). The major disadvantage of SVD is the high computation cost; however, because the problem is transformed into EOF space, and the reconstructions are limited to the E region, the dimensionality of the problem is significantly reduced to a desktop CPU manageable setting. The details of solving matrix equations using SVD were described in Equations (3.6)–(3.8) in Section 3.2. Therefore, If matrix $\mathbf{C}_E^{t_e}$ is of dimension p by q, through SVD decomposition I can obtain:

$$\mathbf{C}_E^{t_e} = \mathbf{U}\mathbf{D}\mathbf{V}^T \tag{5.9}$$

From Equation (5.8), the final solution can be obtained as

$$\vec{X}_E^{t_e} \approx \mathbf{M}(t_{hr})\mathbf{V}_r\mathbf{D}_r^{-1}\mathbf{U}_r^T\vec{Y}_E^{t_e} \tag{5.10}$$

5.2.2 Validation

The 3-D region to be analyzed covered 24°N–46°N in latitude, 122°E–146°E in longitude, 80 to 1000 km in altitude. In step-1 (step-2), the total number of voxels were 24288

(330000), with the resolution set to 1° (0.4°) in horizontal and 20 km (1 km) in altitude. To avoid reconstructions of highly irregular plasma fluctuations due to geomagnetic storms, particularly in the F region, analysis data were filtered to only include days when the absolute values of the Dst index were less than 30 nT (Ma et al., 2014). Under such smooth conditions, during daytime at midlatitudes, a well-developed and highly conducting E region limits polarization electric fields that could facilitate the E-F coupling (Kelley, 2009). Therefore, to avoid sharp transitions, from a high resolution (1 km) E region to a coarse (20 km) F region, I assumed that E and F regions are separable under different implicit periods of stationarity; 15 min and 1.5 min in step-1 and step-2, respectively. This setup reduced the size of the inverse problems to a Desktop manageable setting with 8 gigabytes of memory. Indeed, the reducing size of systems improved the condition number/stability and the convergence of the iterative procedure to within 7 minutes.

Validation in step 1

Before reconstructions with observational data, I performed a simulation to analyze challenges in reproducing a consistent picture of the F region if enhanced prolate density-like structures existed in the E region. Similar to the results obtained in Ssessanga (2018), the reconstructions were modest, but when a large percentage of the utilized rays traversed the prolate structures, the MART algorithm subtly reconstructed the E-region features in the F-region. Kunitsyn and Tereshchenko (2003) also detected this under-performance by MART. The authors found that if features are in a region of low density (E-region), MART tended to reconstruct them toward areas of high concentration, around hmF2 point. Therefore, to mitigate the F-region contamination, data ($\vec{Y}$) in Equations (5.3)–(5.4) were filtered to remove rays that traversed sizable Es structures: the rate of TEC index (ROTI<0.1) (Mungufeni et al., 2021), defined as the standard deviation of the change rate of TEC, was used in filtering process (Pi et al., 1997):

$$\mathrm{ROT} = \frac{\mathrm{STEC}(i) - \mathrm{STEC}(i-1)}{\mathrm{T}(i) - \mathrm{T}(i-1)} \tag{5.11a}$$

$$\mathrm{ROTI} = \sqrt{< \mathrm{ROT}^2 > - < \mathrm{ROT} >^2} \tag{5.11b}$$

where T and i represent time (unit of minute) and ith epoch, respectively; $< \cdot >$ denotes the expectation within a certain time interval (usually 5 minutes).

Figure 5.3a illustrates an example of synchronous changes in GNSS STEC and ROTI on 21 May, 2010 (DOY 141). Fortunately, during this event, the satellite (Sat) in view, GPS PRN 29, crossed the Kokubunji ionosonde station location, a yellow triangle in Figure 5.3b. The

solid black line is Sat 29 ground trace, and the black dot represents the ionospheric pierce point (IPP) at 17:15 JST. The synchronous pulse-like changes in STEC and ROTI in Figure 5.3a, are observed to occur at the same epoch, 17:15 JST, when a clear Es layer at altitude ∼106 km is recorded in ionosonde observations in Figure 5.3c. Therefore, changes in ROTI can be a filter or detection for plasma inhomogeneities. Finally, to reduce computational cost and avoid redundancy as in Saito et al. (2017), only data from 280 stations were selected for calculation in step-1.

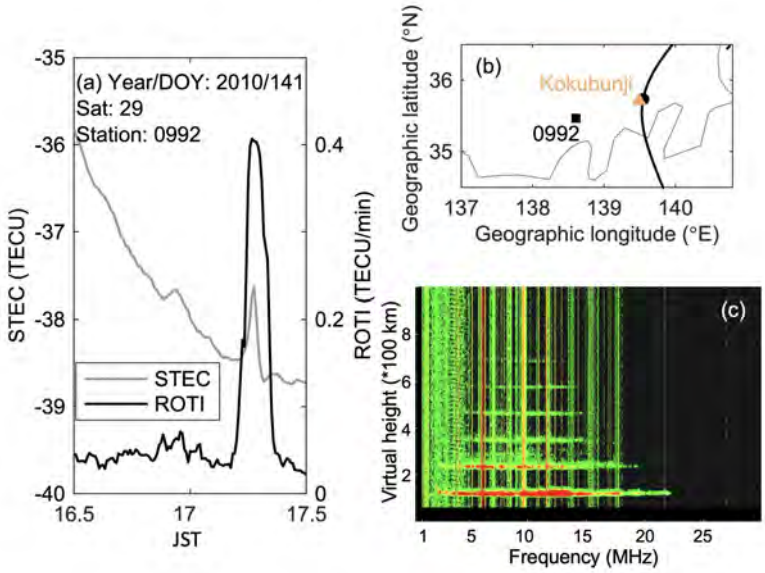

Fig. 5.3 Observations from GNSS and ionosonde near Kokubunji area, where the Es signature happens around 17:15 JST, 21 May, 2010 (DOY 141). (a) Time series of STEC anomalies (gray) and ROTI (black). (b) Trajectories of IPPs at 106 km from station 0992 to Satellite (Sat) 29 passing through the Kokubunji ionosonde (yellow triangle), where the black square and dot represent the location of 0992 receiver and IPP at 17:15 JST, respectively. (c) The 17:15 JST ionogram at Kokubunji, where the highest foEs observed is ∼20 MHz.

In Figure 5.4, a control dataset from more than 100 GEONET receivers is used to assess the accuracy of the reconstructed results. The subplots represent IRI model (a), initial guess using EOFs (b) and MART solution (c), respectively. The three sets of results show improvement in each step (a-c), hence satisfying the requirement for MART quick convergence and good fidelity as discussed in subsection 5.2.1. To evaluate the effectiveness and reliability, metrics of mean absolute error (MAE) and root mean square error (RMSE) are introduced to specify the degree of dispersion of the sampling error (Xiong et al., 2021),

which are computed as follows:

$$MAE = \frac{1}{N}\sum_{i=1}^{N}|y_r - y_o| \tag{5.12}$$

$$RMSE = \sqrt{\frac{1}{N}\sum_{i=1}^{N}(y_r - y_o)^2} \tag{5.13}$$

where N is the amount of the reconstructed values, y_r and y_o are the reconstructed and observation values, respectively. The unit of MAE and RMSE is TECU.

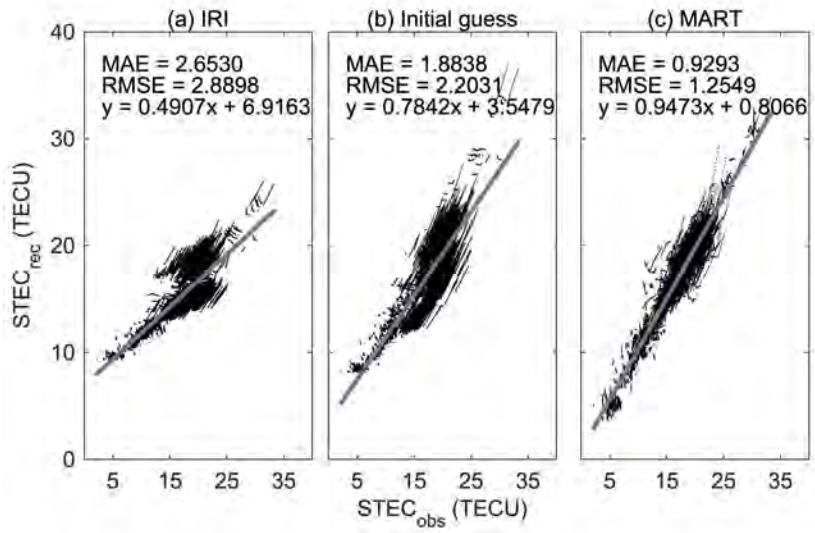

Fig. 5.4 A Scatter of observation and estimates of STEC values during 17:22–17:37 JST, on 21 May, 2010 (DOY 141). Subplots (a–c) represent IRI-2016, initial guess using EOFs and MART, respectively. The least-squares regression lines are in blue, with horizontal as x and vertical y. MART results fit the observations best.

Obvious discrepancy between reconstruction and observation can be observed when the ionosphere is generated by IRI model, where the MAE and RMSE are 2.65 and 2.89 TECU, respectively. After introducing EOFs, the MAE and RMSE decrease to 1.88 and 2.20 TECU. The fitted line gradient improves from 0.49 to 0.78; the higher correlation between reconstruction and observation suggests a confident initial guess was estimated from GNSS observations with EOFs. By applying MART, results converged to minimize the errors, where the MAE and RMSE are 0.93 and 1.25 TECU , respectively. The gradient of the fitted line has been improved to 0.95, which suggests the reconstructed STEC are in good agreement

with the observed STEC. This good consistency indicates the ionosphere is reconstructed with fidelity.

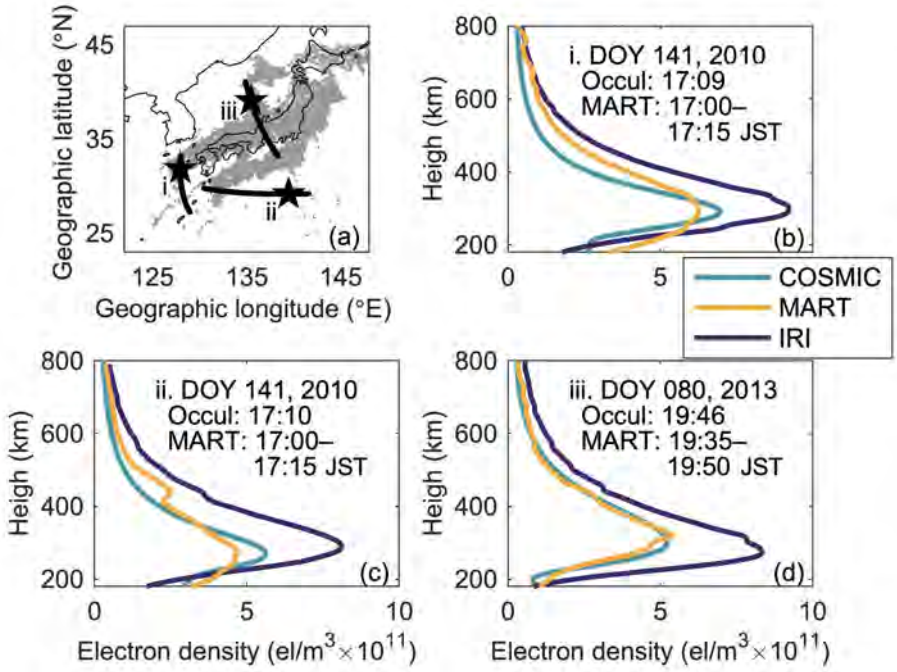

Fig. 5.5 (a) Black solid lines are traces of COSMIC occultation tangent points, black stars are locations of maximum electron density along each trace, and gray dots represent the distribution of ionospheric pierce point (IPP) at 17:10 JST on 21 May, 2010 (DOY 141), at 350 km altitude. (b–d) Comparison of COSMIC constellation vertical electron density profiles (green) with IRI model (purple) and tomography (yellow).

In Figure 5.5, COSMIC constellation electron density vertical profiles are compared to the IRI model and reconstructed results (obtained as a solution to Equation (5.2), while using MART and a calibrated initial guess). Although RO data distribution is globally good, events that locally consistently cover a particular region are difficult to find. Thus, after an exhaustive data search, the presented three RO events fit our analysis best. The comparison is along the geographic locations of the occultation tangent points, shown as solid black lines labeled i, ii, and iii, in Figure 5.5a. Black stars are geographic locations of the maximum electron density along each profile trace. During analysis, the reconstructed ionosphere was assumed stationary for 15 min, with the center point as the epoch to the maximum electron density points. Gray dots show an example of the distribution of GNSS rays IPPs at the 350 km altitude (epoch is 17:10 JST, 21 May, 2010 (DOY 141)). Figures 5.5(b–d) are density profiles corresponding to each trace in Figure 5.5a. The vertical scale limited is to altitudes 180–800 km, where occultation profiles have good accuracy. Compared to the IRI model, the

reconstructed profiles (mainly hmF2 and NmF2) correlate better with the occultation densities, specifically over central Japan with the densest IPP distribution(refer to trace (iii) and Figure 5.5(d)). Outside central Japan, see traces (i) and (ii) and the respective corresponding profiles in Figures 5.5b and 5.5c, deviations between COSMIC and reconstruction maximum electron density are more pronounced consequent to the sparse IPP distribution. Nonetheless, the reconstructions were on average $\sim$30% more accurate than IRI electron density estimation.

Validation in step 2

Analogous to step-1, I carried out a simulation analysis to assess the validity of our reconstructions in the E region. Kokubunji ionosonde observation at 17:30 JST on 21 May, 2010 (DOY 141) were used as a reference in the Es simulation, with Equation (5.5) as the model function. Outside the Es domain, electron densities were computed from the IRI-2016 model. The intensity of Es patchy layers was set to 5×10^{12} el/m^3 (foEs$\approx$20 MHz), at altitude 106 km, with the longest strip stretching $\sim8^\circ$ in East-West (E-W) and 0.4° in North-South (N-S). Figure 5.7a shows the simulated Es strips. Note that the strips are intentionally put at different latitudes to assess the fidelity across the map. The synthetic STEC for analysis were then generated as an integral of electron densities along the ray paths determined from the observation geometry of GNSS satellites and more than 1200 receiver stations from the GEONET. Black dots in Figure 5.7b show the distribution of the GNSS rays IPPs at the Es height of 106 km, corresponding to the synthetic STEC data points.

Before discussing the 3-D simulation results, I use this simulation and revisit the discussion in subsection 5.2.1 to elaborate on the significance of scaling EOFs, as illustrated in Figure 5.6. Although the 98% representation of the original ensemble was constituted by 10 EOFs, for clarity, I have presented only the first three EOFs representing 43.42%, 21.72%, and 12.21% of the ensemble variations. Subplots (a–c) show the modification in the amplitude of EOFs as SF is varied. In the lower plate: the far left subplot (d) illustrates different scale size decay rates (using different SFs) as a function of position ("importance") of an EOF vector in the selected EOF subset. Still, in the lower plate, the three subplots (e–g) showcase an example of the input (dashed gray line) and reconstructed (solid black line) Es layer with largest amplitude using different SFs. Before any scaling (SF=0), the reconstructed profile has multiple peaks artefact. As the SF increasingly varied, the artefact disappears and then slowly reappears when the SF$>$5; most probably due to the combined EOFs vectors nearly representing the same space as EOFs at SF=0. For this analysis, SF=2 was considered the best option: the artefacts are no more, and the profile thickness and height are in good agreement with the input, although I had to trade off some accuracy of the underperformance

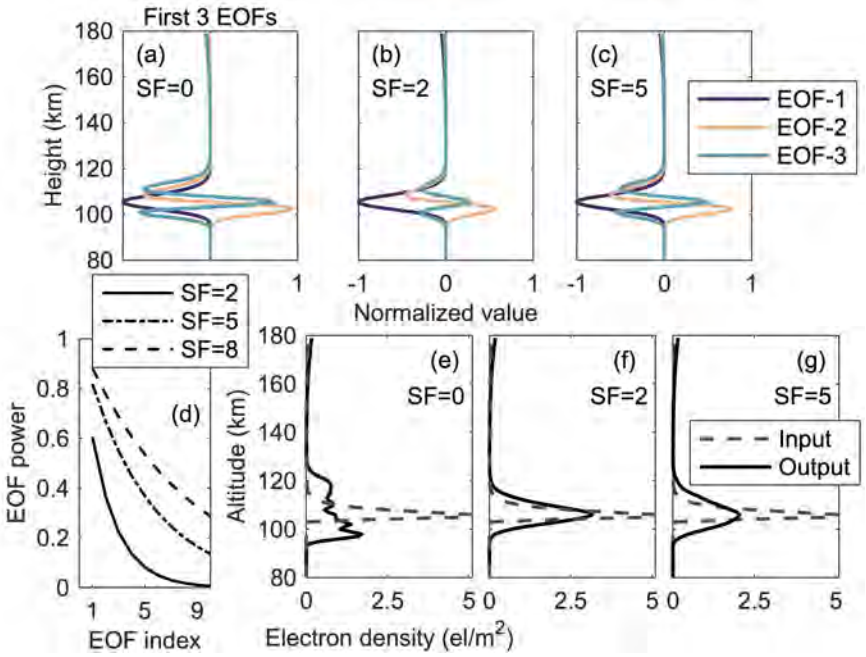

Fig. 5.6 (a–c): The largest three EOFs modified using different scale factors (SFs) at 17:30 JST on 21 May, 2010 (DOY 141). (d) The decay rate of EOF scale size as function EOF position in the EOF subset. (e–g): Reconstructions of the simulated Es structures with largest amplitude, while considering different SFs.

in amplitude estimation. Subsequent to this analysis, all Es reconstructions henceforth are obtained with a scaling of SF=2.

Back to the 3-D simulation reconstructions in Figure 5.7, the minimum boundary conditions and GNSS-receiver geometry constraints limit observations at areas such as Hokkaido (>40°N) and Kyushu (<32°N). Indeed, the strip structures at ∼32°N and ∼40°N are reconstructed with shorter lengths. As expected, the area bound 33°N–40°N and 131°E–141°E with dense IPPs distribution exhibits the best fidelity. The structures with a separation of ∼1° in N-S are distinctively reconstructed. In the radial dimension, the reconstructed electron densities, shown in subplot (d), are well distributed between 100–110 km, and the peak is consistent with the input hmEs of ∼106 km.

5.2.3 Reconstruction Results

In what follows, I shall now use the developed technique to analyze the morphology of Es during different events in 2007, 2010, and 2020. The same event on 21 May, 2010 (DOY 141) was studied by Maeda and Heki (2014), thus our reconstructions can further be validate by comparing their results. The focus is on the region of high fidelity as elaborated in the

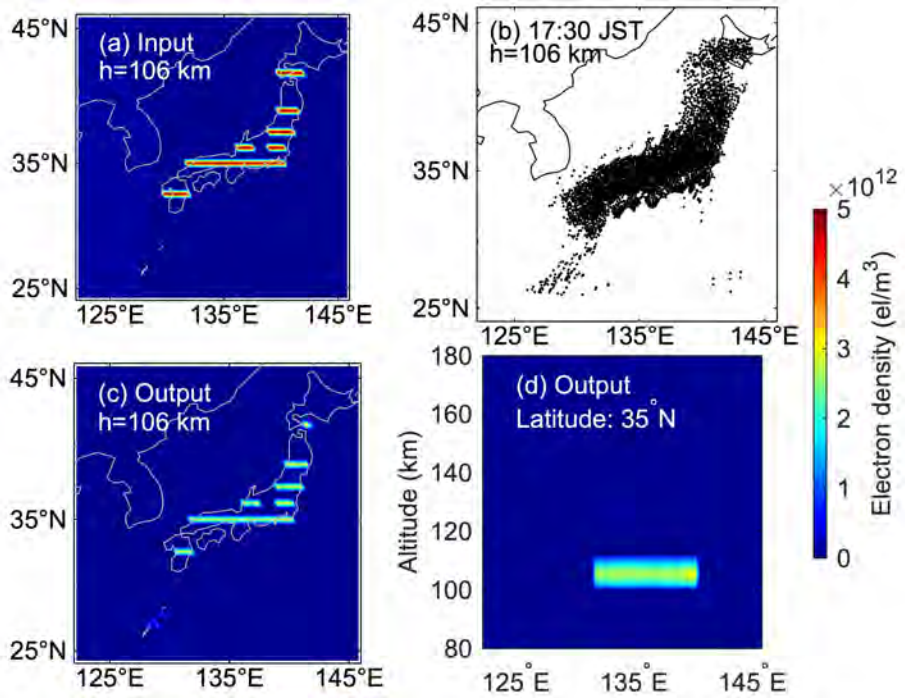

Fig. 5.7 (a) 2-D map of input irregularities at 106 km; (b) Distribution of IPPs at 17:30 JST on 21 May, 2010 (DOY 141), at 106 km; (c) 2-D map of the reconstruction at 106 km; (d) Vertical structure of reconstructed electron densities at ∼35°N. The best reconstruction is around central Japan.

simulation analysis. To ensure that our reconstructions were mainly due to Es variations and reduce the computation cost, the data utilized for E-region reconstruction hereafter were filtered to only include STECs with ROTI≥0.1; refer to Figure 5.3.

Event on 21 May, 2010 (DOY 141)

The 2-D ROTI maps at 100-km altitude for event on 21 May, 2010 (DOY 141) is shown in Figure 5.8. An distinct E-W aligned frontal structure was observed propagating southwestward.

As a measure of accuracy, in Figure 5.9, I have reconstructed the Es structures detected by the Kokubunji ionosonde on 21 May, 2010 (DOY 141). The upper left subplot (a) shows a horizontal 2-D slice at altitude 106 km, epoch 17:30 JST when Es was intense in horizontal scale. The yellow triangle represents the location of Kokubunji ionosonde. The horizontal frontal structure is elongated in E-W, expanding over several hundred kilometers, which agrees with the results in Maeda and Heki (2014). The right upper plot (b) is a vertical slice through the Es structure at 36°N, which indicates the electron density anomalies are concentrated at around 106 km altitude, and do not appear in other layers that are outside the

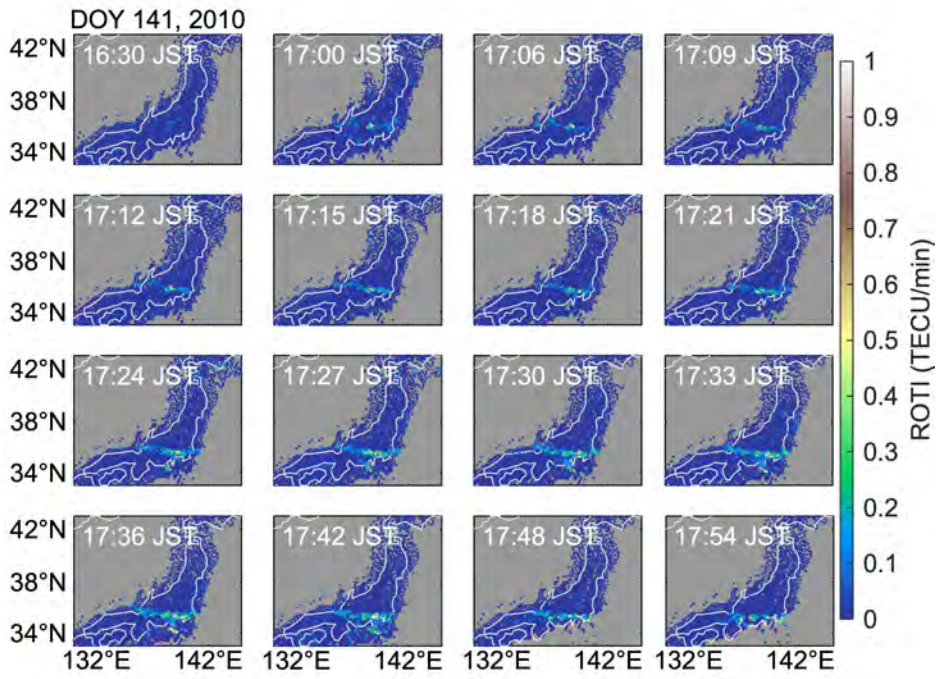

Fig. 5.8 The 2-D ROTI maps at 100 km altitude, during 16:30–17:54 JST, on 21 May, 2010 (DOY 141).

Es height range. In the lower subplot (c), reconstructed E region vertical electron density profiles with maximum Es intensity at the Kokubunji area (35.2°N–36.4°N, 138.8°E–140.0°E) are combined at a resolution of 3 minutes to form a time series image covering 16:30 to 18:00 JST. Yellow triangles indicate the Kokubunji ionosonde hmEs, ought to have remained constant for the entire duration, at ∼106 km, as reflected by the white dashed line from reconstruction results. An intensified Es is eminent through this period. Based on the equation foEs $= \sqrt{80.6 * \mathrm{NmEs}}$ (Haldoupis, 2019), at around 17:15 JST, the reconstructed foEs (14.29 MHz) is about 6 MHz smaller than ionosonde observations (∼20 MHz) as shown in Figure 5.3c. This was expected given the results in the simulation analysis (see SF=2 lower-middle subplot in Figure 5.6). Nonetheless, the reconstructions are still sufficient to draw significant physical underpinnings about Es.

Figures 5.10 shows 2-D horizontal electron density distribution maps obtained by 3-D tomography during 16:30–18:00 JST, on 21 May, 2010 (DOY 141). The slices are at altitudes of maximum Es within the grid. The time resolution for the two middle rows is higher to showcase the Es horizontal evolution. White and gray arrows show the drift and expansion directions of the Es structure, respectively. In the horizontal dimension, the reconstructed Es layers in Figure 5.10 agree well with the Es in ROTI maps in Figure 5.8. Es patches start appearing at ∼17:00 JST, and the frontal structure becomes obvious at ∼17:20 JST in

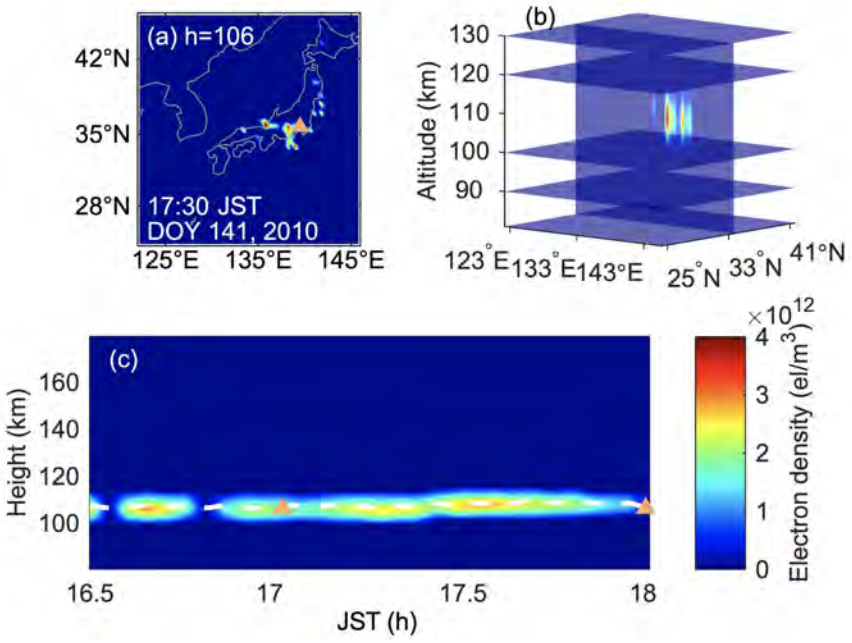

Fig. 5.9 (a) 2-D tomography results at 106 km at 17:30 JST on 21 May, 2010 (DOY 141), yellow triangle represents the location of Kokubunji ionosonde. (b) The vertical slice through the reconstructed structure of reconstruction, at 36°N. (c) Time variation of the vertical structure at Kokubunji area. Yellow triangles and the white dashed line represent the hmEs from Kokubunji ionosonde and reconstructions, respectively.

central Japan (∼35°N), with a distinct alignment in E-W. At around 17:24 JST, on the south side of the main structure, a northwest-southeast (NW-SE) aligned sub-structure starts to accumulate. The different alignment direction and morphology may be related to the internal perturbations, where the velocity and density of each patch are not homogeneous. Of course, the accuracy of STEC and spatial resolution in this analysis are not sufficient to resolve such density inhomogeneity. However, Sun et al. (2020) have analyzed the high Doppler spectral width of the radar echoes in Es, which indicated severe perturbation inside the layer. The band-like main structure reach maximum in scale at ∼17:30 JST, which can be extended to ∼400 km in E-W. Es structures start to dissipate after around 17:42 JST, the lifetime of this strong Es with foEs exceeding 20 MHz can reach approximately 30 minutes, I calculated the approximate speed of the Es peak every 20 min and found the Es patches on the east side to have an eastward velocity of ∼60 m/s, which corroborates the 2-D TEC map analyses of the same event by Maeda and Heki (2014). During this period, the frontal Es structure has an obvious southwestward migration, with a mean speed of ∼75 m/s.

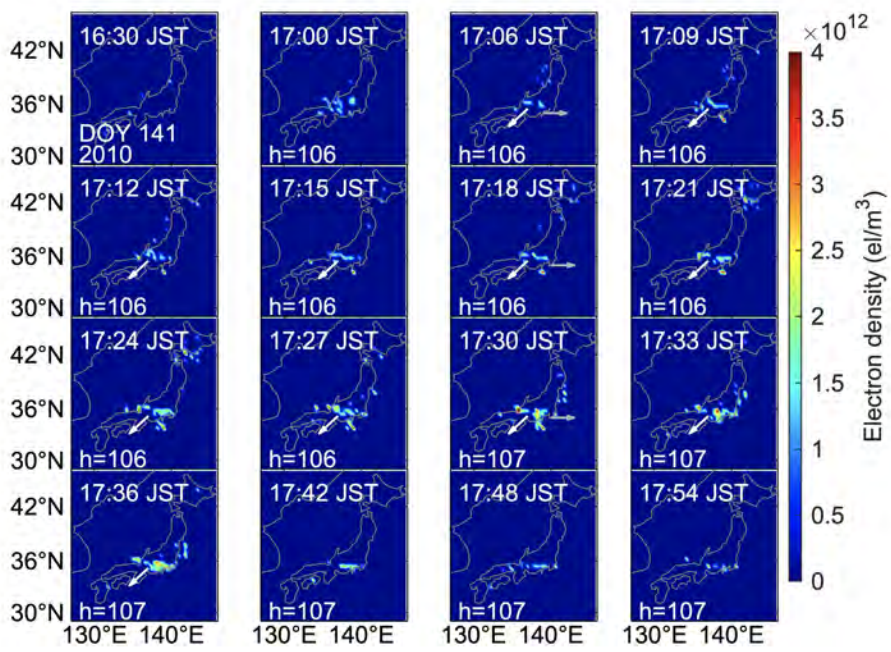

Fig. 5.10 Snapshots of electron density anomaly maps at the height of maximum Es, at various time epochs from 16:30 to 18:00 JST on 21 May, 2010 (DOY 141). White and gray arrows indicate the Es drift and expansion direction, respectively. In the two middle rows, when Es was profound, the time resolution is increased to 3 minutes to adequately capture the time evolution of plasma.

Event on 14 May, 2020 (DOY 135)

The 2-D ROTI maps at 100-km altitude for event on 14 May, 2020 (DOY 135) is shown in Figure 5.11. Two parallel NE-SW aligned frontal structure were observed propagating southwestward.

The reconstructed horizontal electron density distribution maps of daytime Es event from tomography during 16:30–18:00 JST, on 14 May, 2020 (DOY 135) are shown in Figure 5.12. The reconstructed Es layers in the horizontal dimension in Figure 5.12 have a good consistency with the Es in ROTI maps in Figure 5.11. Different from the event in Figure 5.10, Es patches appear enhanced near 39°N just after 16:30 JST, elongated in weak northeast-southwest (NE-SW), and more intense. At 16:45 JST, a frontal structure aligned in E-W and stretching $\sim$150 km is eminent. At $\sim$17:15 JST, two parallel frontal structures aligned in NE-SW with a separation of $\sim 1^{\circ}$ are formed, as confirmed by the ROTI distribution in the upper right subplot. The white dashed lines indicate the azimuth of the Es frontal structure alignment. Similar cases with two individual Es bands were also reported in Sun et al. (2020), which could be generated sequentially by the continuously modulated wind shear system

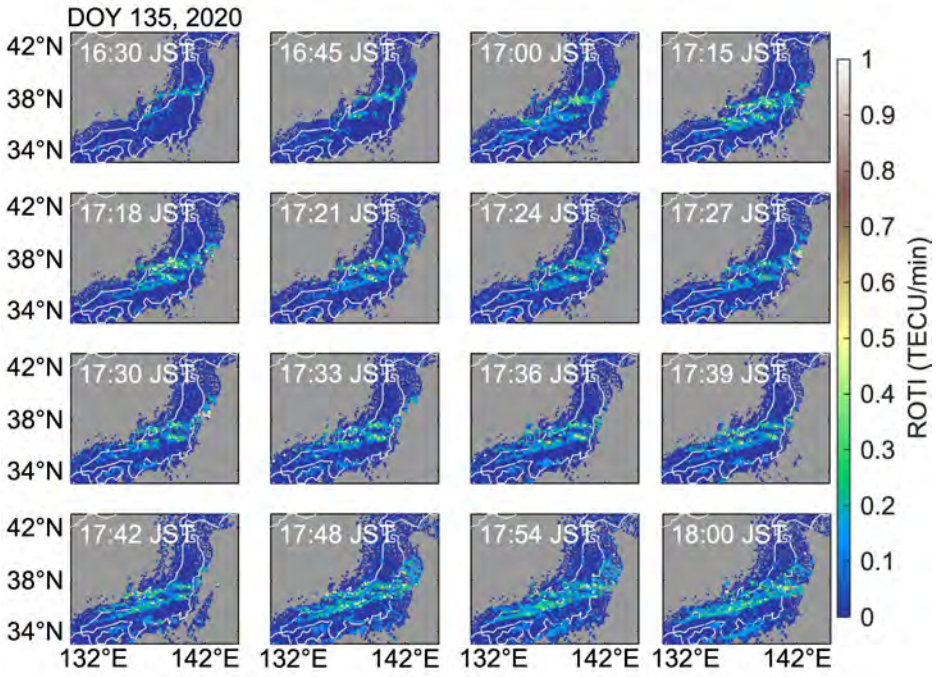

Fig. 5.11 The 2-D ROTI maps at 100 km altitude, during 16:30–18:00 JST, on 14 May, 2020 (DOY 135).

(Sun et al., 2021). From 17:00 to 17:30 JST, these two frontal structures have the same southwestward migration, with a mean speed of ∼70 m/s. After 17:30 JST, the Es speed increased to ∼100 m/s, and the motion component in the west direction became increasingly dominant. The Es peak density is located at an altitude of ∼104 km in the beginning and then decreases to ∼102 km, which agrees with hmEs observed from Kokubunji ionosonde (102 km) at 17:00 JST. For this event, the Es structure can be elongated roughly 600 km in E-W direction.

Event on 31 May, 2007 (DOY 151)

The 2-D ROTI maps at 100-km altitude for event on 31 May, 2007 (DOY 151) is shown in Figure 5.13. A weak E-W aligned frontal structure was observed propagating nearly westward.

Figure 5.14 shows slices of 2-D horizontal Es reconstructions at Es peak altitudes from tomography reconstruction. The yellow triangles represent the location of Kokubunji ionosonde. Still, in the horizontal dimension, the reconstructed Es from tomography in Figure 5.14 show good consistency with the Es layers indicated by ROTI in Figure 5.13. In the central Japan, obvious frontal structures of Es aligned in E-W occur after sunrise from

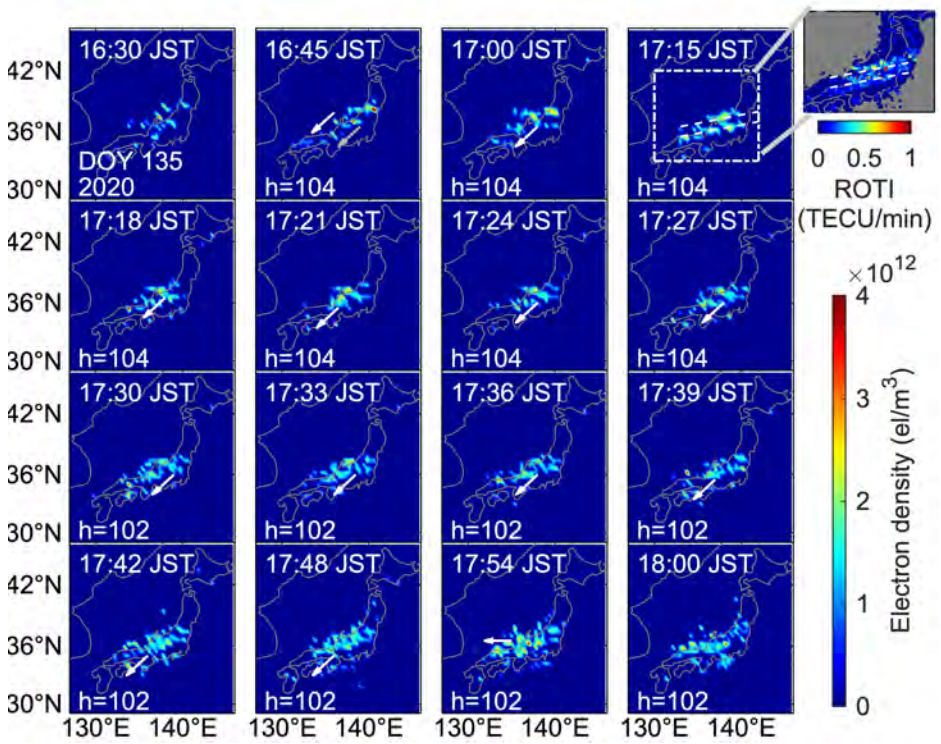

Fig. 5.12 Same as Figure 5.10 but for 14 May, 2020 (DOY 135). The subplot in the upper right corner shows the ROTI distribution in the selected area (within the white dot-dashed lines) at 17:15 JST, where the white dashed lines indicate the azimuth of the Es frontal structure alignment.

∼07:30 to 11:00 JST. In this period, the horizontal scale of Es frontal structure can reach 400 km in E-W. At 08:00 JST, when Es structure shows high intensity, the main Es structure is aligned E-W and spanning over hundreds of kilometers, but the fine constituents of this patch seem to have a strong preference of alignment in the NE-SW direction. This is the first result that clearly shows the morphology of structures that form such larger E-W structures, and future investigation of this phenomenon is vital to infer information on the formation and mechanisms of large Es patches.

Based on Figure 5.10, 5.12 and 5.14, also observed is the main azimuth drift in the northwest (morning) and southwest (afternoon) directions, which are consistent with the conclusions from observations in Maeda and Heki (2015) and simulations in Tsunoda et al. (2004). During this event, from the upper-atmospheric wind data recorded by the MUR (located at 34.9°N, 136.1°E; data accessible at http://www.rish.kyoto-u.ac.jp/mu/meteor/) as shown in Figure 5.15, the directions of reconstructed Es and neutral winds at altitudes ∼100 km are generally consistent (e.g., westward in the zonal direction). Therefore, the

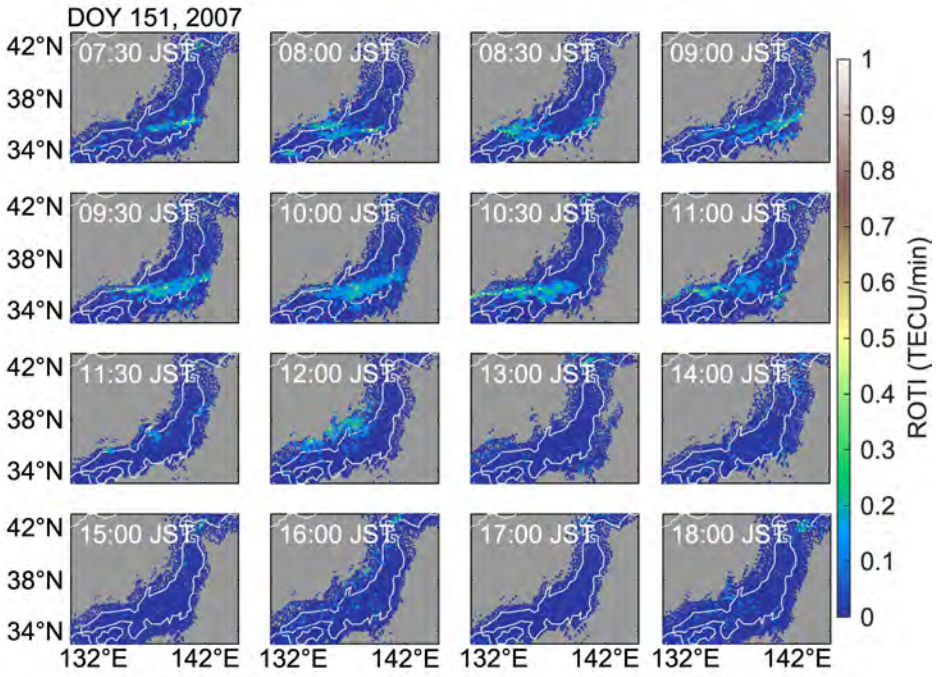

Fig. 5.13 The 2-D ROTI maps at 100 km altitude, during 07:30–18:00 JST, 31 May, 2007 (DOY 151).

background-neutral wind could be a dominant factor in the dynamics of observed strong Es structures.

To manifest the variation of hmEs and foEs at Kokubunji area, in Figure 5.16, vertical electron density profiles with maximum Es intensity from reconstructions in this region were used to generate the time-series image at a resolution of 6 min. White dashed lines show the reconstructed Es layer variation with time. The length of the error bars is hmEs standard deviation used in generating the ensemble from which EOFs applied to a particular time window are computed. To vividly assess the accuracy of the height undulance reproduced in the reconstructions, hmEs (solid yellow triangles) obtained from the Kokubunji ionosonde station are included in the plot. At a height range ∼95–110 km, during ∼07:15–11:15 JST, a frontal Es structure develops. The Es layer of sizable amplitude appears between 08:00–09:15 JST, which is consistent with the foEs variation observed by Kokubunji ionosonde. From 7:00 to 11:00 JST, the reconstructed Es-layer is observed to descend in altitude, which can be attributed to the semi-diurnal and diurnal tides (Haldoupis et al., 2006; Mathews, 1998). Hence, atmospheric tidal winds might be an influential factor in the formation and dynamics of daytime mid-latitude sporadic E.

The merits of the newly developed technique are apparent in tracking the radial-time variation of the Es structure, indicated as a white dashed line in Figure 5.16. Comparison

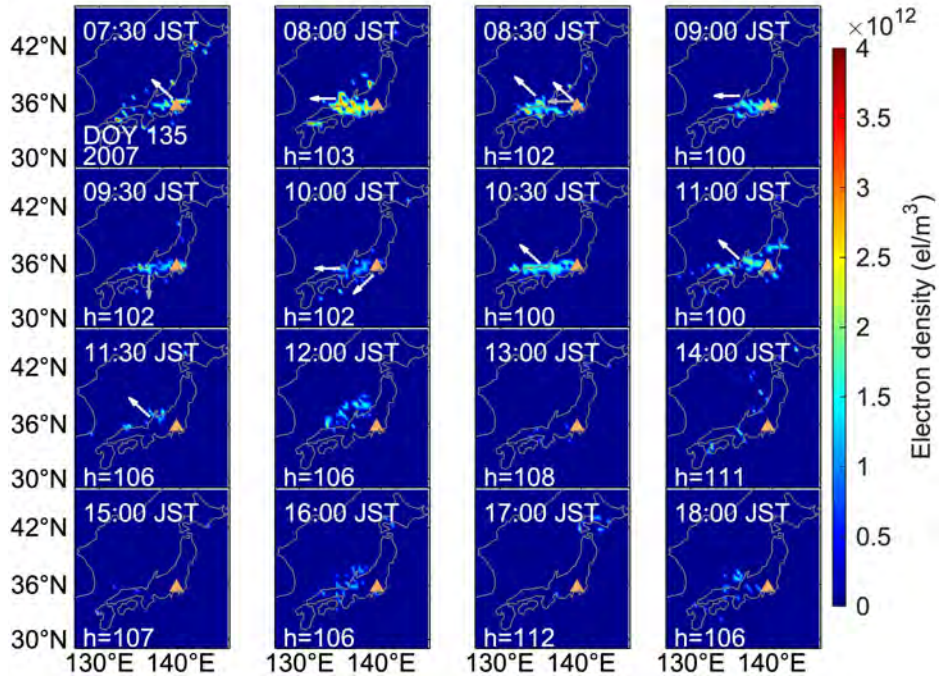

Fig. 5.14 Snapshots of electron density anomaly maps at the height of maximum Es, at various time epochs from 07:30 to 18:00 JST on 31 May, 2007 (DOY 151). White and gray arrows indicate the Es drift and expansion direction, respectively. Yellow triangle indicates location of Kokubunji ionosonde.

of the reconstructed curve and observed hmEs indicates that our technique can capture the relative time-vertical motion of the Es layer, with a mean error of ∼4 km; The ensembles in generating EOF subsets may not fully capture some erratic Es inhomogeneities, for example, when hmEs approaches or exceeds 120 km at 14:00–15:00 JST. There is no literature can be found relating to the use of ground-based GNSS data and CIT to monitor one consistent picture of both the vertical and horizontal distribution of electron density inhomogeneities in the E region. Therefore, to further expound on the complex subject of Es morphology, reconstructions from the current technique can complement other Es observational techniques that might be precise but expensive to run or limited on a spatial and temporal scale. Additionally, the relatively fast computation speed of approximately 7 min on a desktop setting encourages the extension of the developed tomography method into a near real-time 3-D Es now-cast application for industry that utilize trans-ionospheric radio signals.

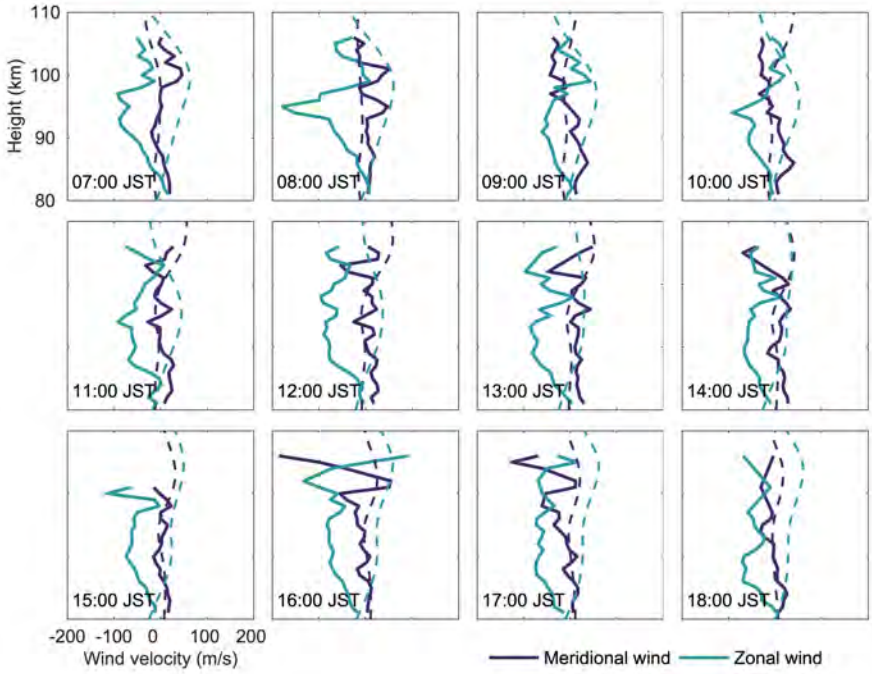

Fig. 5.15 Wind observation from MUR (solid lines) and HWM14 (dashed lines) on 31 May, 2007 (DOY 151).

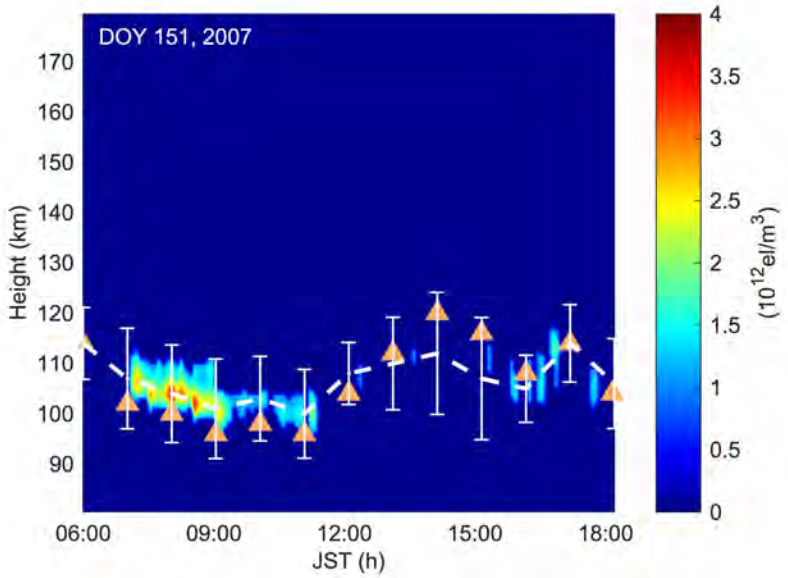

Fig. 5.16 The vertical electron densities at Kokubunji area on 31 May, 2007 (DOY 151). Yellow triangles represent hmEs observed by ionosonde at Kokubunji, white dashed lines show the reconstructed Es layer variation with time, and the length of the error bars indicate standard deviation corresponding to the ensemble used in generating the EOFs applied for a particular epoch.

5.3 3-D Tomography for Nighttime E-F Coupling

The 3-D tomography for nighttime coupled ionosphere is important to the understanding of this intricate E-F coupling process. By using GNSS measurements, Maeda and Heki (2014) have obtained the 2-D maps of daytime Es; Ssessanga et al. (2015) and Ssessanga et al. (2017) have reconstructed the 3-D structures of F-region MSTIDs. In Chapter 3 and 4, I extended the attempt at a more challenging E- and F-region reconstruction at nighttime in 2-D format. In Section 5.2, I successfully reconstructed the daytime Es layer, which had proved difficult to reproduce in earlier tempts at 3-D Es reconstructions. These promising results motivated the attempt of the 3-D tomography for nighttime E-F coupling. Different from the tomography method for daytime Es in Section 5.2:

1. Two different sets of time-dependent EOFs are used to constrain the E- and F-region solutions simultaneously.

2. TEC perturbation components rather than absolute TEC values are used in this research, since Es are thin layers and can be easily shadowed by F-region MSTIDs.

5.3.1 Algorithm

The data used in this research are as in Section 5.2, but the CIT method in this section has several modifications. The region to be analyzed covered 28°N–46°N in latitude and 128°E–146°E in longitude. The plasma density perturbations were assumed to be caused by Es and MSTIDs mainly occur at altitudes of 80–500 km (Haldoupis, 2012; Yang et al., 2015). To balance high spatial resolution and heavy calculation burden, the horizontal and vertical resolutions were set to 0.4° and 5 km respectively, thus the total number of voxels were 170,100 which is manageable on a Desktop setting with 16 gigabytes of memory. The electron density perturbations were assumed stationary for 1 minute, such that the total number of observations during this period is about 10,000 (Saito et al., 1998a).

In CIT analysis, the small-scale irregularities, especially the thin Es layers ($\sim$2 km thickness (Maeda and Heki, 2014)), make the height determination in high-resolution 3-D imaging with ground GNSS-TEC a thorny problem. In response to this, similar with Section 5.2, I again assumed the 3-D ionosphere is spanned by different EOFs (Φ), derived from an electron density ensemble based on ionosonde observations. To constrain the solutions in both E and F regions, two sets of EOFs (Φ_e and Φ_f) were generated separately. For a specific epoch (t_e) in one day, $\Phi(t_{hr})$ (the collection of $\Phi_e(t_{hr})$ and $\Phi_f(t_{hr})$ was generated from an ensemble ($Ens(t_{hr})$) sampled at a time window (t_{hr}) of 3 hours and spanning 90 days centered on a required epoch (t_e) and day. Since Kokubunji ionosonde is located within the

region of most GNSS data points and TECPs rather than absolute TECs were ingested in this study, the amplitude parameters (foEs and foF2) used for generating reference profile were the average values of the manually scale parameters from Kokubunji ionosonde at the particular epoch (t_e) covering 90 days. In addition, from this Kokubunji ionosonde database, we computed the standard deviation (σ_h^{ko}) of hmEs and hmF2 to help clearly reconstruct the height variation of Es and MSTIDs. To avoid large errors, hmEs and hmF2 observed from four ionosondes outside $h_i^{ko} \pm 2\sigma_{hi}^{ko}$ ($i = e, f$ for hmEs and hmF2, h^{ko} is the height parameter provided by Kokubunji ionosonde at t_e) were excluded. Similarly, observation profiles and reference profiles were generated from the Chapman model as in Equation (5.5) (Chapman, 1931), wherein the scale heights of E and F regions were set to 1 and 10 km respectively to mimic the thickness of Es and MSTID structures. The ensemble members (perturbed IED profiles) were then generated according to the differences between the observation and reference profiles. The perturbation profile becomes zero if its peak electron density is equal to or less than the reference threshold. Therefore, the perturbed ionosphere can be assumed to be spanned by a set of EOFs Φ^p, which consists of Φ_e^p and Φ_f^p.

In this calculation, the scale factor (SF) was also introduced to reproduce the exact altitude of electron density peak as in Equation (5.7). The equation matrix is finally solved by using SVD method in Equations (5.8)–(5.10). Since the problem has been transformed into EOF space, the data calculation of each epoch can be reduced to about 7–8 minutes.

5.3.2 Validation

Simulations by using the real geometry of satellite-receiver ray paths at 8:00 UT, 23 June 2012 (DOY 175), was performed to evaluate the effectiveness of this algorithm. Due to the IPP distribution as shown in Figure 5.7(b), the focus is on the region with most data points that exhibits highest fidelity (bounded with pink lines Figure 5.17(a–b)). The 2-D maps of input irregularities are presented in Figure 5.17(a–c): I set the irregularities at around 100 km and 300 km in E and F regions respectively, according to the observations from Kokubunji ionosonde; similar to the typical wavelengths of Es and MSTIDs, the horizontal scales of input irregularities in E and F regions were set to about 150 km and 450 km, respectively; the simulated perturbation profiles were generated from the Chapman model, with integrals of -1–1 TECU in E region and -2–2 TECU in F region, which is the typical amplitude range of medium-intensity Es and MSTID events at nighttime. However, due to the 5-km vertical resolution and insufficient number of EOFs, the maximum input amplitude will be smaller than expected. This is the point that needs to be further improved in the future research. At this specific epoch, about 11,000 real signal rays obtained from GNSS observations were

used, from which the integrals of perturbations along the ray paths were then calculated to generate the simulated slant TECPs.

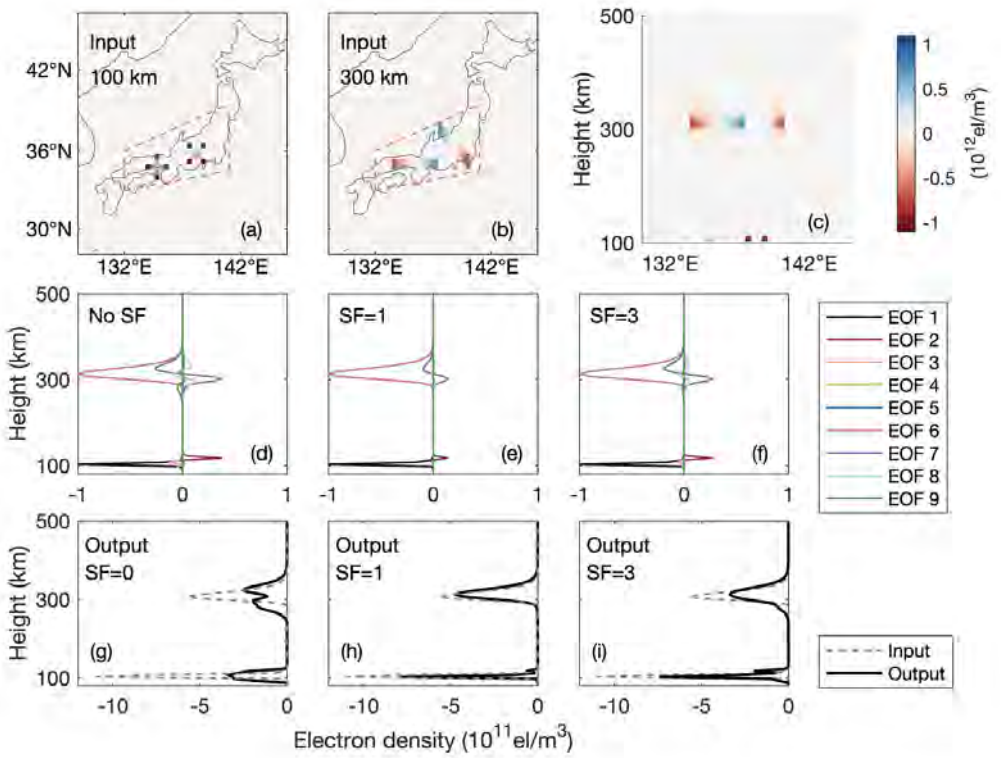

Fig. 5.17 (a–b) 2-D maps of input irregularities. (c) Vertical structure of reconstructed electron densities at 35°N. (d–f) Two sets of EOFs modified using different scale factors (SFs) at 6:00 UT, 23 June 2012 (DOY 175). (g–i) Reconstructed electron density perturbation profiles at (35°N, 134°E) with different SFs.

Based on the ionosonde network observations, two sets of EOFs (5 and 4 for E and F regions, respectively) were generated to constrain the E- and F-region solutions, which represent 98% of the original ensemble. In this simulation case, I also analyzed the importance of introducing scaling EOFs. In Figure 5.17, subplots (d–f) show the modification in the amplitude of EOFs as SF is varied (Φ_e^p: EOF 1–5; Φ_f^p: EOF 6–9). In the lower plate, an example of the reconstructed vertical profile using scaled EOFs at (35°N, 134°E) is presented, wherein the input irregularities at (35°N, 134°E) are -1 and -1.6 TECU in E and F regions, respectively. Similar to the conclusions in Figure 5.6, multiple peak artifacts occur before any scaling (SF=0). In this paper, I set SF=1: the artifact disappears, the input and output results are close to each other. The reconstructed maximum densities in E and F regions are -7.36×10^{11}el/m^3 and -4.82×10^{11}el/m^3, which are 67% and 84% of the input maximum densities, respectively. The integrals of reconstructed perturbations are 0.56 and 1.56 TECU

for E and F regions, respectively. Despite some loss in the reconstruction, especially in the E region, the underestimation of amplitude does not affect our later analysis of the physical underpinnings.

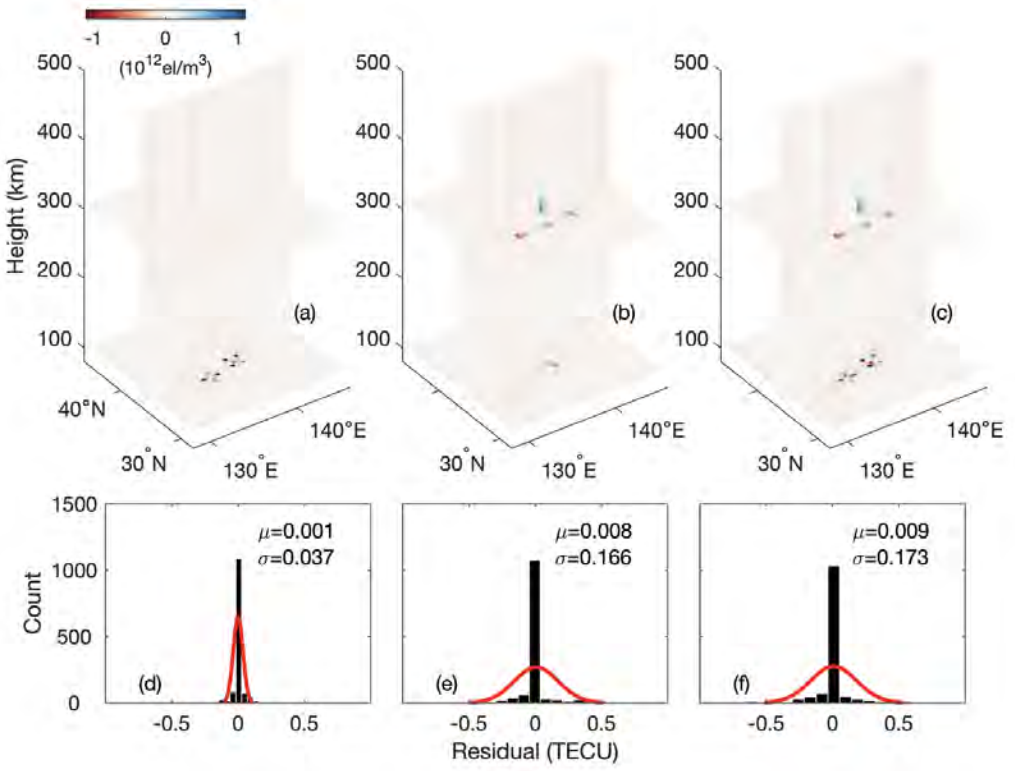

Fig. 5.18 3-D reconstructed results of input irregularities only in E region (a), only in F region (b), and in both E and F regions (c), and the corresponding residual distributions (d–f).

In addition, simulations of three cases were performed to further validate the algorithm: (1) Input irregularities only in E region; (2) Input irregularities only in F region; (3) Input irregularities in both E and F regions. The amplitudes and locations of input irregularities were the same as those in Figure 5.17(a–c). Subplots (a–c) in Figure 5.18 show the slices of two layers (at around 100 and 300 km) with the highest electron density in the E and F regions for the three cases, respectively. The 3-D reconstructed results indicate that the irregularities of different shapes and heights can be well reconstructed in both horizontal position and height in the region with densely distributed GNSS observations. A control data set from about 100 GEONET stations is used to specify the reconstruction precision. The residual distributions corresponding to different cases are shown in subplots (d–f). For case 1–3, the mean (μ) values are close to zero, and the standard deviation (σ) are 0.04, 0.17 and 0.17 TECU, respectively. In subplots (d–f), about 92%, 79%, and 77% of the residuals lie within the first bin (the width of each bin is about 0.03 TECU), about 92%, 89%, and

88% of the residuals lie within $\mu \pm \sigma$. These results suggest a high correlation between input and output values. Compared to subplot (d), the standard deviation (σ) in subplots (e–f) is significantly larger, indicating that the F-region irregularity has a greater impact on the reconstruction results due to the larger input amplitude and scale.

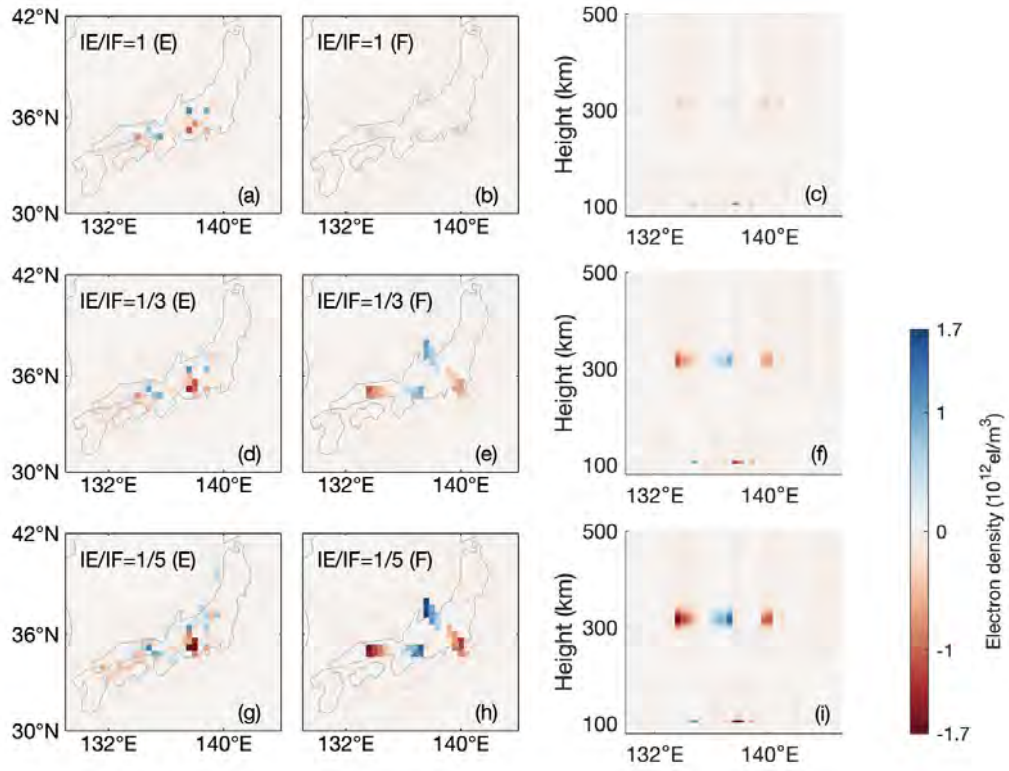

Fig. 5.19 2-D maps of output irregularities at different ratios of E to F region input structure amplitudes (IE/IF). The far-right subplots (c, f, i) are the vertical structures of reconstructed electron density anomalies at 35°N.

Because the nighttime F-region MSTID structures dominate in terms of amplitude and horizontal scale compared to Es layers, a simulation was performed to analyze the algorithm performance in the E region under different ratios of E to F region input structure amplitudes (IE/IF). Similarly, the locations of input irregularities were the same as those in Figure 5.17(a–c). The input amplitude in the E region was unchanged, while the input amplitude in the F region varies with IE/IF. Figure 5.19 shows the reconstruction results for different F-region input structure amplitudes. The vertical structures of reconstructed electron density anomalies at 35°N in subplots (c, f, i) indicate the peak electron density heights are well reconstructed in the radial dimension and consistent with the input shown in Figure 5.17(c). From Figure 5.19, the irregularity structures in the F region may impose large noise on the E-region reconstruction results when the F-region irregularities are intense in amplitude

(IE/IF>3). Under such circumstances, the E-region irregularities, especially those located below strong F-region irregularities, could be affected by large noise.

5.3.3 Reconstruction Results

The simulations in Section 5.3.2 have proven the effectiveness and evaluated the performance of this CIT algorithm. In this section, I applied this algorithm for analyzing the morphology and dynamics of E- and F-region irregularities during the E-F coupling by using the real observations. Same as Chapters 3 and 4, TECPs were obtained after deducting a 30-min data running average. According to the simulation results, small noise in TECPs can cause large errors in the horizontal and vertical reconstruction, especially in the E region. To minimize the noise in TECP obtainment, similar with the process in Section 5.2, the rate of TEC index (ROTI) is introduced. Here the threshold for an ionospheric irregularity to have occurred was set as 0.1 TECU/min, and the observed TECP values were set to zero if ROTI<0.1. Similar with earlier analysis in Chapter 4, events were selected under the condition K<4 and |Dst|<30 to mitigate ionospheric disturbances caused by other factors (e.g., geomagnetic storms). Since MSTID activity and occurrence rate peak in the nighttime summer (Otsuka et al., 2021), three events at this time period were selected: 23 June 2012 (DOY 175), 11 June 2007 (DOY 162), and 22 June 2020 (DOY 174). These three event days all exhibit nighttime MSTIDs, but with different maximum amplitudes. It should be noted that the first two events have been analyzed in Section 4.1 by the double thin-shell model, and the 3-D reconstruction results in this section will be a further validation for the previous results and this tomography technique.

Event on 23 June 2012 (DOY 175)

Figure 5.20(a–h) show the snapshots of electron density perturbation maps at the height of maximum Es and MSTIDs, at different epochs from 19:30 to 23:00 JST on 23 June 2012 (DOY 175). For validation, the 2-D TECP maps obtained by using the conventional single-thin-shell approach at corresponding epochs are also presented in subplots (i–l). The obtainment of 2-D TECP map follows the technique used in Tsugawa et al. (2018), wherein the height and grid were set to 300 km and 0.15°, respectively. In Figure 5.20, black triangles in subplots (a, e, i) represent the location of Kokubunji ionosonde. Black dashed lines in subplots (b–d, f–h, j–l) indicate the alignment azimuth of the apparent frontal structures, and gray arrows in subplots (j, k) indicate the drift direction (read by eye). Black dots in subplots (b–d, f–h) denote arbitrarily chosen points along the wavefront in the E region

and the corresponding points in the F region following geomagnetic equal potential lines estimated from the IGRF model.

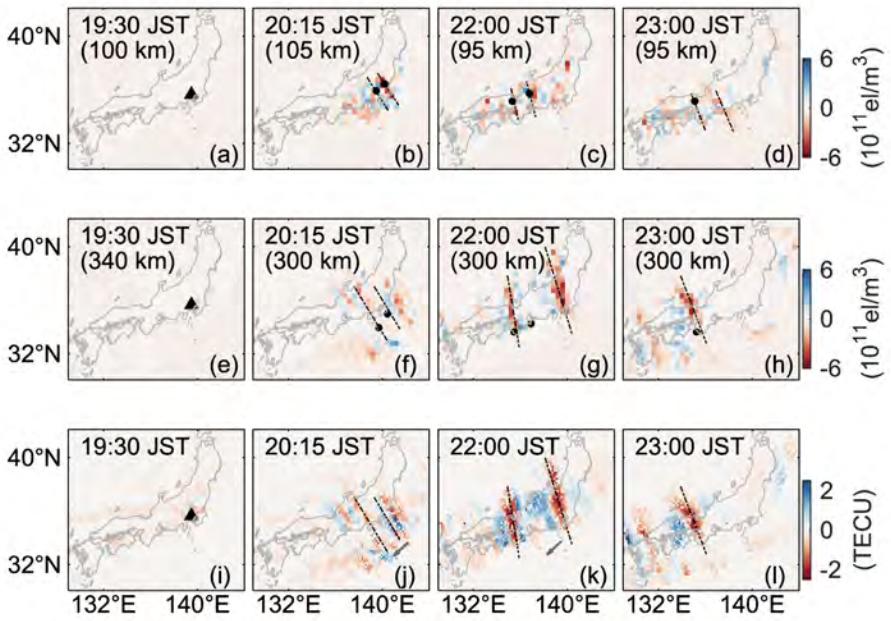

Fig. 5.20 Snapshots of electron density perturbation maps at the height of maximum Es (a–d) and MSTIDs (e–h), at different epochs from 19:30 to 23:00 JST on 23 June 2012 (DOY 175). The bottom subplots (i–l) show the 2-D TECP maps obtained by the single-thin-shell approach at corresponding epochs. Black triangles represent the location of Kokubunji ionosonde, black dashed lines indicate the alignment azimuth of the apparent frontal structures, gray arrows indicate the drift direction, black dots denote the locations at different heights connected by the geomagnetic field line.

From ∼19:30 JST, the irregularities in different regions develop with a small amplitude. At around 20:15 JST, the amplitude of E-region irregularities reaches the maximum and is larger than that of F-region irregularities. From 20:15 JST to 22:00 JST, the amplitude of E-region irregularities decreases slightly, while the amplitude and horizontal scale of MSTIDs is enhanced greatly. At 22:00 JST, the two frontal structures separating ∼200 km are observed in the F region. The major difference occurs at 22:00 JST in the right frontal structure in subplot (c), when the maximum amplitude of the MSTIDs is more than three times that of the Es layers, which makes it difficult to determine the corresponding irregularities in the E region. This situation has also been observed in the simulation of Figure 5.19. Based on the reconstruction results, the Es and MSTIDs share a similar wavefront with an NW-SE alignment and a common southwestward phase velocity of ∼100 m/s. Consistent with electrodynamic theory in E-F coupling, the density enhancements/depletions at different

regions are connected with the same magnetic field lines. The common alignment and propagation parameters suggest the E and F regions are strongly coupled. The average horizontal scales of E- and F-region irregularities are ∼150 and ∼400 km, respectively, which are sufficient to allow the polarized electric field to be effectively mapped along the magnetic field lines, thus triggering the E-F coupling process theoretically (Cosgrove, 2013). The morphological and dynamic characteristics of MSTIDs obtained above agree with the results of statistics analysis in Otsuka et al. (2011). Generally, the 3-D reconstruction results (position, alignment, and horizontal wavelength of the F-region MSTIDs) are consistent with the 2-D reconstruction by using the single-thin-shell model (Figure 5.20(i–l)) and double-thin-shell model (Figure 4.1), indicating a high fidelity of this technique.

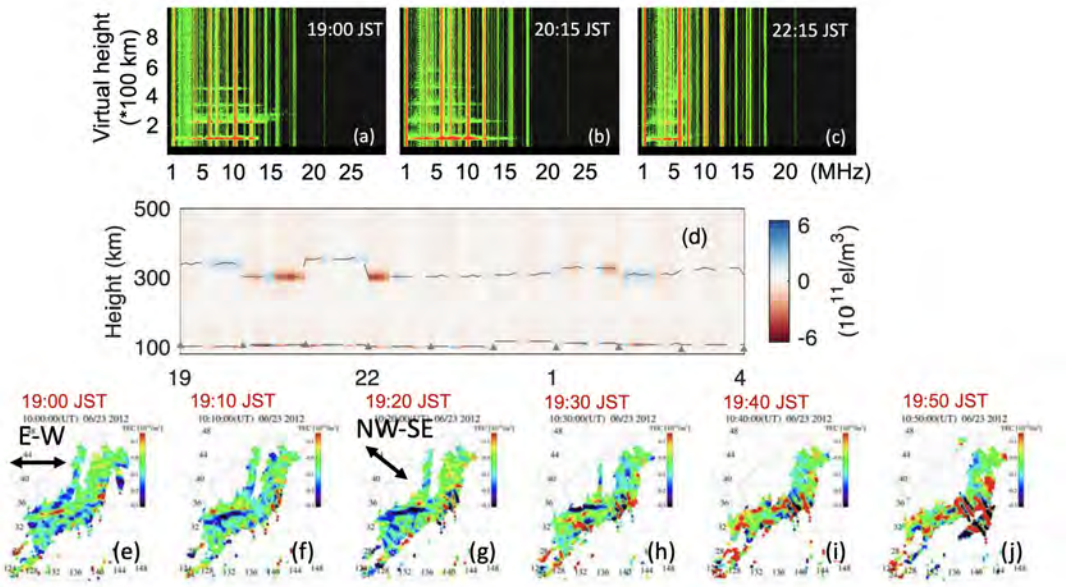

Fig. 5.21 (a–c) Ionograms provided by Kokubunji ionosonde. (d) Time variation of the vertical perturbation profiles over Kokubunji area on the night of 23 June 2012 (DOY 175). Gray triangles represent hmEs from Kokubunji ionosonde. Gray dashed lines in E and F regions denote the reconstructed hmEs and hmF2, respectively. (e–j) 2-D TEC maps over Japan during 19:00–19:50 JST.

Here, I use the Kokubunji ionosonde for validation since it locates within the region of most GNSS data points in Japan. Figure 5.21(a–c) shows the Kokubunji ionograms at 19:00, 20:15, and 22:15 JST, on 23 June 2012 (DOY 175). Subplot (d) shows the vertical electron density perturbations over Kokubunji area (a $1.2^\circ \times 1.2^\circ$ grid) with a temporal resolution of 5 min from 19:00 JST to 4:00 JST. Gray triangles represent hmEs from Kokubunji ionosonde. The determination of hmF2 in ionosonde observations is hindered since the

F-region trace was blanketed by the Es layers. Gray dashed lines in E and F regions denote the reconstructed hmEs and hmF2, respectively. From the reconstruction results with ground-based GNSS-TEC measurements, over the Kokubunji area, the Es layer starts to appear at around 19:30 JST. However, according to the ionograms at 19:00 JST in subplot (a), Es patches have formed earlier but are not detected by GNSS-TEC. Understandably, E-region irregularities are not always associated with amplitude scintillation of GNSS signals because of the amplitudes, scales, and thin thickness of Es layers, elevation angles of ray paths, and frequency of radio signals (Sun et al., 2020). Additionally, from 19:00 to 23:00 JST as in subplots (a–c), the presence of blanketing E indicates a weak structuring of Es layer so that radio waves cannot penetrate to higher heights (Maruyama et al., 2006). I consider this phenomenon could be associated with the MSTIDs seeded by AGWs before sunset. As shown in subplots (e–j), the 2-D TEC maps successfully captured the MSTID structures, which is shown as E-W alignment before $\sim$19:00 JST and changed to NW-SE alignment after this time. Under such conditions, due to the pre-existing polarization electric fields in the F region, the role played by E-region polarization electric field may be less pronounced in seeding and amplifying the Perkins instability, thus leading to a Es layer with smaller amplitude and spatial inhomogeneity. In fact, the existence of polarization electric fields within AGW-seeded MSTIDs has been verified by the MMF observations in Figure 4.18(c–f) at lower latitudes.

After 1:00 JST, the F-region irregularities intensify again but with a lower maximum intensity than the previous day. This has also been observed in Figure 4.3. According to the F-region reconstruction in Figure 5.21(d), the anti-correlation between F2 peak layer and MSTID intensity was observed. The variation of F2 peak layer is about 40–50 km during 19:00–23:00 JST when MSTIDs are strong, and about 5–25 km during 1:00–3:00 JST when MSTIDs become less intense. The F2 peak altitude becomes lower (higher) when perturbations are large (small) at 20:00–21:00 JST, 22:00–23:00 JST, and 2:00–3:00 JST (21:00–22:00 JST and 1:00–2:00 JST). From Figure 5.21(d), the radial-time variation of both Es and MSTIDs are successfully tracked, wherein the deviations between the reconstruction and observation are about 8 km in E region, and the deviation is larger when the electron density perturbation is not significant. In the early phase of E-F coupling process, a small increase of hmEs ($\sim$5 km) was also observed at around 20:00 and 0:00 JST. The time variation of Es layer altitude is not obvious during the E-F coupling process, which may be due to the low resolution in the vertical dimension (5 km).

Event on 11 June 2007 (DOY 162)

In Figure 4.6, the 2-D reconstruction results were validated by using MUR data, which can also be used to further validate our 3-D algorithm and results. Figure 5.22 shows the slices of reconstruction results, at different epochs from 19:30 to 22:30 JST on 11 June 2007 (DOY 162). In subplot (a), red square denotes the location of MUR, black squares at different heights (100 and 300 km) represent radar observations regions where the transmission beam was pointed to the north (azimuth: 17.15° and 17.67°, about the geographic north, zenith: 53.25° and 59.01° in E and F regions, respectively). Gray dash lines denote the geomagnetic field lines estimated from IGRF model. The MSTID structures on 11 June 2007 (DOY 162) is less intense (∼20%) than the event on 23 June 2012 (DOY 175). Consistent with the conclusions in Section 4.1 (Figure 4.5 and 4.7), for this event, the irregularities in the E region appear earlier than those in the F region. At around 19:30 JST in subplot (a), low-intensity E-region irregularities appear while the F-region structures are not obvious. At around 20:30 JST in the region of highest fidelity, distinct NW-SE aligned frontal structures in E and F regions, sharing similar propagation parameters, are connected by a geomagnetic field line.

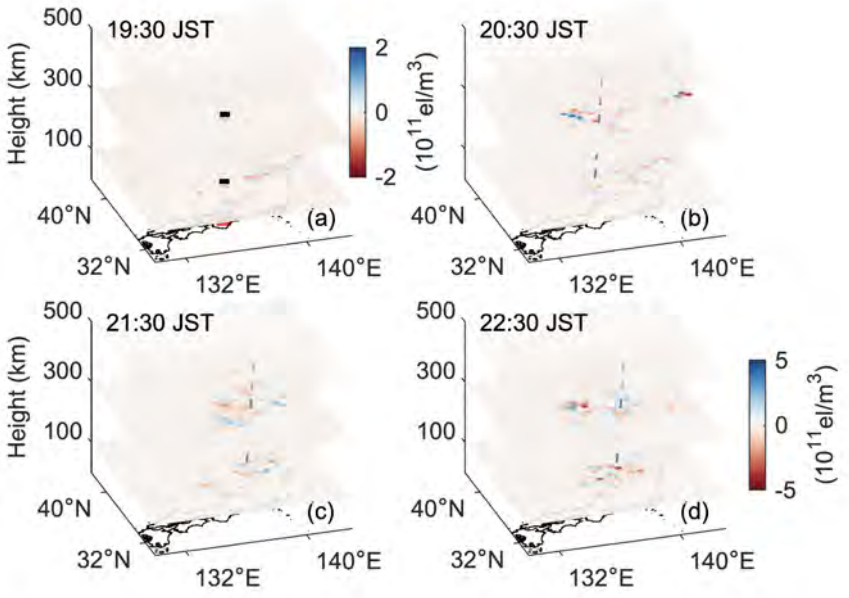

Fig. 5.22 Slices of the reconstructed structures on 11 June 2007 (DOY 162). Red square denotes the location of MUR, black squares at different heights represent radar observations regions where the transmission beam was pointed to the north (azimuth: 17.15° and 17.67°, zenith: 53.25° and 59.01° in E and F regions, respectively). Gray dash lines denote the geomagnetic field lines estimated from IGRF model.

Radar backscatter from FAIs may exist simultaneously in the E and F regions on the same magnetic field line, suggesting a close coupling between the E and F regions (Saito et al., 2007). Figure 5.23(a–d) show the observations of midlatitude F-region irregularities occurring in tandem with Es-layer irregularities over MUR during a geomagnetically quiet period on 11 June 2007 (DOY 162). Two transmission beams (azimuth angles of 0° and 17°) were selected. AZ and ZE represent azimuth and zenith angles of the transmission beams, respectively. Since the size of the irregularities measured by the radar backscatter (several meters) and GNSS–TEC measurements (ten to hundred kilometers) are different, to compare the results from radar observation and reconstruction from the general relative change in density, here I assumed that meter-scale structures populate a wider spatial area than the radar field of view. The variation of TECPs ($TECP_{abs}$, the absolute value of electron density integral) along the real radar transmission beams is plotted by the gray solid lines in Figure 5.23. From subplots (a, c), in the F region before ∼24:00 JST, the echo is "short-lived" but with a stronger signal-to-noise ratio (SNR). During ∼0:00–4:00 JST, the echoes become frequent, but the SNR and height are slightly reduced. From subplots (b, d), in the E region, the well-defined quasi-periodic (QP) echoes, manifested as the inclined striation pattern (Tsunoda et al., 1994), are observed from ∼19:30 to 24:00 JST. After ∼24:00 JST, continuous echoes associated with lower altitude are observed. During this period, the TECPs caused by Es layer could be small, since the continuous echoes are less dynamic than the QP echoes, indicating a development of weak spatial structuring in electron density within an Es layer (Maruyama et al., 2006). From Figure 5.23, the variation of reconstructed $TECP_{abs}$ in both E and F regions is consistent with that of SNR.

Subplots (a–c) in Figure 5.24 show the ionograms at 19:00, 20:00, and 21:45 JST on 11 June 2007 (DOY 162) provided by Kokubunji ionosonde. Subplot (d) shows the time variation of the reconstructed vertical structures over the Kokubunji area (a $1.2^\circ \times 1.2^\circ$ grid), with a 5-min resolution. Gray triangles and dots represent hmEs and hmF2 from Kokubunji ionosonde, and Gray dashed lines in E and F regions denote the reconstructed hmEs and hmF2, respectively. The positions of Kokubunji ionosonde and MUR are about 350 km apart, which allows for a comparison of their observation results. Consistent with the conclusions obtained by Maruyama et al. (2006), the transparent Es layers in Figure 5.24(a–b) are observed in close connection with the QP echoes. Comparing with the event on 23 June 2012 (DOY 175) (Figure 5.21(a–b)), the transparent and spread Es trace associated with QP echoes suggests a greater spatial inhomogeneity in sporadic E plasma in the early development stage on 11 June 2007 (DOY 162). In Figure 5.24(d), coinciding with the intense echoes received by MUR, the E-region irregularities over the Kokubunji area appear earlier than the MSTIDs at ∼19:00 JST. The reconstructed maximum amplitude in the F region occurs between 21:00

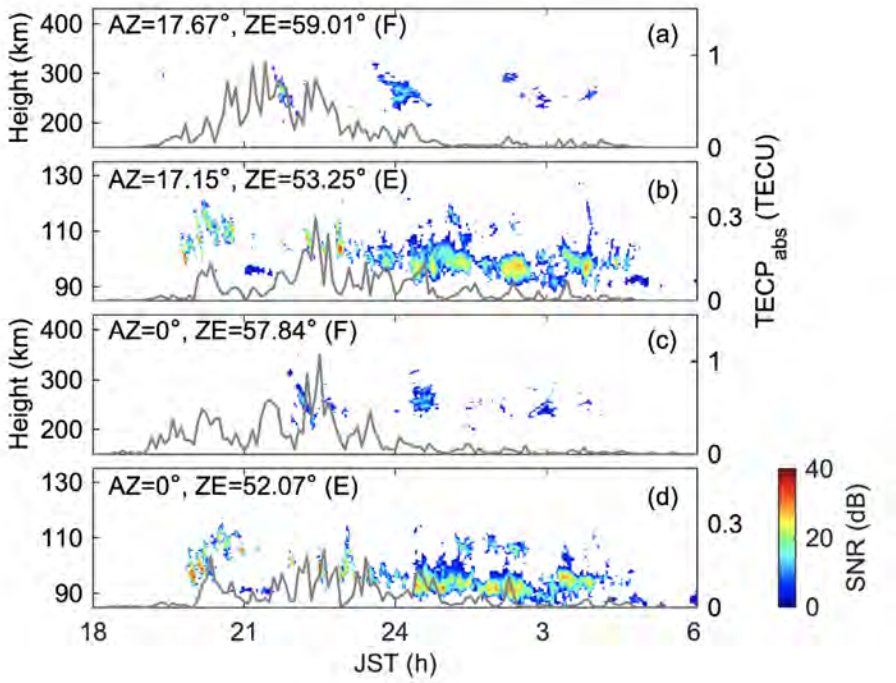

Fig. 5.23 Range-Time-Intensity plots of echo power observed by different beams in MUR on 11 June 2007 (DOY 162). AZ and ZE represent azimuth and zenith angles of the transmission beams, respectively. Gray solid lines denote the mean variation of TECPs along the radar beams.

and 22:00 JST, and the E-region irregularities during this period need to be determined by analyzing both the amplitude and morphology due to the "shadow" effect from the strong irregularities in the F region. From the ionosonde observation as shown in Figure 5.24(c), the Es layer is highly developed and fully blanketing the F layer during this time in which the F-region maximum amplitude occurs, which could be due to the thin thickness of Es layers that need less time to saturate. In addition, the cessation of blanketing does not necessarily mean it is weak, it may become more structured (Cosgrove, 2013). During the E-F coupling process, the variation of hmEs is not obvious (<5 km) at around 21:00–22:00 JST although the amplitude is greatly enhanced, which could be due to the limited vertical resolution. In the F-region reconstruction, similar to the results in Figure 5.21(d), the variation of F2 peak layer in altitude is about 15–30 km during 19:00–24:00 JST, and the F2 peak altitude becomes lower (less than 300 km) when perturbations are large during 21:00–22:00 JST. The reconstructed hmEs (hmF2) and observed hmEs (hmF2) in Figure 5.24(d) show an average error of $\sim$7 ($\sim$20) km, indicating a high fidelity for the hmEs (hmF2) reconstruction.

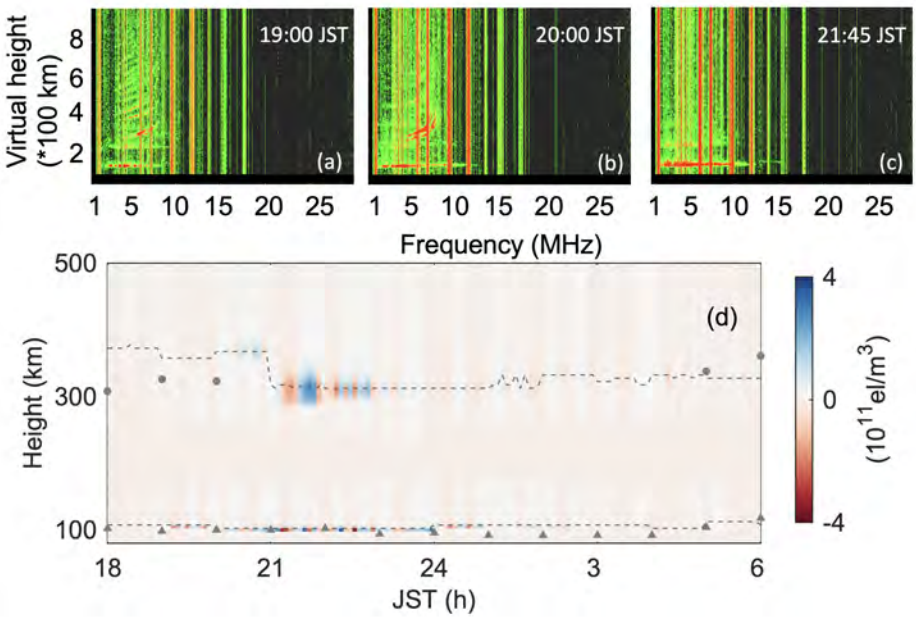

Fig. 5.24 (a–c) Ionograms provided by Kokubunji ionosonde at different epochs on 11 June 2007 (DOY 162). (d) Time variation of the vertical structure over Kokubunji area. Gray triangles and dots represent hmEs and hmF2 from Kokubunji ionosonde, respectively. Gray dashed lines in E and F regions denote the reconstructed hmEs and hmF2.

Event on 22 June 2020 (DOY 174)

The event on 22 June 2020 (DOY 174) is less intense than the two previously analyzed events, but the coupled E and F regions are still observed. Figure 5.25 shows the 2-D TECP maps obtained by the single-thin-shell approach (a–c) at 20:00, 21:00 and 21:30 JST, and the corresponding slices of reconstructed electron densities (d–f) along the line from northeast to southwest indicated as the black solid lines in subplots (a–c). Gray dashed lines in E and F regions denote the reconstructed hmEs and hmF2. The black triangle represents the location of Kokubunji ionosonde. The black arrows indicate a good correlation between the electron density enhancements observed in the reconstruction and the 2-D TECP maps. The nearly sinusoidal variations of the reconstructed F2 peak layer are observed. From subplots (d–f), the F-region peak-to-peak variation in altitude is 5–25 km, which is within the range obtained by Ssessanga et al. (2017) through the statistical analysis. Still, the vertical reconstruction is insufficient, e.g., the peak-to-peak variation of hmF2, which could be resulted from the limited number of EOFs.

Same as Figure 5.24, Figure 5.26(a–c) show the ionograms at 20:00, 20:45, and 21:00 JST on 22 June 2020 (DOY 174) provided by Kokubunji ionosonde. From the reconstruction

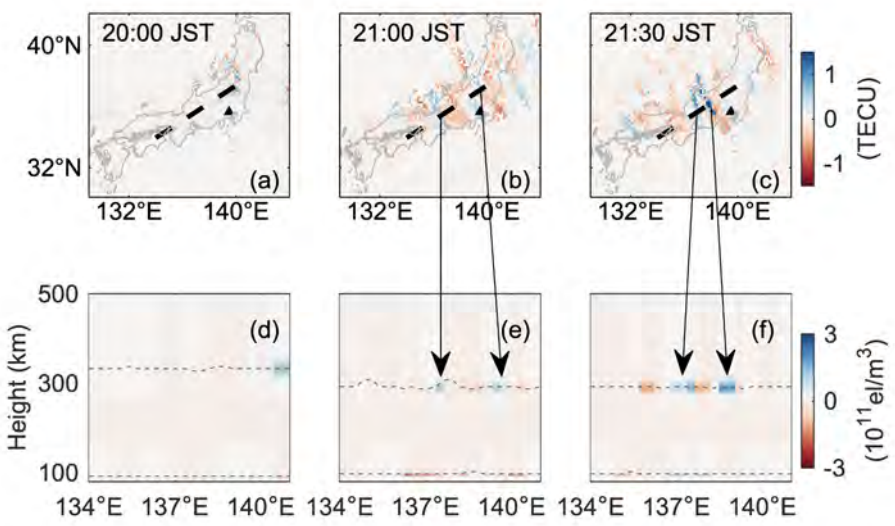

Fig. 5.25 (a–c) 2-D TECP maps obtained by the single-thin-shell approach on 22 June 2020 (DOY 174). (d–f) Slices of reconstructed electron densities at the corresponding epochs along the black dashed lines shown in subplots (a–c). Gray dashed lines in E and F regions denote the reconstructed hmEs and hmF2. The black arrows indicate a good correlation between the electron density enhancements observed in the reconstruction and the 2-D TECP maps. The black triangle represents the location of Kokubunji ionosonde.

results, over the Kokubunji area, the Es layer appears at ∼20:15 JST, which is earlier than the MSTIDs at ∼20:45 JST. As shown in the ionograms, a less developed Es trace is observed at 20:00 JST. The transparent and nearly spread Es trace at 20:45 JST indicates a large electron density spatial inhomogeneity in the Es layer. After 15 min, the Es layer fully blanketing the F region. At this moment, the F-region irregularities show a great enhancement in amplitude according to the reconstruction results. I consider that this phenomenon is related to the occurrence of E-F coupling: the Es layer plays a major role in seeding the perturbations (Perkins instability) in the F region, but becomes weaker in the mid- and late-phase of the E-F coupling process due to its thin thickness. During E-F coupling process, a small increase of hmEs (∼5 km) is observed at around 21:00 JST. After 22:00 JST, the amplitude of Es layer decreases, but the F-region irregularities are enhanced and the F2 peak layer extends to higher altitude. From the reconstruction results in Figure 5.26(d), the variation of the reconstructed hmEs (hmF2) and observed hmEs (hmF2) is consistent, wherein the average error is ∼8 (∼20) km.

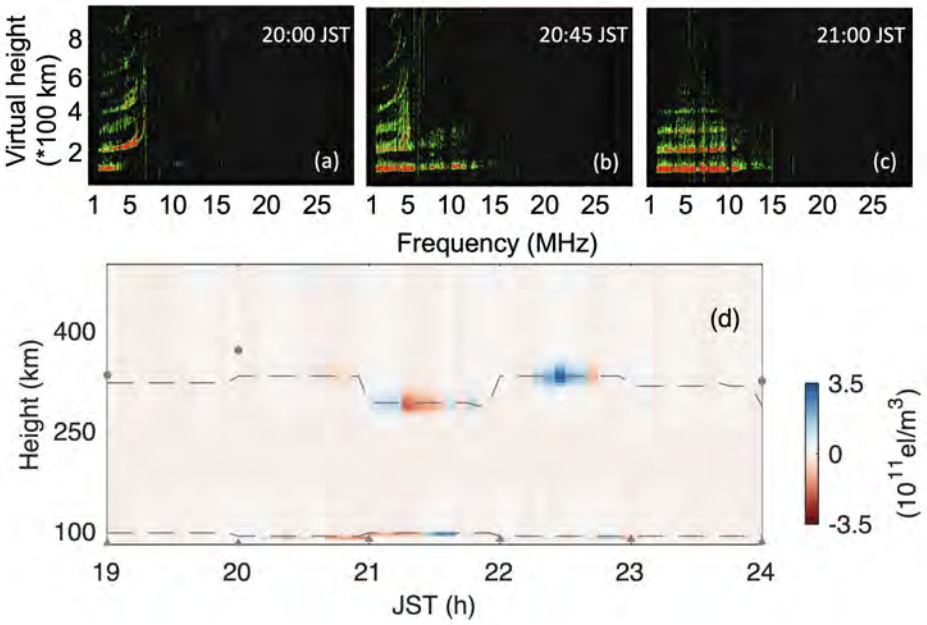

Fig. 5.26 Same as Figure 5.24 but for 22 June 2020 (DOY 174).

5.4 Discussion

In Section 5.2 and 5.3, the 3-D structures of daytime sporadic E layers and nighttime coupled ionosphere have been reconstructed successfully by using the tomography technique. To facilitate CIT, TEC measurements were adopted from a dense receiver network, GEONET, located over Japan with more than 1,200 stations. The time-dependent EOFs generated from a Chapman model function tuned to manually-scaled observations from a network of four ionosondes over Japan were used to vertically constrain the solution in E or both E and F regions. For the first time, computerized ionospheric tomography with ground-based GNSS-TEC is shown to reproduce the altitude-time variation of the ionospheric irregularities, especially sporadic E, which had proved difficult to reproduce in earlier tempts at 3-D ionospheric reconstructions.

The horizontal and vertical variations of daytime Es layer, e.g., in Figure 5.14 and 5.16, have further verified that the daily variation of Es layers could be mainly driven by atmospheric tidal winds (Mathews, 1998). A more interesting phenomenon is the vertical variation of Es layers in the nighttime coupled ionosphere. According to the reconstruction results in Figures 5.21 and 5.26, a small increase of hmEs ($\leq$5 km) was observed during the E-F coupling process. Due to the limited vertical resolution, the detailed mechanism of this small Es layers rise is still not clear. The electrodynamic factors could be the most

possible explanation for this phenomenon, as the rise in Es-layer altitude coincides with the appearance of coupling. From the 3-D reconstruction of the coupled ionosphere, during the nighttime coupling process, the coexistence, similar wavefronts, and common propagation parameters of Es layers and MSTIDs confirm a strong coupling between the ionospheric E and F regions. On 23 June 2012 (DOY 175), from Figure 5.21(e–j), a pre-existing MSTIDs with E-W alignment is observed, which could lead to the less pronounced role played by Es layer in the coupling process (the presence of blanketing E as shown in Figure 5.21(a–c)), due to the polarization electric fields within the AGW-seeded MSTIDs.

Events on 11 June 2007 (DOY 162) and 22 June 2020 (DOY 174) are slightly different with the first event, as shown in Figures 5.24 and 5.26. The Es layers appear $\sim$30 min earlier than the MSTIDs and show a great spatial inhomogeneity within the Es layer in the early development stage (the presence of transparent and spread Es trace associated with QP echoes). This early appearance of Es layer was also observed in the 2-D analysis of E-F coupling in Figure 4.7, which is consistent with the simulations of the E- and F-region response in the initial phase of E-F coupling process (Cosgrove, 2007; Yokoyama et al., 2009). For this coupling form, the pre-existing Es layer could be forcibly modulated by the neutral wind perturbations, which produces polarized electric field along magnetic field lines mapping to the F region and beyond, thus causing the F-region irregularities aligned in NW-SE (in the Northern Hemisphere) (Cosgrove, 2013). From Figures 5.24(d) and 5.26(d), the F-layer altitudes rise ($\sim$10 km) in the initial phase of coupling process, which can generate a substantial polarization field and cause the evolution of the original electric field (Cosgrove, 2013). In Figures 5.24 and 5.26, the Es layer ceases to be blanketing while the F-region amplitude is greatly enhanced at around 21:00 JST, which might be mainly due to the thin thickness of Es layers that needs less time to saturate, and the short growth time required for the MSTID formation in the E-F coupling process (Yokoyama et al., 2009). In Figure 5.25(d–f), the nearly sinusoidal variation of the F2 peak height (5–25 km) could be mainly driven by the Perkins instability caused by passage of gravity waves, which has been described in Equation (2.26) (Otsuka et al., 2013; Ssessanga et al., 2015).

Based on the subplot (d) in Figures 5.21, 5.24 and 5.26, the peak-to-peak variation (5–50 km) of F2 layer associated with the intensity of MSTIDs were observed. The altitude of F2 peak layer tends to become lower (higher) when the F-region perturbations are large (small). This anti-correlation between F2 peak heights and electron density perturbations could be related to the unstable balance between the gravitational force that lower the F layer and the forces from winds and electric fields that raise the F layer (Kelley and Fukao, 1991). In addition, one noteworthy exception is that during 22:00–23:00 JST on 22 June 2020 (DOY 174) in Figure 5.26(d), the Es layer amplitude is decreased while the F-region irregularities

are enhanced. The increase of the F2 peak layer in altitude during this time period could be associated with the incomplete development of Perkins instability (Ssessanga et al., 2017), caused by the weakened polarization electric field from the E region. That is, based on this inference, there might be a mutual influence of E and F regions on each other in the coupling process.

By using this newly developed algorithm, the time-vertical motion of the Es and F2 peak layers can be successfully tracked, with an average error of about 8 and 20 km in E and F regions, respectively. The reconstruction results provide an alternative perspective for observing and analyzing the E-F coupling instabilities, which can well complement other observational techniques with higher precision but limited by spatial and temporal scales (e.g., ionosondes, radars), thus deepening our understanding of the generation mechanisms of ionospheric irregularities. Still, there are some improvements that need to be made for this study, e.g., quantify the noise impact in E and F regions through simulation, increase the vertical resolution and EOF numbers to fully capture the variation and reconstruct the structures of ionospheric irregularities.

Chapter 6

Summary and Conclusions

This research focuses on the imaging and analysis of mid-latitude ionospheric irregularities using ground-based GNSS-TEC measurements. Japan is the analyzed region of most interest due to its dense GNSS receiver network (GEONET) with more than 1200 stations and a mean distance of $\sim$25 km between receivers, which makes GNSS-TEC measurements over Japan an ideal tool for analyzing small-scale perturbations in ionospheric electron density. At mid- and low-latitudes, two primary ionospheric irregularities are frequently observed: sporadic E (Es) in the E region and medium-scale traveling ionospheric disturbances (MSTIDs) in the F region. These irregularities scintillate GNSS signals and affect/hinder applications using trans-ionospheric radio waves, which makes the understanding of ionospheric irregularities significant.

Es and MSTIDs are ionospheric irregularities of different altitudes and scale sizes. One of the intriguing aspects of nighttime mid-latitude Es and MSTIDs is the NW-SE (NE-SW) aligned frontal structures propagating toward the equator-westward direction in the Northern (Southern) Hemisphere. Earlier theoretical analysis and simulation results support the theory that electrodynamic forces, that is, the Es-layer instability in the E region and the Perkins instability in the F region, are the probable mechanisms behind these irregularities; Es and MSTIDs are coupled through geomagnetic field lines. In addition, the E-F coupling process is more intricate, to the extent that MSTIDs are simultaneously observed in the geomagnetic conjugate regions (different hemispheres) with matching crests and troughs. In this process, the polarization electric fields generated by E- and F-region irregularities can be mapped to opposite hemisphere along the geomagnetic field lines with a certain attenuation. However, due to the limited observation area, resolution, and methods, comparing the temporal relationship between the occurrence of Es and MSTIDs is difficult, and thus the causal relationship in the E-F and interhemispheric coupling is not yet fully understood. In

response to this problem, a coherent 2-D and 3-D picture and a comprehensive analysis of the coupled ionosphere is required to deepen our understanding of such ionospheric irregularities.

Usually, the TECs used in the ionospheric studies are obtained based on a single-thin-shell approximation, wherein the 3-D ionosphere is represented as an infinitesimally thin layer at a constant altitude. Although this single-thin-shell model is effective for ionospheric studies in most cases, its exploitation in the nighttime coupling process is difficult due to the mixture of E- and F-region electron densities. Therefore, novel methods need to be developed to reconstruct the E- and F-region perturbations simultaneously. Heuristically, in Chapter 3, a double-thin-shell model has been developed to parameterize the integrated three-dimensional density perturbations. In this model, the mid-latitude nighttime plasma instabilities are assumed to be concentrated at E (100 km) and F (300 km) layers; at each shell, perturbation components are assumed identical at any point within a given grid block; the TEC perturbation in E and F regions were reconstructed on horizontal grids of 0.15° and 0.5°, respectively. For the first time, the morphology and dynamics of the ionosphere perturbations in both E and F regions can be obtained simultaneously with ground-based GNSS-TEC.

In Chapter 4, four events of nighttime MSTIDs, but with different amplitudes, were used to investigate the E-F and interhemispheric coupling. The double-thin-shell model was used to analyze the ionospheric responses in E and F regions over Japan during the nighttime coupling processes. Results show that the newly developed technique can infer several horizontal characteristics on E–F coupled instabilities; the coexistence of NW–SE aligned irregular structures in E and F regions is evident. Both E- and F-region irregularities share similar propagation parameters, a shred of clear evidence of strong coupling. Further, the hemisphere-coupled ionospheres over Japan and Australia (geomagnetic conjugate regions) are observed and analyzed using TEC measurements, supplemented with multi-source observations from ionosondes, ICON (neutral wind), COSMIC (electron density) and Swarm (magnetic field). The analyses in 2-D format allowed for the following contributions:

1. By using GNSS-TEC and taking a double-thin-shell approach, Es layer was observed only in the summer hemisphere when F-region conjugate structures simultaneously occur in both hemispheres; Es layers in the summer hemisphere appear $\sim$30 min earlier than the MSTIDs in the F region, and followed by the coupled E- and F-region irregularities, as well as the geomagnetic conjugate MSTIDs. These results support the evidence that the F-region conjugate irregularities in both hemispheres are mainly driven by the Es layers in the summer hemisphere during the interhemispheric coupling process.

2. The sporadic and blanketing E layers with small amplitudes in the winter hemisphere were observed to show intensity reduction or even dissipation after the interhemispheric coupling, which may be related to the variation in ionospheric conductivity caused by the thermospheric winds in the winter hemisphere and the conjugate MSTIDs (more importantly).

3. Thermospheric winds play an important role in the MSTID generation and development. In addition, the MSTID intensity decreases more rapidly in the winter hemisphere, which may be related to the decoupling from the summer hemisphere.

4. A combination of thermospheric winds and non-equipotential magnetic field lines leads to a weaker mapping of polarization electric between conjugate hemispheres. Hence the asymmetry in the amplitude of hemispheric conjugate MSTIDs and the slower growth rate of MSTID structures in the winter hemisphere.

Although such results are encouraging, the missing height dimension in these 2-D analyses may pose limitations on the information that we can infer. Therefore, a continuous and broad 3-D structure of ionosphere is required. However, the 3-D reconstruction for the coupled ionosphere with GNSS-TEC is difficult due to the thin thickness of Es and the representation errors in tomography. Therefore, the reconstruction of Es layer is pivotal for the tomography of the nighttime E-F coupling. In Section 5.2, a novel two-step CIT technique was first developed to reconstruct the 3-D maps of daytime sporadic-E based on ground-based GNSS observations. First, on a coarse grid of 1° in the horizontal, 20 km in altitude, and a 15-min assumption of ionosphere stationarity, a more accurate F region structure is reconstructed from a smooth background using the MART algorithm. Then, using the SVD algorithm and a finer grid of 0.4° in the horizontal, 1 km in altitude, and 1.5 min in time, a 3-D E region, 80–180 km in height, is estimated from TEC residues after deducting the F region contribution. To vertically constrain the solution, time-dependent EOFs generated from a Chapman model function tuned are used to manually scaled Es observations from a network of four ionosondes over Japan. Results from simulation and real observations exhibit that the technique can reconstruct Es structure with a high degree of fidelity, specifically during strong Es (foEs$>$20 MHz). Moreover, 2-D horizontal slices at the height of maximum Es, corroborate the earlier analyses and expositions on the morphology and dynamics of Es. That is: Es shows E-W large elongated frontal structures that can extend several hundred kilometers; the migration is northwestward in the morning and southwestward in the afternoon, with a velocity of 60–100 m/s; the duration of Es frontal structures can reach tens of minutes to a few hours. For the first time, computerized ionospheric tomography with ground-based GNSS-TEC is shown to reproduce the Es-layer altitude time variation.

In Section 5.3, this 3-D tomography technique has been modified and applied to the reconstruction of the nighttime coupled ionosphere. Different with the previous 3-D tomography for daytime sporadic E, two sets of time-dependent EOFs are used to constrain the E- and F-region solutions simultaneously; TEC perturbation components rather than absolute TEC values are used in this research. On a grid of 0.4° in horizontal and 5 km in altitude, the vertical solutions in E and F regions were constrained by using the time-dependent EOFs from a Chapman model function based on manually scaled observations from four ionosondes. Validation from simulation results indicates a high fidelity of this algorithm in reconstructing the irregularities in E and F regions. Three event days of nighttime MSTIDs with different maximum amplitudes were selected for analyzing the E- and F-region irregularity structures during the E-F coupling. Results suggest that the horizontal and vertical structures of the coupled ionosphere can be successfully reconstructed. The coexistence, similar wavefronts, and common propagation parameters of Es and MSTIDs confirm the strong coupling between the ionospheric E and F regions. In the vertical dimension, a small rise in Es layer was observed during the coupling process; the peak-to-peak variation of the F2 layer is about 5–50 km, which is related to the intensity of MSTIDs: the F2 peak altitude tends to become lower (higher) when the F-region perturbations are large (small). The 3-D reconstruction results suggest that the electrodynamic forces dominate the morphology and dynamics of Es and MSTIDs during the nighttime coupling process. By using this newly developed algorithm, the time-vertical motion of the Es and F2 peak layers can be successfully tracked, with an average error of about 8 and 20 km in E and F regions, respectively. The reconstruction results provide an alternative perspective for observing and analyzing the E-F coupling instabilities, which can well complement other observational techniques with higher precision but limited by spatial and temporal scales (e.g., ionosondes or radars), thus deepening our understanding of the generation mechanisms of ionospheric irregularities.

As GNSS data sets expand in the coming years, it will be possible to perform more detailed analyses to investigate the physical mechanisms of ionospheric irregularities. The spatial as well as the temporal resolution will be improved by expanding the deployment of ground-based receivers and including additional GLONASS, Galileo and Beidou signals. In such cases, the developed double-thin-shell model could be upgraded to triple-thin-shell model to estimate the plasmaspheric TEC perturbations, which cannot be neglected especially during magnetic storms. As for the 3-D tomography technique for the coupled ionosphere, the noise in both E and F regions need to be quantified; the vertical resolution (5 km) is still not high enough (limited by computer performance), resulting in insufficient EOF number that cannot fully captured the vertical Es and MSTID structures. Furthermore, it is not straightforward to determine the height of maximum MSTIDs from ionosonde

hmF2 observations. To this effect, perturbation profiles of IED generated by physics-based functions, e.g., Chapman function, or observed by multiple instruments, e.g., ionosondes and occultation, may contribute to the generation of ensembles for EOFs with higher vertical resolution.

This study presented the imaging methods and analyses of ionospheric irregularities in 2-D and 3-D formats by using GNSS-TEC measurements. For the first time, results confirm the theoretically predicted nighttime coupling processes between E-F and the hemispheres with observational data. The coupling phenomena of the nighttime ionosphere were further elucidated, especially regarding the generation and development of ionospheric irregularities. Thus, this thesis is a valuable contribution to the understanding of physical mechanisms behind ionospheric irregularities, which would help improve our skills in predicting and mitigating ionospheric signal scintillation in the near future.

References

Aarons, J. and Whitney, H. E. (1968). Ionospheric scintillations at 136 MHz from a synchronous satellite. *Planetary and Space Science*, 16(1):21–28.

Abdu, M., De Souza, J., Batista, I., Santos, A., Sobral, J., Rastogi, R., and Chandra, H. (2014). The role of electric fields in sporadic E layer formation over low latitudes under quiet and magnetic storm conditions. *Journal of Atmospheric and Solar-Terrestrial Physics*, 115:95–105.

Alken, P., Thébault, E., Beggan, C. D., Amit, H., Aubert, J., Baerenzung, J., Bondar, T., Brown, W., Califf, S., Chambodut, A., et al. (2021). International geomagnetic reference field: the thirteenth generation. *Earth, Planets and Space*, 73(1):1–25.

Andoh, S., Saito, A., and Shinagawa, H. (2021). Temporal evolution of three-dimensional structures of metal ion layer around Japan simulated by a midlatitude ionospheric model. *Journal of Geophysical Research: Space Physics*, 126(6):e2021JA029267.

Andoh, S., Saito, A., and Shinagawa, H. (2022). Numerical simulations on day-to-day variations of low-latitude Es layers at Arecibo. *Geophysical Research Letters*, 49(7):e2021GL097473.

Appleton, E. V. (1932). Wireless studies of the ionosphere. *Journal of the Institution of Electrical Engineers*, 71(430):642–650.

Arras, C. (2010). *A global survey of sporadic E layers based on GPS Radio occultations by CHAMP, GRACE and FORMOSAT–3/COSMIC*. PhD thesis, Deutsches GeoForschungsZentrum GFZ Potsdam.

Arras, C. and Wickert, J. (2018). Estimation of ionospheric sporadic E intensities from GPS radio occultation measurements. *Journal of Atmospheric and Solar-Terrestrial Physics*, 171:60–63.

Austen, J. R., Franke, S. J., and Liu, C. (1988). Ionospheric imaging using computerized tomography. *Radio Science*, 23(03):299–307.

Axford, W. (1963). The formation and vertical movement of dense ionized layers in the ionosphere due to neutral wind shears. *Journal of Geophysical Research*, 68(3):769–779.

Barrington, R. and Hartz, T. (1968). Satellite ionosonde records: Resonances below the cyclotron frequency. *Science*, 160(3824):181–184.

Belehaki, A., Jakowski, N., and Reinisch, B. (2004). Plasmaspheric electron content derived from GPS TEC and digisonde ionograms. *Advances in Space Research*, 33(6):833–837.

Berkner, L. and Wells, H. (1934). F-region ionosphere-investigations at low latitudes. *Terrestrial Magnetism and Atmospheric Electricity*, 39(3):215–230.

Beynon, W. and Williams, P. J. (1978). Incoherent scatter of radio waves from the ionosphere. *Reports on Progress in Physics*, 41(6):909.

Bilitza, D., Altadill, D., Truhlik, V., Shubin, V., Galkin, I., Reinisch, B., and Huang, X. (2017). International Reference Ionosphere 2016: From ionospheric climate to real-time weather predictions. *Space weather*, 15(2):418–429.

Bilitza, D., Huang, X., Reinisch, B. W., Benson, R. F., Hills, H. K., and Schar, W. B. (2004). Topside ionogram scaler with true height algorithm (TOPIST): Automated processing of ISIS topside ionograms. *Radio Science*, 39(1):1–7.

Borries, C., Jakowski, N., and Wilken, V. (2009). Storm induced large scale TIDs observed in GPS derived TEC. *Annales Geophysicae*, 27(4):1605–1612.

Bowman, G. (1990). A review of some recent work on mid-latitude spread-F occurrence as detected by ionosondes. *Journal of geomagnetism and geoelectricity*, 42(2):109–138.

Buonsanto, M. and Foster, J. (1993). Effects of magnetospheric electric fields and neutral winds on the low-middle latitude ionosphere during the March 20-21, 1990, storm. *Journal of Geophysical Research: Space Physics*, 98(A11):19133–19140.

Buonsanto, M., Foster, J., Galasso, A., Sipler, D., and Holt, J. (1990). Neutral winds and thermosphere/ionosphere coupling and energetics during the geomagnetic disturbances of March 6–10, 1989. *Journal of Geophysical Research: Space Physics*, 95(A12):21033–21050.

Burke, W., Martinis, C., Lai, P., Gentile, L., Sullivan, C., and Pfaff, R. F. (2016). C/NOFS observations of electromagnetic coupling between magnetically conjugate MSTID structures. *Journal of Geophysical Research: Space Physics*, 121(3):2569–2582.

Chapman, S. (1931). The absorption and dissociative or ionizing effect of monochromatic radiation in an atmosphere on a rotating earth. *Proceedings of the Physical Society (1926-1948)*, 43(1):26.

Chartier, A. T., Smith, N. D., Mitchell, C. N., Jackson, D. R., and Patilongo, P. J. (2012). The use of ionosondes in GPS ionospheric tomography at low latitudes. *Journal of Geophysical Research: Space Physics*, 117(A10).

Chen, J., Lei, J., Zhang, S., Wang, W., and Dang, T. (2020). A simulation study on the relationship between field-aligned and field-perpendicular plasma velocities in the ionospheric F region. *Journal of Geophysical Research: Space Physics*, 125(1):e2019JA027350.

Cherniak, I., Zakharenkova, I., Braun, J., Wu, Q., Pedatella, N., Schreiner, W., Weiss, J.-P., and Hunt, D. (2021). Accuracy assessment of the quiet-time ionospheric F2 peak parameters as derived from COSMIC-2 multi-GNSS radio occultation measurements. *J. Space Weather Space Clim.*, 11:18.

Chimonas, G. and Axford, W. (1968). Vertical movement of temperate-zone sporadic E layers. *Journal of Geophysical Research*, 73(1):111–117.

Cosgrove, R. (2007). Generation of mesoscale F layer structure and electric fields by the combined Perkins and Es layer instabilities, in simulations. *Annales Geophysicae*, 25(7):1579–1601.

Cosgrove, R. (2013). Mechanisms for E–F coupling and their manifestation. *Journal of Atmospheric and Solar-Terrestrial Physics*, 103:56–65.

Cosgrove, R. B. and Tsunoda, R. T. (2002). A direction-dependent instability of sporadic-E layers in the nighttime midlatitude ionosphere. *Geophysical Research Letters*, 29(18):11–1.

Cosgrove, R. B. and Tsunoda, R. T. (2004). Instability of the E-F coupled nighttime midlatitude ionosphere. *Journal of Geophysical Research: Space Physics*, 109(A4).

Das, S. K. and Shukla, A. K. (2011). Two-dimensional ionospheric tomography over the low-latitude indian region: An intercomparison of ART and MART algorithms. *Radio Science*, 46(02):1–13.

Drob, D. P., Emmert, J. T., Meriwether, J. W., Makela, J. J., Doornbos, E., Conde, M., Hernandez, G., Noto, J., Zawdie, K. A., McDonald, S. E., et al. (2015). An update to the Horizontal Wind Model (HWM): The quiet time thermosphere. *Earth and Space Science*, 2(7):301–319.

Ejiri, M. K., Nakamura, T., Tsuda, T. T., Nishiyama, T., Abo, M., She, C.-Y., Nishioka, M., Saito, A., Takahashi, T., Tsuno, K., et al. (2019a). Observation of synchronization between instabilities of the sporadic E layer and geomagnetic field line connected F region medium-scale traveling ionospheric disturbances. *Journal of Geophysical Research: Space Physics*, 124(6):4627–4638.

Ejiri, M. K., Nakamura, T., Tsuda, T. T., Nishiyama, T., Abo, M., Takahashi, T., Tsuno, K., Kawahara, T. D., Ogawa, T., and Wada, S. (2019b). Vertical fine structure and time evolution of plasma irregularities in the Es layer observed by a high-resolution Ca+ lidar. *Earth, Planets and Space*, 71(1):1–10.

Fan, J. and Ma, G. (2014). Characteristics of GPS positioning error with non-uniform pseudorange error. *GPS Solutions*, 18(4):615–623.

Farley Jr, D. (1959). A theory of electrostatic fields in a horizontally stratified ionosphere subject to a vertical magnetic field. *Journal of Geophysical Research*, 64(9):1225–1233.

Finlay, C. C., Kloss, C., Olsen, N., Hammer, M. D., Tøffner-Clausen, L., Grayver, A., and Kuvshinov, A. (2020). The CHAOS-7 geomagnetic field model and observed changes in the South Atlantic Anomaly. *Earth, Planets and Space*, 72(1):1–31.

Fishbach, F. (1965). A satellite method for temperature and pressure below 24 km. *Bull. Am. Meteorol. Soc*, 9(528-532):1–1.

Fjeldbo, G. and Eshleman, V. R. (1968). The atmosphere of Mars analyzed by integral inversion of the Mariner iv occultation data. *Planetary and Space Science*, 16(8):1035–1059.

Forbes, J. M., Bruinsma, S. L., Miyoshi, Y., and Fujiwara, H. (2008). A solar terminator wave in thermosphere neutral densities measured by the CHAMP satellite. *Geophysical Research Letters*, 35(14).

Golub, G. H. and Van Loan, C. F. (2013). *Matrix computations*. JHU press.

Gordon, W. E. (1958). Incoherent scattering of radio waves by free electrons with applications to space exploration by radar. *Proceedings of the IRE*, 46(11):1824–1829.

Granat, R. A. and Na, H. (2000). Estimating dynamic ionospheric changes without a priori models. *Radio Science*, 35(2):341–349.

Gylvan Meira Jr, L. (1971). Rocket measurements of upper atmospheric nitric oxide and their consequences to the lower ionosphere. *Journal of Geophysical Research*, 76(1):202–212.

Hajj, G. A. and Romans, L. J. (1998). Ionospheric electron density profiles obtained with the Global Positioning System: Results from the GPS/MET experiment. *Radio Science*, 33(1):175–190.

Haldoupis, C. (2011). *A Tutorial Review on Sporadic E Layers*, pages 381–394. Springer Netherlands, Dordrecht.

Haldoupis, C. (2012). Midlatitude sporadic E. a typical paradigm of atmosphere-ionosphere coupling. *Space science reviews*, 168(1):441–461.

Haldoupis, C. (2019). An improved ionosonde-based parameter to assess sporadic E layer intensities: A simple idea and an algorithm. *Journal of Geophysical Research: Space Physics*, 124(3):2127–2134.

Haldoupis, C., Kelley, M. C., Hussey, G. C., and Shalimov, S. (2003). Role of unstable sporadic-E layers in the generation of midlatitude spread F. *Journal of Geophysical Research: Space Physics*, 108(A12).

Haldoupis, C., Meek, C., Christakis, N., Pancheva, D., and Bourdillon, A. (2006). Ionogram height–time–intensity observations of descending sporadic E layers at mid-latitude. *Journal of atmospheric and solar-terrestrial physics*, 68(3-5):539–557.

Haldoupis, C., Pancheva, D., Singer, W., Meek, C., and MacDougall, J. (2007). An explanation for the seasonal dependence of midlatitude sporadic E layers. *Journal of Geophysical Research: Space Physics*, 112(A6).

Haldoupis, C., Schlegel, K., and Farley, D. (1996). An explanation for type 1 radar echoes from the midlatitude E-region ionosphere. *Geophysical research letters*, 23(1):97–100.

Harding, B. J., Chau, J. L., He, M., Englert, C. R., Harlander, J. M., Marr, K. D., Makela, J. J., Clahsen, M., Li, G., Ratnam, M. V., et al. (2021). Validation of ICON-MIGHTI thermospheric wind observations: 2. green-line comparisons to specular meteor radars. *Journal of Geophysical Research: Space Physics*, 126(3):e2020JA028947.

Harding, B. J., Wu, Y.-J. J., Alken, P., Yamazaki, Y., Triplett, C. C., Immel, T. J., Gasque, L. C., Mende, S. B., and Xiong, C. (2022). Impacts of the January 2022 Tonga volcanic eruption on the ionospheric dynamo: ICON-MIGHTI and Swarm observations of extreme neutral winds and currents. *Geophysical Research Letters*, 49(9):e2022GL098577.

He, M., Liu, L., Wan, W., and Zhao, B. (2011). A study on the nighttime midlatitude ionospheric trough. *Journal of Geophysical Research: Space Physics*, 116(A5).

Heelis, R. (2004). Electrodynamics in the low and middle latitude ionosphere: A tutorial. *Journal of Atmospheric and Solar-Terrestrial Physics*, 66(10):825–838.

Heelis, R., Crowley, G., Rodrigues, F., Reynolds, A., Wilder, R., Azeem, I., and Maute, A. (2012). The role of zonal winds in the production of a pre-reversal enhancement in the vertical ion drift in the low latitude ionosphere. *Journal of Geophysical Research: Space Physics*, 117(A8).

Hernández-Pajares, M., Juan, J., and Sanz, J. (1999). New approaches in global ionospheric determination using ground GPS data. *Journal of Atmospheric and Solar-Terrestrial Physics*, 61(16):1237–1247.

Hines, C. O. (1960). Internal atmospheric gravity waves at ionospheric heights. *Canadian Journal of Physics*, 38(11):1441–1481.

Hong, J., Kim, Y. H., Chung, J.-K., Ssessanga, N., and Kwak, Y.-S. (2017). Tomography reconstruction of ionospheric electron density with empirical orthonormal functions using Korea GNSS network. *Journal of Astronomy and Space Sciences*, 34(1):7–17.

Hooke, W. H. (1968). Ionospheric irregularities produced by internal atmospheric gravity waves. *Journal of Atmospheric and Terrestrial Physics*, 30(5):795–823.

Houminer, Z., Russell, C., Dyson, P., and Bennett, J. (1997). Study of sporadic-E clouds by backscatter radar. *Annales Geophysicae*, 14(10):1060–1065.

Huang, C. Y., Helmboldt, J., Park, J., Pedersen, T., and Willemann, R. (2019). Ionospheric detection of explosive events. *Reviews of Geophysics*, 57(1):78–105.

Huang, X. and Reinisch, B. (1996). Vertical electron density profiles from the digisonde network. *Advances in Space Research*, 18(6):121–129.

Hunsucker, R. D. (1982). Atmospheric gravity waves generated in the high-latitude ionosphere: A review. *Reviews of Geophysics*, 20(2):293–315.

Hysell, D., Larsen, M., Fritts, D., Laughman, B., and Sulzer, M. (2018). Major upwelling and overturning in the mid-latitude F region ionosphere. *Nature Communications*, 9(1):1–11.

Kelley, M. C. (2009). *The Earth's ionosphere: Plasma physics and electrodynamics*. Academic press.

Kelley, M. C. and Fukao, S. (1991). Turbulent upwelling of the mid-latitude ionosphere: 2. theoretical framework. *Journal of Geophysical Research: Space Physics*, 96(A3):3747–3753.

Kelley, M. C. and Makela, J. J. (2001). Resolution of the discrepancy between experiment and theory of midlatitude F-region structures. *Geophysical Research Letters*, 28(13):2589–2592.

Kelley, M. C. and Miller, C. A. (1997). Electrodynamics of midlatitude spread F 3. electrohydrodynamic waves? A new look at the role of electric fields in thermospheric wave dynamics. *Journal of Geophysical Research: Space Physics*, 102(A6):11539–11547.

Kil, H. and Paxton, L. J. (2017). Global distribution of nighttime medium-scale traveling ionospheric disturbances seen by Swarm satellites. *Geophysical Research Letters*, 44(18):9176–9182.

Kopp, E. (1997). On the abundance of metal ions in the lower ionosphere. *Journal of Geophysical Research: Space Physics*, 102(A5):9667–9674.

Kotake, N., Otsuka, Y., Ogawa, T., Tsugawa, T., and Saito, A. (2007). Statistical study of medium-scale traveling ionospheric disturbances observed with the GPS networks in Southern California. *Earth, planets and space*, 59(2):95–102.

Kunitsyn, V. E. and Tereshchenko, E. D. (2003). *Ionospheric tomography*. Springer Science & Business Media.

Lanyi, G. E. and Roth, T. (1988). A comparison of mapped and measured total ionospheric electron content using global positioning system and beacon satellite observations. *Radio Science*, 23(4):483–492.

Larsen, M. (2002). Winds and shears in the mesosphere and lower thermosphere: Results from four decades of chemical release wind measurements. *Journal of Geophysical Research: Space Physics*, 107(A8):SIA–28.

Lee, W. K., Kil, H., and Paxton, L. J. (2021). Global distribution of nighttime MSTIDs and its association with E region irregularities seen by CHAMP satellite. *Journal of Geophysical Research: Space Physics*, 126(5):e2020JA028836.

Liou, Y.-A. (2010). *Radio occultation method for remote sensing of the atmosphere and ionosphere*. BoD–Books on Demand.

Liu, Y., Zhou, C., Tang, Q., Kong, J., Gu, X., Ni, B., Yao, Y., and Zhao, Z. (2019). Evidence of mid-and low-latitude nighttime ionospheric E–F coupling: Coordinated observations of sporadic E layers, F-region field-aligned irregularities, and medium-scale traveling ionospheric disturbances. *IEEE Transactions on Geoscience and Remote Sensing*, 57(10):7547–7557.

Liu, Y., Zhou, C., Xu, T., Wang, Z., Tang, Q., Deng, Z., and Chen, G. (2020). Investigation of midlatitude nighttime ionospheric E-F coupling and interhemispheric coupling by using COSMIC GPS radio occultation measurements. *Journal of Geophysical Research: Space Physics*, 125(3):e2019JA027625.

Lu, W., Ma, G., and Wan, Q. (2021a). A review of voxel-based computerized ionospheric tomography with GNSS ground receivers. *Remote Sensing*, 13(17):3432.

Lu, W., Ma, G., Wan, Q., Li, J., Wang, X., Fu, W., and Maruyama, T. (2021b). Virtual reference station-based computerized ionospheric tomography. *GPS Solutions*, 25(1):1–12.

Lühr, H., Rother, M., Maus, S., Mai, W., and Cooke, D. (2003). The diamagnetic effect of the equatorial Appleton anomaly: Its characteristics and impact on geomagnetic field modeling. *Geophysical Research Letters*, 30(17).

Luo, J., Liu, H., and Xu, X. (2021). Sporadic E morphology based on COSMIC radio occultation data and its relationship with wind shear theory. *Earth, Planets and Space*, 73(1):1–17.

Ma, G., Gao, W., Li, J., Chen, Y., and Shen, H. (2014). Estimation of GPS instrumental biases from small scale network. *Advances in Space Research*, 54(5):871–882.

Ma, G. and Maruyama, T. (2003). Derivation of TEC and estimation of instrumental biases from GEONET in Japan. *Annales Geophysicae*, 21(10):2083–2093.

Ma, X., Maruyama, T., Ma, G., and Takeda, T. (2005). Determination of GPS receiver differential biases by neural network parameter estimation method. *Radio Science*, 40(1):1–13.

Maeda, J. and Heki, K. (2014). Two-dimensional observations of midlatitude sporadic E irregularities with a dense GPS array in Japan. *Radio Science*, 49(1):28–35.

Maeda, J. and Heki, K. (2015). Morphology and dynamics of daytime mid-latitude sporadic-E patches revealed by GPS total electron content observations in Japan. *Earth, Planets and Space*, 67(1):1–9.

Makela, J. J., Baughman, M., Navarro, L. A., Harding, B. J., Englert, C. R., Harlander, J. M., Marr, K. D., Benkhaldoun, Z., Kaab, M., and Immel, T. J. (2021). Validation of ICON-MIGHTI thermospheric wind observations: 1. Nighttime red-line ground-based fabry-perot interferometers. *Journal of Geophysical Research: Space Physics*, 126(2):e2020JA028726.

Maksyutin, S., Sherstyukov, O., and Fahrutdinova, A. (2001). Dependence of sporadic-E layer and lower thermosphere dynamics on solar activity. *Advances in Space Research*, 27(6-7):1265–1270.

Mannucci, A., Wilson, B., Yuan, D., Ho, C., Lindqwister, U., and Runge, T. (1998). A global mapping technique for GPS-derived ionospheric total electron content measurements. *Radio science*, 33(3):565–582.

Martinis, C., Baumgardner, J., Mendillo, M., Wroten, J., MacDonald, T., Kosch, M., Lazzarin, M., and Umbriaco, G. (2019). First conjugate observations of medium-scale traveling ionospheric disturbances (MSTIDs) in the Europe-Africa longitude sector. *Journal of Geophysical Research: Space Physics*, 124(3):2213–2222.

Maruyama, T., Fukao, S., and Yamamoto, M. (2000). A possible mechanism for echo striation generation of radar backscatter from midlatitude sporadic E. *Radio Science*, 35(5):1155–1164.

Maruyama, T., Hozumi, K., Ma, G., Supnithi, P., Tongkasem, N., and Wan, Q. (2021). Double-thin-shell approach to deriving total electron content from GNSS signals and implications for ionospheric dynamics near the magnetic equator. *Earth, Planets and Space*, 73(1):1–21.

Maruyama, T., Saito, S., Yamamoto, M., and Fukao, S. (2006). Simultaneous observation of sporadic E with a rapid-run ionosonde and VHF coherent backscatter radar. *Annales Geophysicae*, 24(1):153–162.

Mathews, J. (1998). Sporadic E: current views and recent progress. *Journal of atmospheric and solar-terrestrial physics*, 60(4):413–435.

McNamara, L. F. (1991). *The ionosphere: communications, surveillance, and direction finding*. Krieger publishing company.

Mendillo, M., Baumgardner, J., Nottingham, D., Aarons, J., Reinisch, B., Scali, J., and Kelley, M. (1997). Investigations of thermospheric-ionospheric dynamics with 6300-å images from the Arecibo Observatory. *Journal of Geophysical Research: Space Physics*, 102(A4):7331–7343.

Miller, K. and Smith, L. (1975). Horizontal structure of midlatitude sporadic-E layers observed by incoherent scatter radar. *Radio Science*, 10(3):271–276.

Miyoshi, Y., Fujiwara, H., Forbes, J. M., and Bruinsma, S. L. (2009). Solar terminator wave and its relation to the atmospheric tide. *Journal of Geophysical Research: Space Physics*, 114(A7).

Muafiry, I. N., Heki, K., and Maeda, J. (2018). 3d tomography of midlatitude sporadic-E in Japan from GNSS-TEC data. *Earth, Planets and Space*, 70(1):1–12.

Mungufeni, P., Kim, Y. H., and Ssessenga, N. (2021). Observations of ionospheric irregularities and its correspondence with sporadic E occurrence over South Korea and Japan. *Advances in Space Research*, 67(7):2207–2218.

Narayanan, V., Shiokawa, K., Otsuka, Y., and Neudegg, D. (2018). On the role of thermospheric winds and sporadic E layers in the formation and evolution of electrified MSTIDs in geomagnetic conjugate regions. *Journal of Geophysical Research: Space Physics*, 123(8):6957–6980.

Narayanan, V., Shiokawa, K., Otsuka, Y., and Saito, S. (2014). Airglow observations of nighttime medium-scale traveling ionospheric disturbances from Yonaguni: Statistical characteristics and low-latitude limit. *Journal of Geophysical Research: Space Physics*, 119(11):9268–9282.

Nishimura, Y., Verkhoglyadova, O., Deng, Y., and Zhang, S.-R. (2021). *Cross-scale Coupling and Energy Transfer in the Magnetosphere-ionosphere-thermosphere System*. Elsevier.

Norberg, J., Roininen, L., Vierinen, J., Amm, O., McKay-Bukowski, D., and Lehtinen, M. (2015). Ionospheric tomography in Bayesian framework with Gaussian Markov random field priors. *Radio Science*, 50(2):138–152.

Nygren, T., Jalonen, L., Oksman, J., and Turunen, T. (1984). The role of electric field and neutral wind direction in the formation of sporadic E-layers. *Journal of atmospheric and terrestrial physics*, 46(4):373–381.

Olsen, N., Hulot, G., Lesur, V., Finlay, C. C., Beggan, C., Chulliat, A., Sabaka, T. J., Floberghagen, R., Friis-Christensen, E., Haagmans, R., et al. (2015). The Swarm initial field model for the 2014 geomagnetic field. *Geophysical Research Letters*, 42(4):1092–1098.

Otsuka, Y. (2021). Medium-scale traveling ionospheric disturbances. *Ionosphere Dynamics and Applications*, pages 421–437.

Otsuka, Y., Kotake, N., Shiokawa, K., Ogawa, T., Tsugawa, T., and Saito, A. (2011). Statistical study of medium-scale traveling ionospheric disturbances observed with a GPS receiver network in Japan. In *Aeronomy of the Earth's Atmosphere and Ionosphere*, pages 291–299. Springer.

Otsuka, Y., Onoma, F., Shiokawa, K., Ogawa, T., Yamamoto, M., and Fukao, S. (2007). Simultaneous observations of nighttime medium-scale traveling ionospheric disturbances and E region field-aligned irregularities at midlatitude. *Journal of Geophysical Research: Space Physics*, 112(A6).

Otsuka, Y., Shinbori, A., Tsugawa, T., and Nishioka, M. (2021). Solar activity dependence of medium-scale traveling ionospheric disturbances using GPS receivers in Japan. *Earth, Planets and Space*, 73(1):1–11.

Otsuka, Y., Shiokawa, K., Ogawa, T., and Wilkinson, P. (2002). Geomagnetic conjugate observations of equatorial airglow depletions. *Geophysical Research Letters*, 29(15):43–1.

Otsuka, Y., Shiokawa, K., Ogawa, T., and Wilkinson, P. (2004). Geomagnetic conjugate observations of medium-scale traveling ionospheric disturbances at midlatitude using all-sky airglow imagers. *Geophysical Research Letters*, 31(15).

Otsuka, Y., Suzuki, K., Nakagawa, S., Nishioka, M., Shiokawa, K., and Tsugawa, a. (2013). Gps observations of medium-scale traveling ionospheric disturbances over Europe. *Annales Geophysicae*, 31(2):163–172.

Otsuka, Y., Tani, T., Tsugawa, T., Ogawa, T., and Saito, A. (2008). Statistical study of relationship between medium-scale traveling ionospheric disturbance and sporadic E layer activities in summer night over Japan. *Journal of Atmospheric and Solar-Terrestrial Physics*, 70(17):2196–2202.

Pancheva, D., Haldoupis, C., Meek, C., Manson, A., and Mitchell, N. (2003). Evidence of a role for modulated atmospheric tides in the dependence of sporadic e layers on planetary waves. *Journal of Geophysical Research: Space Physics*, 108(A5).

Park, J., Lühr, H., Kervalishvili, G., Rauberg, J., Michaelis, I., Stolle, C., and Kwak, Y.-S. (2015). Nighttime magnetic field fluctuations in the topside ionosphere at midlatitudes and their relation to medium-scale traveling ionospheric disturbances: The spatial structure and scale sizes. *Journal of Geophysical Research: Space Physics*, 120(8):6818–6830.

Park, J., Lühr, H., Stolle, C., Rodriguez-Zuluaga, J., Knudsen, D. J., Burchill, J. K., and Kwak, Y.-S. (2016). Statistical survey of nighttime midlatitude magnetic fluctuations: Their source location and Poynting flux as derived from the Swarm constellation. *Journal of Geophysical Research: Space Physics*, 121(11):11–235.

Park, J., Lühr, H., Stolle, C., Rother, M., Min, K., and Michaelis, I. (2009a). The characteristics of field-aligned currents associated with equatorial plasma bubbles as observed by the CHAMP satellite. In *Annales Geophysicae*, volume 27, pages 2685–2697. Copernicus GmbH.

Park, J., Lühr, H., Stolle, C., Rother, M., Min, K. W., Chung, J.-K., Kim, Y. H., Michaelis, I., and Noja, M. (2009b). Magnetic signatures of medium-scale traveling ionospheric disturbances as observed by CHAMP. *Journal of Geophysical Research: Space Physics*, 114(A3).

Perkins, F. (1973). Spread F and ionospheric currents. *Journal of Geophysical Research*, 78(1):218–226.

Pi, X., Mannucci, A., Lindqwister, U., and Ho, C. (1997). Monitoring of global ionospheric irregularities using the worldwide GPS network. *Geophysical Research Letters*, 24(18):2283–2286.

Pitteway, M. and Hines, C. (1963). The viscous damping of atmospheric gravity waves. *Canadian Journal of Physics*, 41(12):1935–1948.

Plane, J. M. (2003). Atmospheric chemistry of meteoric metals. *Chemical reviews*, 103(12):4963–4984.

Qian, L., Solomon, S. C., Roble, R. G., and Kane, T. J. (2008). Model simulations of global change in the ionosphere. *Geophysical Research Letters*, 35(7).

Ratcliffe, J. A. et al. (1972). *An introduction to ionosphere and magnetosphere*. CUP Archive.

Raymund, T. D., Austen, J. R., Franke, S., Liu, C., Klobuchar, J., and Stalker, J. (1990). Application of computerized tomography to the investigation of ionospheric structures. *Radio Science*, 25(5):771–789.

Razin, M. R. G. and Voosoghi, B. (2016). Regional application of multi-layer artificial neural networks in 3-D ionosphere tomography. *Advances in Space Research*, 58(3):339–348.

Rieger, M. and Leitinger, R. (2002). Assessment of TID activity from GPS phase data collected in a dense network of GPS receivers. *Acta Geodaetica et Geophysica Hungarica*, 37(2-3):327–341.

Rishbeth, H. and Garriott, O. K. (1969). Introduction to ionospheric physics. *Introduction to ionospheric physics*.

Rius, A., Ruffini, G., and Cucurull, L. (1997). Improving the vertical resolution of ionospheric tomography with GPS occultations. *Geophysical Research Letters*, 24(18):2291–2294.

Rocken, C., Anthes, R., Exner, M., Hunt, D., Sokolovskiy, S., Ware, R., Gorbunov, M., Schreiner, W., Feng, D., Herman, B., et al. (1997). Analysis and validation of GPS/MET data in the neutral atmosphere. *Journal of Geophysical Research: Atmospheres*, 102(D25):29849–29866.

Rodger, A. and Jarvis, M. (2000). Ionospheric research 50 years ago, today and tomorrow. *Journal of Atmospheric and Solar-Terrestrial Physics*, 62(17-18):1629–1645.

Rodrigues, F. d. S. (2008). Incoherent and coherent scatter radar studies of the equatorial F region.

Saito, A., Fukao, S., and Miyazaki, S. (1998a). High resolution mapping of TEC perturbations with the GSI GPS network over Japan. *Geophysical research letters*, 25(16):3079–3082.

Saito, A., Iyemori, T., Blomberg, L., Yamamoto, M., and Takeda, M. (1998b). Conjugate observations of the mid-latitude electric field fluctuations with the MU radar and the Freja satellite. *Journal of atmospheric and solar-terrestrial physics*, 60(1):129–140.

Saito, A., Iyemori, T., Sugiura, M., Maynard, N., Aggson, T., Brace, L., Takeda, M., and Yamamoto, M. (1995). Conjugate occurrence of the electric field fluctuations in the nighttime midlatitude ionosphere. *Journal of Geophysical Research: Space Physics*, 100(A11):21439–21451.

Saito, A., Nishimura, M., Yamamoto, M., Fukao, S., Kubota, M., Shiokawa, K., Otsuka, Y., Tsugawa, T., Ogawa, T., Ishii, M., et al. (2001). Traveling ionospheric disturbances detected in the FRONT campaign. *Geophysical research letters*, 28(4):689–692.

Saito, A., Nishimura, M., Yamamoto, M., Fukao, S., Tsugawa, T., Otsuka, Y., and Miyazaki, S. (2002). Observations of traveling ionospheric disturbances and 3-m scale irregularities in the nighttime F-region ionosphere with the MU radar and a GPS network. *Earth, planets and space*, 54(1):31–44.

Saito, S., Suzuki, S., Yamamoto, M., Saito, A., and Chen, C.-H. (2017). Real-time ionosphere monitoring by three-dimensional tomography over Japan. *Navigation: Journal of the Institute of Navigation*, 64(4):495–504.

Saito, S., Yamamoto, M., and Hashiguchi, H. (2008). Imaging observations of nighttime mid-latitude f-region field-aligned irregularities by an MU radar ultra-multi-channel system. *Annales geophysicae*, 26(8):2345–2352.

Saito, S., Yamamoto, M., Hashiguchi, H., Maegawa, A., and Saito, A. (2007). Observational evidence of coupling between quasi-periodic echoes and medium scale traveling ionospheric disturbances. *Annales Geophysicae*, 25(10):2185–2194.

Sardon, E., Rius, A., and Zarraoa, N. (1994). Estimation of the transmitter and receiver differential biases and the ionospheric total electron content from Global Positioning System observations. *Radio science*, 29(03):577–586.

Šauli, P. and Bourdillon, A. (2008). Height and critical frequency variations of the sporadic-E layer at midlatitudes. *Journal of atmospheric and solar-terrestrial physics*, 70(15):1904–1910.

Schaer, S., Beutler, G., Mervart, L., Rothacher, M., and Wild, U. (1996). Global and regional ionosphere models using the GPS double difference phase observable. In *Proceedings of the IGS Workshop*.

Scherliess, L., Schunk, R. W., Sojka, J. J., and Thompson, D. C. (2004). Development of a physics-based reduced state Kalman filter for the ionosphere. *Radio Science*, 39(1):1–12.

Schreiner, W. S., Sokolovskiy, S. V., Rocken, C., and Hunt, D. C. (1999). Analysis and validation of GPS/MET radio occultation data in the ionosphere. *Radio Science*, 34(4):949–966.

Schunk, R. and Nagy, A. F. (1978). Electron temperatures in the F region of the ionosphere: Theory and observations. *Reviews of Geophysics*, 16(3):355–399.

Shiokawa, K., Ihara, C., Otsuka, Y., and Ogawa, T. (2003a). Statistical study of nighttime medium-scale traveling ionospheric disturbances using midlatitude airglow images. *Journal of Geophysical Research: Space Physics*, 108(A1).

Shiokawa, K., Otsuka, Y., Ihara, C., Ogawa, T., and Rich, F. (2003b). Ground and satellite observations of nighttime medium-scale traveling ionospheric disturbance at midlatitude. *Journal of Geophysical Research: Space Physics*, 108(A4).

Shubin, V. (2015). Global median model of the F2-layer peak height based on ionospheric radio-occultation and ground-based Digisonde observations. *Advances in Space Research*, 56(5):916–928.

Shubin, V., Karpachev, A., and Tsybulya, K. (2013). Global model of the F2 layer peak height for low solar activity based on GPS radio-occultation data. *Journal of Atmospheric and Solar-Terrestrial Physics*, 104:106–115.

Shukla, A. K., Das, S., Nagori, N., Sivaraman, M., and Bandyopadhyay, K. (2009). Two-shell ionospheric model for indian region: A novel approach. *IEEE transactions on geoscience and remote sensing*, 47(8):2407–2412.

Sinno, K., Ouchi, C., and Nemoto, C. (1964). Structure and movement of Es detected by LORAN observations. *Journal of geomagnetism and geoelectricity*, 16(2):75–88.

Ssessanga, N. (2018). A tomographic Investigation of mid-latitude nighttime ionospheric E-F coupling. In *42nd COSPAR Scientific Assembly*, volume 42, pages C1.5–7–18.

Ssessanga, N., Kim, Y. H., and Jeong, S.-H. (2017). A statistical study on the F2 layer vertical variation during nighttime medium-scale traveling ionospheric disturbances. *Journal of Geophysical Research: Space Physics*, 122(3):3586–3601.

Ssessanga, N., Kim, Y. H., and Kim, E. (2015). Vertical structure of medium-scale traveling ionospheric disturbances. *Geophysical Research Letters*, 42(21):9156–9165.

Ssessanga, N., Yamamoto, M., Saito, S., Saito, A., and Nishioka, M. (2021). Complementing regional ground GNSS-STEC computerized ionospheric tomography (CIT) with ionosonde data assimilation. *GPS solutions*, 25(3):1–15.

Sun, W., Ning, B., Hu, L., Yue, X., Zhao, X., Lan, J., Zhu, Z., Huang, Z., and Wu, Z. (2020). The evolution of complex Es observed by multi instruments over low-latitude China. *Journal of Geophysical Research: Space Physics*, 125(8):e2019JA027656.

Sun, W., Zhao, X., Hu, L., Yang, S., Xie, H., Chang, S., Ning, B., Li, J., Liu, L., and Li, G. (2021). Morphological characteristics of thousand-kilometer-scale Es structures over China. *Journal of Geophysical Research: Space Physics*, 126(2):e2020JA028712.

Tepley, C., Robles, E., García, R., Santos, P., Brum, C., and Burnside, R. (2011). Directional trends in thermospheric neutral winds observed at Arecibo during the past three solar cycles. *Journal of Geophysical Research: Space Physics*, 116(A2).

Tsugawa, T., Nishioka, M., Ishii, M., Hozumi, K., Saito, S., Shinbori, A., Otsuka, Y., Saito, A., Buhari, S. M., Abdullah, M., et al. (2018). Total electron content observations by dense regional and worldwide international networks of gnss. *Journal of Disaster Research*, 13(3):535–545.

Tsunoda, R. T. (2006). On the coupling of layer instabilities in the nighttime midlatitude ionosphere. *Journal of Geophysical Research: Space Physics*, 111(A11).

Tsunoda, R. T. and Cosgrove, R. B. (2001). Coupled electrodynamics in the nighttime midlatitude ionosphere. *Geophysical Research Letters*, 28(22):4171–4174.

Tsunoda, R. T., Cosgrove, R. B., and Ogawa, T. (2004). Azimuth-dependent Es layer instability: A missing link found. *Journal of Geophysical Research: Space Physics*, 109(A12).

Tsunoda, R. T., Fukao, S., and Yamamoto, M. (1994). On the origin of quasi-periodic radar backscatter from midlatitude sporadic E. *Radio Science*, 29(01):349–365.

Valladares, C. E. and Sheehan, R. (2016). Observations of conjugate MSTIDs using networks of GPS receivers in the American sector. *Radio Science*, 51(9):1470–1488.

Wan, X., Xiong, C., Wang, H., Zhang, K., and Yin, F. (2020). Spatial characteristics on the occurrence of the nighttime midlatitude medium-scale traveling ionospheric disturbance at topside ionosphere revealed by the Swarm satellite. *Journal of Geophysical Research: Space Physics*, 125(8):e2019JA027739.

Whitehead, J. (1961). The formation of the sporadic-E layer in the temperate zones. *Journal of Atmospheric and Terrestrial Physics*, 20(1):49–58.

Whitehead, J. (1972). The structure of sporadic E from a radio experiment. *Radio Science*, 7(3):355–358.

Whitehead, J. (1989). Recent work on mid-latitude and equatorial sporadic-E. *Journal of Atmospheric and Terrestrial Physics*, 51(5):401–424.

Woodman, R. and Hagfors, T. (1969). Methods for the measurement of vertical ionospheric motions near the magnetic equator by incoherent scattering. *Journal of Geophysical Research*, 74(5):1205–1212.

Wu, D. L., Ao, C. O., Hajj, G. A., de La Torre Juarez, M., and Mannucci, A. J. (2005). Sporadic E morphology from GPS-CHAMP radio occultation. *Journal of Geophysical Research: Space Physics*, 110(A1).

Xie, H., Li, G., Zhao, X., Ding, F., Yan, C., Yang, G., and Ning, B. (2020). Coupling between E region quasi-periodic echoes and F region medium-scale traveling ionospheric disturbances at low latitudes. *Journal of Geophysical Research: Space Physics*, 125(5):e2019JA027720.

Xiong, P., Zhai, D., Long, C., Zhou, H., Zhang, X., and Shen, X. (2021). Long short-term memory neural network for ionospheric total electron content forecasting over China. *Space Weather*, 19(4):e2020SW002706.

Yamamoto, M., Itsuki, T., Kishimoto, T., Tsunoda, R. T., Pfaff, R. F., and Fukao, S. (1998). Comparison of E-region electric fields observed with a sounding rocket and a Doppler radar in the SEEK campaign. *Geophysical research letters*, 25(11):1773–1776.

Yamamoto, M., Komoda, N., Fukao, S., Tsunoda, R. T., Ogawa, T., and Tsuda, T. (1994). Spatial structure of the E region field-aligned irregularities revealed by the MU radar. *Radio Science*, 29(1):337–347.

Yang, T.-Y., Kwak, Y.-S., Kil, H., Lee, Y.-S., Lee, W. K., and Lee, J.-j. (2015). Occurrence climatology of F region field-aligned irregularities in middle latitudes as observed by a 40.8 MHz coherent scatter radar in Daejeon, South Korea. *Journal of Geophysical Research: Space Physics*, 120(11):10107–10115.

Yao, Y., Kong, J., and Tang, J. (2014). A new ionosphere tomography algorithm with two-grid virtual observations constraints and three-dimensional velocity profile. *IEEE Transactions on geoscience and remote sensing*, 53(5):2373–2383.

Yizengaw, E., Moldwin, M., Galvan, D., Iijima, B., Komjathy, A., and Mannucci, A. (2008). Global plasmaspheric TEC and its relative contribution to GPS TEC. *Journal of Atmospheric and Solar-Terrestrial Physics*, 70(11-12):1541–1548.

Yokoyama, T. (2013). Scale dependence and frontal formation of nighttime medium-scale traveling ionospheric disturbances. *Geophysical research letters*, 40(17):4515–4519.

Yokoyama, T. (2014). Hemisphere-coupled modeling of nighttime medium-scale traveling ionospheric disturbances. *Advances in Space Research*, 54(3):481–488.

Yokoyama, T. and Hysell, D. L. (2010). A new midlatitude ionosphere electrodynamics coupling model (MIECO): Latitudinal dependence and propagation of medium-scale traveling ionospheric disturbances. *Geophysical Research Letters*, 37(8).

Yokoyama, T., Hysell, D. L., Otsuka, Y., and Yamamoto, M. (2009). Three-dimensional simulation of the coupled Perkins and Es-layer instabilities in the nighttime midlatitude ionosphere. *Journal of Geophysical Research: Space Physics*, 114(A3).

Yokoyama, T., Jin, H., and Shinagawa, H. (2015). West wall structuring of equatorial plasma bubbles simulated by three-dimensional HIRB model. *Journal of Geophysical Research: Space Physics*, 120(10):8810–8816.

Yokoyama, T., Otsuka, Y., Ogawa, T., Yamamoto, M., and Hysell, D. L. (2008). First three-dimensional simulation of the Perkins instability in the nighttime midlatitude ionosphere. *Geophysical Research Letters*, 35(3).

Yokoyama, T. and Stolle, C. (2017). Low and midlatitude ionospheric plasma density irregularities and their effects on geomagnetic field. *Space Science Reviews*, 206(1):495–519.

Yokoyama, T., Yamamoto, M., Fukao, S., and Cosgrove, R. (2004). Three-dimensional simulation on generation of polarization electric field in the midlatitude E-region ionosphere. *Journal of Geophysical Research: Space Physics*, 109(A1).

Yokoyama, T., Yamamoto, M., Fukao, S., Takahashi, T., and Tanaka, M. (2005). Numerical simulation of mid-latitude ionospheric E-region based on SEEK and SEEK-2 observations. In *Annales geophysicae*, volume 23, pages 2377–2384. Copernicus GmbH.

Zeng, Z. and Sokolovskiy, S. (2010). Effect of sporadic E clouds on GPS radio occultation signals. *Geophysical Research Letters*, 37(18).

List of Publications

Refereed Journals

1. Fu, W., Yokoyama, T., Ssessanga, N., Ma, G., & Yamamoto, M. (2022). Study of nighttime midlatitude E-F coupling in geomagnetic conjugate regions using multi-source data. *Journal of Geophysical Research: Space Physics*, under review.

2. Fu, W., Yokoyama, T., Ssessanga, N., Yamamoto, M., & Liu, P. (2022). On using a double-thin-shell approach and TEC perturbation component to sound night-time mid-latitude E–F coupling. *Earth, Planets and Space*, 74(1), 1-17. doi: 10.1186/s40623-022-01639-w

3. Fu, W., Ssessanga, N., Yokoyama, T., & Yamamoto, M. (2021). High-resolution 3-D imaging of daytime sporadic-E over Japan by using GNSS TEC and ionosondes. *Space Weather*, 19(12), e2021SW002878. doi: 10.1029/2021SW002878

4. Fu, W., Ma, G., Lu, W., Maruyama, T., Li, J., Wan, Q., Fan J., & Wang, X. (2021). Improvement of global ionospheric TEC derivation with multi-source data in modip latitude. *Atmosphere*, 12(4), 434. doi: 10.3390/atmos12040434

5. Liu, P., Yokoyama, T., Fu, W., & Yamamoto, M. (2022). Statistical analysis of medium-scale traveling ionospheric disturbances over Japan based on deep learning instance segmentation. *Space Weather*, e2022SW003151. doi: 10.1029/2022SW003151

6. Lu, W., Ma, G., Wan, Q., Li, J., Wang, X., Fu, W., & Maruyama, T. (2021). Virtual reference station-based computerized ionospheric tomography. *GPS Solutions*, 25(1), 1-12. doi: 10.1007/s10291-020-01039-1

Oral Presentations

1. Fu, W., Yokoyama, T., Ssessanga, N., Ma, G., and Yamamoto, M.. Study of nighttime midlatitude E-F coupling in geomagnetic conjugate regions using multi-source data. The 152 th SGEPSS General Assembly and Outreach Event, Sagamihara, Japan. Nov. 3–7, 2022.

2. Fu, W., Ssessanga, N., Yokoyama, T., Peng Liu, and Yamamoto, M.. 3-D imaging of nighttime E-F coupling over Japan by using ground-based GNSS-TEC and ionosondes. 16th International Symposium on Equatorial Aeronomy, Uji, Japan. Sep. 12–16, 2022.

3. Fu, W., Ssessanga, N., Yokoyama, T., Peng Liu, and Yamamoto, M.. 3-D tomography of GEONET for nighttime E-F coupling over Japan. Team Meeting of the International Space Science Institute, online. Jul. 11–15, 2022.

4. Fu, W., Yokoyama, T., Ssessanga, N., and Yamamoto, M.. Sounding of E-F coupling over Japan by using ground-based GNSS TEC with a double-thin-shell approach. Japan Geoscience Union Meeting 2022, Chiba, Japan. May 22–27, 2022.

5. Fu, W., Ssessanga, N., Yokoyama, T., and Yamamoto, M.. 3-D imaging of daytime mid-latitude sporadic E over Japan with ground-based GNSS data. The 150th SGEPSS General Assembly and Outreach Event, online. Oct. 31–Nov. 4, 2021.

6. Fu, W., Ssessanga, N., Yokoyama, T., and Yamamoto, M.. 3-D imaging of daytime mid-latitude sporadic E over Japan with ground-based GNSS data. The 15th MUR-EAR Symposium, online. Sep. 9–10, 2021